

# Fluid descriptions of externally heated tokamak plasmas

Zhisong Qu

A thesis submitted for the degree of  
Doctor of Philosophy of  
The Australian National University

November, 2016

©Copyright by Zhisong Qu 2016

---

# Declaration

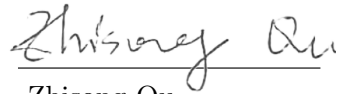
---

This thesis is an account of research undertaken between October 2012 and November 2016 at Research School of Physics and Engineering, the Australian National University, Canberra ACT 2601, Australia. Except where acknowledged in the customary manner, the material presented in this thesis is, to the best of my knowledge, original and has not been submitted in whole or part for a degree in any university.

The supervisory panel of this thesis includes

- A/Prof. Matthew J. Hole (ANU, Panel chair),
- Dr. Michael Fitzgerald (Culham Centre for Fusion Energy, Advisor),
- Em. Prof. Robert L. Dewar (ANU, Advisor),
- Dr. Boyd D. Blackwell (ANU, ANSTO co-supervisor).

Part of this thesis was accomplished in collaboration with Dr. Brett Layden (ANU).



Zhisong Qu

November 2016



---

# Publications

---

This thesis is a thesis by compilation. Its main body consists of five of my publications as follows.

- Chapter 2: Z.S. Qu, M. Fitzgerald, M.J. Hole (2014). *Analysing the impact of anisotropy pressure on tokamak equilibria*, **Plasma Phys. Control. Fusion**, 56, 075007.  
90% my work, 90% my writing
- Chapter 3: Z.S. Qu, M.J. Hole, M. Fitzgerald (2015). *Modeling the effect of anisotropic pressure on tokamak plasmas normal modes and continuum using fluid approaches*, **Plasma Phys. Control. Fusion**, 57, 095005.  
90% my work, 90% my writing
- Chapter 4: B. Layden, Z.S. Qu, M. Fitzgerald, M.J. Hole (2016). *Impact of pressure anisotropy on magnetic configuration and stability*, **Nuclear Fusion**, 56, 112017.  
35% my work, 30% my writing
- Chapter 5: Z.S. Qu, M.J. Hole, M. Fitzgerald (2016). *Energetic Geodesic Acoustic Modes Associated with Two-Stream-like Instabilities in Tokamak Plasmas*, **Phys. Rev. Lett.**, 116, 095004.  
90% my work, 90% my writing
- Chapter 6: Z.S. Qu, M.J. Hole, M. Fitzgerald (2016). *Linear radial structure of reactive energetic geodesic acoustic modes*, **Plasma Phys. Control. Fusion**, 57, 055018  
90% my work, 90% my writing

One of the publications is mentioned in Section 1.2.6 and relevant to the topic, but not included in the main body.

- M. Fitzgerald, M.J. Hole Z.S. Qu (2014). *Magnetohydrodynamic normal mode analysis of plasma with equilibrium pressure anisotropy*, **Plasma Phys. Control. Fusion**, 57, 025018.  
10% my work



---

# Acknowledgements

---

First of all, I would like to give my wholehearted thank to my supervisor Matthew Hole, for the enormous amount of time and efforts he spent on my research and education. I will never forget the time when I gave the first draft of my first paper to him: the physics was a mess, the English was crap, everything was disordered. Matthew didn't tear it apart which I would if given a chance, he instead helped me patiently to revise it for at least six times, until it finally got better. It was not just to improve the writing, he told me to observe my progress step by step and see deeply why and how to get better in each iteration. I also appreciate greatly his attitude to consider me as a colleague, a friend rather than a student and his help in my future career development. I am involved in his conference abstract submission, funding application and decision making process, and also getting funding support to attend conferences, to visit another institute, and to go to the Carolus Magnus Summer School. These really helped me to see more, to know more, to stand beyond the point of view of a PhD student. I would not have achieved anything I have done today without him.

I am also indebted to my advisor Michael Fitzgerald. I can still remember the many afternoons I spent in his office asking silly, basic questions, and I always got nice and friendly, but pin-pointed answers. To be honest, it was him on whom I build up the foundation of my world of plasma physics. Our great collaboration went on after he moved to Culham. He continued to offer me good physics insights as an advisor and considerations as a friend. He shared with me the most cutting-edge research topics, like the EGAMs, which I was able to do research on, and any job opportunities he went by. I really appreciate everything he has done for me.

Bob Dewar is the wise godfather of our group and has very deep physics insights on many aspect of plasma physics. His advice helped me a lot when I faced some difficult physics problems, the fluid closure problem and if they satisfy the first and second law of thermodynamics, for instance. I am grateful to my ANSTO co-supervisor Boyd Blackwell, who enabled the application of my anisotropic and flowing fluid theory designed for a high temperature tokamak, to the MAGPIE linear machine with low temperature.

Luckily I had a chance to work with Boris Breizman during my visit to the University of Texas at Austin, and by Skype and emails afterwards. Working with him is as enjoyable as drinking a great wine. He always tried to dig out the very basics of physics understandings. He helped me to refresh and advance my view and knowledge of plasma physics from the most fundamental level. I have also learned to be strict, to be consistent, and to really looking for the physics instead of publications.

All my co-authors and I gratefully acknowledge Dr. Guido Huysmans and Dr. Sergei Sharapov for providing the MISHKA and HELENA source code and their permission to use the name MISHKA. We would also like to thank Dr. Guoyong Fu and Dr. Alessandro Biancalani for the fruitful discussions on EGAMs, and Dr. Michael Van Zeeland and Dr. Raffi Nazikian for DIII-D data. We are indebted to Prof. Herb Berk for suggesting the boundary conditions and Haijie Zuo for suggesting the Perfectly Matched Layer method.

Many thanks to all my other colleagues, regardless where you are now. I would like to

thank Lei, for being my big brother and teaching me many things in my first year. Thank Brett, for the days we were working together to address the heart-breaking HAGIS issues. Thank Hooman, for enduring my horrible teaching. Thank George, Sebastian, Alexis, Craig, Adelle, Ying and Qixiang, for helping me to solve my problems in life and in research, and for the laughs and fun we had. Thank Graham and Greg, for answering my stupid questions. Thank Uyen and Karen, for giving me the best administrative support. Thank Julie and James, for being my IT support. I also want to give a big thank you to my friends Rouran, Junhong, Xiaoming and Haitao, my housemates Jiahao, Qian, Ziqi and Chenxiang, as well as all other friends in RSPE and Graduate House. My tedious PhD life becomes more colorful and enjoyable because of you.

Finally, I would like to give my special thanks to my parents, who confirm my decision to study plasma physics and are always on my back to support me. I am ashamed that I haven't spent enough time with them since high school. I give the same special thanks to my love Cuiying, to be the warmth in my heart, to help me through the most depressed period and to wait for me in China for two and a half years until I finish my PhD. I owe all of you a lot.

I acknowledge the funding support from the China Scholarship Council to enable my study in Australia. I would like to thank AINSE Ltd. for providing funding assistance (Award-PGRA) to enable the study on MAGPIE. I have also received funding supports from the ANU Vice-Chancellor Travel Grant, Australian ARC Projects No. DP1093797 and No. FT0991899, and from Centre of Plasmas and Fluids and the former Plasma Research Laboratory, of Research School of Physics and Engineering, ANU. This work was part funded by the RCUK Energy Programme (Grant No. EP/I501045).

Let me conclude my acknowledgements with the funny words I found in this thesis template: *I would like to thank my lucky stars, and the cat, for not eating me.* I would like to thank my PhD for not eating me, but making me stronger and maturer in both academia and life.



---

# Abstract

---

External heating methods such as neutral beam injection (NBI) and ion cyclotron resonance heating (ICRH) generate a large amount of fast ions in tokamak plasmas. The widely implemented MHD single fluid theory with isotropic pressure is no longer sufficient to capture the physics of such plasmas. Despite the shortcoming of a fluid theory, such as the fluid closure problem and the lack of wave-particle interactions, the use of a fluid description in a tokamak with external heated fast ions is possible and has proved fruitful due to its simple and intuitive nature, as shown in this thesis.

Due the presence of the fast ions, the total plasma pressure becomes anisotropic. In other words, the pressure parallel to the magnetic field differs from its perpendicular counterpart. We have upgraded the fast ion driven instability tool chain HELENA-MISHKA-HAGIS to new versions with pressure anisotropy, taking the simplification that the whole plasma (electrons, fast and thermal ions) is a bi-Maxwellian fluid. Based on this new tool chain and analytical analysis, we have identified the impact of pressure anisotropy induced by externally heated fast ions on the plasma equilibrium, waves and instabilities. It has been found that if an isotropic model is used to describe an anisotropic plasma, a range of problems will emerge depending on the inverse aspect ratio and the magnitude of anisotropy. These problems include the inconsistency of the poloidal (diamagnetic) current, the constant pressure surface shifting away from the flux surfaces, and finally a distortion of the current and  $q$  profile. Two MAST experimental discharges are analyzed, while in one of them, #29221@190ms, all three problems are presented, confirming the prediction. The equilibrium reconstructions for this discharge with/without anisotropy give different  $q$  profiles. This difference in the  $q$  profile leads to different continua, different  $n = 1$  TAE mode structures, and finally, different growth rates and saturation levels. The tool chain has also been used to carry on other physics studies such as an investigation of the dependency of the continuous spectra on different fluid closures and level of anisotropy.

In addition to the waves that are supported by the thermal plasma, and modified and driven unstable by the fast ions, there are a family of waves, the energetic particle modes (EPMs), whose existence and property are determined by the fast ions, such as the energetic geodesic acoustic modes (EGAMs). The EGAMs are  $m = n = 0$  bursting and chirping modes first observed in DIII-D counter beam experiments. By considering the fast ions as a fluid with a collective flow along the field lines, we have reached a dispersion relationship that gives an unstable branch at half of the thermal GAM frequency. We have also found that when the beam is cold, there is a good agreement between our fluid theory and the existing kinetic theories. However, since the fluid theory does not capture the physics of inverse Landau damping, the source of the instability must be reactive, in contrast to the previous understandings. Furthermore, a smooth transition between the reactive EGAMs and the wave-particle interaction driven EGAMs is found when the beam temperature gradually increases, resembling the transition between the two-stream instability and the bump-on-tail instability in a beam-plasma system. This local fluid model is then extended to a global one to capture the physics of EGAM radial mode

structure in the regime where fast ion drift orbit width is smaller than the mode width. The dependency of the mode structure on the equilibrium  $q$  profiles and the beam injection direction is investigated.

By demonstrating the above two applications of the fluid theory and the corresponding physics discoveries, we have proved the usefulness of a fluid treatment in tokamak plasmas with external heatings, serving to understanding some of the basic fast ions physics and acting as a powerful and indispensable complement to its kinetic counterpart.

---

# Contents

---

<b>Declaration</b>	<b>iii</b>
<b>Publications</b>	<b>v</b>
<b>Acknowledgements</b>	<b>vii</b>
<b>Abstract</b>	<b>ix</b>
<b>1 Introduction</b>	<b>1</b>
1.1 The tokamak and its external heating methods . . . . .	2
1.1.1 The tokamak . . . . .	2
1.1.2 External heating methods . . . . .	4
1.2 The basic theories of plasma as a fluid . . . . .	5
1.2.1 Kinetic theory . . . . .	5
1.2.2 Fluid description . . . . .	6
1.2.3 Magnetohydrodynamics . . . . .	7
1.2.4 Guiding center plasma . . . . .	8
1.2.5 Collisions, plasma thermalization and pressure anisotropy . . . . .	9
1.2.6 Fluid closure problem . . . . .	11
1.3 Plasma equilibrium and fast ion driven instabilities in tokamaks . . . . .	12
1.3.1 The Grad-Shafranov Equation (GSE) and magnetic coordinates . . . . .	12
1.3.2 MHD continuum . . . . .	13
1.3.3 Fast ion driven instabilities . . . . .	16
1.3.4 The ideal MHD fast ion driven instabilities tool chain . . . . .	17
1.3.5 Geodesic acoustic modes and energetic geodesic acoustic modes . . . . .	19
1.4 Aim and structure of this thesis . . . . .	20
<b>2 Impact of anisotropy pressure on tokamak equilibria</b>	<b>23</b>
2.1 Introduction . . . . .	23
2.2 Grad-Shafranov Equation with anisotropic pressure and toroidal flow . . . . .	24
2.2.1 Basic Equations . . . . .	24
2.2.2 Grad-Shafranov Equation in the form of pressure . . . . .	25
2.2.3 Grad-Shafranov Equation in the form of enthalpy . . . . .	26
2.3 Numerical scheme . . . . .	26
2.4 The features of anisotropic equilibria . . . . .	28
2.4.1 Toroidal current decomposition . . . . .	29
2.4.2 Deviation from flux function . . . . .	30
2.5 Performance of isotropic model in reconstruction of anisotropic systems . . . . .	33
2.5.1 Model dependence in equilibrium reconstruction . . . . .	34
2.5.2 Equilibrium reconstruction of a MAST discharge . . . . .	35
2.5.3 Implications of using MHD to reconstruct anisotropic plasma . . . . .	36
2.6 Conclusion . . . . .	37

---

2.7	Appendix: Solvability of $p_{\parallel}, p_{\perp}, B$ and $\Delta$ . . . . .	38
<b>3</b>	<b>Impact of anisotropic pressure on tokamak plasmas normal modes and continuum</b>	<b>39</b>
3.1	Introduction . . . . .	39
3.2	Plasma Model . . . . .	41
3.3	Equilibrium and geometry . . . . .	42
3.4	The perturbed equations in the straight field line coordinates . . . . .	44
3.4.1	The ideal Ohm's law . . . . .	45
3.4.2	The momentum equation . . . . .	45
3.4.3	The fluid closure equation . . . . .	46
3.5	Numerical method . . . . .	47
3.6	Anisotropy impact on plasma continuous spectrum . . . . .	48
3.6.1	the Cylindrical limit . . . . .	49
3.6.2	The BAE gap change due to anisotropy . . . . .	50
3.7	Anisotropy impact on the internal kink mode . . . . .	52
3.8	Conclusion . . . . .	54
3.9	Appendix: Auxiliary formulas . . . . .	55
3.10	Appendix: Matrix elements . . . . .	55
3.10.1	The momentum equation . . . . .	55
3.10.2	The ideal Ohm's law . . . . .	58
3.10.3	The single/double-adiabatic fluid closure equations . . . . .	58
3.10.4	The incompressible fluid closure . . . . .	59
<b>4</b>	<b>Application to MAST discharges and the impact on wave-particle interactions</b>	<b>61</b>
4.1	Introduction . . . . .	61
4.2	Equilibrium and mode calculation . . . . .	63
4.3	Stability . . . . .	65
4.3.1	Physical background and method . . . . .	65
4.3.2	Calculations . . . . .	67
4.4	Conclusion . . . . .	71
<b>5</b>	<b>Fluid theory of the reactive EGAMs: local treatment</b>	<b>73</b>
5.1	Introduction . . . . .	73
5.2	Model . . . . .	74
5.3	Discussion and application to DIII-D . . . . .	77
<b>6</b>	<b>Fluid theory of the reactive EGAMs: global treatment</b>	<b>81</b>
6.1	Introduction . . . . .	81
6.2	Equilibrium . . . . .	83
6.2.1	Geometry . . . . .	83
6.2.2	Fast ion density profile with finite orbit width . . . . .	84
6.3	Linear perturbation treatment . . . . .	86
6.3.1	Bulk plasma . . . . .	87
6.3.2	Fast ions local theory . . . . .	88
6.3.3	Fast ion global theory . . . . .	90
6.4	Solving the dispersion relationship . . . . .	91
6.4.1	Monotonic shear case . . . . .	92

---

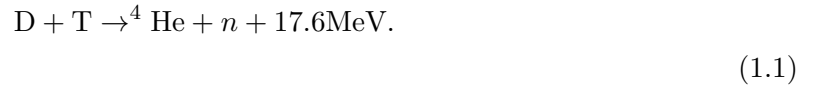
6.4.2	Reversed shear case . . . . .	94
6.4.3	Dependency on injection direction . . . . .	97
6.5	Conclusion . . . . .	99
6.6	Appendix: Higher order $O(\epsilon\delta^l)$ terms in the equilibrium density profile . . .	100
6.7	Appendix: Detail derivation of the higher order fast ion drift current . . . .	100
6.8	Appendix: Auxiliary equations . . . . .	102
<b>7</b>	<b>Conclusion</b>	<b>103</b>
<b>A</b>	<b>Detail derivation of local fluid EGAMs</b>	<b>107</b>
A.1	Model . . . . .	107
A.1.1	Equilibrium . . . . .	107
A.1.2	Ion response . . . . .	109
A.1.3	Electron response . . . . .	110
A.1.4	The momentum equation . . . . .	110
A.2	Dispersion relationship for thermal plasma with bump-on-tail fast ions . . .	111
A.2.1	Bump-on-tail fast ions . . . . .	111
A.2.2	Dispersion relationship in matrix form . . . . .	112
A.2.3	Reduction to a single energy beam . . . . .	113
<b>B</b>	<b>An anisotropic and flowing model for converging magnetic field</b>	<b>115</b>
B.1	Introduction . . . . .	115
B.2	Model . . . . .	116
B.2.1	Magnetic Geometry . . . . .	116
B.2.2	Continuity equation . . . . .	118
B.2.3	Momentum Equation . . . . .	118
B.2.4	Generalized Ohm's law . . . . .	119
B.3	Collisionless plasma . . . . .	120
B.3.1	Isotropic, source/sink-free plasma . . . . .	121
B.3.2	Adding anisotropy . . . . .	122
B.3.3	Adding source term . . . . .	124
B.4	Finite resistivity . . . . .	125
B.5	Conclusion . . . . .	126
	<b>Bibliography</b>	<b>127</b>

---

# Introduction

---

Nuclear fusion happens when two or more light nuclei combine and form one or more (usually) heavier nuclei and neutron(s)/proton(s). The product mass is slightly lighter than the sum of the reactants, and this deficiency in mass is released as kinetic energy of the fusion products. In a fusion power plant, the energetic products of the fusion reactions would heat the surroundings through collisions and the heat would be utilized to generate electricity. The main fusion reaction we are trying to make use of in a fusion reactor is [1]



Deuterium is rich in sea water and tritium can be bred from lithium, the 23<sup>rd</sup> most common element on Earth. The only waste products are helium and neutron with zero greenhouse gas emissions. The cross-section of this reaction has its maximum when the relative energy of the reactants reaches 100keV. In reality, a temperature of 10keV, still 116 million Kelvin, will give a sufficient reaction rate, thanks to the high energy tail of the Maxwellian distribution. With such a high temperature, the reactants are no longer in the state of gas, but known as a plasma, the “fourth state of matter”, in which their electrons and ions are not bonded to each other. A textbook definition [2] of plasma is as follows.

1. A plasma consists of charged particles and sometimes neutrals, but is macroscopically quasi-neutral.
2. A plasma is characterized by its collective interaction with electromagnetic field. The scale length of the system is larger than the Debye shielding length  $\lambda_D = \sqrt{\varepsilon_0 T_e / n_e e^2}$ .
3. The electron-neutral collision frequency is lower than the natural oscillating frequency of the plasma (plasma frequency)  $\omega_{pe} = \sqrt{n_e e^2 / m_e \varepsilon_0}$ , allowing the domination of electromagnetic interactions over ordinary gas dynamics.

Here,  $\varepsilon_0$  is the electric vacuum permittivity constant,  $T_e$  the electron temperature (in energy unit such as keV),  $n_e$  the electron number density,  $e$  the electron charge,  $m_e$  the electron mass.

Plasma is common in the universe: more than 90% of the baryonic matter in the universe is believed to be in the plasma state. In everyday life, although rarely noticed, plasmas can be found in flames, in fluorescent lamps, as well as in lightning strikes. The focus of this thesis will be on the physics of the plasma generated by fusion experiments, i.e. fusion plasma physics.

Reaching the desired temperature is not the only obstacle on the way to fusion as an energy source: we need a sufficiently high density of plasma to be confined for a sufficiently long time, so the power it releases can exceed the power used to heat itself. In other words, the fusion “triple product”, the temperature  $\times$  the density  $\times$  the confinement time must be sufficiently large to achieve “ignition” of the fusion reactor. This is known as the Lawson Criterion [3]. Currently there are two major approaches to harness fusion on Earth: by inertial confinement, or magnetic confinement. The topic of this thesis falls into the latter category.

It is well known that charged particles experience Lorentz force  $\mathbf{F}_L = e_s \mathbf{v} \times \mathbf{B}$ , where  $e_s$  is the charge of the particle species “s”,  $\mathbf{v}$  is the particle velocity and  $\mathbf{B}$  is the magnetic field. Due to the Lorentz force, particles will gyrate around a magnetic field line, limiting their movement across the field lines : they are confined.

In this chapter, we will first introduce the magnetic confinement machine we are studying, the tokamak, and its external heating methods. We will then give some basics of the plasma theories used in this thesis and talk about their limitation and applications. Afterwards, the tokamak equilibrium theory and the fast ion driven instabilities are briefly discussed. Finally, we will give a brief summary of the aims and the major points of this thesis.

## 1.1 The tokamak and its external heating methods

### 1.1.1 The tokamak

If the magnetic field is homogeneous, the particles will stay around one field line unless collisions with other particles take place. However, they are allowed to move freely along the field lines and leak from the two ends, if the confinement space is finite. One approach to confine plasma in a finite volume is by bending the fields into a torus and putting the two ends together. The magnetic field becomes inhomogeneous due to the bending, which gives rise to the cross-field gradient and curvature drift of the particle’s gyro-centre given by [2, 4]

$$\mathbf{v}_d = \frac{m_s v_\perp^2}{2e_s B^3} \mathbf{B} \times \nabla B + \frac{m_s v_\parallel^2}{e_s B^3} \mathbf{B} \times \left( \mathbf{B} \cdot \nabla \frac{\mathbf{B}}{B} \right), \quad (1.2)$$

where  $m_s$  is the mass of the particle species “s”,  $v_\parallel$  and  $v_\perp$  its velocity parallel and perpendicular to the magnetic field, and  $B$  is the strength of the magnetic field. The direction of  $\mathbf{v}_d$  is charge dependent, i.e. the ions will drift up and the electrons will drift down, creating a charge separation in the vertical direction. This charge separation will generate a vertical electric field, leading to the  $\mathbf{E} \times \mathbf{B}$  drift of the particles given by

$$\mathbf{v}_E = \frac{\mathbf{E} \times \mathbf{B}}{B^2}, \quad (1.3)$$

in which  $\mathbf{E}$  is the electric field. The direction of the  $\mathbf{E} \times \mathbf{B}$  drift is pointing outward of the torus, resulting in the loss of plasma. Therefore, a torus with only toroidal magnetic fields cannot confine plasmas effectively.

The way to overcome this difficulty is to add a poloidal magnetic field to the existing toroidal field. When the particles follow the field lines, their gyro-centre will move both toroidally and poloidally. For ions, as the direction of  $\mathbf{v}_d$  always faces up, they drift into the centre of the plasma when they are lower than the mid-plane and away from the centre in the other half of the time. They will therefore on average stay around a field

line without creating any charge separation. For electrons, the situation is similar. There are basically two designs of toroidal magnetic confinement machines with such a poloidal magnetic field: by inducing a large toroidal current in the plasma, namely tokamaks, or by twisting the shape of the plasma, namely stellarators. Schematic views of a tokamak and a stellarator are given in Fig.1.1 (a) and (b), respectively. We will focus on tokamaks in this thesis.

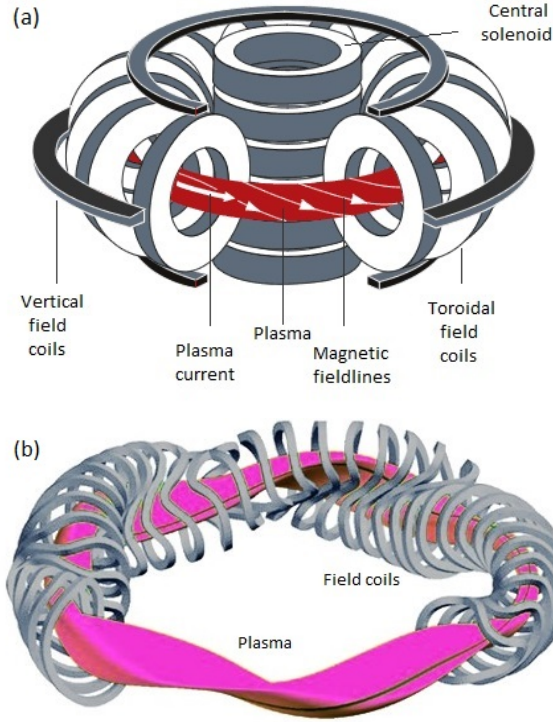


**Figure 1.1:** Schematic plots of (a) a tokamak and (b) a stellarator. Image source: IPP, EURO-Fusion websites.

As shown in Fig.1.1, a typical tokamak setup consists of a set of toroidal field coils, a set of vertical field coils, the first wall facing the plasma, the vacuum chamber, and a central solenoid to induce the plasma current. The field lines in tokamaks can form a surface on which  $\sigma \cdot B = 0$ , where  $\sigma$  is the unit vector perpendicular to the surface. This surface is called the magnetic surface. The safety factor  $q$  is defined in such a way that following a field line on a magnetic surface,

$$q = \frac{\text{Number of toroidal turns}}{\text{Number of poloidal turns}}. \quad (1.4)$$

As we will see from later sections, the safety factor  $q$  is an important parameter that determines the plasma stability.

Another important parameter of a tokamak is the aspect ratio, or the inverse aspect ratio  $\epsilon = a/R$ , with  $R$  the major radius and  $a$  the minor radius of the torus. For traditional tokamaks such as JET, JT-60U, DIII-D and ITER,  $\epsilon \sim 1/3$ . But tighter aspect ratio machines, such as a spherical tokamak (ST), are less vulnerable to the so called ballooning and kink instabilities, and allows a higher  $\beta$  [1], i.e. the ratio of the plasma thermal energy to the magnetic energy. A higher  $\beta$  means that less energy is needed to sustain the same



plasma. The trade off is that the ST has very limited room for the central solenoid, so the Ohmic current drive is limited (see the next section). MAST(Upgrade) and NSTX are two of the world's major ST experiments, with the parameter  $\epsilon \sim 0.7$ .

### 1.1.2 External heating methods

Besides inducing the plasma current and generating the poloidal field, the central solenoid is also used as a transformer to heat the plasma up through  $P = I^2 R$ . The heating is effective when the plasma is cold. However, since the resistivity of the plasma scales as  $T_i^{-3/2}$  [2], this “Ohmic” heating becomes ineffective beyond 1keV. To reach the required 10keV for sufficient fusion reaction, external heating methods are required. There are a variety of external heating methods. We will only focus on two of them in this thesis: the neutral beam injection (NBI) and the ion cyclotron resonance heating (ICRH). A schematic plot of tokamak heating methods is shown in Fig.1.2. Note that the ICRH is a type of radio frequency heating.

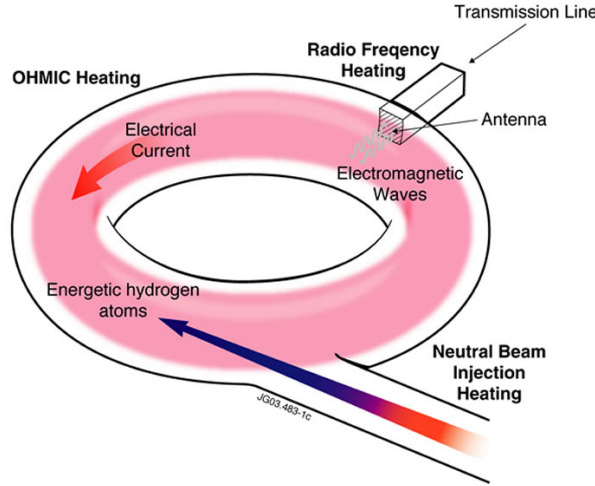


**Figure 1.2:** Tokamak heating methods: Ohmic heating, neutral beam injection and radio frequency heating. Image source: EUROfusion website.

In NBI [1], a small amount of gas, usually hydrogen isotopes, is ionized externally. The ions in the NBI source plasma are accelerated in a electric field to a high energy ( $\sim 100\text{keV}$ , can be up to  $1\text{MeV}$  if negative ion technique is used [5]). These ions are then neutralized so they can penetrate the magnetic field, and are injected into the plasma. The injected neutral particles usually go through charge exchange processes and become ionized again, then gradually deposit their energy to the background plasma through collisions. We call them fast ions due to their excessive energy compared to the background (bulk) plasma ( $< 10\text{keV}$ ). From their nature, NBI fast ions are strongly directional. Their pitch angle (the angle between the magnetic field line and the particle's velocity) will be scattered but mostly preserved during their slowing down in the background plasma [6]. They will have more energy in the parallel motion than in the perpendicular motion, if the injection is parallel to the magnetic field, or reverse if the injection is perpendicular, both leading to strong pressure anisotropy (see Section 1.2.5). In addition, the momentum injected by NBI will induce plasma flow in the direction of injection.

Unlike NBI, ICRH uses radio frequency electromagnetic waves to heat the plasma [1]. The ions in the plasma gyrate around the magnetic field at their cyclotron frequency

$\omega_{Ci} = e_i B / m_i$ , where  $m_i$  is the mass of the ion. They resonate with an electromagnetic wave that has the same frequency, or a harmonic of it, and absorb energy [7]. This is the principle of ICRH. The affected ions can be a proportion of the major ion species in the plasma, or a minor species with a different charge-mass ratio (e.g. protons in a deuterium plasma). Their energy after heating can reach as high as several hundreds of keVs to several MeVs: they are fast ions compared to the background plasma. Since the heating takes place in the direction perpendicular to the magnetic field, the ions tend to gyrate faster and have higher perpendicular energy after heating, while their parallel velocity is less affected [8]. The pressure of ICRH fast ions is thus highly anisotropic.

## 1.2 The basic theories of plasma as a fluid

In this section, we start from the theory of single particle motion in the electromagnetic field, and introduce step by step the kinetic theory, the two(multi)-fluid theory and finally the Magnetohydrodynamics theory and the guiding centre plasma theory. We will also give a discussion about the implications and applicability of three different fluid closures: the MHD adiabatic gas law, the double-adiabatic theory, and the single-adiabatic theory.

### 1.2.1 Kinetic theory

The plasma theory at the most fundamental level describes the motion of each particle in the electromagnetic field through

$$\mathbf{F} = q_s(\mathbf{E} + \mathbf{v} \times \mathbf{B}). \quad (1.5)$$

However, to completely cover every particle in a fusion plasma, we need to follow the motion of at least  $10^{19}$  particles in per cubic metre in 3 dimensions. This is beyond our current computation power. So instead of following each particle, one can assume that the behaviour of a group of particles is similar and follow each group, and use a statistical “distribution function” to indicate how many particles there are in each group. This is the **kinetic** description. The meaning of a distribution  $f$  is the number of particles in a small differential cube  $d^3x d^3v$ , divided by the size of the cube, giving the so called “phase space” density. The kinetic description reduces the problem to solving  $f$  in 6 dimension phase space plus time. The Liouville’s theorem in statistical mechanics gives the evolution of  $f$  over time, i.e. the Vlasov equation, given by

$$\frac{\partial f}{\partial t} + \mathbf{v} \cdot \nabla f + \frac{\mathbf{F}}{m_s} \cdot \nabla_{\mathbf{v}} f = \sum_{s1} C_{s,s1}, \quad (1.6)$$

where  $m_s$  is the mass of particle species “s”, and  $C_{s,s1}$  is the collision operator between two species. That is to say, the distribution function along particle trajectory in the phase space is constant, unless a collision changes it.

Having the distribution function for each species, we still need the Maxwell’s Equations [9] to describe the dynamics of the electromagnetic field. They are given by

$$\nabla \cdot \mathbf{E} = \frac{1}{\varepsilon_0} \sum_s q_s n_s, \quad (1.7)$$

$$\nabla \cdot \mathbf{B} = 0, \quad (1.8)$$

$$\nabla \times \mathbf{E} = -\frac{\partial \mathbf{B}}{\partial t}, \quad (1.9)$$

$$\nabla \times \mathbf{B} = \mu_0 \sum_s q_s n_s \mathbf{V}_s + \varepsilon_0 \mu_0 \frac{\partial \mathbf{E}}{\partial t}, \quad (1.10)$$

where  $\mu_0$  is the magnetic vacuum permittivity while  $n_s$  and  $\mathbf{V}_s$  are the number density and the average velocity of species “s” given by

$$n_s = \int d^3v f_s(\mathbf{x}, \mathbf{v}, t), \quad (1.11)$$

$$\mathbf{V}_s = \frac{1}{n_s} \int d^3v \mathbf{v} f_s(\mathbf{x}, \mathbf{v}, t). \quad (1.12)$$

Now with Eq. (1.6)-(1.10), the system is closed and solvable. We note that the displacement current term (last term) in Eq. (1.10) is often ignored if the phase velocity of the wave is much slower than the speed of light.

When the time scale of the activity is much longer than the particle gyro-period and the space scale of the activity is much larger than the gyro-radius (Lamor radius) of the particles, the gyro motion of the particle can be averaged out. One can use the motion of the “guiding centre”, the centre of the particle gyro orbit to represent the motion of the particle. The distribution function is now reduced to  $f = f(\mathbf{x}, v_{\parallel}, v_{\perp}, t)$  in 5D plus time, leaving out the gyro-angle (see for example Ref. [10]).

### 1.2.2 Fluid description

In Maxwell’s equations, the electromagnetic field only responds to the macroscopic quantities (density and current) of the plasma. The complexity of the system can be further reduced if we can also describe the dynamics of the plasma by their macroscopic quantities (such as density, velocity and pressure), which will reduce the problem to solving the macroscopic quantities in 3D plus time. These quantities are usually intuitive and measurable, and can therefore provide very good physics insights. Taking the moments of the Vlasov equation Eq. (1.6), i.e. multiplying Eq. (1.6) by 1 (zeroth order),  $\mathbf{v}$  (first order),  $\mathbf{v}\mathbf{v}$  (second order),  $\dots$ , and integrating over the velocity space, with a proper choice of collision operator one will get the zeroth and first moment equations given by [9]

$$\frac{\partial n_s}{\partial t} + \nabla \cdot (n_s \mathbf{V}_s) = 0, \quad (1.13)$$

$$m_s n_s \frac{d\mathbf{V}_s}{dt} = q_s (\mathbf{E} + \mathbf{V}_s \times \mathbf{B}) - \nabla \cdot \mathbf{P}_s - \sum_{s1} m_s \nu_{s,s1} (\mathbf{V}_s - \mathbf{V}_{s1}), \quad (1.14)$$

where  $\nu_{s,s1}$  is the collision rate between species “s” and “s1” and  $\mathbf{P}_s$  is the pressure tensor defined by

$$\mathbf{P}_s = \int d^3v m_s (\mathbf{v} - \mathbf{V}_s)(\mathbf{v} - \mathbf{V}_s) f_s(\mathbf{x}, \mathbf{v}, t). \quad (1.15)$$

Equation (1.13) and (1.14) are the continuity equation and the momentum equation. The process of generating moments can be continued to infinite order. The equation of  $n$ th moment will have the presence of the  $n + 1$ ’th moment due to the second term in the Vlasov equation, making the number of variables and equations required to solve the system infinite. This is the **fluid closure** problem (Section 1.2.6).

### 1.2.3 Magnetohydrodynamics

Up to now we distinguish between the dynamics of different species, having a set of Eq. (1.13) and (1.14) for each species (electrons, ions, etc). It has the name “two-fluid” or “multi-fluid” theory depending on the number of species. The system can be further reduced if the behaviour of individual species is less important: we can consider all of them together as one fluid. The most commonly used single-fluid theory is the MagnetoHydroDynamics (MHD) theory, with the equations given by [9]

$$\frac{\partial \rho}{\partial t} + \nabla \cdot (\rho \mathbf{V}) = 0, \quad (1.16)$$

$$\rho \frac{d\mathbf{V}}{dt} = \mathbf{J} \times \mathbf{B} - \nabla p, \quad (1.17)$$

$$\mathbf{E} + \mathbf{V} \times \mathbf{B} = \eta \mathbf{J} + \frac{\mathbf{J} \times \mathbf{B}}{en_e} - \frac{\nabla p_e}{en_e}, \quad (1.18)$$

$$\frac{d}{dt} \left( \frac{p}{\rho^\gamma} \right) = 0, \quad (1.19)$$

where the single-fluid quantities are defined as  $\rho = \sum_s m_s n_s$ ,  $\mathbf{J} = \sum_s q_s n_s \mathbf{V}_s$ ,  $p = \sum_s p_s = \sum_s n_s T_s$  and  $\mathbf{V}$  is the velocity of the centre of mass. One important assumption in MHD is the quasi-neutrality condition, namely

$$\sum_s e_s n_s = 0. \quad (1.20)$$

The quasi-neutrality condition is valid when  $\tau_{\text{wave}} \gg 1/\omega_{\text{pe}}$ , i.e. the electrons move rapidly enough to neutralize the charge separation, and  $L_{\text{wave}} \gg \lambda_D$ , i.e. the ions are well shielded by the surrounding electrons. Here,  $\tau_{\text{wave}}$  and  $L_{\text{wave}}$  are the characteristic time constant and length scale of the phenomenon of interest (e.g. a wave). The quasi-neutrality condition does not mean  $\nabla \cdot \mathbf{E} = 0$ , but only indicates that the overall charge density is too small to be useful elsewhere (e.g. in the momentum equation) [2].

Another key assumption in MHD is the pressure being isotropic, i.e.  $\mathbf{P}_s = p_s \mathbf{I}$ , associated with the condition that the collisionality is high so the distribution will thermalize rapidly. The most commonly used fluid closure of MHD is the adiabatic gas law given by Eq. (1.19), where  $\gamma = 5/3$  is the adiabatic index same as that of a single-atom gas. This fluid closure will be further discussed in Section 1.2.6.

Equation (1.18) is the generalized Ohm’s law. Different terms are retained for the study of different phenomena with different time scales. In this thesis, we use the ideal Ohm’s law, in which the right hand side of Eq. (1.18) is taken to be zero, i.e.

$$\mathbf{E} + \mathbf{V} \times \mathbf{B} = 0. \quad (1.21)$$

The ideal Ohm’s law is also called the “frozen-in-line” condition, where the lack of resistivity will prevent plasmas fluid elements from drifting off its initial magnetic field lines. Under the frozen-in-line condition, the magnetic field lines are like strings with tension and the plasma fluid elements are small masses attached to the string. In reality, if there is a strong magnetic field, the motion of plasma particles will be restricted in the perpendicular direction and they are “attached” to the field lines. The MHD therefore gives a reasonable approximation of perpendicular dynamics and are widely used in the study of shear Alfvén waves, whose perturbed velocity is perpendicular to the magnetic field.

However in a longer time scale, when resistivity is finite, the field lines will diffuse so the plasma elements will not be “frozen-in-line”. Substituting Eq. (1.9) and (1.10) into Eq. (1.18) and drops the last two terms, one reaches

$$\frac{\partial \mathbf{B}}{\partial t} = \nabla \times (\mathbf{V} \times \mathbf{B}) + \frac{\eta}{\mu_0} \nabla^2 \mathbf{B}. \quad (1.22)$$

For a static plasma  $\mathbf{V} = 0$ , Eq. (1.22) shows the diffusion of the magnetic field with time rate  $\tau_R = L_{\text{wave}}^2 \mu_0 / \eta$ . In a 10keV fusion plasma,  $\eta \sim 10^{-8} \text{Ohm/m}$  [4], giving diffusion time  $10^2 L_{\text{wave}}^2 \text{s}$ , with the unit of  $L_{\text{wave}}$  in meter. That is to say, the resistive time scale in a tokamak is much longer than the typical time scale of an Alfvén wave ( $\sim 10^{-5} \text{s}$ ) and even the time scale of a sound wave ( $\sim 10^{-4} \text{s}$ ). Therefore, the resistivity term is usually ignored in the analysis of the aforementioned two waves. The applicability time scale of the ideal Ohm’s law is below (faster than) the resistive time scale, with the exception of tearing modes [1]. It can also be extended to above the resistive time scales, to get qualitative insights into the instabilities that are allowed to develop with no resistivity (ideal instabilities). However, we note that the presence of resistivity breaks the self-adjointness of the force operator, changing its mathematical property. For example, the inclusion of infinitesimal resistivity may help to solve the damping rate of continuum damping [11], while the damped solution is mathematically absent in ideal MHD.

Finally, using Eq. (1.14), one can estimate the relative ratio between the last two terms in Eq. (1.18) and its left hand side to be in the order of  $\omega / \omega_{\text{Ci}}$ . Therefore, the applicability time scale of the ideal Ohm’s law is above (shorter than) the cyclotron time scale, that is to say,

$$1 / \omega_{\text{Ci}} \ll \tau_{\text{wave}} \ll \tau_R. \quad (1.23)$$

In addition, to drop the last two terms, we need the small Larmor radius assumption, i.e.  $L_{\text{wave}} \gg \rho_{L,s}$  [2, 9], where  $\rho_{L,s} = m_s v_{\perp} / q_s B$  is the Larmor radius.

Unlike in the perpendicular direction, particles can stream freely in the parallel direction. For a fluid treatment to be valid, in which the particle’s motion is limited in a fluid element, high collisionality is needed in order to satisfy the criterion  $l_c \ll dr \ll L_{\text{wave}}$ , where  $l_c$  is the free mean path of the particle,  $dr$  is the fluid element and  $L_{\text{wave}}$  is the length scale of the wave. But we will see in the next chapter, that the perpendicular dynamics of MHD is valid even in a collisionless plasma.

### 1.2.4 Guiding center plasma

The guiding centre plasma (GCP) theory is derived from the perspective of a collisionless plasma [12, 13, 14]. GCP is a rigorous limit, the Vlasov equation Eq. (1.6) is solve by expanding around small parameter  $m/e$ , implying that  $\omega_{\text{wave}} / \omega_{\text{Ci}} \ll 1$  and  $L_{\text{wave}} / \rho_{L,s} \gg 1$ . In GCP, all particles are drifting at the  $\mathbf{E} \times \mathbf{B}$  velocity Eq. (1.3) to the lowest order, so the perpendicular direction of Eq. (1.21) is a natural requirement. Also, the cyclotron motion of the particles can be averaged out, so the particles can be represented by their guiding centre, i.e. gyro-averaged particle position. The lowest order Vlasov equation now becomes

$$\begin{aligned} & \frac{\partial f_s}{\partial t} + (\mathbf{V}_E + v_{\parallel} \mathbf{b}) \cdot \nabla f_s \\ & + \left[ -\mathbf{b} \cdot \left( \frac{\partial \mathbf{V}_E}{\partial t} + \mathbf{V}_E \cdot \nabla \mathbf{V}_E + v_{\parallel} \mathbf{b} \cdot \nabla \mathbf{V}_E \right) + \mu B \nabla \cdot \mathbf{b} + \frac{e}{m} E_{\parallel} \right] \frac{\partial f_s}{\partial v_{\parallel}} = 0. \end{aligned} \quad (1.24)$$

Similarly, by taking the moments of Eq. (1.24), a set of fluid-like equations can be obtained, written as

$$\mathbf{V} = \frac{\mathbf{E} \times \mathbf{B}}{B^2} + V_{\parallel} \mathbf{b}, \quad (1.25)$$

$$\frac{\partial \rho}{\partial t} + \nabla \cdot (\rho \mathbf{V}) = 0, \quad (1.26)$$

$$\rho \frac{d\mathbf{V}}{dt} = \frac{1}{\mu_0} (\nabla \times \mathbf{B}) \times \mathbf{B} - \nabla \cdot \mathbf{P}, \quad (1.27)$$

$$\frac{\partial \mathbf{B}}{\partial t} = \nabla \times (\mathbf{V} \times \mathbf{B}), \quad (1.28)$$

where  $\mathbf{P} = \sum_s \mathbf{P}_s$ , and  $\mathbf{b}$  is the unit vector in the direction of the magnetic field. The lowest order pressure tensor  $\mathbf{P}_s$  is in the diagonal form, given by

$$\mathbf{P}_s = p_{\perp s} (\mathbf{I} - \mathbf{b}\mathbf{b}) + p_{\parallel s} \mathbf{b}\mathbf{b}, \quad (1.29)$$

with  $p_{\perp s}$  and  $p_{\parallel s}$  the perpendicular and parallel pressure, respectively. This form of pressure tensor is first found by Chew, Goldberger and Low [15] for a plasma with strong magnetic fields, using identical parameter expansion to the GCP. The two pressures are defined by

$$p_{\perp s} = \int d^3v \frac{1}{2} m_s (v_{\perp} - V_{\perp, s})^2 f_s(\mathbf{x}, \mathbf{v}, t), \quad (1.30)$$

$$p_{\parallel s} = \int d^3v \frac{1}{2} m_s (v_{\parallel} - V_{\parallel, s})^2 f_s(\mathbf{x}, \mathbf{v}, t). \quad (1.31)$$

Up to now, the set of GCP equations Eq. (1.25) to (1.28) matches the ideal MHD equations and the Maxwell equations except for the pressure tensor. That is to say, a lack of collision will not change the property of the plasma perpendicular dynamics derived in MHD.

However, the GCP does not provide a fluid closure equation like Eq. (1.19). Equation (1.27) is closed directly by the kinetic equation Eq. (1.24), while the parallel electric field  $E_{\parallel}$  in Eq. (1.24) is determined by the quasi-neutrality condition given by

$$\sum_s e_s \int f_s d^3v = 0. \quad (1.32)$$

The system is then closed.

The advantage of GCP is obvious, by taking a step back to the kinetic theory, it avoids the problems of fluid closure and Landau damping, while still keeping the niceness and easiness of MHD perpendicular dynamics. The shortcoming of the GCP theory is also obvious, it loses part of the simplicity and intuitive nature inherent in the fluid theory.

There are ways to reduce the complexity of GCP, by deriving a fluid closure for the pressure tensor and avoiding the use of the kinetic equation. The most famous closure is known as the double-adiabatic law or the Chew-Goldberger-Low (CGL) law [15]. We will introduce the CGL law in Section 1.2.6.

### 1.2.5 Collisions, plasma thermalization and pressure anisotropy

The MHD theory in Section 1.2.3 requires high collisionality for a fluid treatment. As a consequence, the pressure tensor is reduced to a scalar pressure  $p$ . In contrast, the GCP theory in Section 1.2.4 is collisionless, while the plasma pressure is different in the direction

parallel/perpendicular to the magnetic field (pressure anisotropy). In this section, we will examine the validity of these assumptions held by the MHD and GCP in a fusion plasma.

The ion-ion collision time, namely the averaged time for the direction ion motion to change  $90^\circ$ , is given by [2]

$$\tau_{ii} = \frac{12\pi^{3/2}\epsilon_0^2\sqrt{m_i}T_i^{3/2}}{\ln\Lambda Z^4 e^4 n_i}, \quad (1.33)$$

where  $Z$  is the ion charge number and  $\ln\Lambda$  is the Coulomb logarithm, a quantity insensitive of the plasma parameters. In fusion experiments  $\ln\Lambda \approx 17$ . The definition of  $\tau_{ii}$  indicates a complete energy mix between the parallel and perpendicular direction in the time scale of  $\tau_{ii}$  and can be used to estimate the thermalization time. The electron-electron collision time is much shorter than the ion-ion collision time due to their lighter weight, giving that

$$\tau_{ee} \sim \sqrt{\frac{m_e}{m_i}} \tau_{ii} \ll \tau_{ii}, \quad (1.34)$$

where  $m_e/m_i = 1840$ . Therefore, the electrons will be well thermalized in the time scale of  $\tau_{ii}$ .

Although Eq. (1.33) is derived for a Maxwellian plasma, its order of magnitude should still holds for a plasma with a different distribution, say a bi-Maxwellian plasma with the distribution written as

$$f_s(v_\perp, v_\parallel) = \left( \frac{m_s^3}{8\pi^3 T_\perp^2 T_\parallel} \right)^{1/2} \exp\left( -\frac{m_s v_\perp^2}{T_\perp} - \frac{m_s v_\parallel^2}{T_\parallel} \right). \quad (1.35)$$

Indeed, Ichimaru and Rosenbluth[16] derived the exact thermalization time scale for a bi-Maxwellian plasma, given by

$$\tau_{i,\text{Maxwellian}} = \frac{30\pi^{3/2}\epsilon_0^2\sqrt{m_i}T_{\text{eff}}^{3/2}}{\ln\Lambda Z^4 e^4 n_i}, \quad (1.36)$$

in which the effective temperature  $T_{\text{eff}}$  is defined by

$$\frac{1}{T_{\text{eff}}^{3/2}} = \frac{15}{4} \int_{-1}^1 d\mu \frac{\mu^2(1-\mu^2)}{[(1-\mu)^2 T_\perp + \mu^2 T_\parallel]^{3/2}}. \quad (1.37)$$

In the limit of  $T_\perp = T_\parallel = T_i$ ,  $T_{\text{eff}}$  will reduce to  $T_i$ . The time evolution of temperature now becomes

$$\frac{dT_\perp}{dt} = -\frac{1}{2} \frac{dT_\parallel}{dt} = -\frac{T_\perp - T_\parallel}{\tau_{i,\text{Maxwellian}}}. \quad (1.38)$$

In a D-D fusion plasma with  $n_i = 10^{19}\text{m}^{-3}$  and  $T_i = 1\text{keV}$ ,  $\tau_{ii} \sim 10^{-3}\text{s}$ , much longer than the typical time scale of an Alfvén wave ( $\sim 10^{-5}\text{s}$ ) and the time scale of a sound wave ( $\sim 10^{-4}\text{s}$ ). Therefore, a collisionless treatment/anisotropic pressure is more appropriate for Alfvénic plasma activities.

For activities on a longer time scale, i.e. equilibrium and transport, the plasma is sufficiently thermalized due to the long confinement time. However, the presence of a source from external heatings will introduce a high energy non-Maxwellian tail on the top of the thermal bulk plasma, as introduced in Section 1.1.2. For example, after slowing

down, the equilibrium distribution of neutral beam fast ions can be approximated by [2]

$$f(E, \Lambda) \sim n_{\text{beam}} \frac{1}{E^{3/2} + E_c^{3/2}} \exp \left[ -\frac{(\Lambda - \Lambda_0)^2}{\Delta \Lambda^2} \right] \Theta(E_{\text{beam}} - E), \quad (1.39)$$

where  $n_{\text{beam}}$  the beam density,  $E$  the ion energy,  $E_c \approx 19T_e$  the critical energy for D-D beam plasma,  $\Lambda = \mu B_0/E$  the pitch angle,  $\Lambda_0$  the injection pitch angle,  $\Delta \Lambda$  the pitch angle spread,  $\Theta(x)$  the step function, and  $E_{\text{beam}}$  the injection energy. Equation (1.39) is highly directional in  $\Lambda_0$ , the injection pitch angle. Thus the beam pressure, and thereby the total pressure, is highly anisotropic given a sufficient beam density.

### 1.2.6 Fluid closure problem

As described in Section 1.2.2, the number of equations of moment hierarchy is infinite: the zeroth moment density is related to the first moment velocity, and then to the second moment pressure, and so on. This hierarchy needs to be stopped at some level to close the system: this is the fluid closure problem. There are usually two ways to find a closure, either by truncating the hierarchy at an arbitrary level, or by proposing a physical assumption which relates the highest order moment to the lower ones.

The Braginskii Equations [17] closes the two fluid equations by assuming a small derivation from the Maxwellian distribution. They are useful in modeling the long term evolution of plasma equilibrium and transport in the collisional regime.

MHD uses the adiabatic gas law given by Eq. (1.19). The key assumption involved is that the phenomena of interest (e.g. waves) in the plasma have a time constant  $\tau_{\text{wave}}$  larger than  $\tau_{\text{ii}}$  in Eq. (1.33), the time constant of thermalization through collisions, but smaller than  $\tau_{\text{heat}}$ , the time constant of heat conduction between neighbouring fluid elements. Writing into equations, this is to say that

$$\tau_{\text{ii}} \ll \tau_{\text{wave}} \ll \tau_{\text{heat}}. \quad (1.40)$$

This MHD adiabatic gas law is widely used in a variety of contexts. However, Eq. (1.40) is not always satisfied in many of its applications. For instance as stated in Section 1.2.5, the first half of Eq. (1.40) is not satisfied in a fusion plasma: the plasma pressure is usually not isotropic. Nevertheless, the adiabatic gas law gives very useful insights into many problems due to its simple and intuitive nature, and due to its versatility to choose the index  $\gamma$  to fit particular results, ranging from isothermal ( $\gamma = 1$ ) to adiabatic ( $\gamma = 5/3$ ).

The double-adiabatic law, or the Chew-Goldberger-Low (CGL) law [15], is derived from an entirely different perspective: the plasma is collisionless. Unlike the adiabatic gas law, the parallel pressure and the perpendicular pressure in CGL are assumed to do adiabatic work independently. If the assumption of a negligible heat flow holds, one obtains

$$\frac{d}{dt} \left( \frac{p_{\perp} B}{\rho} \right) = 0, \quad (1.41)$$

$$\frac{d}{dt} \left( \frac{p_{\parallel}}{\rho B^2} \right) = 0, \quad (1.42)$$

which is valid when

$$\tau_{\text{col}} \gg \tau_{\text{wave}}, \quad \tau_{\text{heat}} \gg \tau_{\text{wave}}, \quad (1.43)$$



where  $\tau_{\text{col}}$  is the slowest collision frequency ( $\tau_{\text{ii}}$  for example), and  $\tau_{\text{heat}} \sim L_{\text{wave}}/v_{\text{s, th}}$ , with  $v_{\text{s, th}}$  the thermal velocity of the fastest particle. The CGL law is consistent with the pressure being anisotropic in a collisionless plasmas in a strong magnetic field. There are nevertheless problems associated with the CGL law when Eq. (1.43) does not hold, mostly when the heat flow terms are not negligible if the wave frequency is comparable or lower than the thermal frequency [18, 19], especially for the electrons. As an improvement, one can extend the applicability of CGL by treating electrons and ions differently, with the former taken to be isothermal and the latter CGL.

The CGL law gives very different results from the MHD adiabatic gas law even when the pressure is isotropic [20]. For instance, the ion sound wave frequency in these two models is given by

$$\omega_{\text{ISW, MHD}} = k_{\parallel} \sqrt{\frac{\gamma p}{\rho}}, \quad \omega_{\text{ISW, CGL}} = k_{\parallel} \sqrt{\frac{3p}{\rho}}, \quad (1.44)$$

with  $k_{\parallel}$  the parallel wave number and  $\gamma \neq 3$ . In order to extend the widely used MHD adiabatic gas law into the context when the pressure is anisotropic while retaining its simple and intuitive nature, the following assumption can be made to construct the perturbed pressure:

$$\tilde{P} = \tilde{p} \mathbf{l}, \quad (1.45)$$

i.e. the perturbed pressure is isotropic, or we only take the isotropic part of the perturbed pressure, where  $\mathbf{l}$  is the unit dyad. The resulting fluid closure equation is given by

$$\begin{aligned} \frac{\partial \tilde{p}_{\parallel}}{\partial t} = \frac{\partial \tilde{p}_{\perp}}{\partial t} = & -\tilde{\mathbf{V}} \cdot \nabla \left( \frac{1}{3} p_{\parallel} + \frac{2}{3} p_{\perp} \right) \\ & - \left( \frac{1}{3} p_{\parallel} + \frac{4}{3} p_{\perp} \right) \nabla \cdot \tilde{\mathbf{V}} - \left( \frac{2}{3} p_{\parallel} - \frac{2}{3} p_{\perp} \right) \mathbf{b} \cdot (\mathbf{b} \cdot \nabla \tilde{\mathbf{V}}), \end{aligned} \quad (1.46)$$

with the name “single-adiabatic” (SA) closure [20]. The assumption of adiabaticity still holds in the single adiabatic closure.

There are many other fluid closures such as the double-polytropic law [21], the 16-momentum closure [22] and the truncation at higher order moments [23, 24]. Some kinetic closures [25, 26] are also proposed to overcome the difficulty of fluid closure, with GCP theory being one of them.

## 1.3 Plasma equilibrium and fast ion driven instabilities in tokamaks

### 1.3.1 The Grad-Shafranov Equation (GSE) and magnetic coordinates

We can derive a second order differential equation to describe the plasma equilibrium force balance in a tokamak in the context of MHD with an isotropic pressure. We now use a cylindrical coordinate  $(R, \varphi, Z)$ , and take the central vertical axis of the torus as the symmetric axis of the coordinate. If we assume axisymmetry in the toroidal direction  $\nabla \varphi$ , the magnetic field can be written as

$$\mathbf{B} = \nabla \Psi \times \nabla \varphi + F \nabla \varphi, \quad (1.47)$$

where we have also used  $\nabla \cdot \mathbf{B} = 0$ . We substitute Eq. (1.47) into the force balance equation given by

$$0 = \mathbf{J} \times \mathbf{B} - \nabla p. \quad (1.48)$$

By inspecting the  $\nabla\varphi$ ,  $\nabla B$  and  $\nabla\Psi$  direction of Eq. (1.48), it is possible to show that  $F = F(\Psi)$ ,  $p = p(\Psi)$ , and finally,

$$\nabla \cdot \left( \frac{\nabla\Psi}{R^2} \right) = -p' - \frac{FF'}{R^2}. \quad (1.49)$$

Equation (1.49) is known as the Grad-Shafranov Equation, first derived by Grad [13] and Shafranov [27]. It is usually solved with a fixed boundary condition which specifies the shape of the plasma, or a free boundary condition, which specifies the external coil currents. The solution  $\Psi = \Psi(R, Z)$  gives the poloidal field and flux surfaces (magnetic surfaces) of the system, where  $\nabla\Psi \cdot \mathbf{B} = 0$

Using  $\Psi$  as the radial coordinate, we can write the components of the magnetic field as  $B_\theta$  and  $B_\varphi$ , where  $\theta$  is the poloidal angle. However, in  $(\Psi, \theta, \varphi)$  coordinates, the magnetic field is not a straight line, i.e.  $B_\varphi/B_\theta$  is not a constant, causing inconvenience for further stability treatments. There exists another set of curvilinear coordinates  $(\Psi, \vartheta, \xi)$ , in which

$$\frac{B^\xi}{B^\vartheta} = \frac{\mathbf{B} \cdot \nabla\xi}{\mathbf{B} \cdot \nabla\vartheta} = q(\Psi), \quad (1.50)$$

where  $q$  is the safety factor defined in Eq. (1.4) and is a function of  $\Psi$  only, while  $B^\xi$  and  $B^\vartheta$  are **contravariant** components of the magnetic field. These curvilinear coordinates are called the magnetic coordinates. The magnetic coordinates are not unique. Some popular choices include the Boozer coordinates [28] and the Hamada coordinates [29], with the additional requirement  $\nabla\Psi \times \mathbf{B}$  and  $\mathbf{J}$  being straight, respectively. In this thesis, we will be using the ‘‘symmetric coordinates’’ [30] where  $\xi = \phi$ . Assuming isotropic pressure, the relationship between  $\theta$  and  $\vartheta$  is given by

$$\vartheta(\theta) = \frac{F(\Psi)}{q(\Psi)} \int_\Psi \frac{dl}{R|\nabla\Psi|}, \quad (1.51)$$

with the integration starting from the low field side mid-plane clockwise facing the direction of  $\nabla\varphi$ .

### 1.3.2 MHD continuum

We now take the fluid equations and linearize them to get the plasma linear wave and stability. We define the ‘‘displacement vector’’ as  $\partial\xi/\partial t = \tilde{\mathbf{V}}$  and  $\partial/\partial t \sim -i\omega$ . Next, we substitute this definition into Eq. (1.9), (1.10), (1.17) and (1.21) and eliminate all other variables, reaching a second order differential equation given by [9]

$$-\rho\omega^2\xi(\mathbf{x}, t) = \mathcal{F}(\xi), \quad (1.52)$$

where the linear force operator  $\mathcal{F}$  is given by

$$\mathcal{F}(\xi) = -\mathbf{B} \times (\nabla \times \mathbf{Q}) + (\nabla \times \mathbf{B}) \times \mathbf{Q} - \nabla\tilde{p}, \quad (1.53)$$

with

$$\tilde{p} = -\gamma p \nabla \cdot \xi - \xi \cdot \nabla p, \quad (1.54)$$

$$\mathbf{Q} = \nabla \times (\boldsymbol{\xi} \times \mathbf{B}). \quad (1.55)$$

Note that the MHD adiabatic gas law Eq. (1.19) is used here. By this way, we reduce the system into three coupled differential equations, with the three components of  $\boldsymbol{\xi}$  as unknowns, thereby the system is closed. When the boundary conditions are specified, for example for a rigid wall,  $\boldsymbol{\xi} \cdot \mathbf{n} = 0$  at the wall ( $\mathbf{n}$  is the unit vector perpendicular to the wall), and the radial component of  $\boldsymbol{\xi}$  being zero on axis, the system defines an eigenvalue problem of  $\omega$ . It has been proved that the operator  $\mathcal{F}$  is a self-adjoint operator [9, 31], so the eigenvalues  $\omega^2$  must be real: the system is either purely oscillatory, or exponentially growing/damping.

There are two major points of view to solve the same problem: by solving the differential equation Eq. (1.52) directly, or by constructing a quadratic form and implementing the variational principle. The latter method is more convenient in finding instabilities ( $\omega^2 < 0$ ), or to determine the boundary value of equilibrium quantities that lead to marginal stability ( $\omega^2 = 0$ ). On the other hand, the two points of view are equivalent in finding the oscillatory solutions ( $\omega^2 > 0$ ) [9]. Since the focus of this thesis lays more on the oscillatory modes, we will use the point of view from the differential equations.

The MHD spectral theory [30] of an inhomogeneous plasma reveals the existence of modes with discrete frequencies, as well as the continuous spectra, much like a quantum mechanics system in solid state physics. In an axisymmetric cylindrical plasma homogeneous along the  $z$  axis, the coordinates  $(r, \theta, z)$  are separable, i.e. the form of the solution is given by  $\boldsymbol{\xi} = \hat{\boldsymbol{\xi}}(r)e^{im\theta + ik_z z - i\omega t}$ , and the modes with different mode numbers  $m$  and  $k_z$  are not coupled to each other. Continuous modes are present if either the radial pressure gradient or the magnetic shear ( $dq/dr$ ) is non-zero. When the frequency matches the local shear Alfvén frequency or sound wave frequency given by

$$\omega^2 = k_{\parallel}^2 v_A^2 = \left(m \frac{B_{\theta}}{B_z r} + k_z\right)^2 \frac{B_z^2}{\mu_0 \rho}, \quad (1.56)$$

or

$$\omega^2 = k_{\parallel}^2 v_S^2 = \left(m \frac{B_{\theta}}{B_z r} + k_z\right)^2 \frac{\gamma p B_z^2}{(\gamma p + B^2) \rho}, \quad (1.57)$$

the coefficient of the highest (second) order derivatives in Eq. (1.52) vanishes on a particular radius, say  $r_{\text{res}}$ , and the corresponding solution  $\boldsymbol{\xi}$  shows a singular behaviour around  $r_{\text{res}}$ . More specifically,  $\xi_r \sim \ln|r - r_{\text{res}}|$  and  $\xi_{\theta}, \xi_z \sim 1/(r - r_{\text{res}})$ . Using this unique property of the continuous modes, a scan can be carried for all  $\omega$ ,  $m$  and  $k_z$  to obtain the frequency of all the continuous modes and the corresponding singular radius, namely the continuous spectra, or the **continuum**. A typical shear Alfvén continuum of a cylindrical plasma is shown in Fig.1.3 with the dashed lines.

If we ignore the effect of toroidicity, a tokamak can be viewed as a cylinder bending to join the two ends together. The continuum in a tokamak will be similar to that of a cylinder if we set  $k_{\parallel} = (m/q + n)/R_0$ , with  $k_z$  replaced by  $n/R_0$  in Eq. (1.56) and (1.57) and  $q \approx rB_{\varphi}/RB_{\theta}$ . Note that  $m$  and  $n$  are the poloidal and toroidal mode numbers, respectively. However, in a tokamak,  $B \sim 1/R$  and therefore the Alfvén frequency is not a constant on flux surfaces, introducing a coupling between the neighbouring  $m$  and  $m + 1$  continuum. The coupling becomes the strongest on the flux surface where the frequencies of these two branches coincide, forming a gap as shown in Fig.1.3. Besides toroidicity, other effects may also induce a frequency gap at the crossing of two continuum branches, including the effect of finite beta (pressure), and the ellipticity and triangularity of the flux

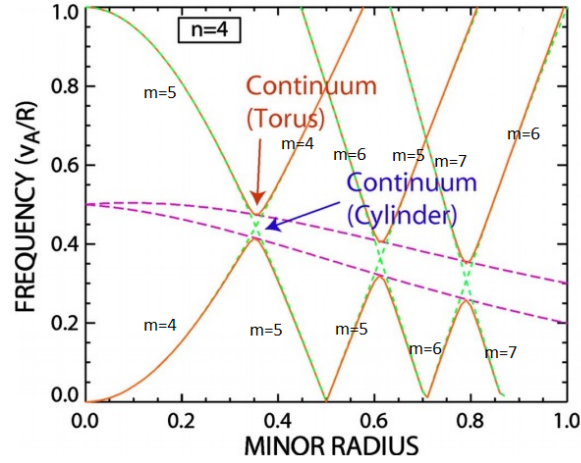


**Figure 1.3:** Shear Alfvén continuum frequency as a function of radius with  $m = 4 - 7$  and  $n = 4$ , for a cylinder (dashed lines) and a tokamak (solid lines). The gap induced by toroidicity is marked between horizontal dashed lines. Image source: Heidbrink[32]

surfaces. These gaps are labeled in Fig.1.4, which shows typical continuum in a tokamak and the zoo of fast ion driven instabilities.

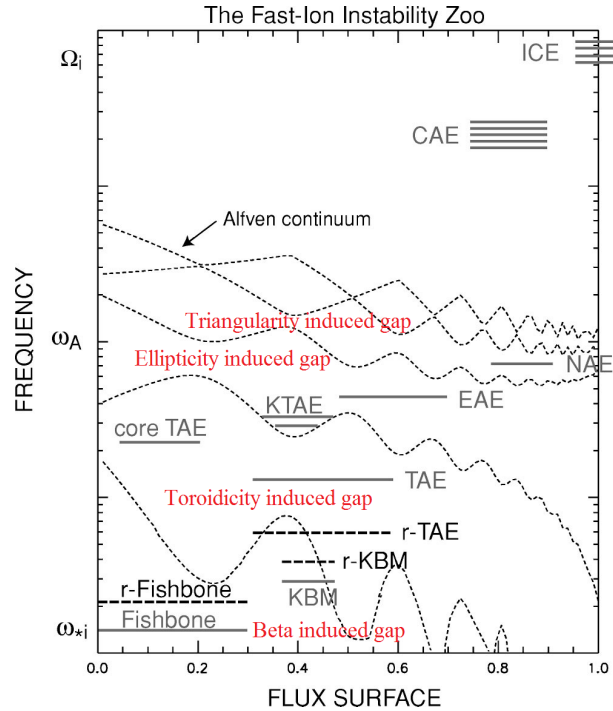


**Figure 1.4:** Alfvén continuum frequency as a function of flux surface with  $n = 3$  (dashed lines). The beta, toroidicity, ellipticity and triangularity induced gaps are labeled in red fonts. The short horizontal lines mark the frequency and radial localization of some fast ion driven instabilities observed experimentally: kinetic ballooning modes (KBM), toroidicity-induced Alfvén eigenmodes (TAE), kinetic toroidicity-induced Alfvén eigenmodes (KTAE), ellipticity-induced Alfvén eigenmodes (EAE), triangularity-induced Alfvén eigenmodes (NAE), compressional Alfvén eigenmodes (CAE) and ion cyclotron emission (ICE). Image source: Heidbrink[33]

When the frequency of another discrete mode hits the continuum at some radius, a

mode-mode interaction will occur at that radius, transferring the energy from the discrete mode to the continuum and eventually dissipating it, causing its amplitude to damp. Usually, the physics of continuum damping cannot be captured by standard ideal MHD methods: one needs to add non-ideal effects such as resistivity or FLR effects, or to implement special treatments such as the singular finite elements or complex contour integration (see Ref. [11, 34, 35] and references therein).

### 1.3.3 Fast ion driven instabilities

In fusion plasmas, the fast ions generated by external heating methods as well as fusion reactions can drive one or many waves, making them unstable through the wave-particle interaction. Wave-particle interaction is the phenomena that when a wave shares the same phase velocity with a group of particles, the particles are static in the frame moving with the wave, so they can be constantly accelerated or decelerated, allowing the exchange of energy between the particles and the wave. The amplitude of the wave will therefore increase or decrease over time depending on the particle distribution function. In tokamaks, the speed of fast ions is usually comparable with or faster than the Alfvén speed, allowing the fast ions to resonate with the Alfvén waves in tokamaks. Moreover, there is free energy coming from a negative fast ion radial density gradient, or from a positive energy gradient available to drive the wave. When the drive exceeds the damping (including the continuum damping, the collisional damping, the radiative damping and/or the ion Landau damping from the thermal ions), the mode will grow and be observed in experiments. These instabilities can cause abnormal transport of fast ions, inducing fast ion loss and thereby degrading the fast ion confinement and limiting plasma performance [36]. Thorough theoretical and experimental investigation of the fast ion driven instabilities is therefore crucial to the operation and the design improvement of existing and future tokamaks. Figure 1.4 illustrates the zoo of these fast ion driven instabilities.

The background plasma can support a variety of shear Alfvén normal modes by itself, as predicted by the MHD theory. There are three types [37] of modes carried by the background plasma: continuum, extremum and gap modes. Figure 1.5 shows the frequency and radial mode structure of each type. As introduced in Section 1.3.2, the continuum modes show a typical localized singular behaviour at the singular radius. The other two types, on the other hand, have robust non-singular global structures. When a continuum extrema is presented, a mode with discrete frequency can be found just below/above the extrema as in Fig.1.5 (b). This is known as the extremum type. One of the famous examples is the reversed shear Alfvén eigenmodes (RSAEs) or Alfvén Cascades (ACs) [38], having a radial peak at the reversal point of the  $q$  profile. Other extremum modes include the beta-acoustic-induced and beta-induced Alfvén eigenmodes (acronym BAAE[39] and BAE[40]), due to the extremes induced by Alfvén -acoustic coupling. It is also possible for a global mode to exist in the continuum gaps, as depicted in Fig.1.5 (c) and known as gap modes. The most commonly driven member of this class is the toroidicity-induced Alfvén eigenmodes (TAEs)[41], residing in the toroidicity induced continuum gap. Other examples include the ellipticity-induced and triangularity-induced Alfvén eigenmodes (acronym EAE and NAE, respectively[42]), corresponding to each gap induced by the named effect.

A fast ion driven instability could come from the above background plasma supported modes, or modes that do not exist with only the bulk plasma, known as the energetic particle modes (EPMs), whose frequency and mode structure are non-perturbatively determined by the fast ions. In the shear Alfvén frequency range, the dominant damping

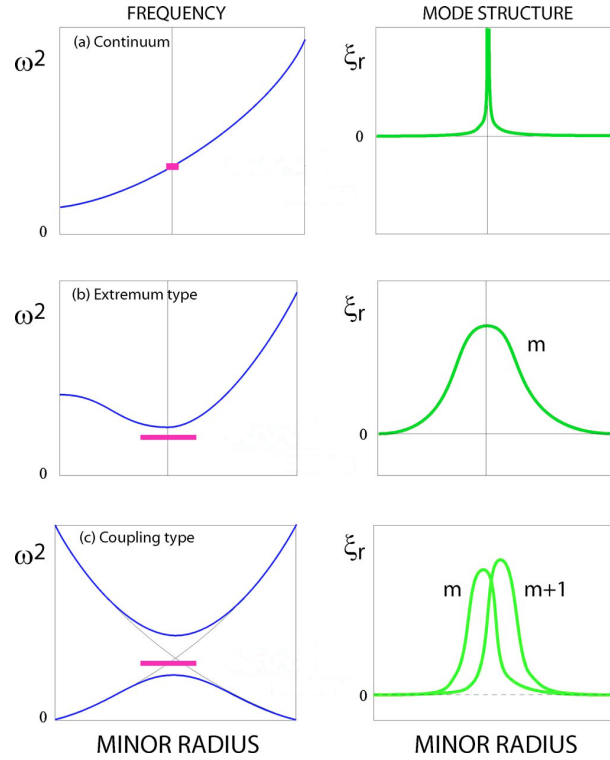


**Figure 1.5:** A schematic classification of background plasma supported shear Alfvén modes, their frequency (left) and radial mode structure (right). (a) A “continuum” mode with a singular radial behaviour. (b) A “extremum type” global mode emerges from an extrema of the continuum with reduced continuum damping. (c) A “coupling type” global mode resides in the continuum gaps with reduced continuum damping. Image source: Heidbrink[32]

mechanism is the continuum damping. The extremum modes and gap modes, residing either at a continuum extrema or in a continuum gap, have a reduced continuum damping and can be driven unstable with less efforts. It is possible that the fast ion drive is enough to overcome the strong damping of a continuum mode, resulting in an instability to develop. A non-singular radial mode structure is usually seen when the fast ions are taken into account, with the peak located at where the fast ion drive is the strongest [43]. They are therefore categorized as EPs, with the precessional fishbone being one of the examples [44]. Finally, there are other EPs that are not emerging from a shear Alfvén continuum, such as the energetic geodesic acoustic modes (EGAMs) [45, 46].

The rough classification of fast ion driven instabilities into background supported modes and EPs is based on their linear properties. Their nonlinear development may sometimes become more complicated: for example, a chirping EPM may emerge from the bulk ion supported modes such as TAEs after a nonlinear Bernstein-Greene-Kruskal (BGK) mode [47] is formed from nonlinear wave-particle interactions [48]. A theory explanation of such behaviours is provided by the Berk-Breizman model [49, 50, 51, 52, 53].

#### 1.3.4 The ideal MHD fast ion driven instabilities tool chain

A suite of numerical tools are routinely used to model the experimentally observed fast ion driven instabilities in complicated tokamak geometries. The different components in this tool chain, as well as the data flows, are shown in Fig.1.6. First, experimental

data such as the external magnetics, the plasma current, and profiles from the advanced diagnostics (such as the magnetic pitch angle profile from the Motional Stark Effects [54]) are used as constraints to the free-boundary GSE equilibrium reconstruction code EFIT [55]. EFIT calculates a least square fit of the profiles and the flux surfaces  $\Psi$  to the data with the force balance satisfied, through a current-field iteration. This first “guess” of the flux surfaces, along with other data like the  $n_e$  profile from the Thomson Scattering [56], are used in the transport code TRANSP [57] to estimate the background plasma and fast ion pressure profiles. In some cases, the pressure profile is in turn fed back into EFIT as kinetic constraints. With these additional constraints, improved estimation of flux surfaces can be constructed.

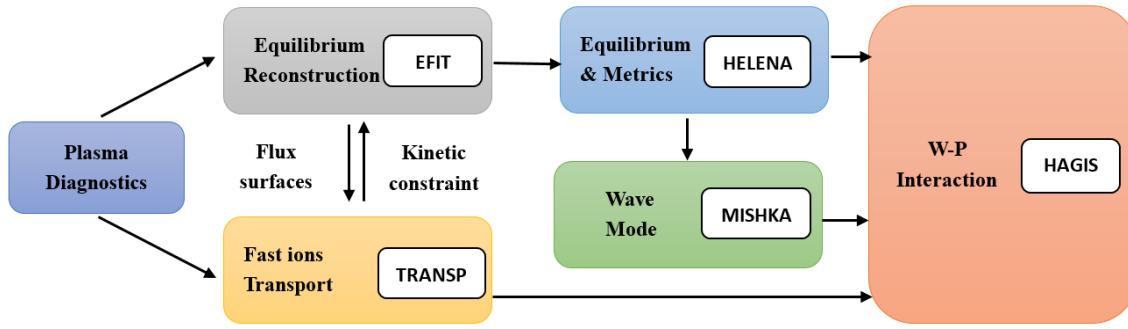


**Figure 1.6:** The isotropic ideal MHD tool chain from equilibrium, wave mode to wave-particle interaction.

The fix-boundary equilibrium code HELENA[58] is a bridge step between EFIT and further stability treatment. It takes the EFIT last closed flux surface and flux functions as input and solves the GSE again in the magnetic coordinates. Such a design allows HELENA to obtain the metric elements of the magnetic coordinates (symmetric coordinates) in high precision. On the other hand, HELENA is also capable of calculating equilibria with analytically prescribed flux functions so as to carry on parameter scans.

Using these equilibrium profiles and the metrics calculated by HELENA, the plasma normal mode code MISHKA[59] solves the ideal MHD equations Eq. (1.52) as an eigenvalue problem. The outputs of MISHKA are the radial mode structure and its frequency, for a given toroidal mode number  $n$  and a range of poloidal mode number  $m$ , containing both the continuous modes and the discrete modes. Corresponding continuum solvers, namely CSCAS[60] and CSMISH, are also available to obtain the continuum frequency on each flux surface.

Finally, the wave-particle interaction code HAGIS[37, 61] evolves the nonlinear amplitude and frequency of the mode calculated by MISHKA, based on the equilibrium provided by HELENA and fast ion distribution function provided by TRANSP. It launches a number of markers, following their trajectory in phase space under the equilibrium and perturbed fields, and adds their contribution to the fields. One can then compare the growth rate, saturation level and chirping behaviours of the mode to the magnetic spectrogram, or synthetic fast ion diagnostics to understand the physics of wave-particle interaction. Further studies can also be carried out to estimate the fast ion losses as a consequence of wave activities.

### 1.3.5 Geodesic acoustic modes and energetic geodesic acoustic modes

The geodesic acoustic modes (GAMs) are axisymmetric modes found in a toroidally confined plasma resulting from finite plasma compressibility and the geodesic curvature of magnetic field lines [62]. They possess common features of a zonal flow: the radial electric field perturbations are poloidally and toroidally symmetric, along with coupled  $m = \pm 1, n = 0$  density/pressure perturbations. GAMs have caught the attention of the fusion community for the important roles they can play in suppressing turbulence transport, enhancing the confinement of the plasma, and ultimately, helping to achieve the long term goal of fusion energy [63, 64, 65, 66].

There are two major types of GAMs in toroidal fusion devices. The first type of GAMs are edge coherent modes observed in a number of experiments (see the topical review [67] and references therein, and [68, 69] for recent results on DIII-D and MAST). They are  $n = 0$  fluid continuum and are excited by the nonlinear interaction with turbulences [70, 71]. The name “conventional” (or “standard”) GAMs is given because the mode frequency were found to scale with  $\omega_{\text{GAM}} \sim \sqrt{\gamma_i T_i + \gamma_e T_e + O(q^{-2})}$ , verifying the prediction of the fluid theory [62]. The coefficients  $\gamma_i$  and  $\gamma_e$  are adiabatic indexes and given by  $\gamma_i = \gamma_e = 5/3$  in MHD. Later, calculations based on the kinetic theory [72, 73] reveal the adiabatic indexes to be  $\gamma_i = 7/4$  and  $\gamma_e = 1$  in a collisionless plasma. These indexes are recently recovered in fluid theory [74, 75] by the implementation of the CGL closure on ions and the isothermal closure on electrons, assuming that the ion perpendicular and parallel pressure are doing work independently in the limit of the safety factor  $q \rightarrow \infty$ , where the GAM frequency is far from the thermal ion transit frequency.

The derivation of the conventional GAM in MHD can be found in Winsor *et al* [62] and is briefly given as follows with the equilibrium current and pressure gradient ignored. After taking the cross product with  $\mathbf{B}$  on both sides, the equation of motion Eq. (1.5) becomes

$$-\rho\omega^2 \boldsymbol{\xi} \times \mathbf{B} = \nabla(\gamma p \nabla \cdot \boldsymbol{\xi}) \times \mathbf{B} - \tilde{\mathbf{J}} B^2 + (\tilde{\mathbf{J}} \cdot \mathbf{B}) \mathbf{B}. \quad (1.58)$$

We now take the perturbed electric field to be  $m = n = 0$ , i.e.  $\mathbf{E} = -\nabla\phi(\Psi)$ . Using Eq. (1.21) and the definition of  $\boldsymbol{\xi}$ , we reach

$$\boldsymbol{\xi} = \frac{i}{\omega} \frac{\mathbf{B} \times \nabla\phi}{B^2}. \quad (1.59)$$

Note that we have ignored the parallel component of  $\boldsymbol{\xi}$  which is responsible for the GAMs' coupling to sound waves. Substituting Eq. (1.59) into Eq. (1.58), we get

$$\tilde{\mathbf{J}} - (\tilde{\mathbf{J}} \cdot \mathbf{b}) \mathbf{b} = i\rho\omega \frac{\nabla\phi}{B^2} + \frac{i}{\omega} \nabla \left( \gamma p \nabla\phi \cdot \nabla \times \frac{\mathbf{B}}{B^2} \right) \times \left( \nabla \times \frac{\mathbf{B}}{B^2} \right). \quad (1.60)$$

Taking the divergence of both sides and using  $\nabla \cdot \tilde{\mathbf{J}} = 0$ , the quasi-neutrality condition, Eq. (1.60) is transformed into

$$\omega^2 \nabla \cdot \frac{\rho(\Psi)}{B^2} \nabla\phi - i\omega \nabla \cdot [(\tilde{\mathbf{J}} \cdot \mathbf{b}) \mathbf{b}] = \nabla \cdot \left[ \left( \gamma p(\Psi) \nabla\phi \cdot \nabla \times \frac{\mathbf{B}}{B^2} \right) \nabla \times \frac{\mathbf{B}}{B^2} \right]. \quad (1.61)$$

We will reach finally after a flux surface average that

$$\phi'(\Psi) \left[ \frac{\gamma p}{\rho} \left\langle \left( \frac{\nabla\Psi}{|\nabla\Psi|} \cdot \nabla \times \frac{\mathbf{B}}{B^2} \right)^2 \right\rangle \left\langle \frac{1}{B^2} \right\rangle^{-1} - \omega^2 \right] = 0, \quad (1.62)$$



with  $\langle \dots \rangle$  indicating flux surface averages. The solutions of Eq. (1.62) are given by

$$\phi' = \delta(\Psi - \Psi'), \quad \omega^2 = \omega_{\text{GAM}}^2(\Psi'), \quad (1.63)$$

where  $\omega_{\text{GAM}}^2(\Psi')$  equals to the first term in the bracket of Eq. (1.62). In a large aspect ratio, low beta and circular cross section tokamak,  $\omega_{\text{GAM}}^2(\Psi')$  is approximately given by

$$\omega_{\text{GAM}}^2(\Psi') = \frac{2\gamma p(\Psi')}{\rho(\Psi') R_0^2}. \quad (1.64)$$

The second type of GAM is associated with injected beam particles, with its first experimental observation quoted in Fig.1.7 [45]. Figure 1.7 (a)-(c) show a turn-on of the mode right after the beam is switched on. Bursting and chirping  $n = 0$  nonlinear signal is observed on the spectrogram, while each burst leads to apparent fast ion losses (a decrease in the neutron signal). In Fig.1.7 (d), the radial extent of the mode is measured with beam emission spectroscopy, showing its localization to be at mid-radius. It was initially very confusing since the mode frequency is at half of the local conventional GAM frequency, as shown in Fig.1.7 (f). Later, a kinetic model was developed by Fu [46] proving that the mode is indeed a GAM. But instead of supported by the bulk plasma only, it corresponds to an EPM, and was given the name “energetic geodesic acoustic modes (EGAMs)” since its frequency and growth rate are non-perturbatively determined by the fast ions.

Still, one puzzle remains unsolved. In nearly all the kinetic theories of EGAM, the modes are claimed to be driven unstable by the wave-particle interaction, which, however, cannot explain its immediate turn-on right after the beam switches on: the positive slope needed to drive the mode has not yet developed. This puzzle is addressed in this thesis using a fluid treatment.

## 1.4 Aim and structure of this thesis

Besides the problems of parallel dynamics and the fluid closure, there is another weak point of the fluid theories: they cannot capture the physics of wave-particle interaction, owing to the fact that the wave-particle interaction is only affecting a small fraction of particles near the resonance, while the fluid theory deals with the macroscopic quantities. Explicitly, the fluid treatment does not feature a resonance condition. Moreover, the energy of the fast ions is usually much higher than the “bulk” plasma, i.e. the thermalized plasma that are confined for sufficiently long time. They may have very distinct properties and behaviour compared to the bulk. As a result of these two considerations, most of the existing theories use the kinetic description for the fast ions, while the bulk plasma is modeled either kinetically (full kinetic description), or by MHD (hybrid description).

Nevertheless, treating the externally heated plasmas as fluids is possible, but its value is often underestimated or overlooked. A fluid description can simplify the problems that may otherwise be complicated to solve, meanwhile providing intuitive physics insights to understand them in a variety of cases. With a careful consideration of applicability range, it can be used in modeling various aspects of an externally heated fusion plasma, with significant physics insights.

In Chapter 2-4, we will describe the fast ions and the bulk plasma as a single fluid, and study the plasma equilibrium, stability and wave-particle interaction, mainly from the perspective of the pressure anisotropy induced by fast ions originated from external heatings, and its implication on fast ion driven instabilities. From the aspect of the

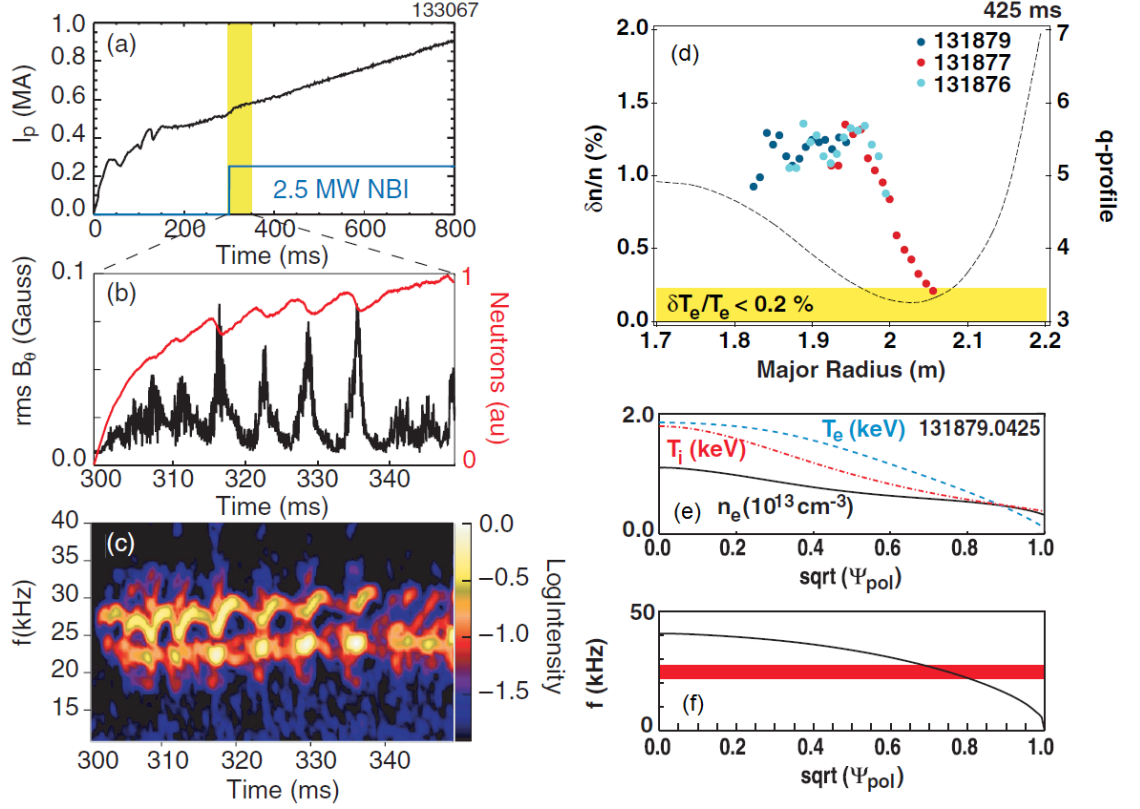


**Figure 1.7:** Experimental data of EGAM activities observed on DIII-D. (a) The plasma current and the beam power. (b) Mirnov coil signal (black) and neutron rate (red). (c) Magnetic spectrogram show bursting and chirping  $n = 0$  wave activities. (d) The density fluctuation level measured by the beam emission spectroscopy, and the  $q$  profile vs major radius  $R$ . (e) The electron density, electron and ion temperature profile. (f) The calculated conventional GAM frequency versus the normalized flux surface, with the red shade indicating the frequency range of the observed mode. Image source: Nazikian *et al* [45].

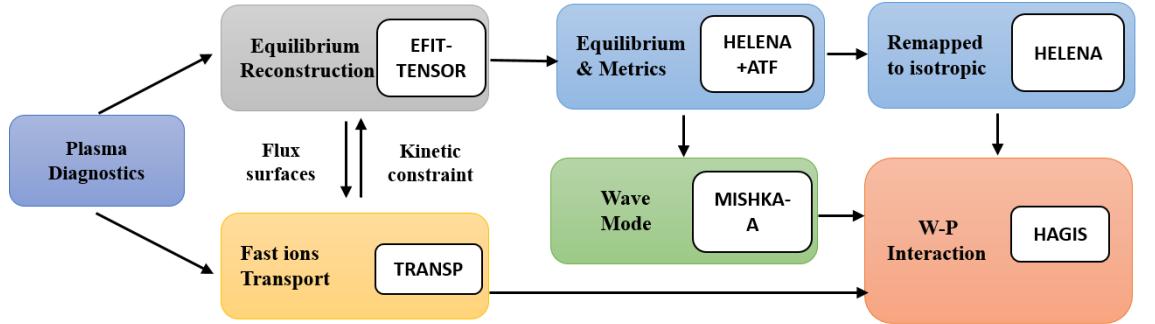


**Figure 1.8:** The anisotropy-extended ideal MHD tool chain from equilibrium, wave mode to wave-particle interaction.

numerical tools, we have developed an extended version of the MHD tool chain with pressure anisotropy. A schematic plot of the new tool chain is shown in Fig.1.8. From the aspect of physics, we have found that the inclusion of pressure anisotropy is increasingly important in machines with lower aspect ratio and stronger external heatings: it may affect

significantly the  $q$  profile, the radial current, the TAE mode frequency and structure, the growth rate and its nonlinear saturation level. In Chapter 5 and 6, a three-fluid theory is used: the electrons, the bulk ions, and the fast ions from neutral beam injection. We will show its application to the energetic geodesic acoustic modes (EGAMs), demonstrating the capacity of a fluid treatment in resolving EPs, meanwhile addressing the puzzle of the EGAMs' immediate turn-on in experiments. It is found that the EGAMs can transit between a reactive fluid instability and a wave-particle interaction driven (dissipative) instability which is otherwise confused in its previous kinetic theories.

The two major parts of this thesis share the same motivation, as well as the same bigger picture. That is, to explore the possibility and the physics discovery of describing the externally heated tokamak plasmas as a fluid/fluids, and to shed lights on physical phenomena that routinely described kinetically. This forms the aim of the thesis.

The thesis is organized as follows.

- Chapter 2 analyses the impact of pressure anisotropy on plasma equilibria, introducing the Grad-Shafranov fix-boundary solver HELENA+ATF. The characteristics of an anisotropic equilibrium is studied with MAST-like profiles and boundaries, while the performance of using an isotropic model on an anisotropic equilibrium is evaluated.
- Chapter 3 develops the normal mode stability solver MISHKA to incorporate the physics of pressure anisotropy, with different considerations of fluid closure. The plasma continuum, and the idea internal kink mode, are investigated using this new code.
- Chapter 4 completes the final part of the tool chain, by driving a wave-particle interaction calculation for an anisotropic plasma. The tools developed in Chapter 2 and 3 are utilized to compute the equilibrium and wave field for a highly anisotropic MAST discharge.
- Chapter 5 derives the local EGAM dispersion relationship from basic fluid equations. The unstable solutions of the dispersion relationship show agreement with the kinetic theory, and are interpreted as reactive two-stream-like instabilities.
- Chapter 6 extends the local reactive EGAM theory in Chapter 5 by adding the fast ion FOW effects, and gives the radial model structure, but still stays in the fluid picture.

The appendices consist some of the supplementary materials and some of my other works that are not relevant to the topic.

- In Appendix A, detail derivation of Chapter 5 is provided.
- An anisotropic model for a linear pinched device and the application on the Magnetized Plasma Interaction Experiment (MAGPIE) is reported in Appendix B.

---

# Impact of anisotropy pressure on tokamak equilibria

---

## Abstract

Beam injection or ICRH induces pressure anisotropy. The axisymmetric plasma equilibrium code HELENA has been upgraded to include anisotropy and toroidal flow. With both analytical and numerical methods, we have studied the determinant factors in anisotropic equilibria and their impact on flux surfaces, magnetic axis shift, the displacement of pressures and density contour from flux surface. Their differences from isotropic cases are almost linear functions of anisotropy. With  $p_{\parallel}/p_{\perp} \approx 1.5$ ,  $p_{\perp}$  can vary 20% in a MAST like equilibrium. We have also re-evaluated the widely applied MHD approximation to anisotropy in which  $p^* = (p_{\parallel} + p_{\perp})/2$ , the average of parallel and perpendicular pressure, is taken as the approximate isotropic pressure. We find that in a MAST shot with  $p_{\parallel}/p_{\perp} \approx 1.25$ , isotropic and anisotropic inference have a 4.5% difference in toroidal field but a 66% difference in poloidal current.

## 2.1 Introduction

Auxiliary heatings, such as neutral beam injection (NBI) and ion cyclotron resonance heating (ICRH), are widely implemented in modern tokamaks. Unlike Ohmic heating, NBI and ICRH generate a large population of fast ions. The NBI induced energetic ions mainly come with a large energy parallel to injection, while ICRH heats the ions into higher velocities perpendicular to magnetic field.[36] The distribution functions of these fast ions in phase space are thus distorted into anisotropic forms with  $p_{\perp} \neq p_{\parallel}$ , where  $p_{\perp}$  or  $p_{\parallel}$  refers to the total pressure of both the thermal and the fast population perpendicular or parallel to the magnetic field. These heating methods also drive plasma rotation. The resulting magnitude of anisotropy in a tokamak can be very large according to recent studies. In JET, anisotropy magnitude reaches  $p_{\perp}/p_{\parallel} \approx 2.5$  [76] with ICRH. In MAST, the beam pressure reaches  $p_{\perp}/p_{\parallel} \approx 1.7$  during NBI heating [77].

However, in the magnetohydrodynamic(MHD) description of plasma, pressure is assumed to be isotropic. Three questions are raised immediately. How is an anisotropic equilibrium different from an isotropic one? How accurate is the MHD model for anisotropic equilibria? How does the change in equilibrium affect the further study of a plasma (such as stability and transport)?

The theory of tokamak anisotropic equilibrium has been studied by many authors [13, 78, 79, 80, 81]. One basic result is that the two pressures  $p_{\parallel, \perp}$  and the density  $\rho$  are no longer flux functions [82, 83, 84]. At the same time, anisotropy could add to or subtract the magnetic axis outward shift (Shafranov-shift [85]) [83, 86, 87]. The latter result has been confirmed by numerical code FLOW [88]. Some authors also find the experimentally inferred equilibrium assuming single pressure and anisotropic pressure can be quite different [76, 77, 89].

In this work, we address the first two questions with analytical and numerical approaches. We show how  $p_{\parallel}$ ,  $p_{\perp}$  and the “nonlinear” part separately contribute to the force balance and deviate from flux functions. We also answer the second question of what problem a scalar pressure model will lead to in equilibrium reconstruction, and its dependency on aspect ratio and the magnitude of anisotropy.

This work is organized as follows: In Section 2.2, the anisotropic and toroidal flow-modified Grad-Shafranov equation we use in our analytical and numerical study is derived and presented. Section 2.3 briefly describes the numerical methods and the code HELENA+ATF. The features of an anisotropic equilibrium are studied in Section 2.4. Section 2.5 evaluates the widely used MHD scalar pressure approximation to anisotropic pressure.

## 2.2 Grad-Shafranov Equation with anisotropic pressure and toroidal flow

### 2.2.1 Basic Equations

Our assumptions of plasma equilibrium are based on guiding center plasma theory (GCP) [13, 79] with ideal MHD Ohm’s law. The basic equations are (in S.I. units):

$$\rho(\mathbf{u} \cdot \nabla \mathbf{u}) + \nabla \cdot \mathbf{P} = \mathbf{J} \times \mathbf{B}, \quad (2.1)$$

$$\nabla \times \mathbf{B} = \mu_0 \mathbf{J}, \quad (2.2)$$

$$\nabla \cdot \mathbf{B} = 0, \quad (2.3)$$

$$\nabla \times \mathbf{E} = 0, \quad (2.4)$$

$$\mathbf{E} + \mathbf{u} \times \mathbf{B} = 0, \quad (2.5)$$

$$\mathbf{P} = p_{\perp} \mathbf{I} + \frac{\Delta}{\mu_0} \mathbf{B} \mathbf{B}, \quad \Delta \equiv \mu_0 \frac{p_{\parallel} - p_{\perp}}{B^2}, \quad (2.6)$$

where  $\rho$  is the mass density,  $\mathbf{u}$  the single fluid velocity,  $\mathbf{P}$  the pressure tensor,  $\mathbf{J}$  the current density,  $\mathbf{B}$  the magnetic field,  $\mathbf{E}$  the electric field, and  $\mu_0$  the vacuum permeability constant. Equation (2.1) is the GCP force balance. Equation (2.2), (2.3) and (2.4) are Maxwell equations. Equation (2.5) is the ideal Ohm’s law. Equation (2.6) is the GCP assumption of anisotropic pressure, which assumes the pressure tensor consists of two components,  $p_{\perp}$  and  $p_{\parallel}$ , with  $\mathbf{I}$  the identity tensor. The fast ion finite orbit width (FOW) effects are ignored in our fluid model. FOW effects can be important for tokamaks with fast ion heating, especially in tight aspect ratio tokamaks. For example, the fast ion orbit width can be as large as 20% of the minor radius in MAST with parallel on-axis beam. The inclusion of these effects in equilibrium requires a kinetic/gyro-kinetic treatment of the fast ions (e.g. the inclusion in fast ion currents and thus the equilibrium, when fast

ion proportion is low [90, 91]).

With axisymmetric cylindrical coordinate system  $(R, Z, \varphi)$  and Eq. (2.3),  $\mathbf{B}$  is written as

$$\mathbf{B} = \nabla\Psi \times \nabla\varphi + RB_\varphi\nabla\varphi, \quad (2.7)$$

where  $\Psi$  is the poloidal magnetic flux and  $B_\varphi$  the toroidal magnetic field. Current density in toroidal and poloidal direction can be deduced from the Ampere's Law (Eq. (2.2)) :

$$\mu_0 J_\varphi = -R\nabla \cdot \frac{\nabla\Psi}{R^2}, \quad \mu_0 \mathbf{J}_p = \nabla(RB_\varphi) \times \nabla\varphi. \quad (2.8)$$

If only the toroidal part of flow is important, with  $\nabla \times (\mathbf{u} \times \mathbf{B}) = 0$  from Eq. (2.4) and (2.5), the form of  $\mathbf{u}$  becomes

$$\mathbf{u} = \Omega(\Psi)R^2\nabla\varphi, \quad (2.9)$$

in which  $\Omega$  is the toroidal angular velocity and a flux function for zero resistivity.

Two different forms of toroidal flow and anisotropic modified Grad-Shafranov equations (modified GSE) [12, 85] can be derived from the above equations using different variables. The pressure form of the GSE has pressures as a function of three variables  $(R, B, \Psi)$  :  $p_{\parallel,\perp} = p_{\parallel,\perp}(R, B, \Psi)$  [12, 92, 81, 82, 87]. The enthalpy form uses  $\rho$  as a variable instead of  $R$ , which means  $p_{\parallel,\perp} = p_{\parallel,\perp}(\rho, B, \Psi)$  [92, 83, 88].

### 2.2.2 Grad-Shafranov Equation in the form of pressure

To obtain the modified GSE in the pressure form, the momentum equation is rearranged into a form, as mentioned by many authors (for example [13, 92, 78, 83, 84, 88]) :

$$\mu_0 \nabla p_{\parallel} = \Delta \nabla \frac{B^2}{2} + \nabla \times [(1 - \Delta)\mathbf{B}] \times \mathbf{B} + \mu_0 \rho \Omega^2 R \nabla R. \quad (2.10)$$

Substituting  $p_{\parallel} = p_{\parallel}(R, B, \Psi)$  into Eq. (2.10), the component of Eq. (2.10) in  $\nabla\varphi$ ,  $\nabla B$ ,  $\nabla R$  and  $\nabla\Psi$  directions each gives

$$F(\Psi) \equiv RB_\varphi(1 - \Delta), \quad (2.11)$$

$$\left( \frac{\partial p_{\parallel}}{\partial B} \right)_{\Psi, R} = \frac{\Delta B}{\mu_0}, \quad (2.12)$$

$$\left( \frac{\partial p_{\parallel}}{\partial R} \right)_{\Psi, B} = \rho R \Omega^2, \quad (2.13)$$

$$\nabla \cdot \frac{(1 - \Delta)\nabla\Psi}{R^2} = -\frac{FF'}{(1 - \Delta)R^2} - \mu_0 \left( \frac{\partial p_{\parallel}}{\partial \Psi} \right)_{R, B}. \quad (2.14)$$

We note that  $F = RB_\varphi(1 - \Delta)$ , instead of  $RB_\varphi$ , becomes a flux function. The restrictions for  $p_{\parallel}(R, B, \Psi)$  are Eq. (2.12) and (2.13): these also guarantee the parallel force balance (multiplying Eq. (2.10) by  $\mathbf{B}$ ) is satisfied. In the limit of no toroidal flow, Eq. (2.12) can also be deduced from the parallel force balance. Finally, Eq. (2.14) is the modified GSE for anisotropic and toroidally rotating system.

### 2.2.3 Grad-Shafranov Equation in the form of enthalpy

A detailed derivation of the enthalpy form of the modified GSE can be found in [92, 83, 88]. Starting from the energy conservation equation, the relationships between the enthalpy  $W(\rho, B, \Psi)$  and plasma pressures as well as rotation are derived. A new flux function  $H$ , which defines as

$$H(\Psi) = W(\rho, B, \Psi) - \frac{1}{2}\Omega^2 R^2, \quad (2.15)$$

is inferred from these relationships.

In order to close the set of equations, a certain equation of state is needed. In our work, the bi-Maxwellian distribution model is chosen. This is the simplest distribution function that will capture anisotropy. The two pressures are now products of plasma density and the parallel and perpendicular temperatures, and the thermal closure chosen is that parallel temperature is a flux function:

$$p_{\parallel}(\rho, B, \Psi) = \rho T_{\parallel}(\Psi), \quad p_{\perp}(\rho, B, \Psi) = \rho T_{\perp}(B, \Psi). \quad (2.16)$$

The two temperatures  $T_{\parallel}$  and  $T_{\perp}$  are in units of energy per mass. Inserting the bi-Maxwellian assumptions yields an expression for  $W(\rho, B, \Psi)$  and  $T_{\perp}(B, \Psi)$  [92, 83], written as

$$W(\rho, B, \Psi) = T_{\parallel} \ln \frac{T_{\parallel} \rho}{T_{\perp} \rho_0}, \quad \rho = \rho_0 \frac{T_{\perp}}{T_{\parallel}} \exp \frac{H + \frac{1}{2} R^2 \Omega^2}{T_{\parallel}}, \quad (2.17)$$

$$T_{\parallel} = T_{\parallel}(\Psi), \quad T_{\perp} = \frac{T_{\parallel} B}{|B - T_{\parallel} \Theta(\Psi)|}, \quad (2.18)$$

with  $\rho_0$  a constant and a new flux function  $\Theta$  indicating the magnitude of anisotropy.

Considering the  $\nabla \Psi$  direction of Eq. (2.10) will give the enthalpy form of the modified GSE :

$$\begin{aligned} \nabla \cdot \frac{(1 - \Delta) \nabla \Psi}{R^2} = & - \frac{F F'}{(1 - \Delta) R^2} \\ & - \mu_0 \rho \left[ T'_{\parallel} + H' + R^2 \Omega \Omega' - \left( \frac{\partial W}{\partial \Psi} \right)_{\rho, B} \right], \end{aligned} \quad (2.19)$$

with  $F$  defined by Eq. (2.11). The system is specified by five functions  $\{T_{\parallel}, H, \Omega, F, \Theta\}$  of  $\Psi$  and the boundary conditions on  $\Psi$ .

The pressure form of the modified GSE (Eq. (2.14)), when closed with Eq. (2.18), is equivalent to the enthalpy form of the modified GSE. The enthalpy form of the modified GSE with bi-Maxwellian assumption is numerically solved. We have used the pressure form of the modified GSE to explore physics of anisotropic plasma.

## 2.3 Numerical scheme

Based on the modified GSE in Eq. (2.19), we altered and updated the axisymmetric plasma equilibrium code HELENA [93] to its anisotropy and toroidal flow version HELENA+ATF. Since the internal physical assumptions and equations are completely changed, we have rewritten most of its matrix element calculations and post-processing, but have retained subroutines for isoparametric meshing. HELENA+ATF uses the same isoparametric bicubic Hermite elements as HELENA [30, 93].

Equation (2.19) is solved in its weak form. That is, with the spatial discretization in Ref. [30] and [93], the PDE system is transformed into a linear algebra problem by integrating both sides after multiplied by each Hermite element. Here, a Picard iteration is used to solve the system. The flux functions and  $\Delta$  of  $n$ 'th iteration is used to calculate the flux surfaces  $\Psi(R, Z)$  of  $(n + 1)$ 'th iteration.

If  $p_{\parallel} > p_{\perp}$ ,  $1 - \Delta$  can go from positive to negative. In this case, the shear Alfvén wave becomes purely growing [19], labeled as the firehose instability. On the other hand, if  $p_{\parallel} < p_{\perp}$ , the mirror instability may occur, with the non-oscillating mode becoming unstable [19]. The firehose and mirror stability criteria given by [13, 94] are

$$1 - \Delta > 0, \quad (2.20)$$

$$1 + \frac{\mu_0}{B} \frac{\partial p_{\perp}}{\partial B} > 0, \quad (2.21)$$

which guarantee Eq. (2.19) to be elliptic all the time [12, 83]. These criteria are also sufficient conditions for the solvability (see Appendix 2.7) of the four interdependent variables  $p_{\parallel}$ ,  $p_{\perp}$ ,  $B$  and  $\Delta$  (Eq. (2.6) (2.7) and (2.11)). In this work, we only discuss equilibria within these stability criteria. With bi-Maxwellian Eq. (2.18), the stability criteria are written as

$$\frac{3\beta_E + 2 + \sqrt{(3\beta_E + 2)^2 + 12\beta_E}}{6\beta_E} > \frac{p_{\perp}}{p_{\parallel}} > \frac{3\beta_E - 2}{3\beta_E + 4}, \quad (2.22)$$

with  $\beta_E = \mu_0(4p_{\perp}/3 + 2p_{\parallel}/3)/B^2$  the local ratio of the kinetic energy to the magnetic energy. Even in a tokamak with  $\beta_E = 0.4$ , we still have the upper limit 3 and lower limit below zero. Therefore, these stability criteria are satisfied in most scenarios, although the mirror instability criterion may be approached in high  $\beta$  tokamaks with strong ICRH or perpendicular NBI heating.

In order to benchmark force balance convergence of HELENA+ATF, we consider a test case with constant  $F$  and  $\Theta$  profiles, linear  $T_{\parallel}$  profile ( $\sim 1 - \Psi$ ), and quadratic  $H$  and  $\Omega^2$  profiles ( $\sim (1 - \Psi)^2$ ). The plasma boundary is set to have elongation  $\kappa = 1.2$ , triangularity  $\delta = 0.2$  and inverse aspect ratio  $\epsilon = 0.3$ . In anisotropic test cases,  $p_{\parallel}/p_{\perp} = 1.5$  on the axis, while in test cases with toroidal flow,  $\bar{\Omega}^2/\bar{T}_{\parallel} = 0.5$  on the axis.

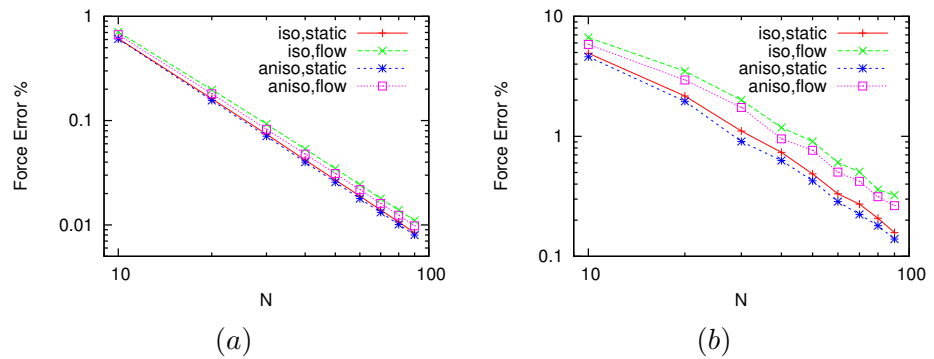


**Figure 2.1:** (a) The average force balance error of all grid cells and (b) maximum force balance error in four test cases.  $NR=NP=N$  is the number of radial and poloidal grid points. Force balance error per cell means  $\Delta F/F = 2|\text{RHS-LHS}|/|\text{RHS+LHS}|$  of Eq. (2.19) in percent. Average force balance is calculated by  $\sum(\Delta F/F)/N^2$ .

Figure 2.1 shows the average force balance error of all grid cells and the maximum



force balance error in four test cases. The force balance error decreases logarithmically as grid resolution increases. To explain the difference between Fig. 2.1 (a) and (b), we mention that the force balance error is close to zero near the core but reach its maximum at the boundary. This is not only because the grid is more concentrated at the core, but also a sharp boundary approaching an X point or triangular point will cause numerical degrading with a singular Jacobian.

Once the equilibrium is computed, HELENA+ATF also provides high precision coordinate information for stability codes. The solution of the modified GSE is mapped into the straight field line coordinate  $(s, \vartheta, \varphi)$ , which is defined as

$$s = \sqrt{\Psi/\Psi_0}, \quad \vartheta(\theta) = \frac{F(\Psi)}{q} \int_{\Psi} \frac{dl}{R(1-\Delta)|\nabla\Psi|}, \quad (2.23)$$

where  $q$  is defined as

$$q(\Psi) = \frac{F(\Psi)}{2\pi} \oint_{\Psi} \frac{dl}{R(1-\Delta)|\nabla\Psi|}. \quad (2.24)$$

The metric coefficients  $g^{ij}$  and Jacobian  $J$  can then be calculated.

## 2.4 The features of anisotropic equilibria

There are three major effects of anisotropic pressure that we can infer from our model and Eq. (2.19):

- (i)  $p_{\perp}$  and  $p_{\parallel}$  contribute separately to the toroidal current;
- (ii) the term, “ $1 - \Delta$ ” inside the LHS operator will modulate the poloidal flux and form a new “nonlinear current”;
- (iii) pressures and density contours no longer lie on surfaces of constant poloidal flux.

Effect (i) and (ii) will be explained in Section 2.4.1, and (iii) in Section 2.4.2. In this section, flow is turned off unless otherwise specified. We choose profiles that represent the general shape and trend of the EFIT-TENSOR reconstructed profiles with TRANSP[57] constraint of MAST discharge #18696 at 290ms [92]. They are

$$\begin{aligned} T(\Psi) &= C_0(1 - \Psi)^2 + C_1, \quad H(\Psi) = \frac{C_0}{2}(1 - \Psi)^3 + C_2, \\ F(\Psi) &= F_0, \quad \Theta(\Psi) = \Theta_0, \end{aligned} \quad (2.25)$$

where  $C_0, C_1, C_2, F_0$  and  $\Theta_0$  are adjustable constants. Constants  $C_1$  and  $C_2$  are small values to make density and current profiles vanish at the plasma edge. By varying  $F_0$ , we can adjust  $q_0$ . The parameter  $\Theta_0$  is associated with the magnitude of anisotropy.

For these profiles we examine four equilibrium configurations. Equilibrium A is guided by a MAST like boundary with triangularity  $\delta = 0.4$ , elongation  $\kappa = 1.7$  and inverse aspect ratio  $\epsilon = 0.7$ . Anisotropy of the case is chosen to be  $p_{\parallel}/p_{\perp} \approx 1.5$  at core, with a monotonic  $q$  profile and  $q_0 \approx 1$ . Equilibrium B examines the dependence with aspect ratio:  $\epsilon$  is changed to 0.3, and  $F_0$  adjusted to leave  $q_0$  unchanged. Equilibrium C examines the isotropic limit:  $\Theta_0$  is set to zero, and  $F_0$  adjusted to leave  $q_0$  unchanged. Finally, equilibrium D examines the impact of toroidal flow, with  $\Omega^2 \sim (1 - \Psi)^3$ , such that the ion thermal Mach number  $M_{t\varphi}$  peaks at 0.7 on axis and vanishes at the edge, where

$M_{t\varphi} = v_\varphi / \sqrt{k_B T_i / m_i}$  and  $T_i$  is the ion temperature. This is the typical upper limit of toroidal flow in MAST [95]. In all cases anisotropy peaks at the core due to the flat  $\Theta$  profile we have chosen. Table 2.1 shows parameters of these equilibria.

**Table 2.1:** Parameters of equilibrium A, B, C and D.

Equilibrium	$\epsilon$	$q_0$	$\Delta$	Anisotropy	Flow
A	0.7	1.04	5.0%	$p_{\parallel}/p_{\perp} \approx 1.5$	none
B	0.3	1.04	1.5%	$p_{\parallel}/p_{\perp} \approx 1.5$	none
C	0.3	1.01	0.0%	none	none
D	0.7	1.05	0.0%	none	$M_{t\varphi} \approx 0.7$ on axis

### 2.4.1 Toroidal current decomposition

In a cylindrical plasma with straight field lines and infinite length, the perpendicular force balance is determined by  $p_{\perp}$ . In a tokamak, there is a  $p_{\parallel}$  contribution [87] to perpendicular force balance. If flow is ignorable, we can rewrite Eq. (2.14) and decompose  $J_{\varphi}$  as

$$\mu_0 J_{\varphi} = \underbrace{\mu_0 R \sin^2 \alpha \left( \frac{\partial p_{\parallel}}{\partial \Psi} \right)_B}_{J_{p_{\parallel}}} + \underbrace{\mu_0 R \cos^2 \alpha \left( \frac{\partial p_{\perp}}{\partial \Psi} \right)_B}_{J_{p_{\perp}}} + \underbrace{\frac{1 - \Delta}{2R} \left( \frac{\partial (RB_{\varphi})^2}{\partial \Psi} \right)_B}_{J_{tf}(\text{toroidal field})} - \underbrace{R \nabla \cdot \frac{\Delta \nabla \Psi}{R^2}}_{J_{nl}(\text{nonlinear})}, \quad (2.26)$$

where  $\alpha$  is the field pitch angle, i.e.  $\tan \alpha \equiv B_p / B_{\varphi}$ , with  $B_p$  the poloidal magnetic field. The flux surface is determined by  $J_{\varphi}$  through Eq. (2.8). The four contributing terms,  $J_{p_{\parallel}}$ ,  $J_{p_{\perp}}$ ,  $J_{tf}$  and  $J_{nl}$  are identified here. This equation shows that the balance of  $J_{p_{\perp}}$  and  $J_{p_{\parallel}}$  is determined by the pitch angle  $\alpha$ .

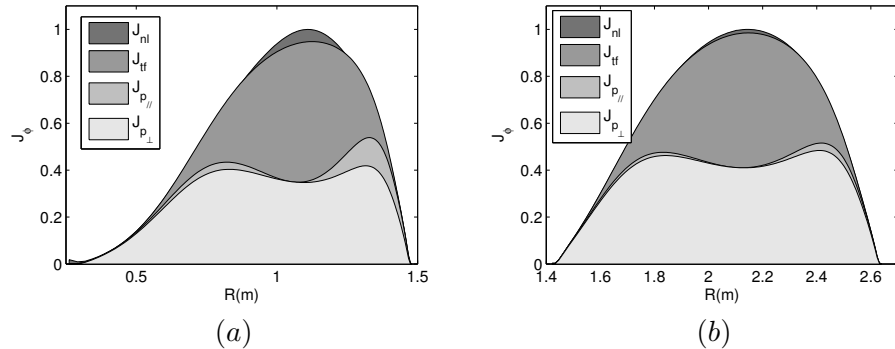


**Figure 2.2:** Contribution of each component to  $J_{\varphi}$  across the mid-plane in (a) equilibrium A with  $\epsilon = 0.7$ , (b) equilibrium B with  $\epsilon = 0.3$ . Shaded areas with different gray levels indicate different components. Maximum of  $J_{\varphi}$  is normalized to unity.

Figure 2.2 shows the decomposition of  $J_{\varphi}$  along the mid-plane for equilibrium A and B. These two equilibria have similar profiles and their major difference is the aspect ratio. In both cases,  $J_{\varphi}$  is dominated by  $J_{p_{\perp}}$  and  $J_{tf}$ , which roughly equal. The  $J_{p_{\parallel}}$  component

is zero on the magnetic axis, consistent with  $\sin^2 \alpha = B_p^2/B^2$  and  $B_p = 0$  on axis. For a low  $\beta$  plasma,  $\sin^2 \alpha = B_p^2/B^2 \sim \epsilon^2/q^2$ . We would thus expect, and observe, an increasing contribution from  $J_{p\parallel}$  with increasing  $\epsilon$ . For  $\epsilon = 0.7$ ,  $J_{p\parallel}$  peaks at 20% on the low field side. Therefore, if the contribution of  $p_{\parallel}$  is ignored, or in other words, attributed to  $p_{\perp}$ , the current profile, and thus the  $q$  profile will be changed up to 10% with  $p_{\parallel}/p_{\perp} \approx 1.5$ . Like  $J_{p\parallel}$ , we observe  $J_{nl}$  scales with  $\epsilon$ , but the reason is different. The change in  $J_{nl}$  with  $\epsilon$  is an artifact: it is a consequence of preserving  $q_0$ .

Figure 2.3 explores the on-axis contribution of  $J_{nl}$  to  $J_{\varphi}$  with changing anisotropy. It shows that  $J_{nl}$  linearly depends on  $\Delta$ , but has no dependency on  $p_{\parallel}/p_{\perp}$ , consistent with Eq. (2.26). The result stresses that for analytic working and numerical codes in which  $\Delta = 0$  approximation is used but anisotropy retained, care should be taken when anisotropy appears along with  $\beta$  above a few percent, as the effect of this approximation is to delete the nonlinear current.

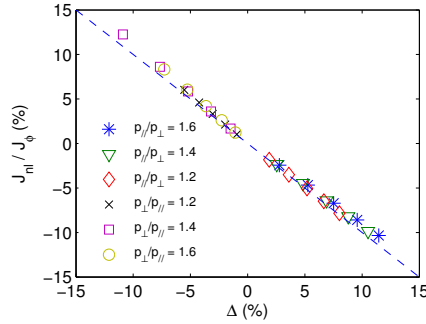


**Figure 2.3:** The contribution of nonlinear current  $J_{nl}$  to total toroidal current  $J_{\varphi}$  in percent as a function of  $\Delta$ . Different markers indicate different magnitude of anisotropy on axis.

Inspection of Fig. 2.2 and 2.3 shows that at large aspect ratio and low  $\Delta$ ,  $J_{\varphi} \approx J_{p\perp} + J_{tf}$ . Thus, we would expect the global magnetic and current parameters to be insensitive to other changes, if  $p_{\perp}$  and  $RB_{\varphi}$  profiles remain fixed. To demonstrate this, we have examined the change in global parameters with changing  $\xi = 2(\overline{p_{\perp}} - \overline{p_{\parallel}})/(\overline{p_{\perp}} + \overline{p_{\parallel}})$ , but fixed flux surface average profiles  $\langle \rho \rangle$ ,  $\langle RB_{\varphi} \rangle$  and  $\langle p_{\perp} \rangle$  about isotropic equilibrium C, with “ $\overline{\cdot}$ ” the volume average operator and  $\langle \cdot \rangle$  the flux surface average operator. During the scan, we change  $\Theta_0$  and adjust  $T, H$  and  $F$  profiles to keep the above flux surface average profiles identical to equilibrium C. The percentage change of global parameters is recorded in Fig. 2.4(a), which shows that with the exception of Shafranov-shift (See Section 2.4.2), other global parameters do not change much. This confirms the dominant role of  $J_{p\perp} + J_{tf}$  in large aspect ratio tokamaks. For a comparison, in Fig. 2.4(b), we keep  $\langle p^* \rangle$  instead of  $\langle p_{\perp} \rangle$ , with  $p^* = (p_{\parallel} + p_{\perp})/2$  the standard MHD isotropic pressure approximation (See Section 2.5). As shown in Fig. 2.4(b), all global parameters will change significantly in the magnitude of  $\xi$ . The result shows that  $\langle p_{\perp} \rangle$  is much better than  $\langle p^* \rangle$  to retain global parameters, if  $\langle \rho \rangle$  and  $\langle RB_{\varphi} \rangle$  are also unchanged.

## 2.4.2 Deviation from flux function

### Impact on pressure and density

It is clear that with the isotropic assumption  $p_{\parallel} = p_{\perp} = p$  and static assumption, we have  $\nabla p \cdot \mathbf{B} = 0$ , which means pressure is a flux function. But now with the additional

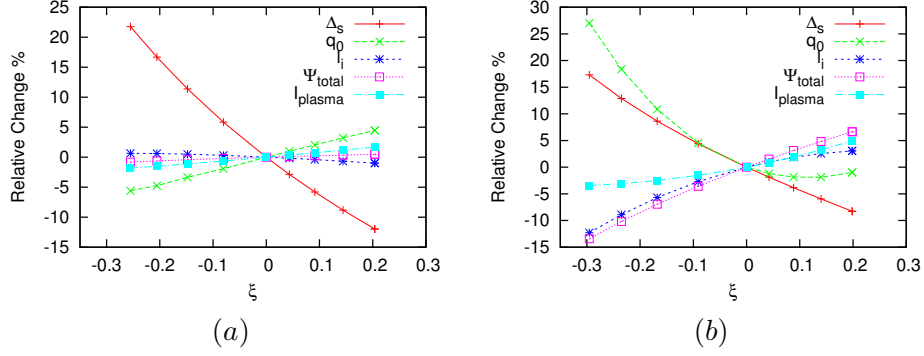


**Figure 2.4:** The change of global parameters: Shafranov-shift( $\Delta_s$ ),  $q_0$ ,  $l_i$  (Eq.(2.32)), total flux, total current due to the changing magnitude of anisotropy based on equilibrium C, if the following quantities are hold unchanged for each flux surface: (a)  $\langle p_\perp \rangle$ ,  $\langle \rho \rangle$  and  $\langle RB_\varphi \rangle$ , (b)  $\langle p^* \rangle$ ,  $\langle \rho \rangle$  and  $\langle RB_\varphi \rangle$ . For instance, the change of  $\Delta_s$  is in the form of  $(\Delta_{s,aniso} - \Delta_{s,iso})/\Delta_{s,iso} \times 100\%$ .

term  $\Delta \mathbf{B}\mathbf{B}$  in Eq. (2.6), the two pressures and the density are not flux functions. This subsection will focus on their variation over a certain flux surface.

If aspect ratio is large, which means the variation of magnetic field on a flux surface,  $(B_{max} - B_{min})/B$  is small, we can Taylor expand  $p_\parallel$  about  $B_0 = B(R_0)$ , with  $R_0$  the major radius of the magnetic axis. We use Eq. (2.12) to substitute the partial derivative and derive the difference  $\Delta p_\parallel \equiv p_{\parallel,out} - p_{\parallel,in}$ , where the subscript “out” denotes the most outward point and “in” the most inward point on a flux surface. Generally  $B \approx B_0 R_0 / (R_0 + r \cos \theta)$  on a flux surface, in which  $r$  is minor radius of a certain flux surface and  $\theta$  the poloidal angle. Combined, we obtain

$$\frac{\Delta p_\parallel}{p_\parallel} \approx \frac{2r}{R_0} \left( \frac{p_\perp - p_\parallel}{p_\parallel} \right)_{R=R_0}. \quad (2.27)$$

We note here to reach Eq. (2.27), we don’t need any kinetic assumptions. Similarly, an expansion of  $\rho$  and  $p_\perp$  about  $B_0$ , using Eq. (2.16), (2.17) and (2.18), yields the difference of  $\rho$  and  $p_\perp$  on a flux surface :

$$\frac{\Delta \rho}{\rho} \approx \frac{2r}{R_0} \left( \frac{p_\perp - p_\parallel}{p_\parallel} \right)_{R=R_0}, \quad \frac{\Delta p_\perp}{p_\perp} \approx \frac{4r}{R_0} \left( \frac{p_\perp - p_\parallel}{p_\parallel} \right)_{R=R_0}, \quad (2.28)$$

where the meaning of  $\Delta \rho$  and  $\Delta p_\perp$  is similar to  $\Delta p_\parallel$ . Equation (2.27) and (2.28) indicate the linear dependence of  $\rho$  and  $p_{\parallel,\perp}$ ’s non-flux-function effect on the magnitude of anisotropy and  $\epsilon$ . These equations also give the direction of contour shift. If  $p_\perp > p_\parallel$  ( $p_\perp < p_\parallel$ ), the shift of pressures and density contour respect to flux surfaces is outward (inward), which can be compared to previous findings [82, 83].

We also study the non-flux function effect numerically. In Fig. 2.5, we plot  $p_\parallel$  and  $p_\perp$  on different flux surfaces for equilibrium A. Moving outward from the core, anisotropy decreases and reaches  $p_\perp = p_\parallel$  at the boundary, while  $r/R_0$  increases from zero to its maximum at the boundary. The competition between these two factors makes the difference peak at  $s = 0.5$ , with  $\Delta p_\parallel/p_\parallel \approx 10\%$  and  $\Delta p_\perp/p_\perp \approx 20\%$ . This figure demonstrates the deviation of profiles from a function of flux in a single equilibrium. Figure 2.6 shows the maximum in  $\Delta \rho/\rho$  as a function of  $\epsilon$  and  $\xi$ , scanning about the isotropic equilibrium C. Inspection clarifies the change of density on a flux surface is almost linear with aspect

ratio and anisotropy. Similar behavior is found for  $\Delta p_{\parallel}/p_{\parallel}$  and  $\Delta p_{\perp}/p_{\perp}$ . Thus, the results of Eq. (2.27) and (2.28) can be extrapolated to tight aspect ratio tokamaks.

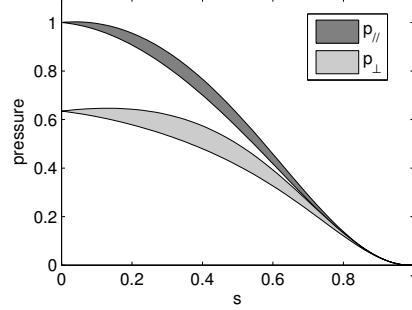


**Figure 2.5:** Pressure on flux surfaces for equilibrium A.  $s = \sqrt{\Psi/\Psi_0}$  is the standard flux label. The upper boundaries of the shaded areas are the maximum value of pressure on certain flux surfaces and the lower boundaries show the minimum. The shaded areas indicate the range of value on flux surfaces. Pressures are normalized to  $p_{\parallel}$  on axis.

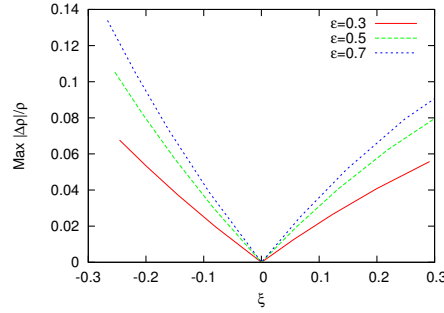


**Figure 2.6:** Maximum deviation of  $\rho$  from a flux function with different amplitude of anisotropy and different aspect ratio.

To demonstrate the magnitude of the non-flux-function effect, we compare the pressure profiles from anisotropic equilibrium A to flowing isotropic equilibrium D. Figure 2.7 shows the pressure profile on flux surfaces for equilibrium D. The pressure difference peaks at 7% at  $s = 0.4$ , which is comparable to the difference in  $p_{\parallel}$  for static anisotropic equilibrium A. For equilibrium A, the pressure difference in  $p_{\perp}$  is larger than equilibrium D.

### Impact on Shafranov Shift

Using methods in [30, 85, 86, 87], for large aspect ratio ( $\epsilon = a/R_0 \ll 1$ ), low  $\beta$  ( $\beta \sim \epsilon^2$ ) plasma, we have to zero's order in  $\epsilon$ , the modified GSE:

$$\frac{d}{d\hat{r}}(\mu_0 \langle p_{\perp} \rangle) + \frac{1}{2} B_{\varphi 0}^2 + \frac{B_{p0}}{\hat{r}} \frac{d}{d\hat{r}}(\hat{r} B_{p0}) = 0. \quad (2.29)$$

Replacing  $p_{\perp}$  by  $p$  will return to the original isotropic and static case. This also confirms our result that flux surface is mostly decided by  $p_{\perp}$  in large aspect ratio scenario.

The next order contribution,  $O(\epsilon)$ , along with bi-Maxwellian relationships Eq. (2.18),

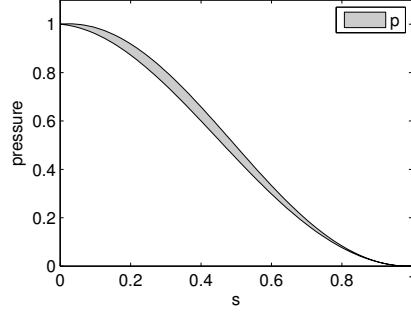


**Figure 2.7:** Pressure on flux surfaces for equilibrium D. The upper boundary of the shaded area is the maximum value of pressure on certain flux surfaces and the lower boundary shows the minimum. The shaded area indicates the range of value on flux surfaces. Pressure normalized to 1 at the magnetic axis.

yields the formulation of Shafranov-Shift:

$$\Delta'_s(\hat{r}) = -\frac{1}{\hat{r}R_0B_{p0}^2} \int_0^{\hat{r}} \hat{r} d\hat{r} r \times \left\{ 2\hat{r}\mu_0 \left\langle p_{\perp} \left[ 1 + \left( \frac{p_{\parallel} - p_{\perp}}{2p_{\perp}} \right) + \left( \frac{T_i}{2T_{\perp}} M_{t\varphi}^2 \right) \right] \right\rangle' - B_{p0}^2 \right\}. \quad (2.30)$$

This result is same as [86, 87]. The variables  $B_{p0}$  and  $\langle p_{\perp} \rangle$  are related through Eq. (2.29), and are independent to  $p_{\parallel}$ . Anisotropy and flow contribute to the Shafranov-Shift only through  $p_{\parallel}$  and  $M_{t\varphi}^2$ , and their effect is to scale  $p_{\perp}$ . An example of how anisotropy influence Shafranov-shift is provided in Fig. 2.4(a), where  $\langle p_{\perp} \rangle$  and  $\langle RB_{\varphi} \rangle$  are fixed. The figure shows that  $p_{\parallel} > p_{\perp}$  ( $p_{\parallel} < p_{\perp}$ ) indicates more (less) Shafranov-shift and the magnitude of this change is linear in  $\xi$ .

## 2.5 Performance of isotropic model in reconstruction of anisotropic systems

In this section we examine the implications of the choice of model in equilibrium reconstruction. A useful starting point are global invariants obtained by integrating momentum conservation. Following this procedure, Cooper and Lao [55, 96] reached the following relationship between global parameters for large aspect ratio tokamaks (Eq.(12) of [97]):

$$\frac{1}{2}(\beta_{p\perp} + \beta_{p\parallel}) + W_{pt} + \frac{l_i}{2} = \frac{S_1}{4} + \frac{S_2}{4} \left( 1 + \frac{R_t}{R_0} \right), \quad (2.31)$$

with  $R_0$  the major radius,  $R_t$  a volume dependent constant and

$$\beta_{p\parallel} \equiv \frac{2\mu_0 \overline{p_{\parallel}}}{B_{pa}^2}, \quad \beta_{p\perp} \equiv \frac{2\mu_0 \overline{p_{\perp}}}{B_{pa}^2}, \quad W_{pt} \equiv \frac{\mu_0 \overline{\rho u^2}}{B_{pa}^2}, \quad l_i \equiv \frac{\overline{B_p^2}}{B_{pa}^2}, \quad (2.32)$$

in which  $B_{pa}$  is average poloidal field at boundary and  $u$  is the rotation velocity. The terms  $\beta_{p\parallel}$  is the parallel poloidal beta,  $\beta_{p\perp}$  the perpendicular poloidal beta,  $W_{pt}$  the rotation poloidal beta and  $l_i$  the internal inductance. In this section, we consider static equilibria in which  $W_{pt} = 0$ . The constants  $S_1, S_2$  are integrals of external fields and currents

and therefore can be measured [98]. For a given set of data from magnetic probes,  $S_1$  and  $S_2$  are exactly determined. Equation (2.31) provides a good measurement of fit for reconstructions using both anisotropic models and MHD model with  $p = p^* = (p_{\parallel} + p_{\perp})/2$  approximation and  $\beta = (\beta_{p\perp} + \beta_{p\parallel})/2$  (ideal MHD). This is the historical reason to use  $p^*$  as the approximate scalar pressure. The section intends to answer the question that if plasma is anisotropic and we still reconstruct using ideal MHD, how good are the reconstructed profiles, compared to using an anisotropic model.

### 2.5.1 Model dependence in equilibrium reconstruction

The impact of different models on the inferred pressure and current gradient profiles can be examined by comparison of the toroidal current profile at large aspect ratio. For the ideal MHD model, the GSE gives

$$\mu_0 R J_{\varphi MHD} = \mu_0 R^2 p'_{MHD}(\Psi) + F_{MHD} F'_{MHD}(\Psi). \quad (2.33)$$

where we have added the subscript MHD to tag these functions with an ideal MHD model. A similar functional form can be written for the toroidal current using an anisotropy modified MHD model. At large aspect ratio, the approximations  $R \approx R_0 + r \cos \theta$  and  $B \approx B_0 R_0/R$  can be applied. We also take  $\Psi$  derivative on both sides of Eq. (2.12), and use it to substitute the cross derivative in the Taylor expansion of  $\partial p_{\parallel}/\partial \Psi$  about  $B_0$ . If flow is ignorable, the RHS of the modified GSE Eq. (2.14) can thus be rearranged into

$$\mu_0 R J_{\varphi m} \approx \mu_0 R^2 p'_{0,m} + \left( F_m F'_m + \mu_0 R_0^2 \frac{p'_{\parallel 0m} - p'_{\perp 0m}}{2} \right) + O\left(\frac{r^2}{R^2}\right), \quad (2.34)$$

where we have similarly added the subscript  $m$  to tag the functions with the anisotropy modified MHD model. The functions  $p_{\parallel 0m}$ ,  $p_{\perp 0m}$  and  $p_{0m}^*$  are those quantities on the flux surface at point  $R = R_0$ . Higher order term are written as  $O(r^2/R^2)$ .

Providing internal current profile information (such as MSE) is available,  $J_{\varphi MHD} = J_{\varphi m}$  in any reconstruction: the current profile is unique. To  $O(r/R)$ , the RHS of Eq. (2.33) and Eq. (2.34) have the same variables and functional dependence with  $R^2$ , that is, a  $R^2$  flux surface varying part and a flux surface invariable part. By equating these two parts respectively, reconstructions using different models but the same data will yield

$$p'_{MHD} = p'_{0,m}, \quad (2.35)$$

$$F_{MHD} F'_{MHD} = F_m F'_m + \mu_0 R_0^2 \frac{p'_{\parallel 0m} - p'_{\perp 0m}}{2}. \quad (2.36)$$

Consequently the inferred pressure profile will be identical to the usual  $p^*$  approximation, but toroidal flux function, and thus the poloidal current profile will be different in the GSE and the modified GSE models. This is consistent with Fig. 2.4(b) which shows the plasma cannot preserve its global parameters, if we fix both  $\langle p^* \rangle$  and  $\langle R B_{\varphi} \rangle$  but vary anisotropy.

At tight aspect ratio, we should consider  $O(r^2/R^2)$  contribution to the modified GSE, with the second term in Taylor expansion of Eq. (2.16), (2.17) and (2.18). The result is

$$f\left(O\left(\frac{r^2}{R^2}\right)\right) = -\mu_0(p_{\parallel 0} - p_{\perp 0}) \left(1 + \frac{p_{\perp 0}}{p_{\parallel 0}}\right) \frac{r^2}{R_0^2} \cos^2 \theta + O\left(\frac{r^3}{R^3}\right). \quad (2.37)$$

Due to the  $\cos^2 \theta$  dependent, it is not possible to resolve  $J_\varphi$  into two MHD flux functions, as done to the zeroth and first parts of Eq. (2.34). Equation (2.37) reveals the dependency of the higher order term on the product of  $(p_{\parallel 0} - p_{\perp 0})/p_{\parallel 0}$  and  $r^2/R^2$ . Thus, in tight aspect ratio tokamaks with large anisotropy, the reconstructed  $J_\varphi$  and  $q$  profile formed by the two flux functions may be distorted, in comparison to the results from anisotropic reconstruction.

### 2.5.2 Equilibrium reconstruction of a MAST discharge

We here study a pair of reconstructions from a single discharge. The example is from EFIT-TENSOR reconstruction for MAST( $\epsilon \approx 0.7$ ) discharge #18696 at 290ms, using either an anisotropic model or isotropic model. In this discharge, MSE data is not available. The constraints we used are magnetic probes, total currents and pressures from TRANSP. These constraints are identical in both reconstructions, except for the anisotropic reconstruction,  $p_{\parallel}$  and  $p_{\perp}$  are constrained to TRANSP  $p_{\parallel}$  and  $p_{\perp}$  respectively, and for the isotropic reconstruction, isotropic pressure is constrained to  $p^* = (p_{\parallel} + p_{\perp})/2$ .

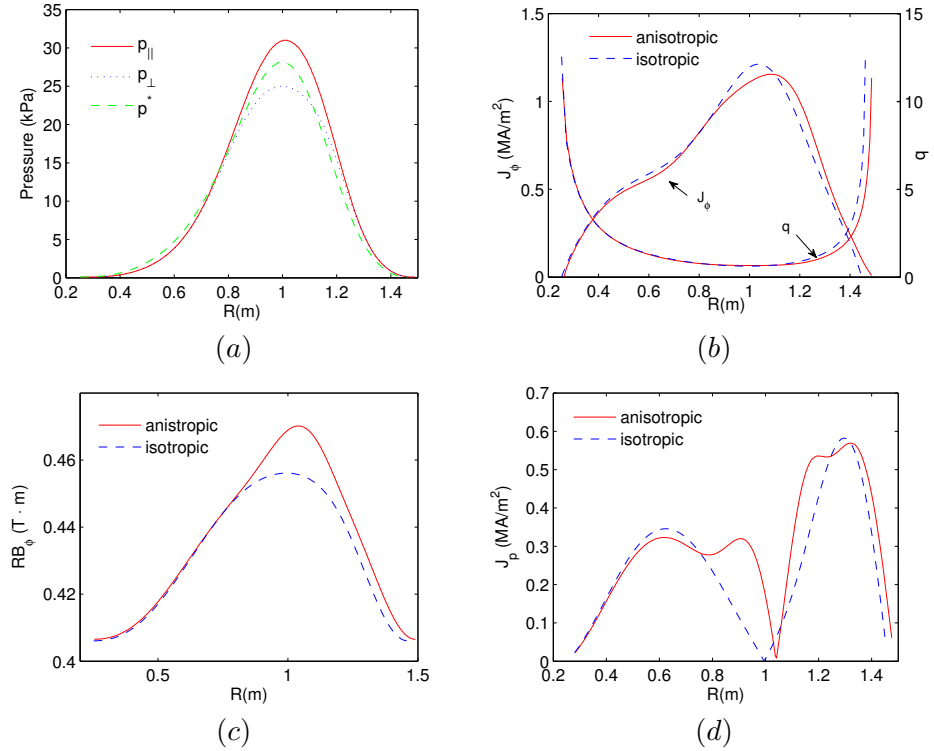


**Figure 2.8:** (a) Pressures on the mid-plane in anisotropic reconstruction (two pressures with solid and dash dot line) and in isotropic reconstruction ( $p^*$  with dot line) for MAST discharge 18696 at 290ms. (b) The reconstructed  $J_\varphi$  profile and  $q$  profile on the mid-plane. (c) The reconstructed  $RB_\varphi$  profile on the mid-plane. (d) The reconstructed poloidal current profile on the mid-plane

In this discharge, NBI is parallel and we have  $p_{\parallel}/p_{\perp} \approx 1.25$  on the magnetic axis, as shown in Fig. 2.8(a). We can see from Fig. 2.8(b) that the two reconstructions gives almost the same  $J_\varphi$  profiles, with a small difference in the core region. We also notice that these two reconstructions give slightly different boundaries, causing the difference of  $q$  and  $J_\varphi$  profile on the low field side. Both inference differences arise because the EFIT-TENSOR



reconstruction is not constrained by a  $J_\varphi$  profile. Despite these differences, the  $q$  profile is found to be nearly identical as a function of flux in the two cases. In our previous work [77], we recorded a 15% lift in  $q_0$  due to anisotropy, which is not observed here. The reason is that in Hole *et al*, the two equilibria with/without anisotropy had fixed profiles, not fixed external constraints of equilibrium, as studied here. In addition, modelled anisotropy in Hole *et al* was  $p_\perp/p_\parallel = 1.7$  (only the beam pressure was considered).

As predicted by Eq. (2.36), the MHD reconstructed toroidal field is underestimated in comparison to the anisotropic reconstruction. This prediction is verified by Fig. 2.8(c), showing that  $RB_\varphi$  is underestimated by 3% at the core. When looking at  $J_p$  profiles of the two cases in Fig. 2.8(d), we discover a large discrepancy near the core region, which peaks at  $R = 0.9\text{m}$  with isotropic  $J_p$  only 1/3 of its anisotropic reconstruction. The difference can be explained by Eq. (2.36). Since the two models infer different  $RB'_\varphi$ ,  $J_p$  is different through  $\mu_0 J_p = |\nabla RB_\varphi|/R$  from Eq. (2.8). In this case the maximum contribution of the  $O(r^2/R^2)$  term is 1.5% to the total current, so the higher order contribution is ignorable.

### 2.5.3 Implications of using MHD to reconstruct anisotropic plasma

Based on the above findings, if single pressure MHD is used to reconstruct a purely anisotropic plasma, the following four problems will occur according to aspect ratio and magnitude of anisotropy.

- (i) The poloidal current is different.

This problem is demonstrated in Section 2.5.1 and 2.5.2 and occurs when the variation of  $F$  profile is comparable to the variation of  $p_\parallel - p_\perp$  across flux surfaces.

- (ii) The anisotropic profiles are not flux functions.

In MHD,  $p$ ,  $RB_\varphi$  and  $\rho$  are flux functions. As shown in Section 2.4.2, they deviate from flux functions. According to Eq.(2.27), (2.28) and Fig. 2.5, this problem linearly increases with  $\epsilon$  and  $\xi$ .

- (iii) Force balance is only satisfied to  $O(r/R)$  with two flux functions.

At tight aspect ratio and large anisotropy, we should take into account terms  $O(r^2/R^2)$  in the modified GSE. It is not possible to decompose the  $J_\varphi$  profile into the combination of two flux functions as we demonstrated in Section 2.5.2. If MHD reconstruction is used, the reconstructed  $J_\varphi$  profile formed by two flux functions may be distorted. Inspection of Eq. (2.37) reveals that this problem is a linear function of  $\epsilon^2\xi$ .

- (iv) The nonlinear current  $J_{nl}$  is important at high  $\beta$  and large anisotropy.

In Section 2.4.1, we showed that  $J_{nl}$  is proportional to  $\Delta$ . The ideal MHD reconstruction neglects  $J_{nl}$ , which might impact the accuracy of the reconstructed  $J_\varphi$  profile and the  $q$  profile in a plasma with high  $\beta$  and large anisotropy.

To illustrate the problems in  $\epsilon - \xi$  space, we have sketched regimes where each problem might occur. The corresponding contours are shown in Fig. 2.9, which consist of four regions with a different number of problems. The lower boundaries are: for problem (i)  $|\xi| = 0.05$  which represents 5% difference between  $p_\parallel$  and  $p_\perp$  on average; for problem (ii)  $|\Delta\rho|/\rho = 5\%$  calculated from Fig. 2.6, taking the average of  $\xi > 0$  and  $\xi < 0$ ; for problem (iii) maximum contribution of the  $O(r^2/R^2)$  term to  $J_\varphi$  equals to 5% , which is obtained

by scanning around equilibrium C. Projection of problem (iv) is not meaningful in  $\epsilon - \xi$  space, as it is a function of  $\Delta$  thus  $\beta$  and  $\xi$ , not  $\epsilon$ .

We have identified the #18696 MAST equilibrium and our equilibrium A and B in these contours. Also,  $p_{\perp}/p_{\parallel} \approx 2.5$  was found in a JET discharge ( $\epsilon \approx 0.3$ ) during ICRH heating [76]. The parameter  $|\xi|$ , if assumed to reach one third of its maximum local value, is 0.3. Problem (ii) is significant in this case, with maximum  $\Delta p_{\parallel}/p_{\parallel} \approx 17\%$ . Recent unpublished MAST data suggests the existence of discharges with  $|\xi| > 0.3$ , and thus encounter Problems (i)-(iii). We will include the study of this discharge in our later publications. Finally, Problem (iv) appears in discharges with relative high  $\beta$ . To date, we haven't identified a discharge with  $\Delta > 5\%$  in MAST. However, a  $> 40\%$  volume average  $\beta$  is observed in NSTX discharges with strong parallel injection [99]. Also, the beam power will increase to 7.5MW in MAST Upgrade [100], providing possibility to trigger Problem (iv) and to enrich our study in the future.

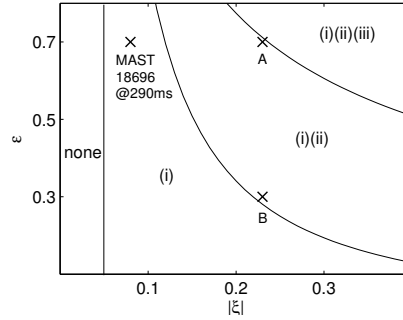


**Figure 2.9:** Problems with ideal MHD reconstructions in  $\epsilon - \xi$  space. The indexes 'i', 'ii' and 'iii' each indicates problem i - iii occur(s) if parameters of an equilibrium is in this region. The 'x' markers represent the positions of the MAST #18696 shot, equilibrium A and B in  $\epsilon - \xi$  space, respectively.

## 2.6 Conclusion

The impact of pressure anisotropy to plasma equilibrium is studied analytically and numerically. To achieve the latter, we have extended the fixed boundary equilibrium and mapping code HELENA to include toroidal flow and anisotropy (HELENA+ATF). We decompose the toroidal current into contributions from both pressures, the toroidal field and the nonlinear part and find the dependence of  $J_{p_{\parallel}}$  on the ratio  $B_p^2/B^2$ . We find a dominant role of  $J_{p_{\perp}}$  over  $J_{p_{\parallel}}$  in the anisotropy and toroidal flow modified Grad-Shafranov equation in large aspect ratio tokamaks. However in a MAST like equilibrium, the  $J_{p_{\parallel}}$  contribution can reach 20% of the total current with  $\epsilon = 0.7$  and  $p_{\parallel}/p_{\perp} \approx 1.5$  which should not be ignored. The impact of this is a 10% change in the current profile, and thus the  $q$  profile, with corresponding implication for plasma stability. The nonlinear current  $J_{nl}$  is proportional to  $\Delta$ , and should not be neglected when anisotropy appears in a high  $\beta$  plasma. We have also found that the deviation of profiles from flux functions is in the order of  $\epsilon|p_{\parallel} - p_{\perp}|/p_{\parallel}$ , showing a larger contour shift with tighter aspect ratio and larger anisotropy.

Motivated by these analysis, we find that depending upon the aspect ratio and the magnitude of anisotropy, the following problems may be encountered when the ideal MHD model with  $p^* = (p_{\parallel} + p_{\perp})/2$  is used to reconstruct an anisotropic plasma. First, the

poloidal current is different. This occurs when the variation of  $F$  profile is comparable to the variation of  $p_{\parallel} - p_{\perp}$  across flux surfaces. Second, the anisotropy profiles are not flux functions, their difference on a flux surface linearly increases with the magnitude of anisotropy and  $\epsilon$ . Third, the  $O(r^2/R^2)$  contribution to  $J_{\varphi}$  is not considered. This may distort the  $J_{\varphi}$  and  $q$  profiles in tight aspect ratio tokamaks with large anisotropy. Finally, the nonlinear current is neglected, degrading the accuracy of the result in a plasma with high  $\beta$  and large anisotropy.

In future work, we plan to study the impact of anisotropy on the magnetic configurations, from a range of experimental discharges and machines, to address this problem empirically. We also plan to study the anisotropic effect on plasma stability.

## 2.7 Appendix: Solvability of $p_{\parallel}, p_{\perp}, B$ and $\Delta$

Here, we demonstrate that Eq. (2.20) and (2.21) are a set of sufficient conditions for the four interdependent variables  $p_{\parallel}, p_{\perp}, B$  and  $\Delta$  (Eq. (2.6) (2.7) and (2.11)) to have one and only one root.

The  $n$ th Picard iteration gives  $\Psi_n(R, Z)$  and thus  $B_{p,n} = |\nabla \Psi_n|$ . To calculate the magnetic field  $B$  after the  $n$ th iteration at a certain grid point:  $B_n(R, Z)$ , the following equations need to be solved for unknown  $B_n$ , with known  $\Psi_n, B_{p,n}$  and  $R$ :

$$B_n^2 = \frac{F^2(\Psi_n)}{(1 - \Delta_n)^2 R^2} + B_{p,n}^2, \quad (2.38)$$

$$\Delta_n = \frac{\mu_0 [p_{\parallel}(\Psi_n, B_n, R) - p_{\perp}(\Psi_n, B_n, R)]}{B_n^2}. \quad (2.39)$$

Rearranging Eq. (2.39) and taking the derivative lead to

$$\begin{aligned} g(B_n) &= (B_n^2 - B_{p,n}^2)(1 - \Delta_n)^2 - \frac{F^2(\Psi_n)}{R^2} = 0, \\ g'(B_n) &= 2B_n(1 - \Delta_n) \\ &\quad \times \left[ \left(1 - \frac{B_{p,n}^2}{B_n^2}\right) \left(1 + \frac{\mu_0}{B_n} \frac{\partial p_{\perp}(\Psi_n, B_n, R)}{\partial B_n}\right) + \frac{B_{p,n}^2}{B_n^2} (1 - \Delta_n) \right]. \end{aligned} \quad (2.40)$$

With Eq. (2.20), (2.21) and  $B > B_p$ , we have  $g'(B_n) > 0$ . Therefore  $g(B_n)$  is monotonically increasing from  $B_{p,n}$  to  $+\infty$ . Providing that  $g(B_{p,n}) < 0$  and  $g(+\infty) \rightarrow +\infty$ , Eq. (2.40) should have one and only one root in region  $[B_{p,n}, +\infty)$ .

---

# Impact of anisotropic pressure on tokamak plasmas normal modes and continuum

---

## Abstract

Extending the ideal MHD stability code MISHKA, a new code, MISHKA-A, is developed to study the impact of pressure anisotropy on plasma stability. Based on full anisotropic equilibrium and geometry, the code can provide normal mode analysis with three fluid closure models: the single adiabatic model (SA), the double adiabatic model (CGL) and the incompressible model. A study on the plasma continuous spectrum shows that in low beta, large aspect ratio plasma, the main impact of anisotropy lies in the modification of the BAE gap and the sound frequency, if the  $q$  profile is conserved. The SA model preserves the BAE gap structure as ideal MHD, while in CGL the lowest frequency branch does not touch zero frequency at the resonant flux surface where  $m + nq = 0$ , inducing a gap at very low frequency. Also, the BAE gap frequency with bi-Maxwellian distribution in both model becomes higher if  $p_{\perp} > p_{\parallel}$  with a  $q$  profile dependency. As a benchmark of the code, we study the  $m/n = 1/1$  internal kink mode. Numerical calculation of the marginal stability boundary with bi-Maxwellian distribution shows a good agreement with the generalized incompressible Bussac criterion [A. B. Mikhailovskii, Sov. J. Plasma Phys 9, 190 (1983)]: the mode is stabilized(destabilized) if  $p_{\parallel} < p_{\perp}$  ( $p_{\parallel} > p_{\perp}$ ).

## 3.1 Introduction

The magnetohydrodynamics (MHD) theory is widely applied in fusion plasma, providing a great aid in explaining various plasma instabilities and the plasma oscillating spectra below the ion cyclotron frequency. In modern toroidal magnetic confinement devices, the plasma contains significant fast populations originated from neutral beam injection (NBI) and ion cyclotron resonance heating (ICRH), inducing strong pressure anisotropy [36]. The magnitude of anisotropy can reach  $p_{\parallel} \approx 1.7p_{\perp}$  in a MAST beam heated discharge [77, 101], or  $p_{\perp} \approx 2.5p_{\parallel}$  in a JET ICRH discharge [76], with  $p_{\parallel}$  and  $p_{\perp}$  the pressure parallel and perpendicular to the magnetic field lines, respectively. However, the physics of pressure anisotropy is not covered by the isotropic MHD theory.

In the regime where wave-particle interaction is not important, a fluid approach is often used with a reasonable fluid closure (like the adiabatic condition for ideal MHD) for phenomena only related to the macroscopic quantities such as density, current and pressure. Many attempts have been made to incorporate anisotropy into the fluid theory. Chew, Goldberger and Low (CGL) [15] first introduced the widely-applied form of pressure tensor and derived the double-adiabatic (CGL) closure, with its energy principle later derived by Bernstein *et al* [102]. Unlike MHD, CGL assumes parallel and perpendicular pressures doing work independently in a collisionless plasma, therefore cannot reduce to MHD in the isotropic limit. It was found that CGL overestimates  $\delta W$ , the perturbed potential energy, compared to the kinetic theory, while MHD underestimates it [25, 26]. Also, the mirror stability limit given by CGL does not match the result of kinetics theory [18, 19]. The major problem with CGL comes from the ignored heat flow when the mode frequency is comparable or smaller than the particle streaming frequency, especially in the vicinity of marginal stability boundary [14, 103]. Still, the CGL closure is implemented in many stability treatments, such as the ballooning modes [104, 105]. To overcome these drawbacks of CGL, some authors have proposed alternative fluid closures, for instance the double polytropic laws [21], a higher-order-momentum closure [23, 24], and recently, the single adiabatic (SA) model [20] which has the unique property of producing the same results as the MHD model for isotropic equilibria. Another pathway to overcome the drawbacks of CGL is to use hybrid approaches, in which thermal components are described by MHD and the fast ions by kinetics. The impact of pressure anisotropy is often investigated using kinetics energy principles [25, 26, 106]. In tokamaks, efforts have been made to study sawtooth modes (see Graves *et al* [107] and Chapman *et al* [108] and references therein) and interchange modes [109]. There are also significant developments in stellarators. The ANIMEC code [110] solves the 3D anisotropic equilibrium with the fast ion described by a guiding center distribution function, and is further applied to model anisotropy on LHD [111]. An energy principle which assumes non-interacting hot particles [112] is implemented in the ideal MHD code TERPSICHORE [113] to model anisotropic-pressure interchange modes in a beam heated LHD discharge [114]. Despite its shortcoming, the fluid approach can aid in the understanding of various effects due to its simple and intuitive nature. To date, there are few numerical studies on the oscillating spectrum of a toroidal anisotropic plasma.

In the regime where significant wave-particle resonance exists, a perturbative approach, in which the equilibrium and the linear mode eigenfunctions are modeled by fluid theory and the wave-particle interaction by kinetic theory, is widely implemented. In tokamaks, one of the most utilized tool chains is the HELENA-MISHKA-HAGIS combination [59, 61, 93], with the equilibrium, geometry and mode eigenfunctions calculated by ideal MHD, while the fast ion response and non-linear mode evolution are described by drift-kinetics equations. It has been successful in resolving the fast-particle-excited global Alfvén eigenmodes (see reviews [115, 116] and references therein). Recently, several equilibrium codes [92, 88, 101] have been developed to study the equilibrium of anisotropic and toroidally rotating plasmas. For linear stability problem, efforts have been made to include the physics of diamagnetic drift and toroidal flow into MISHKA [117, 118] for an isotropic equilibrium, while the impact of pressure anisotropy based on a full anisotropic equilibrium and geometry remains untouched. Our previous study using current remapping techniques shows that anisotropy can modify the  $q$  profile in MAST, inducing double TAE modes with different localization [77, 89], and thus a double wave-particle resonance. This also serves as a motivation to develop a MISHKA-like code to study the impact of

anisotropy on linear stability, meanwhile drive a kinetic code using a fully anisotropic framework.

This work is organized as follows. In Section 3.2, we state our basic assumptions and list the plasma equations used in the paper. Section 3.3 briefly describes the anisotropic equilibria and introduce the straight field line coordinates, serving as a base point for the stability treatment. Then in Section 3.4, we derive the linearized momentum equation, ideal Ohmic's law and the fluid closure equations which are ready to use in a MISHKA-like numerical code. Section 3.5 introduces the implementation of the derived equations into a global normal mode code, MISHKA-A, and a continuous spectrum code, CSMISH-A. Using these tools, we study the impact of anisotropy on the plasma continuous spectrum and the internal kink mode, shown in Section 3.6 and Section 3.7, respectively. We also compare the numerical results with existing analytical theory, serving as a code benchmark. Finally, Section 3.8 summarizes the paper and draws the conclusion.

## 3.2 Plasma Model

We start from a plasma described by the first two moments of the Vlasov Equation (the continuity and the momentum equation), the Maxwell Equations and the ideal Ohmic law. The basic equations are

$$\frac{d\rho}{dt} + \rho(\nabla \cdot \mathbf{V}) = 0, \quad (3.1)$$

$$\rho \frac{\partial \mathbf{V}}{\partial t} = -\nabla \cdot \mathbf{P} + \mathbf{j} \times \mathbf{B}, \quad (3.2)$$

$$\frac{\partial \mathbf{B}}{\partial t} = \nabla \times (\mathbf{V} \times \mathbf{B}), \quad (3.3)$$

$$\mathbf{j} = \nabla \times \mathbf{B}, \quad (3.4)$$

$$\nabla \cdot \mathbf{B} = 0, \quad (3.5)$$

where  $\rho$  is the mass density,  $\mathbf{V}$  the mass velocity,  $\mathbf{P}$  the second rank pressure tensor,  $\mathbf{j}$  the current density and  $\mathbf{B}$  the magnetic field. For simplicity, we use a natural MHD unit system where  $\mu_0$ , the vacuum permeability, is set to 1. All electromagnetic fields, fluxes and vector potentials can be restored to S.I. units with a transformation  $\cdots \rightarrow \cdots / \sqrt{\mu_0}$  (e.g.  $B \rightarrow B / \sqrt{\mu_0}$ ) and all currents with  $j \rightarrow \sqrt{\mu_0} j$ . Equation (3.1) is the continuity equation. Equation (3.2) is the momentum equation. Equation (3.3), (3.4) and (3.5) are the Maxwell Equations with ideal Ohmic law ignoring the displacement currents. The pressure tensor  $\mathbf{P}$  takes the CGL form, i.e.

$$\mathbf{P} = p_{\perp} \mathbf{I} + \Delta \mathbf{B} \mathbf{B}, \quad \Delta = \frac{p_{\parallel} - p_{\perp}}{B^2}, \quad (3.6)$$

with  $\mathbf{I}$  the identity tensor,  $p_{\perp}$  and  $p_{\parallel}$  the pressure perpendicular and parallel to the magnetic field, respectively. In our treatment, the finite Larmor radius (FLR) and the finite orbit width (FOW) effects are ignored. These effects can be important for fast particles, but resolving them requires FLR correction of non-diagonal pressure tensor terms (such as Chhajlani *et al* [119] for CGL) or kinetics/gyro-kinetics approaches, which are not considered in this paper.

In this paper, we implement the standard linearization method, which expands all quantities into a combination of a time-averaging equilibrium part and a small time-

dependent part, which varies with  $e^{\lambda t}$ . The mode frequency  $\omega$  and growth rate  $\gamma$  are related to  $\lambda$  through the relationship  $\lambda = \gamma - i\omega$ . By substituting these representatives into the plasma equations and considering the zeroth and the first order separately, the equations are then converted into a time-independent equilibrium problem and a linearized stability problem. We drop the subscripts “0” for equilibrium quantities for convenience.

To close the set of equations, one needs to introduce a “fluid closure” which relates  $p_{\parallel}$  and  $p_{\perp}$  to other known variables. In this work, we examine three fluid closures: the single adiabatic model [20], the double adiabatic model [15], and the incompressible limit given by Mikhailovskii [120]. The single adiabatic model serves as a generalization of MHD. While keeping the adiabaticity assumption of MHD, it assumes that the parallel and perpendicular pressure are doing joint work, and therefore resolves the isotropic part of the pressure perturbation. This fluid closure equation is given by

$$\begin{aligned} \frac{\partial \tilde{p}_{\parallel}}{\partial t} = \frac{\partial \tilde{p}_{\perp}}{\partial t} = & -\tilde{\mathbf{V}} \cdot \nabla \left( \frac{1}{3}p_{\parallel} + \frac{2}{3}p_{\perp} \right) \\ & - \left( \frac{1}{3}p_{\parallel} + \frac{4}{3}p_{\perp} \right) \nabla \cdot \tilde{\mathbf{V}} - \left( \frac{2}{3}p_{\parallel} - \frac{2}{3}p_{\perp} \right) \mathbf{b} \cdot (\mathbf{b} \cdot \nabla \tilde{\mathbf{V}}), \end{aligned} \quad (3.7)$$

in which the unit vector  $\mathbf{b} = \mathbf{B}/B$  is the direction of the magnetic field line. In contrast, the double adiabatic model assumes that parallel and perpendicular pressure do adiabatic work independently. The fluid closure equations,  $d/dt(p_{\perp}/\rho B) = d/dt(p_{\parallel}B^2/\rho^3) = 0$ , after substituting Eq. (3.1) for  $d\rho/dt$  and  $\mathbf{B}$  direction of Eq. (3.3) for  $dB/dt$ , are rewritten as

$$\frac{\partial \tilde{p}_{\parallel}}{\partial t} = -\tilde{\mathbf{V}} \cdot \nabla p_{\parallel} - p_{\parallel}(\nabla \cdot \tilde{\mathbf{V}}) - 2p_{\parallel}\mathbf{b} \cdot (\mathbf{b} \cdot \nabla \tilde{\mathbf{V}}), \quad (3.8)$$

$$\frac{\partial \tilde{p}_{\perp}}{\partial t} = -\tilde{\mathbf{V}} \cdot \nabla p_{\perp} - 2p_{\perp}(\nabla \cdot \tilde{\mathbf{V}}) + p_{\perp}\mathbf{b} \cdot (\mathbf{b} \cdot \nabla \tilde{\mathbf{V}}). \quad (3.9)$$

Finally, the incompressible closure is obtained when the Lagrangian perturbed distribution function is set to zero, i.e.  $d\tilde{f}/dt = \partial\tilde{f}/\partial t + \tilde{\mathbf{V}}_{\perp} \cdot \nabla f_0 = 0$ , where  $\tilde{f}$  is the Euler perturbed distribution function and  $f_0$  is the equilibrium distribution function. After integrating over the velocity space, the incompressible fluid closure is given by

$$\frac{\partial \tilde{p}_{\parallel}}{\partial t} = -\tilde{V}^1 \left( \frac{\partial p_{\parallel}}{\partial s} \right)_B, \quad (3.10)$$

$$\frac{\partial \tilde{p}_{\perp}}{\partial t} = -\tilde{V}^1 \left( \frac{\partial p_{\perp}}{\partial s} \right)_B, \quad (3.11)$$

where  $\tilde{V}^1$  is the contravariant component of the straight field line coordinates  $(s, \vartheta, \varphi)$ , which will be introduced in the next section.

### 3.3 Equilibrium and geometry

For the zeroth order equilibrium problem, the time derivatives  $\partial/\partial t = 0$ . In this work, we ignore all equilibrium flows, i.e.  $\mathbf{V}_0 = 0$ . Using Eq. (3.5) in an axisymmetric tokamak geometry, the equilibrium magnetic field in cylindrical coordinate  $(R, Z, \varphi)$  is written as

$$\mathbf{B} = \nabla \Psi \times \nabla \varphi + F \nabla \varphi, \quad (3.12)$$

where  $\Psi$  is the poloidal magnetic flux,  $F \equiv RB_\varphi$ , and  $B_\varphi$  is the toroidal magnetic field. We note that unlike plasma with isotropic pressure, we do not require  $F$  to be a flux function.

Substituting Eq. (3.4), (3.6) and (3.12) into Eq. (3.2), the component in  $\nabla\varphi$  direction gives rise to a flux function  $F_M(\Psi) \equiv RB_\varphi(1 - \Delta)$ , while the  $\nabla\Psi$  direction gives the anisotropy modified Grad-Shafranov Equation (GSE). The modified GSE have two equivalent forms, the pressure form and the enthalpy form (See [101] and references therein). In the pressure form of the GSE, the input profiles are specified by  $F_M(\Psi)$  and a 2D profile  $p_\parallel(\Psi, B)$ . This 2D pressure profile is usually obtained by taking the moments of guiding center distribution functions [83] either analytically [82] or numerically [81] (see Takeda *et al* [121] for a brief review). The enthalpy form of the GSE, when solved assuming the distribution functions are bi-Maxwellian and the parallel temperature is a flux function  $T_\parallel = T_\parallel(\Psi)$ , requires four flux functions  $\{H, T_\parallel, F_M, \Theta\}$  as input, corresponding to the density, parallel temperature, toroidal field and anisotropy, respectively. The profile  $H(\Psi)$  gives the radial shape of the density profile, and in isotropic plasma we have  $\rho = \exp(H/T_\parallel)$ . The profile  $\Theta(\Psi)$  defines the anisotropy magnitude  $p_\perp/p_\parallel$ , which is given by

$$\frac{p_\perp}{p_\parallel} = \frac{B}{|B - \Theta T_\parallel|}. \quad (3.13)$$

The density and pressures are then linked to these profiles through

$$\rho = \frac{p_\perp}{p_\parallel} \exp \frac{H}{T_\parallel}, \quad (3.14)$$

and

$$p_\parallel = \rho T_\parallel, \quad p_\perp = \rho T_\perp = \rho T_\parallel \frac{B}{|B - \Theta T_\parallel|}. \quad (3.15)$$

These equation are identical to taking the moments of a bi-Maxwellian distribution function of the form in McClements *et al* [122], written as

$$F(\mu, E, \Psi) = n_r(\Psi) \frac{A(\Psi)}{\sqrt{2\pi T_\perp(\Psi)}^3} \exp \left[ -\frac{|E - \mu B_0|}{T_\parallel(\Psi)} - \frac{\mu B_0}{T_\perp(\Psi)} \right], \quad (3.16)$$

where  $A(\Psi)$  is a normalization factor and  $\Theta$  is just a convenient representation of the combination

$$\Theta = \left( \frac{1}{T_\parallel(\Psi)} - \frac{1}{T_\perp(\Psi)} \right) B_0. \quad (3.17)$$

In this paper, we will use this bi-Maxwellian model to explore the impact of anisotropy on stability, since it is the simplest model that captures pressure anisotropy for both ICRH and NBI. The model has limitations, such that it takes all species as a single bi-Maxwellian therefore cannot reproduce the long tail of ICRH fast ions, and that it omits any physics due to fine structure of pitch angle dependency of the distribution function (i.e. non-bi-Maxwellian structure). However, it does give the correct  $\langle p_\parallel \rangle$  and  $\langle p_\perp \rangle$ , as well as  $\Delta p_\parallel/p_\parallel$ ,  $\Delta\rho/\rho$  (the change of these profiles on a flux surface), and anisotropy  $\Delta$ , which are not determined by a choice of the shape of the distribution function [83]. Here,  $\langle \dots \rangle$  means flux surface average. We also mention that our stability treatment later on does not rely on the choice of equilibrium distribution function, as long as the modified GSE is solved self-consistently, and can provide  $\Psi$  as a function of  $(R, Z)$ , i.e. the flux surfaces, for the



stability treatment.

The solution  $\Psi(R, Z)$  for the modified GSE is then mapped into the straight field line coordinates  $(s, \vartheta, \varphi)$ , with  $s = \sqrt{\Psi}$  and  $\vartheta$  defined by

$$\vartheta \equiv \int_{\Psi} \frac{B_{\varphi} dl}{q R B_p}, \quad q(\Psi) \equiv \frac{1}{2\pi} \oint_{\Psi} \frac{B_{\varphi} dl}{R B_p}, \quad (3.18)$$

in which  $B_p$  is the poloidal field and  $q$  the safety factor. The integrals are performed on a constant  $\Psi$  surface clockwise facing the direction of  $\mathbf{e}_{\varphi}$  and starting from  $Z = Z_0$ , in which  $Z_0$  is the  $Z$  coordinate for the magnetic axis. The metric coefficients of this curvilinear coordinate,  $g_{ij}$  and  $g^{ij}$ , as well as the Jacobian  $J$ , are defined by

$$g_{ij} \equiv \nabla x^i \cdot \nabla x^j, \quad g^{ij} \equiv \frac{\partial \mathbf{r}}{\partial x^i} \cdot \frac{\partial \mathbf{r}}{\partial x^j}, \quad (3.19)$$

$$J \equiv \sqrt{\det(g_{ij})} = \frac{f q R}{F}, \quad (3.20)$$

where  $f = d\Psi/ds$  and  $\det$  is the determinant operator, with  $(x^1, x^2, x^3) = (s, \vartheta, \varphi)$ . In the straight field line coordinates, the contravariant equilibrium current is given by

$$\begin{aligned} j^1 &= \frac{1}{J} \frac{\partial F}{\partial \vartheta}, \quad j^2 = -\frac{1}{J} \frac{\partial F}{\partial s}, \\ j^3 &= \frac{1}{J} \left( \frac{\partial}{\partial s} \frac{g_{22} F}{q R^2} - \frac{\partial}{\partial \vartheta} \frac{g_{12} F}{q R^2} \right), \end{aligned} \quad (3.21)$$

and the contravariant magnetic field components are given by

$$B^1 = 0, \quad B^2 = \frac{F}{q R^2}, \quad B^3 = \frac{F}{R^2}. \quad (3.22)$$

For the GSE with anisotropy in the straight field line coordinates, one can refer to Fitzgerald *et al* [20], as we will not restate it here.

### 3.4 The perturbed equations in the straight field line coordinates

In this section, we write our first order perturbed equations in the straight field line coordinates using contravariant and/or covariant representatives. Same as the original MISHKA, a set of “optimized” projections of  $\tilde{\mathbf{V}}$  and  $\tilde{\mathbf{B}}$  is used instead of the contra/co-variant projections. We use circumflexes to label these projections in order to distinguish them from the contra/co-variant projections, which are labeled by tildas. The perturbed fluid velocity  $\tilde{\mathbf{V}}$  is expressed in its contravariant normal component  $\hat{V}^1$ , its binormal projection  $\hat{V}^2$  and its parallel projection  $\hat{V}^3$ , with

$$\hat{V}^2 = [\tilde{\mathbf{V}} \times \mathbf{B}]_1, \quad \hat{V}^3 = \frac{\tilde{\mathbf{V}} \cdot \mathbf{B}}{B^2}. \quad (3.23)$$

The perturbed magnetic field  $\tilde{\mathbf{B}}$  is calculated by taking the curl of the perturbed magnetic vector potential  $\tilde{\mathbf{A}}$  (i.e.  $\tilde{\mathbf{B}} = \nabla \times \tilde{\mathbf{A}}$ ). Then similarly,  $\tilde{\mathbf{A}}$  is expressed in its covariant normal

component  $\tilde{A}_1$ , its binormal projection  $\hat{A}_2$  and its parallel projection  $\hat{A}_3$ , with

$$\hat{A}_2 = \frac{[\tilde{\mathbf{A}} \times \mathbf{B}]^1}{B^2}, \quad \hat{A}_3 = \frac{\tilde{\mathbf{A}} \cdot \mathbf{B}}{B^2}. \quad (3.24)$$

The conversion between these projections and contra/covariant components of both  $\tilde{\mathbf{V}}$  and  $\tilde{\mathbf{A}}$  can be found in Fitzgerald *et al* [20] and Mikhailovskii *et al* [59], while  $\tilde{B}^1$ ,  $\tilde{B}^2$  and  $\tilde{B}^3$  are related to  $\tilde{A}_1$ ,  $\hat{A}_2$  and  $\hat{A}_3$  through Eq. (90) to (92) in Fitzgerald *et al* [20]. The covariant components are related to contravariant components through  $\tilde{B}_i = \sum_j g_{ij} \tilde{B}^j$ . Finally, the perturbed magnetic field strength is given by  $\tilde{B} = \tilde{\mathbf{B}} \cdot \mathbf{b}$ .

### 3.4.1 The ideal Ohm's law

Equation (3.3), the ideal Ohm's law, stays unchanged moving from isotropic plasma to anisotropic plasma. The equations are therefore identical to Mikhailovskii *et al* :

$$\lambda \tilde{A}_1 = \hat{V}^2, \quad (3.25)$$

$$\lambda \hat{A}_2 = -\tilde{V}_1, \quad (3.26)$$

$$\lambda \hat{A}_3 = 0. \quad (3.27)$$

We recall that  $\lambda = \gamma - i\omega$ . When plasma equilibrium flow and resistivity are ignored,  $\hat{A}_3$  is an ignorable component, henceforth neglected.

### 3.4.2 The momentum equation

Perturbing Eq. (3.2), one obtains

$$\rho_0 \frac{\partial \tilde{\mathbf{V}}}{\partial t} = -\nabla \cdot \tilde{\mathbf{P}} + \mathbf{H}, \quad (3.28)$$

in which

$$\tilde{\mathbf{P}} = \tilde{p}_\perp (\mathbf{I} - \mathbf{b}\mathbf{b}) + \tilde{p}_\parallel \mathbf{b}\mathbf{b} + (\tilde{p}_\parallel - \tilde{p}_\perp) \left( \frac{\tilde{\mathbf{B}}_\perp}{B} \mathbf{b} + \mathbf{b} \frac{\tilde{\mathbf{B}}_\perp}{B} \right), \quad (3.29)$$

and

$$\mathbf{H} = (\nabla \times \mathbf{B}) \times \tilde{\mathbf{B}} - \mathbf{B} \times (\nabla \times \tilde{\mathbf{B}}). \quad (3.30)$$

The first two covariant components of  $\mathbf{H}$ ,  $H_1$  and  $H_2$ , are provided in Fitzgerald *et al* [20] and restated in 3.9 while  $H_3$  is given in 3.9 as well.

After some algebra, we reach the perturbed momentum equation covariantly in the

straight field line coordinates:

$$\begin{aligned} \lambda\rho\tilde{V}_1 = & (1 - \Delta)H_1 - \partial_s\tilde{p}_\perp - \partial_j(\tilde{p}_\parallel - \tilde{p}_\perp - 2\Delta B\tilde{B})\frac{B_1B^j}{|B|^2} \\ & - \Delta\partial_s(B\tilde{B}) - (B^j\tilde{B}_1 + \tilde{B}^jB_1)\partial_j\Delta \\ & - (\tilde{p}_\parallel - \tilde{p}_\perp - 2\Delta B\tilde{B})\left(\frac{B_1}{B}\nabla\cdot\mathbf{b} + \kappa_1\right), \end{aligned} \quad (3.31)$$

$$\begin{aligned} \lambda\rho\tilde{V}_2 = & (1 - \Delta)H_2 - \partial_\vartheta\tilde{p}_\perp - \partial_j(\tilde{p}_\parallel - \tilde{p}_\perp - 2\Delta B\tilde{B})\frac{B_2B^j}{|B|^2} \\ & - \Delta\partial_\vartheta(B\tilde{B}) - (B^j\tilde{B}_2 + \tilde{B}^jB_2)\partial_j\Delta \\ & - (\tilde{p}_\parallel - \tilde{p}_\perp - 2\Delta B\tilde{B})\left(\frac{B_2}{B}\nabla\cdot\mathbf{b} + \kappa_2\right), \end{aligned} \quad (3.32)$$

summing over index  $j = 1, 2, 3$ , in which  $\boldsymbol{\kappa} = \mathbf{b} \cdot \nabla \mathbf{b}$  is the magnetic field line curvature with its covariant components  $\kappa_1$  and  $\kappa_2$  given in 3.9. Taking the dot product of Eq. (3.28) with  $\mathbf{B}$ , the third component of the momentum equation is written as

$$\begin{aligned} \lambda\rho|B|^2\hat{V}^3 = & (1 - \Delta)B^jH_i - B^j\partial_j(\tilde{p}_\parallel - 2\Delta B\tilde{B}) - \Delta B^j\partial_j(B\tilde{B}) \\ & - \partial_j\Delta(\tilde{B}^j|B|^2 + B^jB\tilde{B}) - (\tilde{p}_\parallel - \tilde{p}_\perp - 2\Delta B\tilde{B})(B\nabla\cdot\mathbf{b}), \end{aligned} \quad (3.33)$$

summing over index  $j = 1, 2, 3$ .

### 3.4.3 The fluid closure equation

For the single-adiabatic and double-adiabatic model, the fluid closure equations have similar forms in the straight field line coordinates, which are given by

$$\begin{aligned} \lambda\tilde{p}_\parallel = & -\frac{\gamma_{\parallel 1}}{J}[\partial_s(J\tilde{V}^1) + \partial_\vartheta(J\tilde{V}^2) + \partial_\varphi(J\tilde{V}^3)] - \gamma_{\parallel 2}E \\ & - (\tilde{V}^1\partial_s + \tilde{V}^2\partial_\vartheta)f_\parallel, \end{aligned} \quad (3.34)$$

$$\begin{aligned} \lambda\tilde{p}_\perp = & -\frac{\gamma_{\perp 1}}{J}[\partial_s(J\tilde{V}^1) + \partial_\vartheta(J\tilde{V}^2) + \partial_\varphi(J\tilde{V}^3)] - \gamma_{\perp 2}E \\ & - (\tilde{V}^1\partial_s + \tilde{V}^2\partial_\vartheta)f_\perp, \end{aligned} \quad (3.35)$$

where

$$E = \frac{B^j}{B}\partial_j(B\hat{V}^3) - \tilde{V}^1\kappa_1 - \frac{\hat{V}^2}{fq}\kappa_2. \quad (3.36)$$

For single-adiabatic model, we have

$$\begin{aligned} \gamma_{\parallel 1} = \gamma_{\perp 1} = & \frac{1}{3}p_\parallel + \frac{4}{3}p_\perp, \quad \gamma_{\parallel 2} = \gamma_{\perp 2} = \frac{2}{3}p_\parallel - \frac{2}{3}p_\perp, \\ f_\parallel = f_\perp = & \frac{1}{3}p_\parallel + \frac{2}{3}p_\perp. \end{aligned} \quad (3.37)$$

For double-adiabatic model, we have

$$\begin{aligned} \gamma_{\parallel 1} = p_\parallel, \quad \gamma_{\parallel 2} = 2p_\parallel, \quad f_\parallel = p_\parallel, \\ \gamma_{\perp 1} = 2p_\perp, \quad \gamma_{\perp 2} = -p_\perp, \quad f_\perp = p_\perp. \end{aligned} \quad (3.38)$$

There is no need to restate the incompressible fluid closure here, since Eq. (3.10) and (3.11) are already given in the straight field line coordinates.

### 3.5 Numerical method

Similar to the original MISHKA and its extension MISHKA-D/F, we use the following variables in our anisotropic extension of the MISHKA code, namely MISHKA-A (anisotropy):

$$\begin{aligned} X_1 &= fq\tilde{V}^1, & X_2 &= i\hat{V}^2, & X_3 &= i\tilde{A}_1, & X_4 &= fq\hat{A}_2, \\ X_5 &= if\hat{V}^3, & X_6 &= fp_{\perp}, & X_7 &= fp_{\parallel}. \end{aligned} \quad (3.39)$$

These variables are then expanded poloidally and toroidally in Fourier harmonics with mode number  $m$  and  $n$  respectively, and radially in cubic/quadratic Hermite elements, i.e.

$$X_{\alpha} = e^{\lambda t + in\varphi} \sum_{m=-\infty}^{\infty} \sum_{\nu=1}^N X_{\alpha}^{m\nu} H_{\nu}(s) e^{im\vartheta}, \quad (3.40)$$

in which  $H_{\nu}(s)$  is the cubic/quadratic Hermite elements and  $N$  the number of radial elements. The weak form is constructed by multiplying Eq. (3.31), (3.32), (3.33), (3.25), (3.26), (3.34) and (3.35) respectively by  $\tilde{V}^{1*}/(1-\Delta)$ ,  $\hat{V}^{2*}/fq(1-\Delta)$ ,  $f\hat{V}^{3*}/(1-\Delta)$ ,  $A_1^*/J$ ,  $f^2q^2\hat{A}_2^*/J$ ,  $fp_{\parallel}$  and  $fp_{\perp}$ , converting the system into a linear algebra problem solving

$$\lambda N_i = M_i, \quad (3.41)$$

in which

$$N_i = \sum_{j=1}^8 \int B(i, j) X_i^* X_j J ds d\vartheta, \quad (3.42)$$

and

$$\begin{aligned} M_i &= \sum_{j=1}^8 \int [A(i, j) X_i^* X_j + A(i', j) \frac{\partial X_i^*}{\partial s} X_j \\ &\quad + A(i, j') X_i^* \frac{\partial X_j}{\partial s} + A(i', j') \frac{\partial X_i^*}{\partial s} \frac{\partial X_j}{\partial s}] J ds d\vartheta. \end{aligned}$$

We separate the matrix elements  $A(i, j)$  into

$$A(i, j) = A^0(i, j) + A^A(i, j), \quad (3.43)$$

in which  $A^0(i, j)$  are the common terms for MISHKA (isotropic) and MISHKA-A (anisotropic) and  $A^A(i, j)$  are terms existing only in anisotropic plasmas. These matrix elements are given in Section 3.10.

To obtain the continuous spectrum, we reduced MISHKA-A to a continuum code (CSMISH-A). The method provided in Poedts *et al* [60] (CSCAS) is implemented here, carrying the calculation in the vicinity of the singularity  $\Psi \rightarrow \Psi_0$ .

### 3.6 Anisotropy impact on plasma continuous spectrum

In this section, we study the continuous spectrum of an anisotropic plasma described by the SA and the CGL model, as well as the modification of anisotropy to the continuous spectrum. We present a set of examples with circular cross-section, large aspect ratio ( $\epsilon = 0.3$ ) and low  $\beta$ . The equilibrium solutions are computed by HELENA+ATF [101] using the enthalpy form of the modified GSE with the bi-Maxwellian distribution and the equilibrium thermal closure  $T_{\parallel} = T_{\parallel}(\Psi)$ . We start from an isotropic MHD reference case with

$$\begin{aligned} T(\Psi_N) &= C_0(1 - \Psi_N)^2 + C_1, \quad RB_{\varphi}(\Psi_N) = F_0, \\ H(\Psi_N) &= \frac{C_0}{2}(1 - \Psi_N)^3 + C_2, \end{aligned} \quad (3.44)$$

where  $\Psi_N$  is the normalized flux surface defined as  $\Psi_N = 0$  on axis and  $\Psi_N = 1$  at the edge, and  $C_0, C_1, C_2$  and  $F_0$  are adjustable constants. Constant  $F_0$  indicates vacuum field strength. Constants  $C_1$  and  $C_2$  are small values to make density and current profiles vanish at the plasma edge. The density and pressure profiles are given by Eq. (3.14) and (3.15). The  $q$  profile monotonically increases from  $q_0 = 1.7$  to  $q_{95} = 7$ . We choose  $\beta = 1\%$  on the magnetic axis. In the next step, we add anisotropy to this reference equilibrium. The  $\Theta$  profile, which indicates the magnitude of anisotropy, is chosen to be constant. Therefore, anisotropy decreases from core to edge following the same trend of  $T$ , which is associated with on-axis beam heating or ICRH. For an individual anisotropic equilibrium, we specify a  $\Theta_0$ , then iterate the  $T_{\parallel}$ ,  $F_M$  and  $H$  profiles to keep  $\langle p^* \rangle$ ,  $\langle j \rangle$  and  $\langle \rho \rangle$  on each flux surface identical to the isotropic reference case. Here  $p^* = (p_{\parallel} + p_{\perp})/2$  and  $\langle \dots \rangle$  means flux surface average. In this way the  $q$  profile and the metrics of these anisotropic equilibria are the same as the reference isotropic case to  $O(\epsilon^2(p_{\parallel} - p_{\perp})/p_{\parallel})$ . We have accordingly obtained equilibria ranging from  $p_{\perp} = 1.7p_{\parallel}$  (perpendicular beam or ICRH) to  $p_{\parallel} = 1.8p_{\perp}$  (parallel beam) at core. When we go to higher anisotropy like  $p_{\perp} > 1.7p_{\parallel}$  and  $p_{\parallel} > 1.8p_{\perp}$ , we are unable to reduce the difference of  $q_0$  between an anisotropic case (for example  $p_{\perp} = 2p_{\parallel}$ ) and its opposite case ( $p_{\parallel} = 2p_{\perp}$ ) to less than 1% when we fix other parameters, since the flux surfaces of an anisotropic equilibrium is not completely reproducible by an isotropic equilibrium, or an anisotropic equilibrium with opposite magnitude of anisotropy [101]. Our start point is to identify the difference of anisotropic stability with equilibria in almost same conditions. Consequently, these higher anisotropy regimes are not explored here, because we are unable to keep them in these same conditions. However, our model and code are capable to describe cases with higher anisotropy, such as the  $p_{\perp} = 2.5p_{\parallel}$  discharge in JET.

The continuous spectrum of these examples are then computed by CSMISH-A. Figure 3.1 shows the  $n = -1$  and  $m = 1, 2, 3$  continuous spectrum of three cases :  $p_{\perp} = 1.7p_{\parallel}$ ,  $p_{\perp} = p_{\parallel}$  and  $p_{\parallel} = 1.8p_{\perp}$  on axis, for (a) the SA model and (b) the CGL model. The linear growth rate of the continuous spectra in all these examples is observed to have  $\gamma < 10^{-8}\omega_A$ . We note that the small growth rate here is due to numerical errors (e.g. finite grid resolution) and is reduced by improving numerical precision. Therefore, we conclude that these continuous modes are stable. As in the ideal MHD spectrum, two sets of branches, a shear Alfvén set ( $\omega/\omega_{A0} > 0.1$ ) and a slow sound set ( $\omega/\omega_{A0} < 0.1$ ), appear at higher frequency and lower frequency, respectively. A resonance between  $m = 2$  and  $m = 3$  shear Alfvén branches occurs at  $q = 2.5$  surface and forms the TAE gap ( $\Delta m = 1$  gap) around  $s = 0.6$ . Meanwhile, a resonance between  $m = 1$  and  $m = 3$  forms the

EAE gap ( $\Delta m = 2$  gap) at  $q = 2$  surface around  $s = 0.4$ . The coupling between the shear Alfvén and the slow branches forms the low frequency gaps ( $\Delta m = 0$  BAE gap). Moving to the edge, frequencies of the shear Alfvén branches approach infinity as density approaches zero, while frequencies of the slow waves vanish as pressure goes to zero.

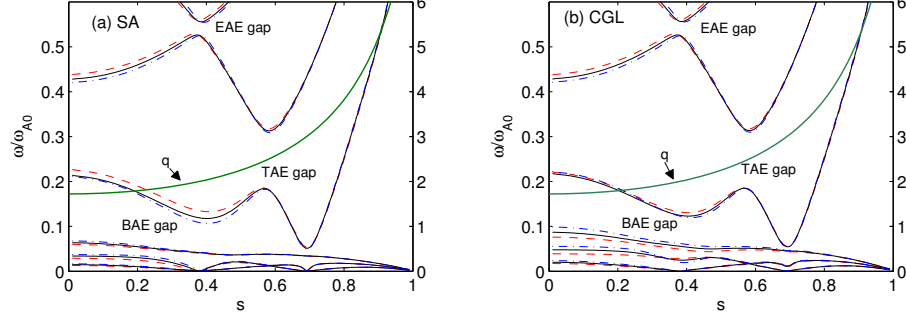


**Figure 3.1:** The  $n = -1$ ,  $m = 1, 2, 3$  continuous spectrum (left axis) and the  $q$  profile (right axis) of a plasma with (a) SA closure (b) CGL closure. The frequency is normalized to  $\omega_{A0}$ , the Alfvén frequency on axis, and  $s = \sqrt{\Psi_N}$  is the standard flux label. The red dash line, black solid line and blue dash dot line shows respectively the cases with  $p_{\perp} = 1.7p_{\parallel}$ ,  $p_{\perp} = p_{\parallel}$  and  $p_{\parallel} = 1.8p_{\perp}$  on axis. The EAE gap, TAE gap and BAE gap are labeled in each figure.

Figure 3.1 also demonstrates the modification of anisotropy to the continuous spectrum. Anisotropy does not modify the main structure of the spectrum and the position of the gaps, but shifts the gaps and branches. For both models, around the core where the magnitude of anisotropy is higher, the difference between the three cases with different anisotropy is more significant. At the edge where anisotropy is vanishing, the three spectra merge to one. For the  $p_{\parallel} = 1.8p_{\perp}$  case described by the SA model, all the shear Alfvén branches are lowered ( $0.01\omega_A$  on axis), while the slow branches are shifted up (7% on axis). For the CGL model, the lowest shear Alfvén branch is almost unchanged, while the frequency of the slow branches increases by 14% on axis. The modification to slow branches will be investigated in Section 3.6.1. The change of the shear Alfvén branches can be explained by the change of these branches' coupling to plasma compressibility through geodesic curvature, with different anisotropy and different model. Also, the  $q$  profile is only conserved to the reference isotropic case to  $O(\epsilon^2(p_{\parallel} - p_{\perp})/p_{\parallel})$ . With  $\epsilon = 0.3$  in our example, the change of  $q_0$  is 0.01 (of 1.7) for the  $p_{\parallel} = 1.8p_{\perp}$  compared to the isotropic reference case, which will slightly modify all the branches. Looking at continuum gaps, the upper and lower accumulation points of both the TAE gap and the EAE gap are almost unchanged, meanwhile the upper accumulation point of the BAE gap is shifted up for both models (8% for SA and 4% for CGL). For the  $p_{\perp} = 1.7p_{\parallel}$  case, all the above modifications are reversed, with a similar magnitude of change.

To understand the modification of anisotropy and the above differences, we study two specific feature of the continuous spectrum: its cylindrical limit and the low frequency BAE gap. The former one determines the main frequency of both the shear Alfvén and the slow branches, and the latter describes the shear Alfvén and slow coupling.

### 3.6.1 the Cylindrical limit

In the cylindrical limit, the equilibrium quantities are free of poloidal angle dependency. Therefore the coupling between two shear Alfvén branches vanishes. Also, the geodesic

curvature, which couples the shear Alfvén branches and the slow branches, is zero. Building on Fitzgerald *et al* [20], we have computed the continuum in the cylindrical limit. We retain the ignored  $(p_{\parallel} - p_{\perp})(\mathbf{b}_1 \mathbf{b} + \mathbf{b} \mathbf{b}_1)$  term in the perturbed pressure tensor in Fitzgerald *et al*, therefore the missing firehose factor  $1 - \Delta$  for the single-adiabatic Alfvén branches is now recovered. The frequency of mode  $(m, n)$  is now simply given by

$$\omega_{A,SA}^2 = \omega_{A,CGL}^2 = \frac{(1 - \Delta)B^2}{\rho R_0^2} (m/q + n)^2, \quad (3.45)$$

$$\omega_{S,SA}^2 = \frac{p_{\parallel} + \frac{2}{3}p_{\perp}}{\frac{1}{3}p_{\parallel} + \frac{4}{3}p_{\perp} + B^2} \frac{B^2}{\rho R_0^2} (m/q + n)^2, \quad (3.46)$$

$$\omega_{S,CGL}^2 = \frac{3p_{\parallel}}{2p_{\perp} + B^2} \frac{B^2}{\rho R_0^2} (m/q + n)^2, \quad (3.47)$$

where  $R_0$  is the major radius of the magnetic axis. Here, “A” in the subscript labels the shear Alfvén branches and “S” labels the slow branches. Inspection of Eq. (3.45) shows that the cylindrical shear Alfvén continuum is not fluid closure dependent. The anisotropy modifies these branches by the firehose factor  $1 - \Delta$ . This is consistent with previous results [18, 123]. In contrast, the slow branches, as shown by Fig.3.1, have strong fluid closure dependency and anisotropy dependency, with  $\omega_{S,SA} \neq \omega_{S,CGL}$  even when the equilibrium is isotropic. In the isotropic limit, the SA model reduces to the result given by ideal MHD with adiabatic gas law, while the CGL model does not converge to ideal MHD. Indeed, the frequency  $\omega_{S,CGL}$  is roughly 35% larger than  $\omega_{S,SA}$  when the plasma is isotropic. As in Eq. (3.46) and (3.47), the frequency of the slow branches with both model are increasing when  $p_{\parallel}/p_{\perp}$  increases, if  $\langle p^* \rangle$  is kept constant, although CGL model shows more significant change compared to SA. We have compared the result from CSMISH-A in the cylindrical limit (very large aspect ratio) with Eq. (3.45) to (3.47) for both SA and CGL, showing very good agreement.

### 3.6.2 The BAE gap change due to anisotropy

The low frequency gap (BAE gap)[40] appears on the resonant flux surface where  $m + nq = 0$ , and is induced by the finite compressibility of the plasma. Inspection of Fig.3.1 shows that for different magnitude of anisotropy, the width of this gap is changed. Also, the gap width is different for the SA and the CGL model, implying its dependency on fluid closure model. Figure 3.2 zooms in into the  $q = 2$  BAE gap in Fig.3.1 for the anisotropic case with  $p_{\parallel} = 1.8p_{\perp}$  on axis. Only the major  $m = 2$  shear Alfvén branch and the  $m = 2 \pm 1$  slow side bands are shown here. In Fig.3.2, the frequency of the upper, middle and lowest branches on the resonant flux surface (located at  $s = 0.38$ ) are labeled as  $\omega_3$ ,  $\omega_2$  and  $\omega_1$  respectively. The BAE gap of the SA model has the same structure as an isotropic plasma described by the MHD model. Its lowest branch approaches zero when  $m + nq = 0$ , i.e.  $\omega_1 = 0$ . To the contrary, in CGL we have  $\omega_1 > 0$ , inducing an additional gap at very low frequency.

In this section, we are only interested in  $\omega_3$ , the upper accumulation point of a BAE gap, which determines the gap width. We study two separate cases, with the gap located at a low  $q$  position ( $q = 1.33$ ) and a high  $q$  position ( $q = 3$ ), as shown in Fig.3.3 (a) and (b), respectively. The frequencies in Fig.3.3 are normalized to the analytic ideal MHD

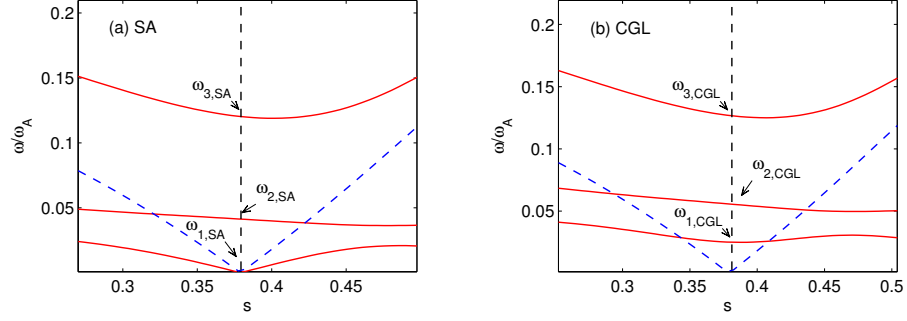


**Figure 3.2:** Zooming into the  $q = 2$  BAE gap of the  $n = -1$  continuous spectrum of the anisotropic case in Fig.3.1 with  $p_{\parallel} = 1.8p_{\perp}$  on axis, for (a) the SA model and (b) the CGL model. The blue dash lines are the incompressible  $m = 2$  shear Alfvén branch. The vertical lines indicate the flux surface where  $q = 2$ , and the incompressible  $m = 2$  shear Alfvén branch hits zero. The red solid lines are the coupled  $m = 2$  shear Alfvén branch and  $m = 1, 3$  slow branches due to finite compressibility (SA or CGL), with the frequency of the upper, middle and lowest branches labeled as  $\omega_3$ ,  $\omega_2$  and  $\omega_1$  at  $q = 2$  surface, respectively.

value of  $\omega_3$  for the reference isotropic case [62], written as

$$\omega_{3,MHD}^2 = \frac{2\gamma p}{(\gamma p + B^2)\rho R_0^2} \left( 1 + \frac{1}{2q^2} \right), \quad (3.48)$$

with  $\gamma = 5/3$ . Figure 3.3 (a) shows that for  $q = 1.33$ , the SA closure gives a greater  $\omega_3$  when  $p_{\parallel} > p_{\perp}$ , and a smaller  $\omega_3$  when  $p_{\parallel} < p_{\perp}$ . It's almost a linear function of  $(p_{\parallel} - p_{\perp})/p^*$ . The change of  $\omega_3$  is roughly 8% for  $p_{\parallel} \approx 1.5p_{\perp}$  or  $p_{\perp} \approx 1.5p_{\parallel}$ , the farthest right and left data points in the figure. For the CGL closure,  $\omega_3$  is 7% higher than the isotropic ideal MHD reference case. It's dependency on  $(p_{\parallel} - p_{\perp})/p^*$  is almost negligible. Moving to Fig.3.3 (b) where  $q = 3$ , in SA model the dependency of  $\omega_3$  on  $(p_{\parallel} - p_{\perp})/p^*$  becomes higher, with a 12% change for  $p_{\parallel} \approx 1.5p_{\perp}$  or  $p_{\perp} \approx 1.5p_{\parallel}$ . Meanwhile, the ratio  $\omega_3/\omega_{3,MHD}$  decreases to 1.03 in the isotropic case, and the  $\omega_3$  for CGL has a weak dependency on anisotropy: about a further 5% change for the extreme cases.

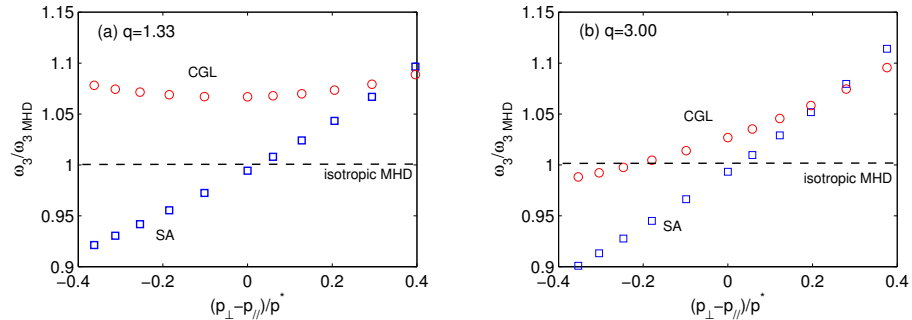


**Figure 3.3:** The change of the BAE gap upper accumulation point frequency ( $\omega_3$ ) due to the change of anisotropy for a BAE gap with (a)  $q = 1.33$ ,  $n = -3$  (b)  $q = 3.00$ ,  $n = -1$ . The local magnitude of anisotropy is described by the relative difference of  $p_{\parallel}$  and  $p_{\perp}$ , i.e.  $(p_{\parallel} - p_{\perp})/p^*$ . The frequency of  $\omega_3$  is normalized to the analytic ideal MHD value of  $\omega_3$  for the reference isotropic case, as shown by the horizontal dash line. The symbols are numerical results from the CSMISH-A code: blue squares and solid lines for SA, red circles and solid lines for CGL.



### 3.7 Anisotropy impact on the internal kink mode

In this section, we study the impact of anisotropy on the  $n = 1$  internal kink mode in a tokamak plasma with large aspect ratio ( $\epsilon = 0.1$ ) and circular cross section. This also serves as a benchmark of MISHKA-A working as a global normal mode code. For simplicity, the equilibrium distribution function is taken to be bi-Maxwellian.

We start from a reference isotropic equilibrium with the current profile and the pressure profile taking the form,

$$\langle j \rangle = j_0(1 - \Psi_N), \quad (3.49)$$

$$p_{\parallel} = p_{\perp} = p_0(1 - \Psi_N), \quad (3.50)$$

where  $j_0$  and  $p_0$  are constants. The density profile is taken to be constant, i.e.  $\rho = \rho_0$ . The safety factor on axis,  $q_0$ , and the ratio of kinetic energy to magnetic energy,  $\beta$ , can then be adjusted by changing the ratio  $p_0/j_0$  and the vacuum field. The safety factor  $q$  is monotonically increasing: only one  $q = 1$  surface exists in the plasma. Similar to Section 3.6, based on this reference isotropic case we change the  $\Theta$  profile with  $\Theta = \Theta_0$  in our equilibrium code HELENA+ATF, meanwhile keeping  $\langle p^* \rangle = (\langle p_{\perp} \rangle + \langle p_{\parallel} \rangle)/2$ ,  $\langle j \rangle$  and  $\langle \rho \rangle$  unchanged. In such a way the  $q$  profile and metrics are identical to our reference isotropic case to  $O(\epsilon^2)$ . The relative anisotropic profile is then approximately given by

$$\frac{\langle p_{\perp} \rangle}{\langle p_{\parallel} \rangle} = \frac{1}{1 - \alpha(1 - \Psi_N)}, \quad (3.51)$$

with which the magnitude of anisotropy peaks on axis and vanishes at the boundary. Here  $\alpha$  is an adjustable constant proportional to  $\Theta_0$ .

In the incompressible limit, the plasma kinetic response to the perturbation is ignored. The stability of the internal kink mode is determined by the sign of the perturbed fluid toroidal potential energy  $\delta W_T$ . When  $\delta W_T < 0$ , the plasma is unstable. According to the analytical calculation of Bussac *et al* [124] and Mikhailovskii [120, 125], the stability criterion of the  $n = 1$  internal kink in such a scenario, namely the generalized Bussac criterion, is described by

$$\delta w + \beta_{pA} > 0, \quad (3.52)$$

where  $\delta w$  is a quadratic function of the value of  $\beta_p$  on the  $q = 1$  surface, with the coefficients determined by the  $q$  profile. The quantity Bussac  $\beta_p$ , as a indication of the pressure gradient, is defined as

$$\beta_p(\Psi) \equiv \frac{2[\bar{p}(\Psi) - p(\Psi)]}{B_p^2(\Psi)}, \quad (3.53)$$

where  $\bar{p}$  is the average pressure inside the certain flux surface, i.e.

$$\bar{p}(\Psi_1) \equiv \int_{\Psi < \Psi_1} p dS / \int_{\Psi < \Psi_1} dS. \quad (3.54)$$

For anisotropic plasma,  $\beta_p$  is replaced by  $\beta_{p*} \equiv (\beta_{p\parallel} + \beta_{p\perp})/2$ . The second term in Eq. (3.52),  $\beta_{pA}$ , is obtained from Eq. (3.53) replacing  $p$  by  $(p_{\parallel} + p_{\perp} + \hat{c})/2$ , and taking the value on the  $q = 1$  surface as well, where  $\hat{c}$  is defined through partial derivative of  $p_{\perp}$  as

$$B \left( \frac{\partial p_{\perp}}{\partial B} \right)_{\Psi} = 2p_{\perp} + \hat{c}. \quad (3.55)$$

For a bi-Maxwellian plasma,  $\hat{c}$  is simplified to

$$\hat{c}_{bM} = -\frac{2p_{\perp}^2}{p_{\parallel}}. \quad (3.56)$$

The generalized Bussac criterion takes into account only the lowest order of the poloidal variation of  $\tilde{p}_{\parallel}$  and  $\tilde{p}_{\perp}$ , and neglects the shaping effect [86] of pressure anisotropy, leading to its discrepancy from full numerical results when the fast particle distribution function has strong and/or complicated poloidal dependency (e.g. with neutral beam heating) [126]. The bi-Maxwellian plasma we use here only has a weak poloidal dependency, satisfying the use of the generalized Bussac criterion. From Eq. (3.56),  $\beta_{pA}$  is positive when  $p_{\parallel} > p_{\perp}$  and negative when  $p_{\parallel} < p_{\perp}$ . We would expect the plasma to become less stable compared to the reference isotropic case if  $p_{\perp} > p_{\parallel}$  ( $\alpha > 0$ ) and more stable when  $p_{\perp} < p_{\parallel}$  ( $\alpha < 0$ ).

To obtain the marginal stability boundary numerically, we plot the internal kink growth rate as a function of  $\beta_p^*$  for different  $\alpha$  in Fig.3.4 (a). Figure 3.4 (a) shows that in anisotropic plasma, same as Bussac *et al*, the linear growth rate of the internal kink mode increases with  $\beta_p^*$ . For the same  $\beta_p^*$ , the growth rate is higher when  $\alpha$  becomes more positive. On the other hand, the growth rate is reduced, or the mode is stabilized, when  $\alpha$  becomes more negative. This is in agreement with the prediction of the generalized Bussac criterion.

The critical  $\beta_p^*$  at marginal stability is extrapolated from Fig.3.4 (a) by fitting  $\gamma$  into a quadratic function of  $\beta_p^*$  and obtaining the fitted curve's intersection with the x axis. Picking different  $q_0$  and different  $\alpha$ , the marginal stability boundary is then plotted in Fig.3.4 (b) with a comparison against Eq. (3.52). Figure 3.4 (b) shows that when  $\alpha = 0$ , i.e. the plasma is isotropic, the stability limit given by MISHKA-A is in good agreement of the analytical Bussac limit. When  $\alpha > 0$  ( $p_{\perp} > p_{\parallel}$ ), the anisotropic incompressible fluid force is destabilizing, reducing the required pressure gradient to drive the instability. On the other hand, if  $\alpha < 0$  ( $p_{\perp} < p_{\parallel}$ ), the anisotropic geometry is stabilizing. We note that when  $q_0$  is close to unity, the stabilizing/destabilizing effect is greater, pushing the stability limit further from the original Bussac limit. This is due to the fact that when  $q_0$  is close to 1, the first term in Eq. (3.52),  $\delta w$ , is smaller. Therefore a tiny change in  $\beta_{pA}$  will lead to a dramatic impact of the stability limit. We also note that the magnitude of anisotropy in Fig.3.4 is small (with  $p_{\perp} = 1.25p_{\parallel}$  on axis for  $\alpha = 0.2$ , or  $p_{\parallel} = 1.2p_{\perp}$  on axis for  $\alpha = -0.2$ ). We would thus expect that a moderate or large anisotropy will have a much greater impact to the  $n = 1$  internal kink mode.

We observe a small discrepancy between the generalized Bussac criterion (lines) and the numerical result (symbols) in Fig.3.4(b) for the  $\alpha < 0$  cases. One possible reason is that in the derivation of the generalized Bussac criterion, the eigenfunction is assumed to stay the same as the isotropic reference case. Also, the perturbed parallel magnetic field  $\tilde{B}$  and the perturbed parallel flow  $\tilde{\mathbf{V}} \cdot \mathbf{b}$  are ignored. These neglected features, when taken into account numerically, may have some impact on the marginal stability limit. Nevertheless, Fig.3.4 (b) gives a fairly good benchmark of the MISHKA-A code.

The above treatment ignores the compressional response of the plasma and keeps only the incompressible part. According to the kinetic theory, the compressional response can either be stabilizing or destabilizing, depending on the fast particle distribution function, the diamagnetic effects, FLR/FOW effects and other non-ideal effects (see for example the review of Graves *et al* [107] and Chapman *et al* [108]). A full treatment of the  $n = 1$  internal kink mode will require a  $\delta f$  method and possibly the involvement of a kinetic code. Nevertheless, we can still conclude on that the anisotropic incompressible fluid force

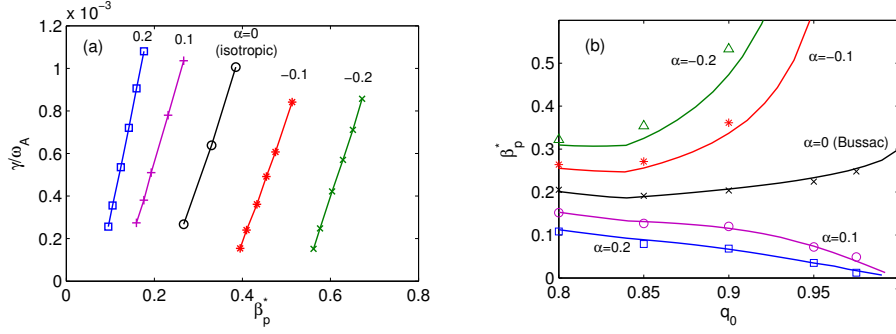


**Figure 3.4:** (a) The growth rate of the  $n = 1$  internal kink mode as a function of  $\beta_p^{*2}$  for a plasma with  $q_0 = 0.9$ . The parameter  $\alpha$  determines the magnitude of anisotropy, with  $p_\perp > p_\parallel$  for  $\alpha > 0$  and  $p_\perp < p_\parallel$  for  $\alpha < 0$ . The growth rate  $\gamma$  is normalized to Alfvén velocity  $V_A$ . (b) The modified Bussac critical  $\beta_p^*$  as a function of  $q_0$  for different anisotropy magnitude  $\alpha$ . The lines are analytical result calculated from Eq. (3.52) and the symbols are numerical results extrapolated from (a).

of a plasma with  $p_\perp < p_\parallel$  ( $\alpha < 0$ ) is more stable than its isotropic counterpart, and therefore needs less stabilizing effects from kinetic response to stabilize, while a plasma with  $p_\perp > p_\parallel$  ( $\alpha > 0$ ) needs more.

Finally, we investigate the compressional response of a plasma described by the CGL model. We couldn't find any unstable modes for our choice of current and pressure profile, despite a scan across parameters  $0.6 < q_0 < 1$ ,  $0 < \beta_p^* < 0.5$  and  $0.5 < p_\perp/p_\parallel < 2$ . It's long been known that for isotropic plasma we have [25, 26]

$$\delta W_{MHD} < \delta W_K < \delta W_{CGL}, \quad (3.57)$$

where  $\delta W_K$  is the perturbed potential energy given by the kinetic theory. For anisotropic plasma, although not rigorously proved, it is very likely to have  $\delta W_K < \delta W_{CGL}$ . With the CGL gives a prediction that the plasma is stable, we can conclude that for our choice of profiles and parameter space, it is possible to stabilize the internal kink mode by plasma compressional response.

### 3.8 Conclusion

We derived and implemented the linearized fluid equations with anisotropy in the straight field line coordinates based on three fluid closures: the double-adiabatic model (CGL), the single-adiabatic (SA) model, and the incompressible model. The ideal MHD normal mode code MISHKA has then been extended to its anisotropic pressure version, MISHKA-A (and the continuous spectrum code, CSMISH-A). Using these numerical tools, we find that anisotropy mainly modifies the continuous spectrum by changing the slow branches and the BAE gap. The change of the slow branches is in accordance with the analytical result, with a different prediction for the SA model and the CGL model. For the BAE gap, the lowest branch touches zero at the resonance flux surface for SA/MHD, but does not for CGL. Meanwhile the change in frequency of the upper accumulation point depends on the local  $q$  value, the magnitude of anisotropy and the fluid closure. Finally, we study the impact of anisotropy to the internal kink mode numerically. If only the incompressible fluid force is considered, we find that for a bi-Maxwellian plasma, the marginal stability boundary is in good agreement with the analytical result of Bussac *et*

*al* and Mikhailovskii: compared to the isotropic case, the plasma is more stable if  $p_\perp < p_\parallel$  and less stable if  $p_\parallel > p_\perp$ . Also, a parameter scan reveals that for our choice of profiles the internal kink mode is stable, if the CGL closure is implemented. This indicates the possibility for these modes to get stabilized by the plasma compressional response, and that CGL is too strong for the estimation of instabilities.

In this work we restrict our study to large aspect ratio, low beta plasma, when the equilibrium can be reproduced similarly by an isotropic equilibrium with an  $O(\epsilon^2(p_\parallel - p_\perp)/p_\parallel)$  difference. In the future, we plan to study the impact of anisotropy on global eigenmodes, and the possibility of using these eigenmodes as MHD spectroscopy to infer pressure anisotropy. For example, as indicated by the change of the BAE gap due to anisotropy, the corresponding modification to a global BAE may serve as an estimation of pressure anisotropy or a validation of the fluid closure model. We also plan to investigate tokamak plasmas with high  $\beta$ , low aspect ratio and large anisotropy, where the current profile and  $q$  profile are dramatically modified by anisotropy, and where the anisotropy shaping effect is important. Finally, we plan to study experimental data from MAST, with the anisotropic equilibria reconstructed by the EFIT-TENSOR code [92], and compute the wave-particle interaction.

### 3.9 Appendix: Auxiliary formulas

Here we present the formular for  $H_1$ ,  $H_2$ ,  $H_3$  and covariant components of the magnetic field line curvature  $\kappa$ :

$$\begin{aligned} H_1 &= J(j^2 \tilde{B}^3 - j^3 \tilde{B}^2) - \frac{F}{qR^2} \partial_s (g_{12} \tilde{B}^1 + g_{22} \tilde{B}^2) \\ &\quad + \frac{F}{qR^2} (\partial_\vartheta + q \partial_\varphi) (g_{11} \tilde{B}^1 + g_{12} \tilde{B}^2) - \frac{F}{R^2} \partial_s (R^2 \tilde{B}^3), \\ H_2 &= J(j^3 \tilde{B}^1 - j^1 \tilde{B}^3) + \frac{F}{R^2} \partial_\varphi (g_{12} \tilde{B}^1 + g_{22} \tilde{B}^2) - \frac{F}{R^2} \partial_s (R^2 \tilde{B}^2), \\ H_3 &= J(j^1 \tilde{B}^2 - j^2 \tilde{B}^1) - B^2 \partial_\varphi (g_{12} \tilde{B}^1 + g_{22} \tilde{B}^2) + B^2 \tilde{B}^3 \partial_\vartheta R^2, \\ \kappa_1 &= -\frac{F}{qBR^2} \left( \frac{\partial}{\partial s} \frac{q|\nabla\Psi|^2}{BF} + q \frac{\partial}{\partial s} \frac{F}{B} + f q \frac{\partial}{\partial \vartheta} \frac{\nabla\Psi \cdot \nabla\vartheta}{BF} \right), \end{aligned} \quad (3.58)$$

$$\kappa_2 = -\frac{F}{R^2 B} \frac{\partial}{\partial \vartheta} \left( \frac{F}{B} \right), \quad (3.59)$$

$$\kappa_3 = -\frac{\kappa_2}{q}. \quad (3.60)$$

### 3.10 Appendix: Matrix elements

#### 3.10.1 The momentum equation

The left-hand sides matrix elements  $B(1, 1)$ ,  $B(1, 2)$ ,  $B(2, 1)$  and  $B(2, 2)$  are identical to those given in the appendix of Huysmans *et al* [117] dividing by  $1 - \Delta$ . Elements  $B(1, 5)$ ,  $B(2, 5)$  and  $B(5, 5)$  are given by

$$B(1, 5) = i\rho_0 \frac{qR^2}{FF_M} \nabla\Psi \cdot \nabla\vartheta, \quad (3.61)$$

$$B(2, 5) = \rho_0 \frac{qR^2}{fFF_M} |\nabla\Psi|^2, \quad (3.62)$$

$$B(5, 5) = \rho_0 \frac{qR^2}{F_M} |B|^2. \quad (3.63)$$

For Eq. (3.31), the matrix elements  $A^0(1, 3)$ ,  $A^0(1', 3)$ ,  $A^0(1, 4)$ ,  $A^0(1, 4')$ ,  $A^0(1', 4)$  and  $A^0(1', 4')$  are same as those in the appendix of Huysmans *et al* and Chapman *et al* [118], except that  $dF/ds$  in Huysmans *et al* and Chapman *et al* is now replaced by  $\partial F/\partial s$ . Other  $A^0(i, j)$  elements coming from Eq. (3.31) are

$$A^0(1', 6) = \frac{R^2}{fF_M}, \quad (3.64)$$

$$A^0(1, 6) = \frac{\partial}{\partial s} \left( \frac{R^2}{F_M} \right) \frac{1}{f} - A^0(1, 7), \quad (3.65)$$

$$\begin{aligned} A^0(1, 7) = \frac{1}{fF_MB} & \left( \frac{|\nabla\Psi|^2}{qB} \frac{dq}{ds} + F \frac{\partial}{\partial s} \frac{BR^2}{F} + fBF \frac{\partial}{\partial \vartheta} \frac{\nabla\Psi \cdot \nabla\vartheta}{F|B|^2} \right) \\ & + i(m + nq) \frac{\nabla\Psi \cdot \nabla\vartheta}{F_M|B|^2}. \end{aligned} \quad (3.66)$$

For Eq. (3.32), the term  $A^0(2, 4)$  is same as Huysmans *et al*, but again changed its  $dF/ds$  terms to  $\partial F/\partial s$ . Other elements are given by

$$A^0(2, 3) = -\frac{1}{fqF} (m\bar{m}F^2 + n^2q^2|\nabla\Psi|^2) - \frac{(\bar{m} - m)m}{fq} F, \quad (3.67)$$

$$A^0(2, 4') = \frac{1}{fqF} (\bar{m}F^2 - nq|\nabla\Psi|^2) + \frac{\bar{m} - m}{fq} F, \quad (3.68)$$

$$A^0(2, 6) = \frac{mR^2}{fF_M} - A^0(2, 7), \quad (3.69)$$

$$\begin{aligned} A^0(2, 7) = \frac{i}{fF_M|B|^3} & (|\nabla\Psi|^2 \partial_\vartheta B - F^2 \partial_\vartheta B + FB \partial_\vartheta F) \\ & + (m + nq) \frac{|\nabla\Psi|^2}{fF_M|B|^2}. \end{aligned} \quad (3.70)$$

Also,  $A^0(i, j)$  elements from right-hand side of Eq. (3.33) are listed as following :

$$A^0(5, 3) = i(m + nq) \frac{F}{qR^2} \frac{\partial F}{\partial \vartheta}, \quad (3.71)$$

$$\begin{aligned} A^0(5, 4) = \frac{m + nq}{qR^2} \frac{\partial |\nabla\Psi|^2}{\partial s} & + \frac{m + nq}{q^2 R^2 F} |\nabla\Psi|^2 \left( F \frac{dq}{ds} - q \frac{\partial F}{\partial s} \right) \\ & + (m + nq) \frac{fF}{qR^2} \frac{\partial}{\partial \vartheta} \frac{\nabla\Psi \cdot \nabla\vartheta}{F} + (m + nq) \frac{F}{qR^2} \frac{\partial F}{\partial s} \\ & - i \frac{F}{q^2 R^2} \frac{\partial F}{\partial \vartheta} \frac{dq}{ds}, \end{aligned} \quad (3.72)$$

$$A^0(5, 6) = -i \frac{1}{(1 - \Delta)B} \frac{\partial B}{\partial \vartheta}, \quad (3.73)$$

$$A^0(5, 7) = \frac{m + nq}{1 - \Delta} - A^0(6, 5). \quad (3.74)$$

The anisotropy related terms are given by

$$A^A(1, 3) = \frac{1}{F_M} (\Delta\beta_1 + R^2\partial_s\Delta) (mh_1 + nh_2) + 2n \frac{\nabla\Psi \cdot \nabla\vartheta}{F_M} \partial_\vartheta\Delta, \quad (3.75)$$

$$A^A(1, 4) = \frac{\partial_\vartheta\Delta}{F_M} \left[ if(m+nq) \left( \frac{F^2}{q^3 R^2 |\nabla\Psi|^2} + \frac{\nabla\Psi \cdot \nabla\vartheta}{q |\nabla\Psi|^2} \right) - \frac{2\nabla\Psi \cdot \nabla\vartheta}{q^2} \frac{dq}{ds} \right] + \frac{\Delta}{F_M} [h_3 + ih_4(m+nq)]\beta_1 + \frac{\partial_s\Delta}{F_M} R^2 h_3, \quad (3.76)$$

$$A^A(1, 4') = \frac{\Delta}{F_M} h_5 \beta_1 + \frac{R^2}{F_M} h_5 \partial_s\Delta + 2 \frac{\nabla\Psi \cdot \nabla\vartheta}{q F_M} \partial_\vartheta\Delta, \quad (3.77)$$

$$A^A(1', 3) = \frac{\Delta R^2}{F_M} (mh_1 + nh_2), \quad (3.78)$$

$$A^A(1', 4) = \frac{\Delta R^2}{F_M} [h_3 + i(m+nq)h_4], \quad (3.79)$$

$$A^A(1', 4') = \frac{\Delta R^2}{F_M} h_5, \quad (3.80)$$

$$A^A(2, 3) = \frac{\Delta}{F_M} (mh_1 + nh_2)\beta_2 + i \frac{R^2 \partial_\vartheta\Delta}{F_M} (mh_1 - nh_2), \quad (3.81)$$

$$A^A(2, 4) = \frac{\Delta}{F_M} [h_3 + i(m+nq)h_4]\beta_2 - i \frac{R^2 \partial_\vartheta}{F_M} h_3 - (m+nq) \frac{|\nabla\Psi|^2 \partial_s\Delta}{fq F_M}, \quad (3.82)$$

$$A^A(2, 4') = \frac{\Delta}{F_M} \beta_2 h_5 + i \frac{F^2 - |\nabla\Psi|^2}{fq F_M} \partial_\vartheta\Delta, \quad (3.83)$$

$$A^A(5, 3) = \frac{f\Delta}{1-\Delta} (mh_1 + nh_2)\beta_3 - in \frac{|B|^2 \partial_\vartheta\Delta}{1-\Delta}, \quad (3.84)$$

$$A^A(5, 4) = \frac{f\Delta}{1-\Delta} [h_3 + i(m+nq)h_4]\beta_3 + i \frac{|B|^2 \partial_\vartheta\Delta}{q^2(1-\Delta)} \frac{dq}{ds} - (m+nq) \frac{|B|^2 \partial_s\Delta}{q(1-\Delta)}, \quad (3.85)$$

$$A^A(5, 4') = \frac{f\Delta}{1-\Delta} \beta_3 h_5 - i \frac{|B|^2 \partial_\vartheta\Delta}{q(1-\Delta)}, \quad (3.86)$$

in which

$$\begin{aligned} \beta_1 = & -\frac{2R^2}{B} \frac{\partial B}{\partial s} - \frac{\partial R^2}{\partial s} + 2 \frac{R^2}{F} \frac{\partial F}{\partial s} - \frac{R^2}{F_M} \frac{dF_M}{ds} \\ & - 2if(\bar{m} + nq) \frac{\nabla \Psi \cdot \nabla \vartheta}{|B|^2} + 2f \frac{\nabla \Psi \cdot \nabla \vartheta}{F|B|^2} \frac{\partial F}{\partial \vartheta} \\ & - \frac{2|\nabla \Psi|^2}{q|B|^2} \frac{dq}{ds}, \end{aligned} \quad (3.87)$$

$$\begin{aligned} \beta_2 = & 2i \frac{F}{|B|^2} \frac{\partial F}{\partial \vartheta} - 2i \frac{R^2}{B} \frac{\partial B}{\partial \vartheta} - i \frac{\partial R^2}{\partial \vartheta} + \bar{m} R^2 \\ & - 2(\bar{m} + nq) \frac{|\nabla \Psi|^2}{|B|^2}, \end{aligned} \quad (3.88)$$

$$\beta_3 = -i \frac{\partial_\vartheta \Delta}{(1 - \Delta)^2} - 2i \frac{1}{B} \frac{\partial B}{\partial \vartheta} - (\bar{m} + nq), \quad (3.89)$$

and

$$\begin{aligned} h_1 = & -\frac{F^2}{fqR^2}, \quad h_2 = \frac{|\nabla \Psi|^2}{fR^2}, \quad h_3 = -\frac{|\nabla \Psi|^2}{fq^2R^2} \frac{dq}{ds}, \\ h_4 = & \frac{\nabla \Psi \cdot \nabla \vartheta}{qR^2}, \quad h_5 = \frac{|B|^2}{fq}. \end{aligned} \quad (3.90)$$

### 3.10.2 The ideal Ohm's law

For the ideal Ohm's law equations (Eq. (3.25) and (3.26)), we have

$$B(3, 3) = A^0(3, 2) = 1, \quad (3.91)$$

$$B(4, 4) = -A^0(4, 1) = 1, \quad (3.92)$$

### 3.10.3 The single/double-adiabatic fluid closure equations

The matrix element  $B(6, 6)$  and  $B(7, 7)$  are identical to Chapman *et al*  $B(7, 7)$ . For the single/double-adiabatic model Eq. (3.34) and (3.35), the  $A^0(i, j)$  elements are given by

$$A^0(6, 1') = -\gamma_{\perp 1} \frac{R^2}{F}, \quad (3.93)$$

$$\begin{aligned} A^0(6, 1) = & -\gamma_{\perp 1} \frac{\partial}{\partial s} \left( \frac{R^2}{F} \right) - if(\bar{m} + nq) \gamma_{\perp 1} \frac{\nabla \Psi \cdot \nabla \vartheta}{F|B|^2} \\ & - f \frac{\nabla \Psi \cdot \nabla \vartheta}{F|B|^2} \frac{\partial}{\partial \vartheta} (f_{\perp} - \gamma_{\perp 1}) - \frac{R^2}{F} \frac{\partial f_{\perp}}{\partial s} \\ & + \gamma_{\perp 2} \left[ -\frac{|\nabla \Psi|^2}{F|B|^2} \frac{dq}{ds} - \frac{q}{B} \frac{\partial}{\partial s} \frac{BR^2}{F} + \frac{fq}{B} \frac{\partial}{\partial \vartheta} \frac{\nabla \Psi \cdot \nabla \vartheta}{BF} \right], \end{aligned} \quad (3.94)$$

$$\begin{aligned} A^0(6, 2) = & \gamma_{\perp 1} \frac{F}{|B|^2} \left( n \frac{q|\nabla \Psi|^2}{F^2} - \bar{m} \right) + i \frac{F}{|B|^2} \frac{\partial}{\partial \vartheta} (f_{\perp} - \gamma_{\perp 1}) \\ & + i \gamma_{\perp 2} \frac{1}{B} \frac{\partial}{\partial \vartheta} \frac{F}{B}, \end{aligned} \quad (3.95)$$

$$A^0(6, 5) = -\gamma_{\perp 1}(\bar{m} + nq) - \gamma_{\perp 2}(m + nq) + i\frac{\partial}{\partial\vartheta}(f_{\perp} - \gamma_{\perp 1}) + i\gamma_{\perp 2}\frac{1}{B}\frac{\partial B}{\partial\vartheta}, \quad (3.96)$$

Replacing  $f_{\perp}$  by  $f_{\parallel}$ ,  $\gamma_{\perp 1}$  by  $\gamma_{\parallel 1}$  and  $\gamma_{\perp 2}$  by  $\gamma_{\parallel 2}$ , we will reach the matrix elements  $A^0(7, 1')$ ,  $A^0(7, 1)$ ,  $A^0(7, 2)$  and  $A^0(7, 5)$ .

#### 3.10.4 The incompressible fluid closure

The matrix element  $B(6, 6)$  and  $B(7, 7)$  are identical to Chapman *et al*  $B(7, 7)$ . The  $A^0(i, j)$  elements originated from Eq. (3.10) and (3.11) are given by

$$A^0(4, 1) = -\frac{R^2}{F} \left( \frac{\partial p_{\perp}}{\partial s} - \frac{\partial_{\vartheta} p_{\perp}}{\partial_{\vartheta} B} \frac{\partial B}{\partial s} \right), \quad (3.97)$$

$$A^0(7, 1) = -\frac{R^2}{F} \left( \frac{\partial p_{\parallel}}{\partial s} - \frac{p_{\parallel} - p_{\perp}}{B} \frac{\partial B}{\partial s} \right). \quad (3.98)$$





---

# Application to MAST discharges and the impact on wave-particle interactions

---

## Abstract

A number of tools have recently been developed to study equilibrium and stability in tokamaks with pressure anisotropy. Here we apply these tools to a Mega Ampere Spherical Tokamak (MAST) discharge to calculate equilibrium, Alfvén continua and eigenmodes, through to linear growth and nonlinear saturation of a toroidal Alfvén eigenmode (TAE); this is the first study of wave growth and saturation for anisotropic equilibria. Comparisons with the standard tools which assume an isotropic pressure reveal various differences in equilibrium and modes: the safety factor profile in the isotropic reconstruction is reversed shear while the anisotropic reconstruction gives normal shear; the isotropic TAE gap is much narrower than the anisotropic gap; and the TAE radial mode structure is wider in the anisotropic case. These lead to a modification in the resonant regions of fast-ion phase space, and produce a 35% larger linear growth rate and an 18% smaller saturation amplitude for the TAE in the anisotropic analysis compared to the isotropic analysis.

## 4.1 Introduction

External heating in modern tokamaks can lead to momentum injection and velocity-space or pressure anisotropy. Such physics can displace flux surfaces outwards, and lead to additional currents that can modify the magnetic configuration and change plasma wave modes and stability. For instance, for values of  $p_{\perp}/p_{\parallel} \approx 1.5$ ,  $p_{\perp}$  can vary by 20% at mid-radius for a spherical tokamak equilibrium [101]. A number of authors report that the experimentally inferred equilibrium, and in particular the on-axis safety factor, can be significantly different if a single pressure is assumed rather than anisotropic pressures [76, 77, 89]. Qu *et al* [101] find that these differences increase with increasing anisotropy and inverse aspect ratio. At high beta the impact of anisotropy is non-perturbative: recent work [127] has shown that at very high beta the impact of non-zero anisotropy is to eliminate the diamagnetic hole that would otherwise be present in isotropic plasmas [128, 129], even with flow [130]. Further discussion on the impact of anisotropy can be found in the contemporary topical reviews by Pustovitov [84] and Hole and Fitzgerald [116].

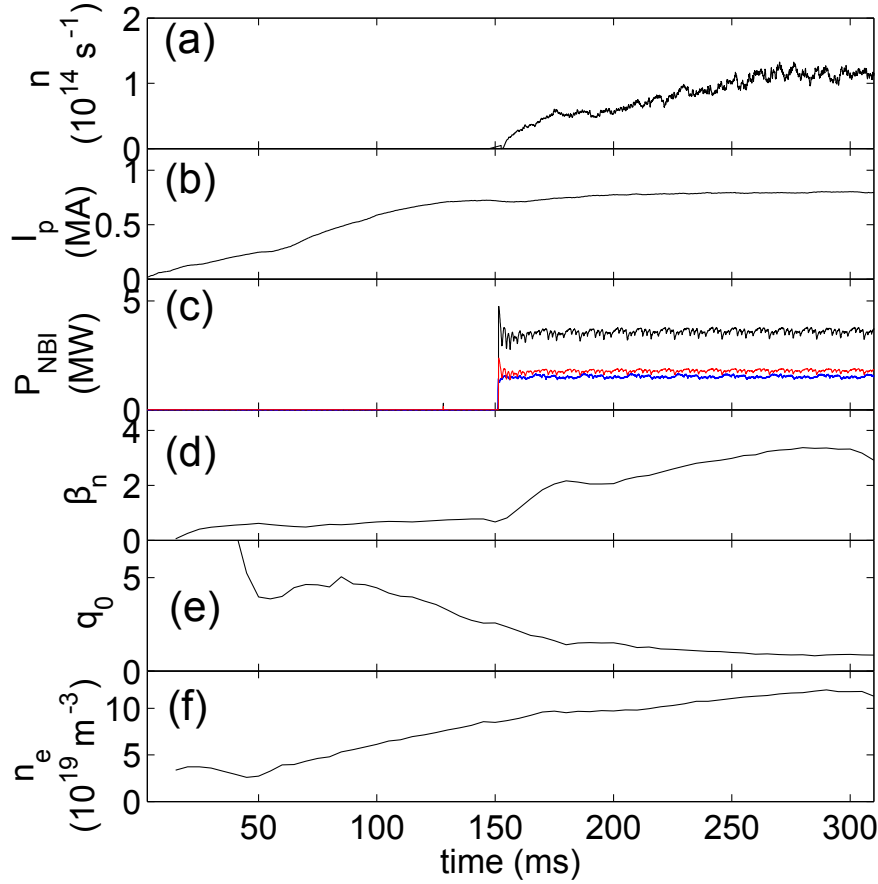


**Figure 4.1:** Evolution of discharge #29221. Figure (a) shows neutron rate, (b) plasma current  $I_p$ , (c) neutral beam power  $P_{\text{NBI}}$  (blue is the SS supercusp beam, red is the SW chequerboard beam, and black is the total), (d) the normalised beta  $\beta_n$ , (e) the core safety factor  $q_0$ , (f) the line integrated electron density  $n_e$ . The quantities  $q_0$  and  $\beta_n$  are inferred quantities computed using EFIT.

In recent years a range of new tools has been developed to model high-performance plasmas and understand the change in plasma wave mode and stability. EFIT TENSOR [92] is a modification of the existing force-balance solver EFIT++, which is constrained to external magnetic measurements and temperature and density profiles, together with user-input constraints of on-axis safety factor. EFIT TENSOR adds kinetic constraints  $p_{\parallel}$  and  $p_{\perp}$  and a toroidal flow profile. HELENA+ATF [101] is a fixed boundary solver that includes anisotropy and toroidal flow, and computes the field configuration in the metric used by MHD stability code MISHKA [59]. We have also developed a new single adiabatic stability theory for anisotropic plasma that reverts to MHD in the isotropic limit [20], and implemented this and double-adiabatic closure in the extended MHD stability code MISHKA-A [131]. In tandem to these developments we have also deployed Bayesian inference techniques to infer both the toroidal and poloidal rotation profiles [77] and energetic particle pressure [89, 132].

In this work we apply these advances in theory and computational models to study mode activity in the UK Mega Ampere Spherical Tokamak (MAST). MAST discharge #29221, produced during a power-density scan set of experiments [133], was a 3.1 MW

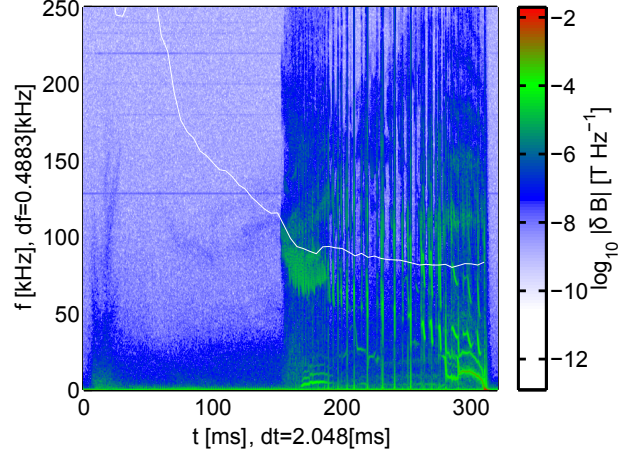


**Figure 4.2:** Spectrogram of discharge #29221. The white trace is the TAE frequency,  $v_A/2q_0R$ , using the  $q_0$  value in Fig.4.1(e).

two-beam heated plasma (a South-South (SS) “supercusp” beam operating at 1.5 MW and a South-West (SW) “chequerboard” beam operating at 1.6 MW) with a plasma current of 0.9 MA and normalised beta  $\beta_n \approx 3$ . Figure 4.1 is time trace of the evolution of the discharge, and Fig.4.2 a spectrogram of magnetic perturbation coil data. The magnetics reveal a rich range of activity, including: suspected low-frequency (10 kHz) tearing modes at 170 ms; toroidal Alfvén eigenmodes (TAEs) from 150 ms to 220 ms with frequency ramping down from 100 kHz to 50 kHz; chirping-down fishbones from 250 ms to 300 ms; and beyond 280 ms, long-lived mode activity. Keeling *et al* [133] focused on the fishbone phase just prior to long-lived mode activity. Our focus is the TAE mode activity at 190 ms, where a high fidelity TRANSP simulation is available. At this time the observed mode frequency is  $\approx 70$  kHz, with a frequency chirp of 20 kHz across a 2 ms slice ( $\approx 80$  kHz mode frequency at 189 ms and  $\approx 60$  kHz at 191 ms). Toroidal mode number analysis shows that  $n = 1$  for these modes.

## 4.2 Equilibrium and mode calculation

In this work, we examine two equilibrium reconstructions for MAST #29221 using different models and assumptions. The first “anisotropic” equilibrium is reconstructed by EFIT TENSOR, from experimental constraints such as the external coils, the total current, the Motional Stark Effect (MSE) spectroscopy, and kinetic constraints ( $p_{\parallel}$  and  $p_{\perp}$ ) from TRANSP simulations with an empirical fast particle diffusivity that provided a match to the measurements of neutron diagnostics. The second “isotropic” equilibrium is reconstructed by EFIT++ (isotropic) with the same constraints, except that the flux-surface averaged  $\langle p^* \rangle$ , where  $p^* \equiv (p_{\parallel} + p_{\perp})/2$ , is used as the kinetic constraint. The isotropic and anisotropic flux surfaces are shown in Fig.4.3. Both reconstructions give strongly shaped flux surfaces with an X-point at  $R \sim 0.55$  m and  $Z \sim 1.2$  m; there is a small relative displacement between the isotropic and anisotropic flux surfaces and magnetic axes. The pressure profiles are plotted in Fig.4.4 as a function of major radius along the midplane ( $Z = Z_{\text{mag}}$ ). It is interesting to note that although both cases are constrained to MSE, the  $q$  profiles are substantially different, as shown in Fig.4.5; here  $q$  is graphed as a function of the normalised poloidal flux coordinate  $s \equiv \sqrt{\psi/\psi_{\text{edge}}}$ . The  $q$

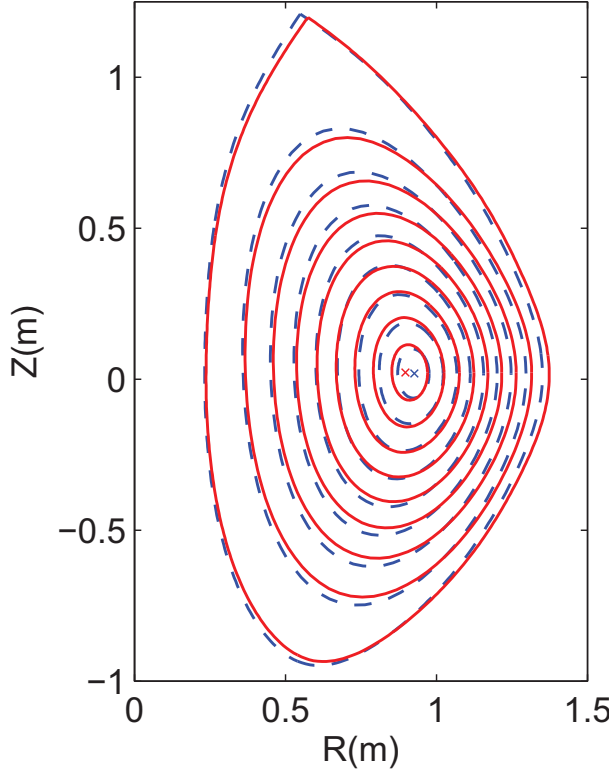


**Figure 4.3:** Flux surfaces for the isotropic (red solid line) and anisotropic (blue dashed line) equilibrium reconstructions, with the crosses showing the location of the respective magnetic axes.

profile in the isotropic equilibrium is reversed shear, while for the anisotropic equilibrium it is normal shear with a “dip” on-axis. Finally, we note that both  $q$  profiles have a flat region for  $s < 0.6$ .

The EFIT++ (EFIT TENSOR) flux functions and the last closed flux surface are used as inputs to the fixed-boundary equilibrium solver HELENA (HELENA+ATF) to obtain the metrics in straight-field-line coordinates for the isotropic (anisotropic) equilibrium. The continuous spectra of the isotropic and anisotropic equilibria are then calculated by CSMISH [117] and CSMISH-A [131], respectively, each using the density profile  $n(s) = n_0(1 - 0.7s^2)$  as a reasonable fit to the Thomson scattering data, with  $n_0 = 2.42 \times 10^{19} \text{ m}^{-3}$  the on-axis number density. Figure 4.6(a) is an overview of the  $n = 1$  incompressible continuum for each equilibrium. Three gaps (TAE, EAE, and NAE, respectively induced by the toroidicity, ellipticity, and triangularity) exist in the frequency range  $0 \leq \omega \leq 1.5\omega_{A0}$  where  $\omega_{A0} = B_0/R_0\sqrt{\mu_0\rho_0}$  is the Alfvén frequency at the magnetic axis. The TAE gap of the isotropic equilibrium is much narrower than that of the anisotropic equilibrium, due mainly to the difference in the  $q$  profile shown in Fig.4.5. The  $m = 1$  and  $m = 2$  continua intersect at the  $q = 1.5$  surface which is located at  $s \approx 0.3$  for the anisotropic equilibrium. However, for the isotropic equilibrium, two  $q = 1.5$  surfaces exist (at  $s = 0.15$  and  $s = 0.5$ ) due to the reverse shear. The intersection at  $s = 0.15$  will create a much narrower gap, since the inverse aspect ratio  $\epsilon = r/R$  is smaller and thus the toroidicity effects are weaker. Finally, we note that the EAE and NAE gaps are closed in both equilibria.

The continuum gaps allow the existence of robust global modes that are free from continuum damping. In this work, we will focus on  $n = 1$  TAEs that are observed on

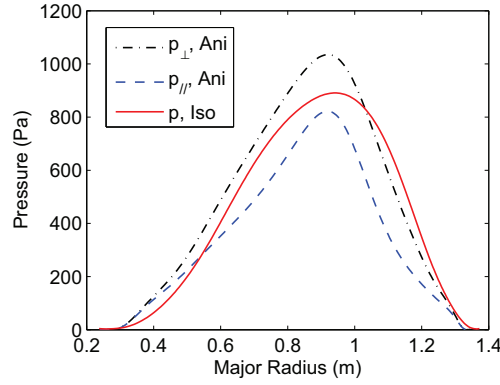


**Figure 4.4:** The pressure profiles along the midplane for the isotropic and anisotropic equilibria.

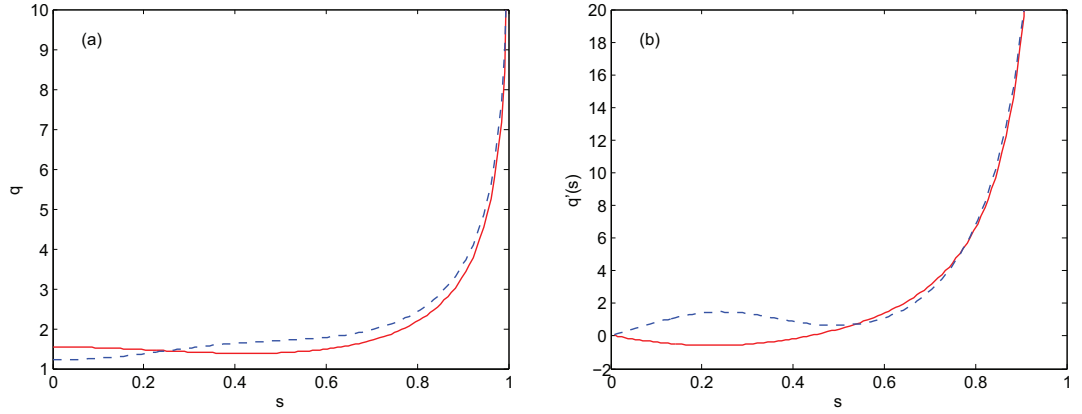


**Figure 4.5:** (a) The  $q$  profile and (b)  $q'(s)$  for the isotropic equilibrium (blue dashed line) and anisotropic equilibrium (red solid line).

the Mirnov coil spectrogram. The corresponding TAE gap is shown in Fig.4.6(b). We use MISHKA and MISHKA-A to calculate the TAEs for the isotropic and anisotropic equilibria, respectively. Two TAEs are found for the isotropic case due to the reverse shear, one of which is core localised ( $s < 0.2$ ) and therefore less likely to be picked up by the external coils. The frequency of this core mode is 78.2 kHz, just 0.1 kHz above the lower continuum tips. The other, however, is a global mode with a frequency of 81.3 kHz, with the radial mode structure shown in Fig.4.7(a). For the anisotropic equilibrium, a global mode is also found at 88.9 kHz. The radial mode structure, especially the  $m = 2$  harmonic, is broader compared to the isotropic one, as seen in Fig.4.7(b).

## 4.3 Stability

### 4.3.1 Physical background and method

Alfvén waves can be driven unstable by fast ions produced by neutral beam injection. For shear Alfvén waves, which are transverse electromagnetic waves, the drift motion of the fast ions gives the dominant contribution to the wave-particle interaction [32]. The power transfer between fast ions and shear Alfvén waves is approximately proportional to  $\mathbf{v}_d \cdot \mathbf{E}_\perp$ , with  $\mathbf{v}_d$  the drift velocity and  $\mathbf{E}_\perp$  the transverse electric field. Net energy transfer therefore requires that  $\mathbf{v}_d \cdot \mathbf{E}_\perp$  averaged over many periods be non-zero, leading to the

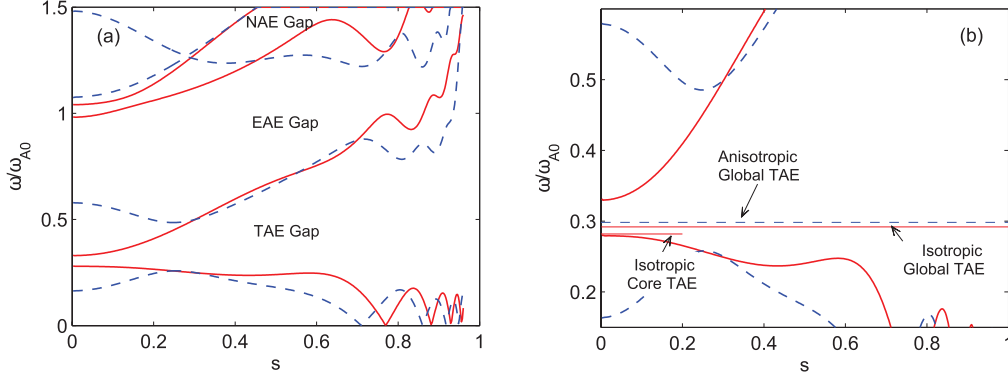


**Figure 4.6:** The  $n = 1$ ,  $m = 1$ —11 incompressible continuous spectrum and the TAE frequencies of the isotropic equilibrium (red solid line) and anisotropic equilibrium (blue dashed line), where the frequency  $\omega$  is normalised by the on-axis Alfvén frequency  $\omega_{A0}$ , and  $s = \sqrt{\psi/\psi_{\text{edge}}}$  is a normalised poloidal flux coordinate. Figure 4.6(a) shows the spectrum over a large frequency range with the TAE, EAE, and NAE gaps labelled, and Fig.4.6(b) shows a magnification of the TAE-gap frequency range, with the horizontal lines representing the TAE frequencies found by MISHKA(-A).

resonance condition [32, 134, 135]

$$\Omega_{n,l} = \omega + l\omega_\theta - n\omega_\phi = 0, \quad (4.1)$$

where  $n$  is the toroidal mode number,  $l$  is an integer,  $\omega$  is the angular wave frequency, and  $\omega_\theta$  and  $\omega_\phi$  are respectively the toroidal and poloidal orbit frequencies.

The energy transfer between waves and particles depends on a number of factors [32]. The first is the relative amplitudes of the poloidal harmonics of the eigenmode, which will affect the strength of the different resonances. The growth rate  $\gamma$  of the wave amplitude depends on the slope of the distribution function at resonance through [32]

$$\gamma \propto \omega \frac{\partial f}{\partial E} + n \frac{\partial f}{\partial P_\phi}, \quad (4.2)$$

where  $P_\phi = mRv_\phi - Ze\psi$  is the toroidal angular momentum. Since  $P_\phi$  increases as  $\psi$  decreases, a negative gradient  $\partial f/\partial\psi$  drives wave growth. Energy transfer is also dependent on the alignment of the particle orbit and eigenmode. The energy transfer is maximised when the drift-orbit width  $\Delta_b$  is comparable to the eigenmode width  $\Delta_m$  [32, 136, 137]. In the case where these widths are not comparable, large orbit-width theory ( $\Delta_b \gg \Delta_m$ ) predicts a reduced power transfer than that obtained in narrow-orbit width theory ( $\Delta_b \ll \Delta_m$ ) [138, 139].

A quantitative treatment of the wave-particle energy transfer requires a numerical solution of the assumed model for the wave-particle interaction. The HAGIS code [61] is a nonlinear perturbative code that solves the drift-kinetic equation in toroidal geometry for a distribution of fast particles and a set of Alfvén eigenmodes. The fast particle motion is described in HAGIS by a guiding-centre Hamiltonian in Boozer coordinates, with the assumption of isotropic bulk plasma pressure.

A rigorous approach to modelling the wave-particle interaction in plasmas with pressure anisotropy requires the use of an anisotropic Hamiltonian. A guiding-centre Hamiltonian in Boozer coordinates for plasmas with pressure anisotropy has been derived

in [140, 141]. Unlike in the isotropic case, it is the lines of *effective* current density  $\mathbf{K} \equiv \nabla \times (\sigma \mathbf{B})/\mu_0$  (with  $\sigma \equiv 1 - \mu_0(p_{\parallel} - p_{\perp})/B^2$ ) which lie on flux surfaces [12, 142]; that is,  $\mathbf{K} \cdot \nabla \psi = 0$  rather than  $\mathbf{J} \cdot \nabla \psi = 0$ , where  $\mathbf{J}$  is the true current density. From the conditions  $\mathbf{K} \cdot \nabla \psi = 0$  and  $\nabla \cdot \mathbf{K} = 0$ , the magnetic field can be expressed in the covariant Boozer representation as  $\sigma \mathbf{B} = g(\psi) \nabla \phi + I(\psi) \nabla \theta + g(\psi) \delta(\psi, \theta) \nabla \psi$ . This modifies the expressions for the canonical momenta relative to the isotropic case, and thus changes the equations of motion. The rigorous approach to modelling the wave-particle interaction with pressure anisotropy would involve implementing these new equations of motion into HAGIS.

In this paper, however, we propose an approximate method for the inclusion of pressure anisotropy in wave-particle interaction studies without the need to modify the HAGIS code. First, the anisotropic equilibrium is computed using HELENA+ATF. Flux surface averages are then calculated for the toroidal current  $J_{\phi}$  and for  $p^* \equiv (p_{\parallel} + p_{\perp})/2$ . We then input these  $\langle J_{\phi} \rangle(\psi)$  and  $\langle p^* \rangle(\psi)$  into the standard HELENA code (with  $\langle p^* \rangle$  taken as the “isotropic” pressure), applying the same boundary conditions as in HELENA+ATF, and rescale the total current such that the  $q$ -profile matches that obtained from HELENA+ATF. The use of this remapped equilibrium and isotropic Hamiltonian is appropriate if the particle orbits match those for the fully anisotropic equilibrium and anisotropic Hamiltonian.

Here, to assess the validity of the approximate approach, we have calculated trapped and passing orbits using the full-orbit code CUEBIT [143] for MAST #29221 for both the full anisotropic and remapped equilibria. We show an example of a co-passing orbit in Fig.4.8 for a given particle energy  $E$  and orbit-invariant  $\Lambda \equiv \mu B_0/E$ . We find that the poloidal orbit frequencies of the passing particle in the full anisotropic and remapped cases are 118.6 kHz and 119.4 kHz respectively, so the remapped orbit frequency is less than 1% larger than the anisotropic orbit frequency. In addition, we see from Fig.4.8 that the guiding-centre particle trajectories are similar. Since the particles have the same initial value of major radius ( $R = R_{\max}$ ) along the equatorial plane ( $Z = Z_{\text{mag}}$ ) on the low-field side, the difference between these particle orbits is largest on the equatorial plane on the high-field side where  $R = R_{\min}$ . We find that the difference in  $R_{\max} - R_{\min}$  is approximately 1 cm, thus the relative difference in  $R_{\max} - R_{\min}$  is approximately 2%. We obtain similar results for passing orbits with different  $E$  and  $\Lambda$  and also for trapped orbits. These results for the particle orbits suggest that our approach will give a good approximation to the wave-particle dynamics. A detailed assessment of the impact of using the approximate approach on the particle orbits in Boozer coordinates will be pursued in future work.

### 4.3.2 Calculations

We now compute with HAGIS the resonant regions of fast-ion phase space for the  $n = 1$  TAE calculated in Section 4.2. The toroidal orbit frequency of ions is calculated using  $\omega_{\phi} = \langle \dot{\phi} \rangle = \oint \dot{\phi} dt / \oint dt = \Delta \phi / \Delta t$ , where the integral is performed over a single poloidal orbit. The poloidal orbit frequency is calculated as  $\omega_{\theta} = 2\pi / \Delta t$ . TRANSP simulations for MAST #29221 show that the fast-ion pitch-angle distribution  $f(\lambda)$  is approximately a Gaussian centred at  $\lambda = \lambda_0 = 0.92$  with a width  $\Delta \lambda = 0.5$ , where  $\lambda \equiv v_{\parallel}/v$  is the pitch taken at the equatorial plane at the low-field side of the plasma cross section ( $R > R_{\text{mag}}$ ). The focus of this paper is to illustrate the difference between the isotropic and anisotropic cases, so here we choose an idealised delta-function distribution,  $f(\Lambda) = \delta(\Lambda)$ , where  $\Lambda$  is related to the pitch via  $\Lambda = B_0(1 - \lambda^2)/B$ . Such a choice of distribution function is



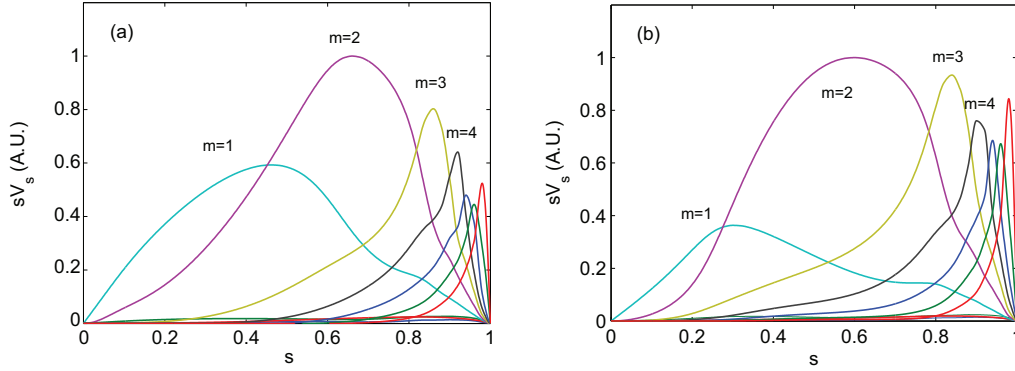


**Figure 4.7:** The  $n = 1$  global TAE radial structure of (a) the isotropic equilibrium and (b) the anisotropic equilibrium.

justified by the fact that most well-confined beam ions in MAST are in passing orbits.

Resonance maps for the  $n = 1$  TAE calculated in Section 4.2 are graphed for the isotropic and anisotropic equilibria and wave frequencies in Fig.4.9 as a function of  $s^2$  and particle energy  $E$ . For both the isotropic and anisotropic cases the  $l = 0$  resonance occurs at  $E \lesssim 3$  keV for all  $s$ . This resonance will not drive wave growth due to the strong energy-gradient damping. The broad  $l = 1$  resonance is significantly different between these cases; for a given particle energy the resonant region is located closer to the magnetic axis in the anisotropic case. No resonances for  $l \geq 2$  are found in the energy range considered. (We note that these resonance maps are qualitatively similar to those in [144] for MAST #29210, calculated for ions with  $\Lambda = 0.3$  resonating with a  $n = 1$  TAE.)

We now examine the difference in the wave amplitude evolution between the isotropic

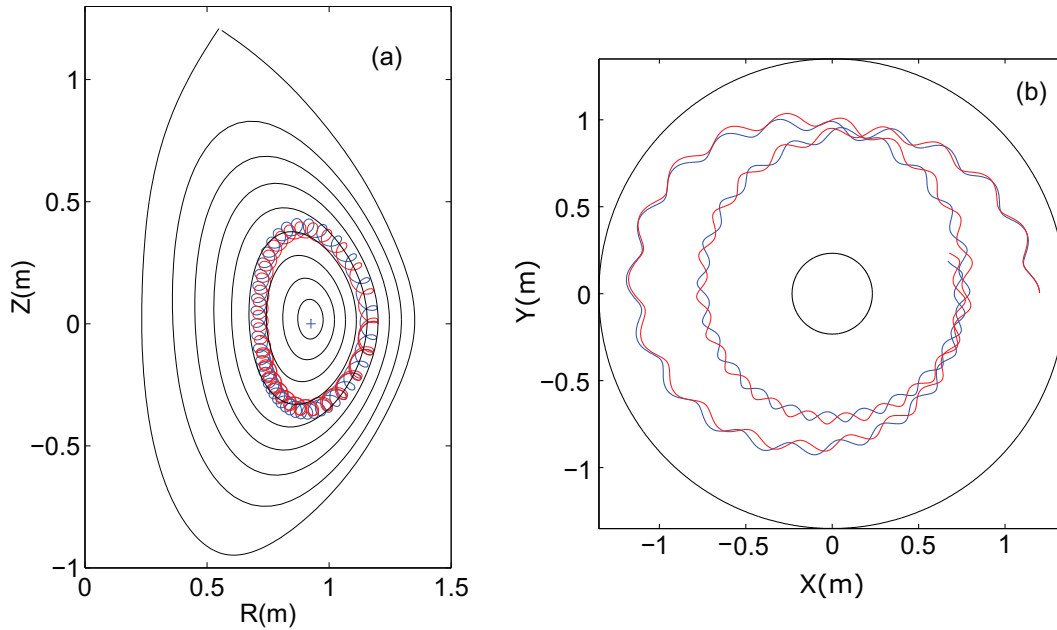


**Figure 4.8:** Fast ion orbits calculated using CUEBIT for the full anisotropic equilibrium (blue) and the remapped equilibrium (red) for MAST #29221 for ions with  $E = 21$  keV and  $\Lambda = 0.72$ , where (a) and (b) show the poloidal projection and top view of the particle orbits respectively.

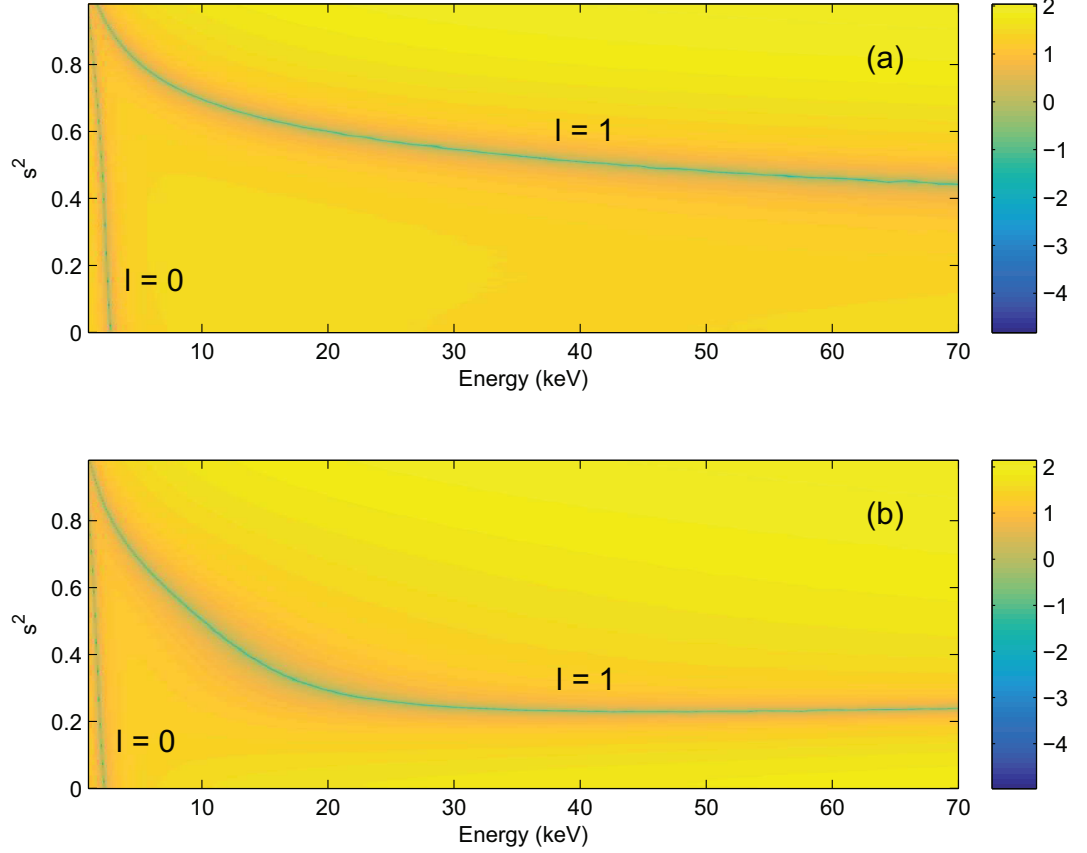


**Figure 4.9:** Resonance maps for ions with  $\Lambda = 0$  for (a) isotropic equilibria and  $n = 1$  TAE of frequency 81.3 kHz, and (b) anisotropic equilibria and  $n = 1$  TAE of frequency 88.9 kHz, with the bounce harmonics  $l$  labeled. Colour indicates the value of  $-\log_{10}(\sum_l 1/|\Omega_{n,l}|)$ , which is large and negative at resonances.

and anisotropic cases. The initial fast ion distribution function  $f_h$  is chosen as a slowing-down distribution in energy and a Gaussian distribution in the radial coordinate  $s$  (as in existing fast-ion physics studies on MAST [145, 146]):

$$f_h(E, s, \Lambda) = \frac{C}{E^{3/2} + E_c^{3/2}} \text{Erfc} \left[ \frac{E - E_0}{\Delta E} \right] \exp \left[ -\frac{s^2}{(\Delta s)^2} \right] \delta(\Lambda). \quad (4.3)$$

Using measured physical quantities at  $t = 0.190$  s and fitting to TRANSP simulation data we estimate the values  $E_c = 16$  keV,  $E_0 = 65$  keV,  $\Delta E = 1.5$  keV,  $\Delta s = 0.5$ , with the normalization constant  $C$  chosen such that the on-axis fast ion density is  $n_h = 3.5 \times 10^{18} \text{ m}^{-3}$ . For our HAGIS simulations we choose 300000 markers to represent the fast ion population, and choose the integrator time step such that both the particle and wave integrators make 64 steps per wave period.

HAGIS calculations of the wave amplitude evolution are shown in Fig.4.10. We find that the linear growth rate for the isotropic case is  $\gamma_{\text{iso}}/\omega_{\text{iso}} = 2.08 \times 10^{-2}$ , while for the anisotropic case  $\gamma_{\text{aniso}}/\omega_{\text{aniso}} = 2.81 \times 10^{-2}$ . To explain this difference of  $\approx 35\%$  in the growth rates we first compare the drift-orbit widths and mode widths. We see from Fig.4.5(a) that  $q_{\text{aniso}} > q_{\text{iso}}$  for  $s \gtrsim 0.25$ . The resonant particles in the isotropic (anisotropic) case are located at  $s \gtrsim 0.7$  ( $s \gtrsim 0.5$ ) (see Fig.4.9) and thus the safety factor is larger in the anisotropic case at the location of all resonant particles. The drift-orbit

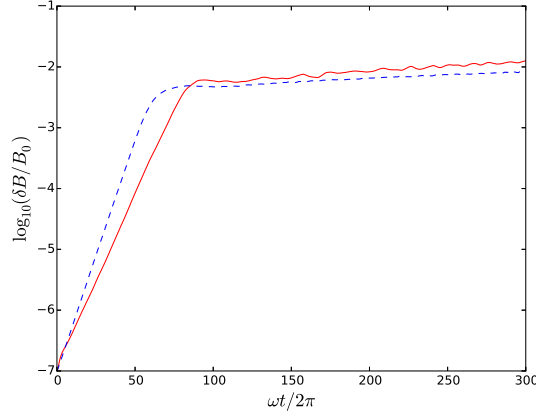


**Figure 4.10:** Wave amplitude  $\delta B/B_0$  for the isotropic (red solid line) and anisotropic (blue dashed line) cases.

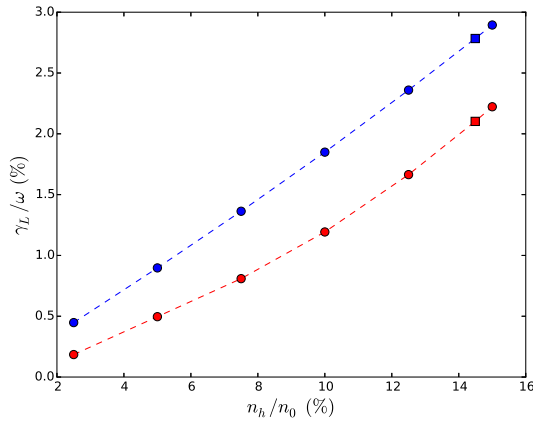


**Figure 4.11:** Linear growth rate  $\gamma_L/\omega$  for different fast-ion density fractions  $n_h/n_0$ , with the isotropic case in red and the anisotropic case in blue. The square markers show the growth rates for the measured MAST #29221 fast-ion density,  $n_h = 3.5 \times 10^{18} \text{ m}^{-3}$ .

width of circulating particles  $\Delta_b$  is dependent on the safety factor through  $\Delta_b \approx q\rho_{\parallel}$  (which was found to be a reasonable approximation for a spherical tokamak [147]), with  $\rho_{\parallel} = v_{\parallel}/\Omega_b$  where  $\Omega_b$  is the beam-ion gyrofrequency. The larger  $q$  in the anisotropic case thus leads to a larger  $\Delta_b$ . Since the mode widths  $\Delta_m$  of the dominant poloidal harmonics satisfy  $\Delta_m \gtrsim \Delta_b$ , the larger orbit widths in the anisotropic case are more comparable to the mode widths and are thus more favourable for mode drive. In addition, the  $l = 1$  resonance shown in Fig.4.9 occurs at smaller  $\psi$  for the anisotropic case; the radial gradient  $\partial f/\partial\psi \propto \exp[-(\psi/\psi_{\text{edge}})/(\Delta s)^2]$  is therefore larger at resonance in the anisotropic case, again leading to a larger growth rate through (4.2). HAGIS calculations for different fast-ion number densities  $n_h$ , shown in Fig.4.11, give larger linear growth rates in the anisotropic case than the isotropic case for each value of fast-ion number density.

Mode saturation is reached when the nonlinear bounce frequency of the trapped particles is similar to the linear growth rate, so that the fast depletion of wave energy by the trapped particles suppresses further wave growth [148]. The bounce frequency scales approximately as  $\delta B^{1/2}$ ; mode saturation thus occurs when the field amplitude is sufficiently

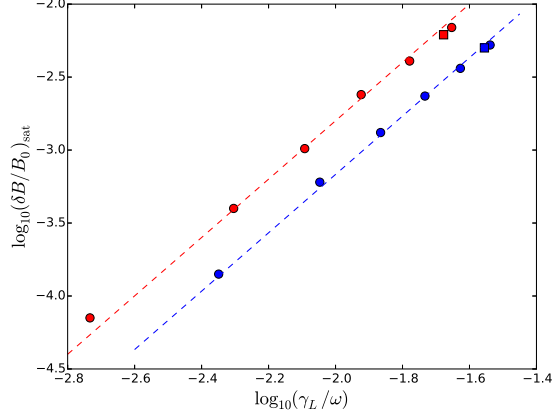


**Figure 4.12:**  $\log_{10}(\delta B/B_0)_{\text{sat}}$  versus  $\log_{10}(\gamma_L/\omega)$ , with the isotropic case in red and the anisotropic case in blue. The square markers show the data points for the MAST #29221 parameters, and the dashed lines show least squares fits to a linear function with slope 2.

large such that  $\omega_b \sim \gamma_L$ , giving  $\delta B_{\text{sat}} \propto \gamma_L^2$ . Although  $\gamma_L$  is larger in the anisotropic case, we find that the wave amplitude in the initial stage of saturation is 18% smaller in the anisotropic case ( $\delta B/B_0 = 4.9 \times 10^{-3}$ ) than in the isotropic case ( $\delta B/B_0 = 6.0 \times 10^{-3}$ ). To help explain this result we show in Fig.4.12 a graph of  $\log_{10}(\delta B/B_0)_{\text{sat}}$  versus  $\log_{10}(\gamma_L/\omega)$ , with the data points corresponding to the linear growth rates in Fig.4.11. Both the isotropic and anisotropic cases are well fitted by the scaling  $\delta B/B_0 = D(\gamma_L/\omega)^2$ , with  $D$  a numerical constant of proportionality. We find in the isotropic case that  $D = 15.8$ , while in the anisotropic case  $D = 6.8$ . The smaller value of the constant  $D$  in the anisotropic case results in a smaller saturation amplitude, despite its larger growth rate. A possible explanation for the significant difference between the proportionality constants is that the bounce frequency is dependent on the equilibrium and mode structure. An analytical estimate of the saturation amplitude for a single poloidal harmonic of a TAE in a tokamak with circular flux surfaces gives a bounce frequency that depends on both the safety factor and magnetic shear (among other quantities) [149]. The safety factor and magnetic shear are significantly different between the isotropic and anisotropic cases (see Fig.4.5), which may substantially account for the difference between the proportionality constants.

## 4.4 Conclusion

We have analysed equilibrium and stability for MAST discharge #29221 with the assumptions of both isotropic and anisotropic pressure. We find that quantities calculated under these two assumptions can be significantly different. The safety factor profile is qualitatively different between the two cases: in the isotropic case it is reversed shear, while in the anisotropic case it is normal shear. This difference leads to the TAE gap of the isotropic equilibrium being much narrower than that of the anisotropic equilibrium. The anisotropic  $n = 1$  TAE is found to have a larger radial width and slightly higher frequency than the isotropic TAE.

We find a significant modification to the resonant regions of phase space between the isotropic and anisotropic cases, with the anisotropic  $l = 1$  resonance shifted radially inward for given particle energy relative to the isotropic case. We also find a 35% larger linear

growth rate in the anisotropic case compared to the isotropic case, while the anisotropic saturation amplitude is 18% smaller than the isotropic saturation amplitude. The linear growth rate for the anisotropic case is larger as the drift-orbit width is a closer match to the mode width, and the radial gradient of the distribution function at resonance is larger. Conversely, the saturation amplitude for the anisotropic case is slightly smaller despite the larger linear growth rate; this may be due to the differences in the safety factor and magnetic shear affecting the nonlinear bounce frequency. Further analysis, including studies of additional discharges and parameter scans of input quantities, will be needed to determine the likely and potential impact of pressure anisotropy on equilibrium and stability.

In these calculations we have neglected wave damping from the background plasma, as well as the effect of collisions on the fast ion distribution. Inclusion of these effects can modify the saturation amplitude and lead to various frequency sweeping behaviours depending on the relative magnitudes of the different collision terms [150]. The frequency sweeping and the mode turn-off occurring 2 ms after onset, observed in the spectrogram in Fig.4.2, indicate that these effects are important in this MAST discharge. The impact of anisotropy on the frequency sweeping behaviour and saturation amplitude when damping and collisions are taken into account will be assessed in future work.

---

# Fluid theory of the reactive EGAMs: local treatment

---

## Abstract

An unstable branch of energetic geodesic acoustic mode (EGAM) is found using the fluid theory with fast ions characterised by their narrow width in energy distribution and collective transit along field lines. This mode, with a frequency much lower than the thermal GAM frequency  $\omega_{\text{GAM}}$ , is now confirmed as a new type of unstable EGAM : a reactive instability similar to the two-stream instability. The mode can have very small fast ion density threshold when the fast ion transit frequency is smaller than  $\omega_{\text{GAM}}$ , consistent with the on-set of the mode right after the turn-on of the beam in DIII-D experiments. The transition of this reactive EGAM to the velocity gradient driven EGAM is also discussed.

Note: Detail derivations are given in Appendix A.

## 5.1 Introduction

Recent experiments [45, 151, 152] with neutral beam injection show bursting  $n = 0$  axisymmetric modes at half of the thermal geodesic acoustic mode (GAM) [62, 73] frequency, which are identified as the energetic-particle-induced GAMs (EGAMs). The presence of EGAMs are found responsible for fast ion losses [153] and may enhance turbulence transport, leading to the destruction of internal transport barriers [66] and the degradation of fusion confinement. Many efforts have been made to model [46, 154, 155, 156, 157] and simulate [158, 159, 160, 161] EGAMs both linearly and nonlinearly using a kinetic or hybrid-kinetic theory. One of the major outcomes is the discovery of multiple branches of GAMs in the presence of fast particles. The lower frequency branch is excited by the inverse Landau damping provided by the fast ions. In tokamaks, most of these works assume a fast ion distribution with a large width in energy (e.g. the slowing down distribution function). However, the magnetic spectrogram in DIII-D experiments [45] showed a turn-on of the mode  $1\text{ms}$  right after the beam switched on, much faster than the beam slowing down time ( $\sim$  tens of  $\text{ms}$ ), indicating that the beam ions are not slowed down when the mode first appears. Also, due to the limited width in energy distribution, the beam may not provide sufficient inverse Landau damping to enable the growth of the mode. One possible explanation is proposed by Berk *et al* [154], in which the early EGAMs are negative energy modes, the presence of whom will reduce the total energy of the system. They are driven unstable by fast ion Landau damping.

Due to its simplicity and intuitive nature, the fluid theory, if its regime of validity is properly considered, may shed light on the underlying physics which may otherwise be confused with wave-particle interaction physics. By using a fluid description of the fast ions, we have found a new class of unstable EGAMs associated with beam ions. These EGAMs are similar to the two stream instabilities rather than driven by the inverse Landau damping. They have a high growth rate ( $\sim 30\%$  mode frequency) which increases steeply as fast ion density increases, consistent with the early turn-on of the mode.

## 5.2 Model

We consider a tokamak plasma with large aspect ratio, circular cross section and low  $\beta$ . The flux surfaces are concentric and labeled by radial coordinate  $r$ , while  $\theta$  and  $\varphi$  give the poloidal and toroidal angle, respectively. In this work, we adopt a local treatment, making  $\rho_s < q\rho_s \ll L_{\text{EGAM}}$  where  $L_{\text{EGAM}}$  is the width of the mode,  $\rho_s$  the Larmor radius and  $q\rho_s$  gives approximately the drift orbit width. The change of equilibrium quantities in radial direction is ignored. We assume that the plasma consists of thermal and fast ions, all with mass  $m_i$  and unity charge  $e$ , as well as electrons with negligible inertia and negative charge  $-e$ . Thermal ions have density  $n_i$  and temperature  $T_i$ , while for fast ions, the density  $n_f$ , the parallel pressure  $p_{\parallel f}$  and the perpendicular pressure  $p_{\perp f}$  are obtained by integrals of the fast ion guiding center distribution. The thermal ions are static with  $V_i = 0$ . The fast ions have an average transit speed  $V_f$  along the field lines.

The dynamics of the system is determined by the linearized momentum equation of each species “s”, given by

$$m_s n_s \left( \frac{\partial \tilde{\mathbf{V}}_s}{\partial t} + \frac{\tilde{n}_s}{n_s} \mathbf{V}_s \cdot \nabla \mathbf{V}_s + \mathbf{V}_s \cdot \nabla \tilde{\mathbf{V}}_s + \tilde{\mathbf{V}}_s \cdot \nabla \mathbf{V}_s \right) = n_s q_s (-\nabla \tilde{\Phi} + \tilde{\mathbf{V}}_s \times \mathbf{B}) - \nabla \cdot \tilde{\mathbf{P}}, \quad (5.1)$$

in which  $q_s$  is the charge,  $\tilde{\Phi}$  the perturbed electrostatic potential,  $\tilde{\mathbf{P}} = \tilde{p}_{\perp} \bar{\mathbf{I}} + (\tilde{p}_{\parallel} - \tilde{p}_{\perp}) \mathbf{b}\mathbf{b}$  the perturbed pressure tensor, with  $\mathbf{b} = \mathbf{B}/B$  and  $\mathbf{B}$  the magnetic field. The subscript “s” labels electrons (e), thermal ions (i) or fast ions (f) and the circumflex labels the perturbed quantities. The perturbed velocity consists of the perpendicular and parallel components, written as

$$\tilde{\mathbf{V}}_s = \tilde{\mathbf{V}}_E + [\tilde{V}_{s+}(r)e^{i\theta} + \tilde{V}_{s-}(r)e^{-i\theta}] \mathbf{b}, \quad (5.2)$$

where  $\tilde{\mathbf{V}}_E$  is the  $\mathbf{E} \times \mathbf{B}$  drift velocity. Considering the small orbit width assumption, we only retain the  $m = 0$  component of  $\tilde{\Phi}$  for the  $\mathbf{E} \times \mathbf{B}$  drift and  $m = \pm 1$  components of parallel velocity that are lowest order in  $q\rho_s$ , while the magnetic gradient/curvature drifts are higher order terms and therefore ignored. Now  $\tilde{\mathbf{V}}_E$  is in the direction of  $\boldsymbol{\pi} = \mathbf{e}_r \times \mathbf{b}$ . Similarly, the perturbed density and pressure are decomposed into  $m = \pm 1$  harmonics, for instance,  $\tilde{n}_i = \tilde{n}_{i+1}e^{i\theta} + \tilde{n}_{i-1}e^{-i\theta}$ .

The ion response to  $\tilde{\mathbf{V}}_E$  is described by the Chew-Goldberger-Low (CGL) law [15], assuming that the ion perpendicular and parallel pressure are doing work independently. An agreement is reached between the CGL and the gyrokinetic theory on the thermal GAM frequency [74, 75]. It has also been shown that when the mode frequency is much higher than the thermal frequency of the bulk ions (in conventional GAM,  $q \gg 1$ ) the CGL law can give a good description of the plasma response [23, 24]. This CGL law is

given by

$$\frac{d\tilde{p}_{\parallel s}}{dt} = -p_{\parallel s} \nabla \cdot \tilde{\mathbf{V}}_s - 2p_{\parallel s} \mathbf{b} \cdot (\mathbf{b} \cdot \nabla \tilde{\mathbf{V}}_s), \quad (5.3)$$

$$\frac{d\tilde{p}_{\perp s}}{dt} = -2p_{\perp s} \nabla \cdot \tilde{\mathbf{V}}_s + p_{\perp s} \mathbf{b} \cdot (\mathbf{b} \cdot \nabla \tilde{\mathbf{V}}_s). \quad (5.4)$$

The response of electrons is assumed to be isothermal, which means

$$\tilde{p}_e = \tilde{n}_e T_e = (\tilde{n}_i + \tilde{n}_f) T_e, \quad (5.5)$$

from the quasi-neutrality condition, while  $\tilde{n}_i$  and  $\tilde{n}_f$  are obtained from the ion continuity equation given by

$$\frac{\partial \tilde{n}_s}{\partial t} = -\nabla \cdot (n_s \tilde{\mathbf{V}}_s + \tilde{n}_s \mathbf{V}_s). \quad (5.6)$$

We can simplify Eq. (5.3), (5.4) and (5.6) using the identity

$$\nabla \cdot \boldsymbol{\pi} \approx -\boldsymbol{\pi} \cdot \nabla \ln B \approx (\mathbf{b} \cdot \nabla \boldsymbol{\pi}) \cdot \mathbf{b} = -\kappa_g \approx -\sin \theta / R, \quad (5.7)$$

which are all considered as geodesic curvature, giving the relationship between the perturbed pressure and perturbed velocity. Recall that  $\boldsymbol{\pi} = \mathbf{e}_r \times \mathbf{b}$ . We substitute these relationships into Eq. (5.1) to eliminate the perturbed pressures.

Adding up Eq. (5.1) for electrons, thermal and fast ions, ignoring electron inertia, imposing the quasi-neutrality condition  $\nabla \cdot \tilde{\mathbf{J}} = 0$  ( $\tilde{\mathbf{J}}$  is the perturbed current) and taking a flux surface average, we obtain the perpendicular momentum equation. The parallel momentum equations for thermal and fast ions are obtained from the parallel component of Eq. (5.1), with the potential terms canceled using the same equation for electrons. These equations close the system and define the dispersion relationship  $D(\omega) = 0$ , where  $\omega$  is the mode complex angular frequency ( $\gamma = \text{Im}(\omega)$  gives the growth rate). In the  $q \gg 1$  limit where the coupling to the thermal ion sound wave is ignored,  $D(\omega)$  is given by

$$D(\omega) = 1 - (1 - \alpha) \frac{\omega_{\text{GAM}}^2}{\omega^2} - \alpha G(\omega), \quad (5.8)$$

where  $\omega_{\text{GAM}}^2 = \frac{2T_i}{m_i R^2} \left( \frac{7}{4} + \frac{T_e}{T_i} + O\left(\frac{1}{q^2}\right) \right)$  is the square of the thermal GAM frequency and  $\alpha \equiv \langle n_f \rangle / n_{\text{total}}$  is the fast population fraction. The exact form of  $G(\omega)$  depends on the fast ion distribution function, but since the fluid theory has ignored Landau Damping effects,  $G(\omega)$  is real if  $\text{Im}(\omega) = 0$ .

We first consider a bump-on-tail distribution function given by

$$F(v_{\parallel}, v_{\perp}) = n_f A \exp \left[ -\frac{m(v_{\parallel} - V_f)^2 + m v_{\perp}^2}{2T_f} \right], \quad (5.9)$$

where  $A$  is a normalization factor,  $v_{\parallel}$  and  $v_{\perp}$  are parallel and perpendicular velocity, respectively. For small  $\alpha$  and negligible energy width  $T_f$ ,  $G(\omega)$  is given by

$$G(\omega) \approx \frac{\frac{3}{2} \omega_b^2 q^2}{\omega^2 - \omega_b^2} + \frac{\omega_b^4 q^2}{(\omega^2 - \omega_b^2)^2}, \quad (5.10)$$

where  $\omega_b \equiv V_f / qR$  is the average fast ion transit frequency. The dispersion relationship now becomes a cubic equation of  $\omega^2$  with three solutions. Properties of the solutions



are determined by the relationship between  $\omega_{\text{GAM}}$  and  $\omega_b$ , as well as  $q$  and the fast ion population.

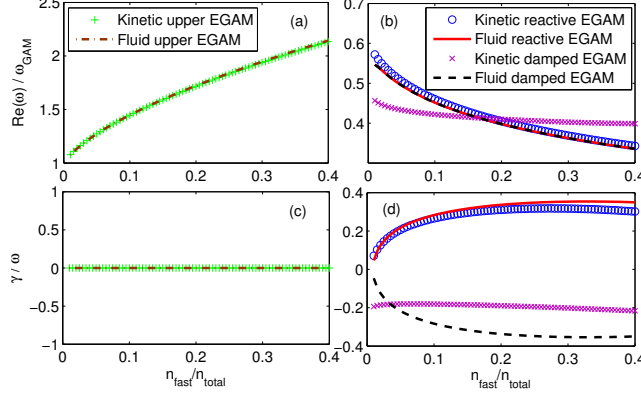


**Figure 5.1:** Real frequency (a)(b) and growth rate (c)(d) versus fast ion density for multi-fluid model with comparison to kinetic theory, for  $q = 4$  and  $\omega_b = 0.58\omega_{\text{GAM}}$ . Lines/symbols: fluid/kinetic results.

In Fig.5.1, we plot the solutions to  $\omega$  with parameters  $q = 4$  and  $\omega_b = 0.58\omega_{\text{GAM}}$ , retaining finite energy width  $T_f = 0.25T_i$ , for fast particle concentration from 1% to 40%. Similar to Fu *et al*, multiple branches of GAMs are present. The frequency of the upper (frequency) EGAM, as seen in Fig.5.1 (a), increases with increasing fast particle population. This branch reduces to the thermal GAM when  $n_f = 0$ . We compare our fluid result to the numerical solution of the kinetic dispersion relationship [161, 162], showing very good agreement. In this case, the Landau damping from the thermal particles is negligibly small. Also, two complex conjugated branches are present in Fig.5.1 (b) and (d) at lower frequency, both having decreasing frequency with higher fast ion fraction. We note that the existence of these branches is due to the Doppler shift of the wave in the static frame of the fast ions, since this is the only effect of the fast ion when  $T_f$  is small. One of these modes is found unstable in kinetic theory, and is previously attributed to the inverse Landau damping. However, the same growth rate is also obtained using the fluid model. Given that no Landau damping is present in the fluid theory, this instability cannot come from the wave-particle interaction, but must be a reactive instability. We name this unstable branch the reactive EGAM from its nature of instability. By solving the dispersion relationship Eq. (5.8) and (5.10), we obtain the growth rate for  $\alpha \ll 1$ , given by

$$\gamma \approx \frac{1}{2}q\omega_b^2(\omega_{\text{GAM}}^2 - \omega_b^2)^{-\frac{1}{2}}\sqrt{\alpha}, \quad (5.11)$$

with no fast ion density threshold. Finally, we find that the fluid theory is valid for the upper EGAM and the reactive EGAM, which are on the real axis or the upper plane, while the other damped EGAM is located on the lower plane and is strongly modified by Landau damping, leading to the deviation of its fluid solution from the kinetic theory.

For the regime  $\omega_b > \omega_{\text{GAM}}$ , the upper EGAM will start at  $\omega_b$  instead of the thermal GAM frequency, as shown in Fig.5.2 (a) with parameters  $T_f = T_i$ ,  $q = 2$  and  $\omega_b = 1.76\omega_{\text{GAM}}$ . The kinetic theory gives a finite Landau damping rate, while in the fluid theory, this mode is predicted to be stable. One of the lower modes starts at  $\omega_{\text{GAM}}$  when  $n_f = 0$ . Unlike Fig.5.1, the lower modes have an instability threshold of  $\alpha > 0.05$ . In Fig.5.2 (b) and (d), the unstable reactive EGAM and a damped EGAM occur between

$0.05 < \alpha < 0.25$  when the two modes have the same real frequency. This real frequency bifurcates at  $\alpha = 0.25$ , with the modes becoming stable at the same time. A parameter scan shows that the two bifurcation points move closer to each other when  $\omega_b$  increases. For  $\omega_b > 2\omega_{\text{GAM}}$ , the two bifurcation points merge and no unstable mode is present for  $0 < \alpha < 0.4$ . Again, Fig.5.2 shows a good match to the kinetic theory.

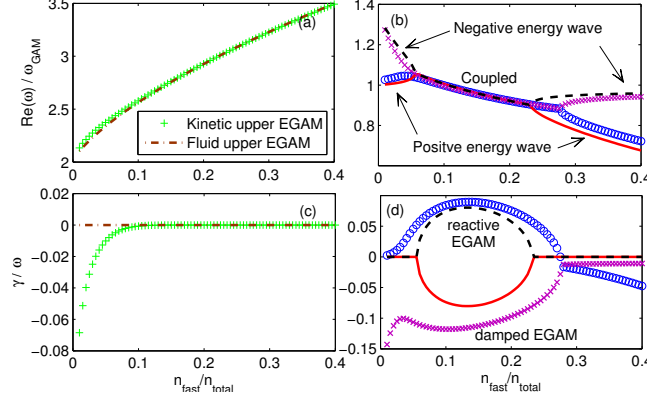


**Figure 5.2:** Real frequency (a)(b) and growth rate (c)(d) versus fast ion density for multi-fluid model with comparison to kinetic theory, for  $q = 2$  and  $\omega_b = 1.76\omega_{\text{GAM}}$ . Lines/symbols: fluid/kinetic results.

### 5.3 Discussion and application to DIII-D

The origin of the instability can be studied by calculating the wave energy of the two lower frequency modes. In Fig.5.2 (b) when  $\alpha > 0.25$ , the lower frequency mode is a positive energy wave ( $dD(\omega)/d\omega > 0$ ) while the other is a negative energy one ( $dD(\omega)/d\omega < 0$ ). The strong coupling of these two modes is achieved when they possess the same real frequency ( $0.05 < \alpha < 0.25$ ), where the reactive EGAM occurs. The energy can transfer from the negative energy wave to the positive energy wave, enabling the growth of both modes meanwhile conserving the total energy [163]. Therefore, this GAM instability shares great similarities to the two-stream instabilities in a beam plasma system [164, 165], which can also be captured by a fluid model.

We now study the relationship between the reactive EGAMs and the inverse Landau damping driven EGAMs (dissipative EGAMs). The unstable EGAM frequency and growth rate versus the fast particle energy width  $T_f$  is plotted in Fig.5.3 for the bump on tail distribution. The parameters are identical to Fig.5.1. Figure 5.3 shows that the unstable EGAMs are reactive for  $T_f/T_i < 1$  where the fluid theory is valid, and dissipative for large  $T_f$  where the kinetic effects are dominant and the fluid treatment breaks down. A smooth transition is found in between these two regimes by solving the kinetic dispersion relationship [161, 162]. The conditions required for finding a reactive EGAM is given by

$$|\omega - \omega_b| > \frac{1}{qR} \left( \frac{2T_f}{m} \right)^{\frac{1}{2}}. \quad (5.12)$$

One can use Eq. (5.11) and  $|\omega - \omega_b| \approx \gamma$  for an estimation if  $\omega_{\text{GAM}} > \omega_b$ . Further study shows that the smooth transition behavior is distribution shape independent.

Again, we have found great similarity between the EGAMs and the two-stream in-

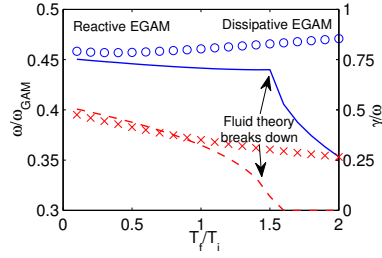


**Figure 5.3:** Real frequency in fluid (blue solid line) and kinetic (blue circle) theory, and growth rate in fluid (red broken line) and kinetic (red cross) theory versus fast particle energy width  $T_f$ , for  $n_f/n_{\text{total}} = 0.1$ ,  $q = 4$  and  $\omega_b = 0.58\omega_{\text{GAM}}$ .

stabilities. It's well known that in a beam plasma system, for a single energy beam, the purely reactive two-stream instability occurs. On the other hand, if the bump slope is gentle, i.e. the beam is warm, the dissipative bump-on-tail instability occurs. With a finite but small beam energy width, the kinetic effects influence the reactive instability by breaking the complex conjugacy of the two fluid modes [166]. A change in the topology of the dispersion relationship is found as the beam thermal spread further increases, after which the dissipative drive become dominant [167]. These statements are also applicable to EGAMs.

Finally, we apply our results to the early turn-on of EGAMs in DIII-D by considering a single energy single pitch beam distribution function, before the slowing down or pitch angle scattering can happen. This distribution function is given by

$$F(E, \Lambda) = \frac{m^2 |v_{||0}| n_f}{2\pi E} \delta(E - E_0) \delta(\Lambda - \Lambda_0), \quad (5.13)$$

where  $E$  is the fast ion energy,  $\Lambda$  the pitch angle and  $\delta(x)$  the Dirac delta function. We note that in reality, the ionized beam will have a finite pitch angle spread and a first orbit loss for counter-injection. Additional studies show that as long as the width of the pitch angle distribution  $\Delta\Lambda \ll \Lambda$  the pitch angle itself, our fluid theory will remain valid. The inclusion of  $\Delta\Lambda$  will not change the result significantly as compared to the one assuming a single pitch angle. The form of  $G(\omega)$  is identical to Eq. (5.10) except the numerators now become a function of both  $E_0$  and  $\Lambda_0$ . For the DIII-D beam in Nazikian *et al* [45], we have  $E_0 = 75\text{keV}$  and  $\Lambda_0 = 0.5$ . We also have  $\omega_b = 0.88\omega_{\text{GAM}}$  obtained from  $T_e = 1.2T_i \approx 1.2\text{keV}$  and  $q = 4$  at the radial localized flux surface  $s = 0.4$ . Similarly we plot the real frequency and growth rate of the reactive EGAM as a function of  $\alpha$  in Fig.5.4 (the other two branches are damped and not discussed here). The frequency of the reactive EGAM stays reasonably close to the observed frequency (28kHz) for  $\alpha > 3\%$ . Also, no density threshold is present in the fluid theory, although in reality the background damping (such as collisional damping) may create a finite threshold. But since the growth rate is large and is a steep function of the fast ion density when the density is low ( $\sim \sqrt{\alpha}$ ), this background damping can be overcome quickly as fast ion density increases, consistent with the early turn-on of the mode. Furthermore, the smooth transition between reactive and dissipative EGAMs indicates the natural conversion from the early turn-on reactive EGAMs to the dissipative EGAMs, when the fast ions are slowed down in background plasma. Slowing down of the fast ions due to the nonlinear phase of the reactive EGAMs is also possible and requires further investigation.

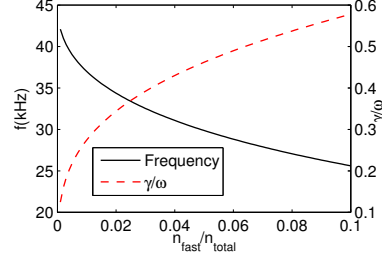


**Figure 5.4:** Real frequency and growth rate of the reactive EGAM using DIII-D parameters on flux surface  $s = 0.4$ .

In summary, we have found a new unstable branch of EGAMs in the presence of beam ions with a small width in energy distribution, known as a reactive instability similar to the two-stream instability. This mode can have a much lower frequency than the thermal GAMs and  $\gamma/\omega$  up to 30% with no turn-on threshold when background damping is not considered. Our work shows that EGAM solutions are not inherent to kinetic approaches and one should not overlook the reactive contribution to the instabilities. A smooth transition from reactive EGAMs to kinetic instabilities happens after the beam ions are slowed down, similar to the transition between the two-stream and bump-on-tail instabilities. We have also demonstrated the consistency of reactive EGAMs with the early turn-on of EGAMs in DIII-D experiments, a scenario that cannot be explained by the previous theories of inverse Landau damping driven EGAMs. In addition, this work gives a good example of how the fluid theory can aid the understanding of fast particle physics. Further discussion about the radial mode structure will be presented in future publications.



---

# Fluid theory of the reactive EGAMs: global treatment

---

## Abstract

In this paper we have developed a fluid model to study the radial mode structure of the reactive energetic geodesic acoustic modes (reactive EGAMs), a branch of GAM that becomes unstable in the presence of a cold fast ion beam. We have solved the resulting dispersion relationship, a second order ODE, both analytically in restricted cases and numerically in general. It is found that the reactive EGAM global mode structure is formed with the inclusion of fast ion finite drift orbit effects. In two cases with typical DIII-D parameters but different  $q$  profiles, the global EGAM frequency is slightly higher than the local EGAM extremum, located either on axis with a monotonic shear or at mid-radius with a reversed shear. The mode wavelength roughly scales with  $L_{\text{orbit}}^{1/2}$  in the core and  $L_{\text{orbit}}$  at the edge, though the dependency is more complicated for the reversed shear case when  $L_{\text{orbit}} < 0.06a$  ( $L_{\text{orbit}}$  is the fast ion drift orbit width and  $a$  the minor radius). Finally, the growth rate of the global mode is boosted by 50% to 100% when switching from co-beam to counter-beam, depending on the fast ion density, which may help to explain the more frequent occurrence of EGAMs with counter-injection in experiments.

## 6.1 Introduction

The energetic-particle-induced geodesic acoustic modes (EGAMs) are  $n = 0$  coherent fluctuations in toroidal magnetic confined plasmas. They were first observed in DIII-D experiments [45] and later in other machines [151, 152]. Their frequencies appear at half of the conventional geodesic acoustic mode (GAM) [62] frequency of the thermal plasma and the beam transit frequency. The EGAMs have caught the interest of the fusion community because they demonstrate a drop of neutron rate during the mode activities that clearly indicates a loss of fast ions [153]. This loss should be minimized in order to achieve a better energy confinement. A suppression of turbulence transport was also observed in accordance with excited EGAMs in a gyrokinetic simulation [66].

The first theory of EGAMs was developed by Fu [46], identifying EGAMs as energetic particle modes (EPMs) whose frequencies and mode structures are non-perturbatively determined by the energetic particles. They were believed to be driven unstable by the fast ions themselves through a positive energy gradient in the distribution function (inverse Landau damping). Follow up theory and simulation studies [155, 156, 157, 158, 159, 160,

161, 168] confirmed these findings when the fast ion distribution function was taken to be a slowing down distribution or a shifted-Maxwellian. It has also been found theoretically [169] and experimentally [170] that the primary unstable EGAM branch can excite a secondary (linearly) overstable EGAM branch, through a combination of fluid and wave-particle nonlinearity. More recently, a new branch of EGAM has been identified in the region where the fast ion magnetic drift frequency dominates the transit frequency [171].

Still, a puzzle remains regarding the turn-on of the mode in 1ms right after beam switch-on, a time scale much shorter than the beam collisional slowing down time, indicating an insufficient drive through the wave-particle interaction. This puzzle has been studied by Cao *et al* [172] and Berk and Zhou [154] separately, giving different explanations. However, it was recently found by Qu *et al* [173] from a fluid model that the unstable EGAMs could exist, even in the case with a mono-energy, mono-pitch-angle fast ion distribution function. In contrast to the former interpretation, reactive contributions, rather than kinetic (dissipative) contributions, dominate the instabilities. This is in strong analogy to the instabilities in a beam-plasma system, in which a cold beam leads to the reactive two-stream instabilities, while the kinetic bump-on-tail instabilities take place when the slope of the fast electron energy distribution function is gentle. Although based on a local theory where the fast ions do not move off the flux surfaces (zero drift orbit width and zero Larmor radius), the theory of reactive EGAMs has helped to solve the puzzle of early turn-on and provided insight to the nature of EGAMs from a fluid perspective.

Nevertheless, as observed experimentally [45], EGAMs are not localized. Rather, their radial wavelength is comparable to the minor radius of the machine. Also, the fast ions drift away from their initial flux surfaces due to the magnetic gradient and curvature drift, making the fast ion finite drift orbit width (FOW) effects important. The radial structure of the kinetically driven EGAMs in DIII-D experiments were reproduced by Fu [46] using hybrid simulations. Using the small expansion factor  $\delta = L_{\text{orbit}}/L_{\text{mode}}$ , where  $L_{\text{orbit}}$  is the fast ion drift orbit width and  $L_{\text{mode}}$  is a measurement of the radial wavelength, Fu has found analytically that the radial wavelength is related to the orbit width of the fast particles, as well as the fast ion density and the radial scale length of the thermal GAM frequency. A similar expansion was adapted by Qiu *et al* [155] in a fully kinetic theory, in which the radial EGAM mode structure was described by a WKB approximation and asymptotic matching, with the continuum damping of the thermal GAM taken into account. With the same expansion factor  $\delta$ , Zhou [174] studied the global EGAMs driven by either trapped and passing fast ions from a variational principle. All the above analysis were intended for EGAMs driven unstable by wave-particle interaction, while the mode structure of the reactive regime remains unexamined. The purpose of this work is to extend the fluid theory in Qu *et al* to resolve the radial mode structure of reactive EGAMs. In this work, we sometimes omit the word “reactive” for simplicity. The wording “EGAM” in this work refers to the reactive EGAM and should not be confused with the wave-particle driven EGAMs in previous works.

We will adapt the same small expansion parameter  $\delta = L_{\text{orbit}}/L_{\text{mode}}$ , where  $L_{\text{orbit}}$  and  $L_{\text{mode}}$  are defined by

$$L_{\text{orbit}} \sim q\rho_{\parallel}, \quad L_{\text{mode}} \sim \left| \frac{d \ln E_r}{dr} \right|^{-1}, \quad (6.1)$$

with  $q$  the safety factor,  $\rho_{\parallel} = m_i v_{\parallel}/eB$  the parallel Larmor radius,  $m_i$  the ion mass,  $e$  the unit charge,  $B$  the magnetic field strength,  $v_{\parallel}$  the parallel velocity and  $E_r$  the radial electric field. We have assumed that the fast ions and the thermal ions are of the

same type of singly charged ions, i.e. having the same mass  $m_i$  and charge  $e$ . Still, the difficulty of fluid closure remains, to truncate the fluid moment hierarchy at the level of pressure. For a local theory where FOW effects are ignored, the CGL theory [15] can give an accurate description of the fast ion response to the field in the high  $q$  limit [75, 156]. However, when FOW effects are not negligible, corrections are needed for the CGL double-adiabatic law (see for example [119]). Ignoring finite Larmor radius (FLR) effects and assuming gyro-orbit symmetry, the pressure tensor can still be written in a diagonal form  $\mathbf{P} = p_\perp(\mathbf{I} - \mathbf{b}\mathbf{b}) + p_\parallel\mathbf{b}\mathbf{b}$ , with  $p_\perp$  the perpendicular pressure,  $p_\parallel$  the parallel pressure,  $\mathbf{I}$  the unit dyad, and  $\mathbf{b}$  the unit vector in the direction of the magnetic field. Due to the smallness of the energy in the drift velocities compared to the energy of the gyro motion ( $O(\epsilon^2\delta^2)$ ), the value of  $p_\perp$  can still be approximated by the moment of  $\mu B$ , where the magnetic moment  $\mu$  is given by  $\mu = mv_\perp^2/2B$  and is a conserved quantity in the absence of FLR effects. The difficulty of fluid closure is avoided in our current work by limiting the fast ions to have a mono-energy, mono-pitch-angle distribution function, with which the effective parallel pressure is zero and the perpendicular pressure perturbation is linked to the density perturbation due to the conservation of  $\mu$ .

In this work, there are three small unitless parameters: the fast particle orbit width over mode width  $\delta$ , the inverse aspect ratio  $\epsilon$  and amplitude of perturbation. All quantities will be equilibrium quantities unless denoted with tilde. Additionally, we consider three species: fast ions, thermal ions and thermal electrons. All quantities will refer to the fast species unless denoted with "e" or "i". Our approach to the problem and structure of work is as follows. Section 6.2 describes the simplified geometry of the problem: a large aspect ratio, low beta tokamak with concentric flux surfaces. A consistent treatment of the equilibrium fast ion density profile with FOW effects included is also given. In Section 6.3, we derive the linear fluid theory of reactive EGAMs. We will start with the local theory, reproducing the dispersion relationship in Qu *et al.*. In new work, we keep higher order terms in  $\delta$ , giving the global dispersion relationship. This dispersion relationship is studied in Section 6.4, with qualitative analytic discussions and numerical solutions. Dependency of the results on different  $q$  profiles is examined. A numerical scan on the relationship between  $L_{\text{mode}}$  and the drift orbit width is also performed. In addition, we have found the distinction in mode frequency and growth rate between the counter/co-injection due to the fact that drift orbits of counter(co)-passing ions shift inward (outward) with respect to the flux surfaces, an element omitted in our previous work. The dependency of growth rate with different injection directions agrees with experimental observations. Finally, Section 6.5 draws the conclusion, and proposes other validation and verification studies.

## 6.2 Equilibrium

### 6.2.1 Geometry

In order to obtain a self-consistent tokamak equilibrium with fast ions, we need to solve the anisotropy and flow modified Grad-Shafranov equation [92, 83, 101] for the equilibrium profiles in radial direction to obtain the poloidal flux function  $\Psi(R, Z)$ . However in this work, we will ignore the influence of the plasma current and pressure on geometry, except for the existence of a poloidal field. We start with a tokamak plasma with large aspect ratio, circular cross section and low  $\beta$ . Large aspect ratio means  $\epsilon \equiv a/R_0 \ll 1$ , in which  $R_0$  is the major radius on axis and  $a$  the minor radius. We can now use a simplified set of coordinate  $(r, \theta, \varphi)$ , labeling the radial coordinate, the poloidal and toroidal angle,



respectively. The outward shift of the flux surfaces, namely the Shafranov shift, is ignored in our treatment. The local major radius and the magnetic field strength are approximately given by  $R \approx R_0[1 + (r/R_0) \cos \theta]$  and  $B \approx B_0[1 - (r/R_0) \cos \theta]$ . Symmetry in equilibrium is assumed for  $\varphi$  direction in a tokamak plasma. For convenience, we define the bi-normal unit vector  $\hat{\pi} \equiv \hat{\mathbf{b}} \times \hat{\mathbf{e}}_r$ . So we now have another set of orthogonal unit vector triad  $(\hat{\mathbf{e}}_r, \hat{\pi}, \hat{\mathbf{b}})$ . We also have the identity

$$\nabla \cdot \hat{\pi} \approx -\hat{\pi} \cdot \nabla \ln B \approx (\hat{\mathbf{b}} \cdot \nabla \hat{\pi}) \cdot \hat{\mathbf{b}} = -\kappa_g \approx -\sin \theta / R_0, \quad (6.2)$$

which are all considered as geodesic curvature.

### 6.2.2 Fast ion density profile with finite orbit width

The fast particle unperturbed guiding centre drift orbits in a tokamak plasma have three constants of motion: the magnetic moment  $\mu$ , the energy  $E$ , and the toroidal canonical momentum  $P_\varphi = -e\Psi + mv_\parallel R$ . That is to say, the equilibrium fast ion distribution function can be written as a function of these three quantities only, i.e.  $F_0 = F_0(E, \mu, P_\varphi, \sigma)$ , where  $\sigma$  denotes the type of particle orbit (co/counter passing, trapped). In a toroidal geometry,  $B$  is not a constant on flux surfaces. The conservation of  $\mu$  will lead to a different perpendicular energy  $\mu B$  at different poloidal angle, and thus inhomogeneous fast ion density and pressure on a flux surface, if the distribution of the fast ions is not an unshifted Maxwellian. Moreover, the deviation of constant  $P_\varphi$  surfaces from constant  $\Psi$  surfaces will contribute to this inhomogeneity, since on a constant  $\Psi$  surface, the density at different poloidal angle corresponds to the distribution function at different  $P_\varphi$ . The contributions from both effects should be taken into account.

The fast ion distribution function is given by

$$F_f = \frac{m_i^{1/2} \sqrt{E - \mu B_0}}{\sqrt{2\pi} E} n_f(P_\varphi) \delta(E - E_0) \delta(\Lambda - \Lambda_0), \quad (6.3)$$

where  $\Lambda \equiv \mu B_0 / E$  is the pitch angle and  $\delta(x)$  the Dirac delta function. All the fast ions now have the same energy  $E_0$  and pitch angle  $\Lambda_0$ , consistent with the early beam injection scenario, while the fast ion density at different radial location is described by  $n_f$ . Equation (6.3) implies that the parallel pressure  $p_{\parallel f} = 0$  and the perpendicular pressure  $p_{\perp f} = n_f E_0 \Lambda_0 + O(\epsilon)$ .

We now write the fast ion fluid's equilibrium velocity as

$$\mathbf{V}_f = V_{f\parallel} \hat{\mathbf{b}} + \mathbf{V}_{f,\text{mag}} + \mathbf{V}_{f,\text{dia}}, \quad (6.4)$$

with  $V_{f\parallel}$ ,  $\mathbf{V}_{f,\text{mag}}$  and  $\mathbf{V}_{f,\text{dia}}$  accounting for the collective transit motion of the fast ions, the magnetic gradient/curvature drift, and the diamagnetic drift, respectively.

Using the ordering in  $\delta$ , we solve the continuity equation and the momentum equation order by order. We can write the fast ion density  $n_f$  into  $n_f = n_{f,\delta^0} + n_{f,\delta} + \dots$  with increasing order in  $\delta$ . Taking the zeroth order in  $\delta$ , the equilibrium continuity equation for the fast ions is written as

$$\nabla \cdot (n_{f,\delta^0} V_{f\parallel} \hat{\mathbf{b}}) = 0. \quad (6.5)$$

Equation (6.5) leads to the well known condition of poloidal flow that  $n_{f,\delta^0} V_f / B$  being a constant on a flux surface. Similarly, we have the lowest order fast ion momentum

equation given by

$$\nabla \cdot [p_{\perp f, \delta^0} \mathbf{1} + (m_f n_{f, \delta^0} V_{f\parallel}^2 - p_{\perp f, \delta^0}) \hat{\mathbf{b}} \hat{\mathbf{b}}] = e n_{f, \delta^0} [\mathbf{V}_{f, \text{mag}} + \mathbf{V}_{f, \text{dia}}] \times \mathbf{B}, \quad (6.6)$$

where  $\kappa = \hat{\mathbf{b}} \cdot \nabla \hat{\mathbf{b}}$  is the field line curvature. Combining Eq. (6.5) and the parallel direction of Eq. (6.6), we will reach that

$$B \left. \frac{\partial n_{f, \delta^0}}{\partial B} \right|_r = n_{f, \delta^0} \left( 1 + \frac{1}{2} \frac{\Lambda_0}{1 - \Lambda_0} \right) = n_{f, \delta^0} (1 + c_f), \quad (6.7)$$

showing the change of density on a flux surface due to  $\mu$  being an orbit invariant and the distribution function being non-Maxwellian. Note that as  $\Lambda_0$  approaches 1, the fast ions approach the limit of trapped particles, in which the fast ion density becomes discontinuous on a flux surface since the ions can't reach the high field side in the magnetic mirror. In such cases, Eq. (6.7) diverges and becomes invalid for these trapped particles. In this work, we will focus on the passing fast ions in reactive EGAMs and will not pursue an improved description for the trapped particles. The perpendicular direction of Eq. (6.6) is used to determine  $V_{f, d}$ , giving that

$$\mathbf{V}_{f, \text{mag}} = - \frac{m V_{f\parallel}^2 + p_{\perp f, \delta^0} / n_{f, \delta^0}}{e B_0 R_0} \left( -R_0 \hat{\mathbf{b}} \times \kappa \right) \approx \bar{V}_{f, \text{mag}} (\hat{\mathbf{e}}_r \sin \theta + \mathbf{e}_\theta \cos \theta) + O(\epsilon^2 \delta), \quad (6.8)$$

where  $\kappa = \hat{\mathbf{b}} \cdot \nabla \hat{\mathbf{b}}$  is the field line curvature. We have used the vacuum field assumption  $\nabla \times \mathbf{B} = 0$ . Taking a flux surface average, the numerator of  $\bar{V}_{f, \text{mag}}$  is approximated by  $(2 - \Lambda_0) E_0$ . Therefore, we reach  $\bar{V}_{f, \text{mag}} / V_{f\parallel} \sim O(\epsilon \delta)$ .

It is more convenient to write  $n_{f, \delta^l} = \bar{n}_{f, \delta^l}(r) (\cos \theta)^l + O(\epsilon \delta^l)$  and thus we have the continuity equation  $\nabla \cdot (n_f \mathbf{V}_f) = 0$  recast into the hierarchy given by

$$\bar{n}_{f, \delta^{l+1}} = \frac{1}{l+1} \frac{q R_0 \bar{V}_{f, \text{mag}}}{V_{f\parallel}} \left( \frac{d}{dr} - \frac{l}{r} \right) \bar{n}_{f, \delta^l} + O(\epsilon \delta^{l+1}), \quad (6.9)$$

showing that  $\bar{n}_{f, \delta^{l+1}} / \bar{n}_{f, \delta^l} \sim O(\delta)$ . Finally, adding the contribution for all the orders of  $\delta$ , we will have the equilibrium density profile with the FOW effects. It will be more verbose to find the  $O(\epsilon \delta^l)$  terms which are later used in our global theory. The details of these terms are given in Appendix 6.6. We note that the inclusion of the diamagnetic current will not contribute to the continuity equation and thereby will not change the fast ion density profile, since the divergence of curl is zero naturally given the form of  $\mathbf{J}_{\text{dia}} = -\nabla \times p_{\perp} \hat{\mathbf{b}} / B$ .

The corresponding solution of the equilibrium profile is justified by comparing to the fast ion guiding centre drift orbits, as shown in Fig.6.1, indicating a very good match between the constant density surface and the orbits as expected. The difference in the sign of  $V_{f\parallel}$  ( $V_{f\parallel} > 0$  for co-passing and  $V_{f\parallel} < 0$  for counter-passing) leads to a different sign in  $\bar{n}_{f, \delta}$ , the first Fourier harmonic of the fast ion density on a flux surface, and therefore a outward/inward shift of the co/counter-passing density contour. As we will show later in the paper, the different sign in  $\bar{n}_{f, \delta}$  results in a different growth rate for different direction of injection. The profiles we have used are  $\bar{n}_{f, 0} = n_0 \exp(-r^2/a^2)$  as the specified density profile and  $q = 3$  being a constant of radius, with  $R_0 = 1.7\text{m}$ ,  $\epsilon = 0.3$ ,  $B = 2\text{T}$ ,  $E_0 = 75\text{keV}$  and  $\Lambda_0 = 0.5$ , i.e. typical DIII-D beam parameters [45]. The density hierarchy is truncated at  $O(\delta^3)$  level. Note that in Fig.6.1 we have ignored the change of density in  $\theta$  direction

due to  $\mu$  being a constant of motion. We have also ignored the effect of particle loss at the boundary.

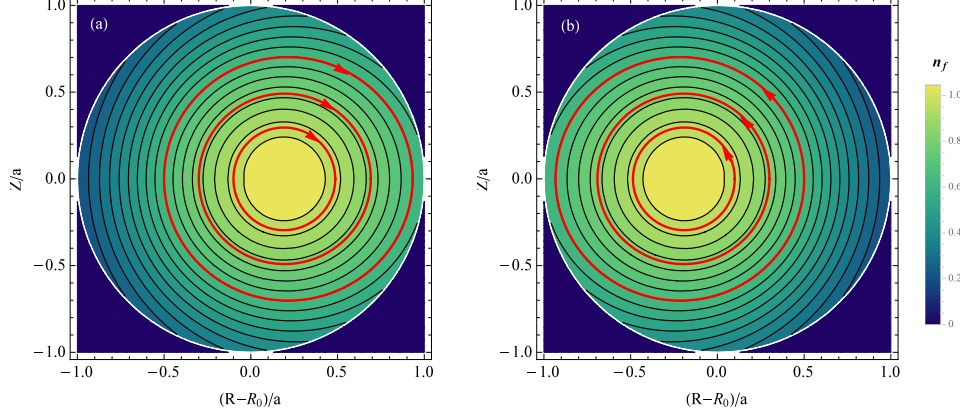


**Figure 6.1:** The equilibrium fast ion density  $n_f$  contour on the plasma cross section, normalized to the on axis value, for co-passing (a) and counter-passing (b) flow direction. The fast ion guiding centre drift orbits for  $E = 75 \text{ keV}$  and  $\Lambda = 0.5$  are overplotted in red lines, with particles released at  $r/a = 0.1, 0.3$  and  $0.5$  (inbound/outbound for co/counter-passing ions), from the most inner to the most outer orbit.

### 6.3 Linear perturbation treatment

The GAMs are electrostatic modes with toroidal mode number  $n = 0$ . We retain only the poloidal mode number  $m = 0$  part of the perturbed electrostatic potential and two sidebands with  $m = \pm 1$ , written as

$$\tilde{\Phi} = \tilde{\Phi}^{m=0}(r)e^{-i\omega t} + \tilde{\Phi}^{m=1}(r)e^{i\theta-i\omega t} + \tilde{\Phi}^{m=-1}(r)e^{-i\theta-i\omega t}, \quad (6.10)$$

in which  $\omega = \omega_r + i\gamma$  is the complex frequency and the tilde labels the perturbed quantities. The radial derivative of  $\tilde{\Phi}$  give rise to the  $\mathbf{E} \times \mathbf{B}$  drift velocity as

$$\tilde{\mathbf{V}}_E \approx \frac{\tilde{E}_r \hat{\mathbf{e}}_r \times \mathbf{B}}{B^2} \approx \frac{\partial_r \tilde{\Phi}^{m=0}}{B} e^{-i\omega t} \hat{\boldsymbol{\pi}} = \tilde{V}_E(r) e^{-i\omega t} \frac{B_0}{B} \hat{\boldsymbol{\pi}}, \quad (6.11)$$

where we have used  $\tilde{\Phi}^{m=0}/\tilde{\Phi}^{m=\pm 1} \gg 1$ , an assumption that we will justify later. The  $\mathbf{E} \times \mathbf{B}$  drift velocity is considered as the  $O(1)$  velocity on which our argument of order is based. The dynamics of the system is determined by the linearized momentum equation of each species “s”, given by

$$\begin{aligned} & m_s n_s \left( \frac{\partial \tilde{\mathbf{V}}_s}{\partial t} + \frac{\tilde{n}_s}{n_s} \mathbf{V}_s \cdot \nabla \mathbf{V}_s + \mathbf{V}_s \cdot \nabla \tilde{\mathbf{V}}_s + \tilde{\mathbf{V}}_s \cdot \nabla \mathbf{V}_s \right) \\ &= n_s e (-\nabla \tilde{\Phi} + \tilde{\mathbf{V}}_s \times \mathbf{B}) - \nabla \cdot [\tilde{p}_{\perp s} \mathbf{I} + (\tilde{p}_{\parallel s} - \tilde{p}_{\perp s}) \hat{\mathbf{b}} \hat{\mathbf{b}}]. \end{aligned} \quad (6.12)$$

We have used the electrostatic approximation, setting the perturbed magnetic field to be zero. We will also need the continuity equation of each species, given by

$$\frac{\partial \tilde{n}_s}{\partial t} = -\nabla \cdot (n_s \tilde{\mathbf{V}}_s + \tilde{n}_s \mathbf{V}_s). \quad (6.13)$$

### 6.3.1 Bulk plasma

The perturbed fluid velocity of bulk ions consists of both the perpendicular and parallel components, written as

$$\tilde{\mathbf{V}}_i = \tilde{V}_E(r) \frac{B_0}{B} e^{-i\omega t} \hat{\boldsymbol{\pi}} + [\tilde{V}_{i\parallel}^{m=1}(r) e^{i\theta - i\omega t} + \tilde{V}_{i\parallel}^{m=-1}(r) e^{-i\theta - i\omega t}] \hat{\mathbf{b}} + \tilde{\mathbf{V}}_{i,\delta}, \quad (6.14)$$

in which  $\tilde{V}_{i\parallel}^{m=\pm 1}$  is the  $O(1)$  parallel velocity and  $\tilde{\mathbf{V}}_{i,\delta}$  the  $O(\delta)$  velocity accounting for the magnetic, polarization and diamagnetic drift. The response of ion pressures,  $\tilde{p}_{\parallel i}$  and  $\tilde{p}_{\perp i}$ , are described by the double-adiabatic (CGL) fluid closure, given by

$$\frac{d\tilde{p}_{\parallel i}}{dt} = -p_i \nabla \cdot \tilde{\mathbf{V}}_i - 2p_i \hat{\mathbf{b}} \cdot (\hat{\mathbf{b}} \cdot \nabla \tilde{\mathbf{V}}_i), \quad (6.15)$$

$$\frac{d\tilde{p}_{\perp i}}{dt} = -2p_i \nabla \cdot \tilde{\mathbf{V}}_i + p_i \hat{\mathbf{b}} \cdot (\hat{\mathbf{b}} \cdot \nabla \tilde{\mathbf{V}}_i). \quad (6.16)$$

For bulk ions, it is sufficient to keep only  $\tilde{\mathbf{V}}_E$ , the  $\mathbf{E} \times \mathbf{B}$  drift velocity in the perturbed perpendicular velocity and ignore the higher order term  $\tilde{\mathbf{V}}_{i,\delta}$ , i.e. bulk ion FOW and FLR effects are ignored. Using Eq. (6.2) and extending  $\tilde{p}_{\parallel i}$  and  $\tilde{p}_{\perp i}$  similarly into poloidal Fourier harmonics, we obtain to the zeroth order of  $\epsilon$ ,  $\tilde{p}_{\parallel i}^{m=0} = \tilde{p}_{\perp i}^{m=0} = 0$  and

$$\tilde{p}_{\parallel i}^{m=\pm 1} = \pm \frac{2p_i}{R_0\omega} \tilde{V}_E \pm \frac{k}{\omega} 3p_i \tilde{V}_{i\parallel}^{m=\pm 1}, \quad (6.17)$$

$$\tilde{p}_{\perp i}^{m=\pm 1} = \pm \frac{3p_i}{2R_0\omega} \tilde{V}_E \pm \frac{k}{\omega} p_i \tilde{V}_{i\parallel}^{m=\pm 1}, \quad (6.18)$$

in which  $k = 1/qR_0$ .

The ion density perturbation is given by the continuity equation Eq. (6.13). Again using Eq. (6.2) and retaining the zeroth order terms in  $\epsilon$ , the  $m = \pm 1$  harmonics of the ion density perturbation are given by

$$\tilde{n}_i^{m=\pm 1} = \pm \frac{n_i}{R_0\omega} \tilde{V}_E \pm \frac{k}{\omega} n_i \tilde{V}_{i\parallel}^{m=\pm 1}, \quad (6.19)$$

and  $\tilde{n}_i^{m=0} = 0$ .

Since the electron transit frequency is much higher than the frequency of the mode, the response of electron is assumed to be isothermal (alias adiabatic in kinetic theory), which means  $\tilde{p}_e = \tilde{n}_e T_e$ , with  $\tilde{p}_e$  and  $\tilde{n}_e$  the perturbed electron pressure and density, respectively. Ignoring electron inertia, the momentum equation of electron gives

$$0 = n_e e \nabla \tilde{\Phi} - n_e e \tilde{\mathbf{V}}_E \times \mathbf{B} - T_e \nabla \tilde{n}_e, \quad (6.20)$$

where  $\tilde{\mathbf{V}}_E$  is the perturbed electron velocity. The parallel direction of Eq. (6.20) gives

$$\tilde{n}_e^{m=\pm 1} = en_e \frac{\tilde{\Phi}^{m=\pm 1}}{T_e}. \quad (6.21)$$

The quasi-neutrality condition is given by

$$\tilde{n}_e^{m=\pm 1} = \tilde{n}_i^{m=\pm 1} + \tilde{n}_f^{m=\pm 1} \quad (6.22)$$

with the perturbed electron pressure obtained by  $\tilde{p}_e = \tilde{n}_e T_e$ . Given the smallness of

the fast ion density, the second term on the right hand side of Eq. (6.22) can often be ignored. Equating Eq. (6.19) and (6.21), one can obtain the following relationship:  $\tilde{\Phi}^{m=\pm 1}/\tilde{\Phi}^{m=0} \sim O(\epsilon\delta\sqrt{T_e/E_0})$  and is thereby ignored in the  $\mathbf{E} \times \mathbf{B}$  drift as stated earlier.

Finally, using Eq. (6.21) and (6.22) to eliminate  $\tilde{E}_{\parallel}$ , the parallel component of Eq. (6.12) in zeroth order of  $\epsilon$  becomes

$$m_i n_i \omega \tilde{V}_i^{m=\pm 1} = \pm k \left( \tilde{p}_{\parallel i}^{m=\pm 1} + \tilde{n}_i^{m=\pm 1} T_e \right). \quad (6.23)$$

The perpendicular components of Eq. (6.12) can be rewritten into a sum of currents as

$$\begin{aligned} \tilde{\mathbf{J}}_{i\perp,\delta} &= \frac{1}{B} (\tilde{p}_{\perp i} + \tilde{p}_{\parallel i} + 2T_e \tilde{n}_i) \hat{\mathbf{b}} \times \boldsymbol{\kappa} \\ &- \nabla \times \left( \frac{\tilde{p}_{\perp i} + T_e \tilde{n}_i}{B} \right) - i\omega \frac{m_i n_i}{B} \hat{\mathbf{b}} \times \tilde{\mathbf{V}}_E, \end{aligned} \quad (6.24)$$

with the three terms on the right hand side accounting for the magnetic drift current, the diamagnetic current and the polarization current, respectively. A flux average quasi-neutrality condition,

$$\langle \nabla \cdot \tilde{\mathbf{J}} \rangle = 0, \quad (6.25)$$

can be imposed to obtain the dispersion relationship, in which  $\tilde{\mathbf{J}}$  is the total current. The flux average simply cancels out the effect of parallel current and in the absence of the fast ions, Eq. (6.25) can simply be replaced by  $\langle \nabla \cdot \tilde{\mathbf{J}}_{i\perp,\delta} \rangle = 0$ , with  $\langle \nabla \cdot \tilde{\mathbf{J}}_{i\perp,\delta} \rangle$  given by

$$\langle \nabla \cdot \tilde{\mathbf{J}}_{i\perp,\delta} \rangle = \frac{1}{r} \frac{\partial}{\partial r} r \left[ i\omega \frac{m_i n_i}{B_0} \tilde{V}_E - \frac{i}{2B_0 R_0} (\tilde{p}_{bulk}^{m=1} - \tilde{p}_{bulk}^{m=-1}) \right], \quad (6.26)$$

where  $\tilde{p}_{bulk}^{m=\pm 1} = (\tilde{p}_{\perp i} + \tilde{p}_{\parallel i} + 2T_e \tilde{n}_i)^{m=\pm 1}$ .

In the absence of fast ions, equating Eq. (6.26) to zero and using Eq. (6.18), (6.17), (6.19) and (6.23) yield a set of three equations with three unknowns  $\tilde{V}_E$ ,  $\tilde{V}_{i\parallel}^{m=1}$  and  $\tilde{V}_{i\parallel}^{m=-1}$ , defining an eigenvalue problem of  $\omega$ , i.e. the dispersion relationship. The dispersion relationship can be solved on each flux surface independently, giving three solutions corresponding to the thermal GAM, the ion sound wave and the low frequency zonal flow with the frequency from the highest to the lowest. The high- $q$  limit of the GAM frequency is given by

$$\omega_{\text{GAM}}^2(r) = \frac{2T_i}{m_i R_0^2} \left( \frac{7}{4} + \tau_e \right) [1 + O(q^{-2})], \quad (6.27)$$

in which  $\tau_e \equiv T_e/T_i$  is the ratio of electron and ion temperature. Equation (6.27) recovers the gyrokinetic adiabatic index  $\gamma_e = 1$  and  $\gamma_i = 7/4$  by Sugama and Watanabe [73], with the coupling to ion sound wave given by the  $O(q^{-2})$  term.

### 6.3.2 Fast ions local theory

We need to calculate the flux average perturbed radial current  $\tilde{\mathbf{J}}_f$  for the fast ions and then use Eq. (6.25) to get the dispersion relationship. This calculation is carried on to the order of  $O(\delta)$  for a local theory and  $O(\delta^3)$  for a global theory, with the former discussed in this section.

We here define  $\omega_b(r) = \langle V_{f\parallel} \rangle / q(r) R_0$  as the fast ion transit frequency. Similarly to the

bulk ions, the  $O(1)$  continuity equation can be simplified to

$$\begin{aligned} \tilde{n}_{f,\delta^0}^{m=\pm 1} = & \pm \frac{1}{2R_0(\omega \mp \omega_b)} \left[ \bar{n}_{f,\delta^0}(1 - c_f) + \bar{n}_{f,\delta} \frac{R_0}{r} \right] \tilde{V}_E \\ & \pm \frac{k}{\omega \mp \omega_b} \bar{n}_{f,\delta^0} \tilde{V}_{f\parallel,\delta^0}^{m=\pm 1}. \end{aligned} \quad (6.28)$$

Note that we have retained the  $O(\delta/\epsilon)$  term proportional to  $n_{f,\delta}$ , which can be an  $O(1)$  contribution given the smallness of  $\epsilon$ . Given the form of the distribution function Eq. (6.3), the fluid closure is simplified to

$$p_{\perp f} \approx \Lambda_0 E_0 \tilde{n}_f, \quad p_{\parallel f} = 0. \quad (6.29)$$

The parallel direction of the momentum equation Eq. (6.12) yields the  $O(1)$  equations for perturbed parallel velocity, given by

$$\tilde{V}_{f\parallel,\delta^0}^{m=\pm 1} = \pm \frac{1 + c_f}{2(\omega \mp \omega_b)} \omega_b q \tilde{V}_E, \quad (6.30)$$

in which we have ignored the contribution from the responding electrons balancing the parallel electric field, due to the argument that  $T_e \ll E_0$  so the fast ion response will dominate over the electrons. The magnetic drift current, derived from the perpendicular direction of Eq. (6.12), has the form

$$\tilde{\mathbf{J}}_{f\perp\text{mag},\delta} = \frac{1}{B} \left[ \tilde{p}_{\perp f,\delta^0} + m_i \tilde{n}_{f,\delta} V_{f\parallel}^2 + 2m_i n_{f,\delta^0} V_{f\parallel} \tilde{V}_{f\parallel,\delta} \right] \hat{\mathbf{b}} \times \boldsymbol{\kappa}, \quad (6.31)$$

while the polarization current is simply given by

$$\tilde{\mathbf{J}}_{f\perp p,\delta} = -i\omega \frac{m_i n_{f,\delta^0}}{B} \hat{\mathbf{b}} \times \tilde{\mathbf{V}}_E. \quad (6.32)$$

We will ignore the diamagnetic current since it does not contribute to the divergence. Adding the current contributions from the bulk ions and fast ions and taking the quasi-neutrality condition Eq. (6.25), we reach the dispersion relationship, written as

$$D(\omega, r) = 1 - [1 - \alpha(r)] \frac{\omega_{\text{GAM}}^2(r)}{\omega^2} - \alpha(r) G(\omega, r), \quad (6.33)$$

in which  $\alpha = \bar{n}_{f,\delta^0}/(n_i + \bar{n}_{f,\delta^0})$  is the fast ion density proportion and  $G(\omega, r)$  is the contribution from the fast ions. We have taken the high- $q$  limit and eliminate the contribution from the bulk ion parallel velocity. With the distribution function described by Eq. (6.3), the form of  $G(\omega, r)$  is given by

$$\begin{aligned} G(\omega, r) = & \frac{1 + c_f}{2} \left[ (3 - c_f) + \frac{R_0}{r} \frac{\bar{n}_{f,\delta}}{\bar{n}_{f,\delta^0}} \right] \\ & \times \frac{\omega_b^2 q^2}{\omega^2 - \omega_b^2} + (1 + c_f)^2 \frac{\omega_b^4 q^2}{(\omega^2 - \omega_b^2)^2}, \end{aligned} \quad (6.34)$$

where  $\omega_b$  and  $q$  are functions of  $r$ . We note that  $c_f = \Lambda_0/(2 - 2\Lambda_0)$  from Eq. (6.7). In the limit  $\Lambda_0 \rightarrow 0$ , i.e. completely tangential beam,  $c_f = 0$  and Eq. (6.34) reduces to the form derived from a bump-on-tail fast ion distribution with ignorable temperature in Qu *et al* [173] and was studied there in detail. While not taken into account in Qu *et*

$al$ , the additional term proportional to  $\bar{n}_{f,\delta}$  originates from the density change on a flux surface due to FOW effects, and is responsible for the distinction between the co-passing and counter-passing injections. We will not study these effects separately here in a local theory, but will study it along with the global theory later in this work. Note that similar interpretation of this additional term can also be found in the work by Berk and Zhou [154].

### 6.3.3 Fast ion global theory

In the absence of bulk ion and fast ion FLR/FOW effects, the perturbations on different flux surfaces cannot communicate to each other and will oscillate at their own local GAM/EGAM frequency. Any global perturbation will disperse quickly into a radially highly oscillating structure and became highly damped due to phase mixing [175]. When fast ion FOW effects are taken into account, the drift orbits of the fast ions act as bridges between flux surfaces and allow the radial propagation of the mode. To take into account the fast ion FOW effects, we carry on the calculation of the fast ion radial current to  $O(\delta^3)$ . We note that the fast ion polarization drift current and diamagnetic current are ignored for higher order calculation. The contribution from the fast ion polarization drift current is a factor of  $\alpha$  smaller than the bulk ion one, while the latter is comparable to the bulk plasma and thus the fast ion magnetic drift current, if the fast ion beta  $\beta_f \sim \beta_{bulk}$  the bulk plasma beta. The fast ion diamagnetic current, whose divergence vanishes and will not contribute to the continuity equation and  $\nabla \cdot \mathbf{J}$ , is also ignored.

The calculation is straight forward, by solving order by order the continuity equation and the momentum equation along with the closure condition Eq. (6.29). The corresponding equilibrium/perturbed variables and their ordering are listed in Table 6.1. We substitute Eq. (6.31) into the  $O(\delta)$  continuity equation Eq. (6.13) to obtain  $\tilde{n}_{f,\delta}$ , while  $\tilde{V}_{f\parallel,\delta}$  is calculated from the parallel direction of the momentum equation Eq. (6.12). The perpendicular direction of Eq. (6.12), is used in turn to get  $\tilde{\mathbf{V}}_{f\perp\text{mag},\delta^2}$  of an order higher. This procedure is repeated to obtain  $\tilde{\mathbf{V}}_{f\perp\text{mag},\delta^3}$  which will be used in Eq. (6.25). All the steps above have retained only the zeroth order terms in  $\epsilon$ . The detail of all the algebra involved is provided in Appendix 6.7.

**Table 6.1:** The equilibrium/perturbed fast ion quantities and their order in  $\delta$

	$n_f$	$\tilde{n}_f$	$\mathbf{V}_f$	$\tilde{\mathbf{V}}_f$
$O(1)$	$n_{f,\delta^0}$	$\tilde{n}_{f,\delta^0}$	$V_{f\parallel}\hat{\mathbf{b}}$	$\tilde{\mathbf{V}}_E + \tilde{V}_{f\parallel,\delta^0}\hat{\mathbf{b}}$
$O(\delta)$	$n_{f,\delta}$	$\tilde{n}_{f,\delta}$	-	$\tilde{V}_{f\parallel,\delta}\hat{\mathbf{b}}$
$O(\delta^2)$	$n_{f,\delta^2}$	$\tilde{n}_{f,\delta^2}$	-	$\tilde{V}_{f\parallel,\delta^2}\hat{\mathbf{b}}$
$O(\delta^3)$	$n_{f,\delta^3}$	$\tilde{n}_{f,\delta^3}$	-	-
$O(\epsilon\delta)$	-	-	$\mathbf{V}_{f,\text{mag}}$	$\tilde{\mathbf{V}}_{f\perp\text{mag},\delta}$
$O(\epsilon\delta^2)$	-	-	-	$\tilde{\mathbf{V}}_{f\perp\text{mag},\delta^2}$
$O(\epsilon\delta^3)$	-	-	-	$\tilde{\mathbf{V}}_{f\perp\text{mag},\delta^3}$

The dispersion relationship, after taken into account the  $O(\delta^3)$  contributions, is now simplified to

$$\begin{aligned} \frac{d}{dr}\rho_{\parallel}^2\frac{1}{r}\left(F_1\frac{d}{dr}B_1 + F_2\frac{d}{dr}B_2\right)r\bar{n}_{f,\delta^0}\tilde{V}_E + \rho_{\parallel}^2\frac{1}{r^2}\left(F_3\frac{d}{dr}B_3 + F_4\frac{d}{dr}B_4\right)r^2\frac{\bar{n}'_{f,\delta^0}}{\omega_b}\tilde{V}_E \\ + \rho_{\parallel}^2F_5\tilde{V}_E + n_{total}D(\omega,r)\tilde{V}_E = 0, \quad (6.35) \end{aligned}$$

in which the brackets in the first and second terms are considered as differential operators and apply to the terms followed. The coefficients are given by

$$F_1(\omega, r) = \frac{1}{8} \frac{\omega_b^4 q^2}{\omega^2} \left( \frac{4}{\omega^2 - 4\omega_b^2} - \frac{1}{\omega^2 - \omega_b^2} \right), \quad (6.36)$$

$$F_2(\omega, r) = \frac{1}{4} \frac{\omega_b^6 q^2}{\omega^2} \left[ \frac{16}{(\omega^2 - 4\omega_b^2)^2} - \frac{1}{(\omega^2 - \omega_b^2)^2} \right], \quad (6.37)$$

and

$$B_1(r) = \left( 7 - c_f + \frac{n_{f,\delta}}{n_{f,\delta^0}} \frac{R_0}{r} \right) (1 + c_f)^3, \quad (6.38)$$

$$B_2 = (1 + c_f)^4, \quad (6.39)$$

with all other terms given in Appendix 6.8.

## 6.4 Solving the dispersion relationship

The global dispersion relationship Eq. (6.35) is solved numerically using a shooting method. The boundary condition we've used is  $\tilde{V}_E(0) = 0$  and the outgoing wave condition at the other end, given the experimentally observed outward propagating behaviour [176]. This outgoing boundary condition is achieved by introducing a perfectly matched layer [177] outside  $r = a$  which strongly absorbs the outgoing wave and allows no reflection. In the perfectly matched layer, we perform the substitution

$$\frac{d}{dr} \rightarrow \frac{1}{1 + i\sigma_0(r/a - 1)^2} \frac{d}{dr}, \quad (6.40)$$

and enforce zero Dirichlet boundary condition  $\tilde{V}_E(b) = 0$  at  $b > a$ . The value of  $\sigma_0$  and  $b$  vary from case to case. They are carefully chosen to be large enough to reach the convergence of the frequency, whilst finite to prevent ill-behaved solutions. Typical values are  $\sigma_0 = 40$  and  $b = 1.2a$ . Based on this numerical scheme, we will perform a parameter scan on various profiles.

We will first explore the dependency of the global modes on the  $q$  profile. Figure 6.2 (a) shows the two quadratic  $q$  profiles we use, having monotonic and reversed shear respectively. In both cases  $q_{\min} = 3$ , but the minimum is reached on axis for the monotonic case and at  $r/a = 0.4$  for the reversed shear case. The bulk plasma temperature profile used is  $T_e = T_i = 1 - r^2/a^2$  in the unit of keV, while the bulk density is taken to be constant. The zeroth order fast ion density profile is given by  $\alpha(r) = 0.1 \exp(-r^2/a^2)$  with the on axis ratio 10%. These profiles are plotted in Fig.6.2 (b). Note that the relative high density of the fast ions is a requirement for our small orbit width expansion which will be explained later. For similar reason, we have chosen  $B_0 = 3T$ , instead of  $B_0 = 2T$  for DIII-D, reducing the orbit width from  $L_{\text{orbit}}/a = 0.12$  to 0.08. Other parameters we've used are  $R_0 = 1.7m$ ,  $\epsilon = 0.3$ ,  $E_0 = 75\text{keV}$ ,  $\Lambda_0 = 0.5$  and deuterium, typical DIII-D beam parameters. The direction of the fast ions is counter-passing.



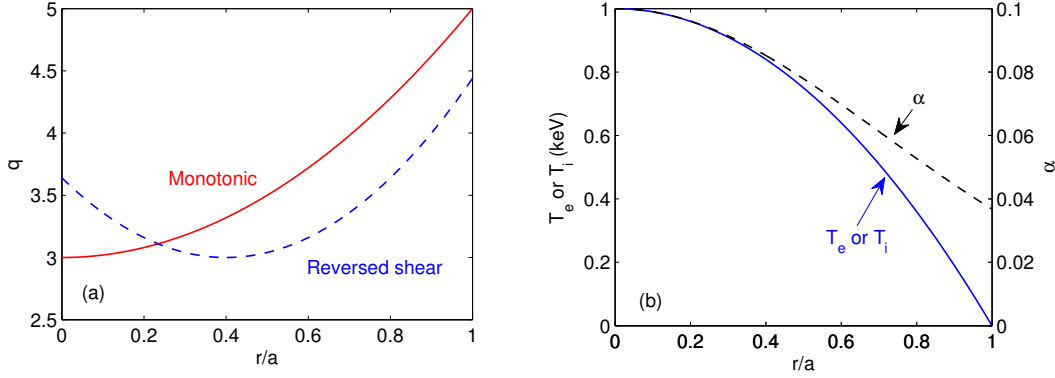


**Figure 6.2:** (a) The  $q$  profile used in the monotonic (red solid line) and reversed shear (blue dashed line) case. (b) The  $T_e$  and  $T_i$  profile and the  $\alpha$  profile.

#### 6.4.1 Monotonic shear case

The radial mode structure,  $\tilde{V}_E$  as a function of minor radius, is plotted in Fig.6.3 (a) for the most unstable solution in the monotonic shear case. The frequency and growth rate are 32.7kHz and 57%. The absolute amplitude is maximized at around  $r/a = 0.3$  and decays outward, showing a outgoing wave pattern (as a result of our boundary conditions). The direction of propagation can be understood by assuming  $\tilde{V}_E(r) \sim \exp(ik_r r)$ , and therefore the peak of  $\Re(\tilde{V}_E) \sim \cos k_r r$  will be ahead of  $\Im(\tilde{V}_E) \sim \cos k_r r$  by a quarter of wavelength if  $k_r > 0$ , in agreement with Fig.6.2(a). By inspection of Fig.6.3 (a),  $L_{\text{mode}}$  is a function of radial position. Instead of using the original definition in Eq. (6.1), we measure  $L_{\text{mode}}$  by the full width at half maximum separately for the real and imaginary part and then takes an average. In the core region,  $L_{\text{mode}}$  is measure between the first two nodes, giving  $L_{\text{wave, core}}$ , while  $L_{\text{wave, edge}}$  is measured between the last two nodes. In addition,  $L_{\text{orbit}}$  is measured at  $r = 0$  and 1 for the core and the edge, respectively. For Fig.6.3 (a),  $L_{\text{mode, core}}/a = 0.25$  with  $\delta = 0.32$ . Our small parameter expansion is thus barely valid in the core. However, in the edge region  $\delta \sim 1$ , and our assumption is not valid. We would expect the inclusion of higher order corrections in  $\delta$  to reduce the mode amplitude at the edge, since when the orbit width is comparable to the radial wavelength, the large drift orbit tends to “average out” the field, leading to a lower fast ion response.

The thermal GAM continuum, the frequency of the EGAM local solution, the transit frequency and the global EGAM frequency are plotted in Fig.6.3 (b). The thermal GAM continuum frequency peaks on axis and monotonically decreases to zero at the edge following the temperature profile. The frequency of the local EGAM is also monotonic with an on-axis extremum, mainly due to the monotonic  $q$  profile and thus a monotonic fast ion transit frequency. The frequency of the global mode is 0.1kHz above the extremum, with a growth rate lower than the local solution (64%) by 7%.

To understand the property of the global solution, we expand the local dispersion relationship around its on-axis extremum. If we explore the case  $L_{\text{mode}} \ll a$ , the radial change of the equilibrium profiles becomes unimportant compared to the mode structure, and thus, our global dispersion relationship Eq. (6.35) can be simplified to

$$\frac{d}{dr} \frac{1}{r} \frac{d}{dr} r \tilde{V}_E(r) + (pr^2 + h\Delta\omega) \tilde{V}_E(r) = 0, \quad (6.41)$$

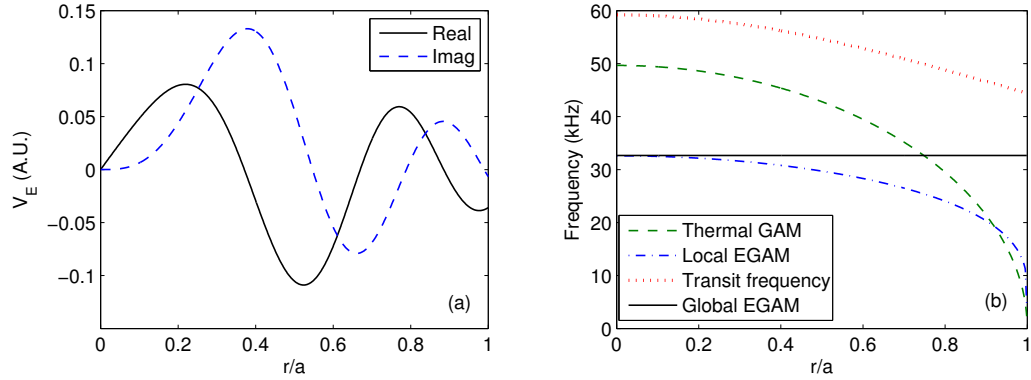


**Figure 6.3:** (a) The radial mode structure of the monotonic shear case. (b) The thermal GAM continuum, the transit frequency as a function of radius, the local EGAM frequency and the global EGAM frequency for the monotonic shear case.

where  $\Delta\omega = \omega - \omega_{\text{EGAM}}(r = 0)$ , with  $p$  and  $h$  given by

$$p = \frac{\partial^2 D}{\partial r^2} / [\alpha \rho_{\parallel}^2 (F_1 B_1 + F_2 B_2)], \quad (6.42)$$

$$h = \frac{\partial D}{\partial \omega} / [\alpha \rho_{\parallel}^2 (F_1 B_1 + F_2 B_2)], \quad (6.43)$$

taken the value on axis and  $\omega = \omega_{\text{EGAM}}(r = 0)$ . The solution of Eq. (6.41), satisfying the zero Dirichlet boundary condition on axis, is given by

$$\tilde{V}_E(r) = \frac{1}{r} e^{\frac{1}{2} i \sqrt{p} r^2} L_{\frac{1}{4} i h \Delta\omega / \sqrt{p}}^{-1}(i \sqrt{p} r^2), \quad (6.44)$$

in which  $L_n^\alpha(z)$  is the generalized Laguerre function, a solution to the Laguerre's equation

$$z y''(z) + (\alpha + 1 - z) y'(z) + n y(z) = 0. \quad (6.45)$$

The asymptotic behaviour of solution Eq. (6.44) at  $+\infty$  is written as

$$\tilde{V}_E(r \rightarrow +\infty) \rightarrow \frac{C_1(p, h \Delta\omega)}{\Gamma\left(-\frac{i h \Delta\omega}{4 \sqrt{p}}\right)} r^{-\frac{i h \Delta\omega}{2 \sqrt{p}} - 1} e^{-\frac{1}{2} i \sqrt{p} r^2} + \frac{C_2(p, h \Delta\omega)}{\Gamma\left(\frac{i h \Delta\omega}{4 \sqrt{p}}\right)} r^{\frac{i p \Delta\omega}{\sqrt{h}} - 1} e^{\frac{1}{2} i \sqrt{p} r^2}, \quad (6.46)$$

in which  $\Gamma(z)$  is the Gamma function, and  $C_1$  and  $C_2$  are non-zero unless  $p = 0$ . If  $\Re(\sqrt{p}) > 0$ , the first term in Eq. (6.46) represents an inward propagating component and the second term is an outward propagating one. To satisfy our outgoing boundary condition, we need the Gamma function in the denominator of the first term to approach infinity, i.e.  $1/\Gamma(z) \rightarrow 0$ . Singularities happens for  $\Gamma(z)$  when  $z$  is a negative integer, leading to the eigenvalue condition

$$\Delta\omega = \begin{cases} -4iN\sqrt{p}/h & \text{if } \Re(\sqrt{p}) > 0, \\ 4iN\sqrt{p}/h & \text{if } \Re(\sqrt{p}) < 0, \end{cases} \quad N = 1, 2, 3, \dots \quad (6.47)$$

For the case demonstrated in Fig.6.3,  $\sqrt{p} = 34.3 + 7.99i$ ,  $h = (7.3 + 1.1) \times 10^{-3}$ , and the calculated frequency and growth rate from Eq. (6.47) with  $N = 1$  are given by 33.7kHz and 53.9%. The deviation of the analytic solution from the numerical solution is a consequence

of  $L_{\text{mode}} \ll a$  being unsatisfied. We note that when  $B_0$  is increased to 9T and  $L_{\text{mode}}$  is reduced to  $0.15a$ , we have got a much better match (frequency 33.4kHz and growth rate 54.1%).

Inspection of Eq. (6.44) shows  $L_{\text{mode}}$  around the axis is approximately given by

$$L_{\text{mode,core}} \sim p^{-1/4} \sim \alpha^{1/4} q^{1/2} L_{\text{orbit}}^{1/2} L_{\text{EGAM}}^{1/2}. \quad (6.48)$$

Away from the core region, a WKB approximation can be applied since the length scale of the equilibrium quantities is comparable to the minor radius, while the mode width is comparable to  $L_{\text{orbit}}$  and  $L_{\text{orbit}} \ll a$ . Given  $\omega_{\text{GAM}}$  vanishes at the edge,  $D(\omega, r) \sim 1$ , and therefore

$$L_{\text{mode,edge}} \sim \alpha^{1/2} q L_{\text{orbit}}, \quad (6.49)$$

matching our observations in Fig.6.3. Equation (6.49) also indicates that  $\delta \ll 1$  is not satisfied at the plasma edge unless an unrealistic  $\alpha$  is assumed.

A numerical parameter scan is performed to study the relationship between the orbit width and the mode width. The drift orbit width is changed by adjusting the field strength  $B_0$ , with the advantage of conserving the EGAM local frequency. As the field strength is increased, the radial model structure gradually changes from Fig.6.3 (a) to Fig.6.4 (a) with a shorter wavelength. Similar to the previous case, we measure the radial mode width by the full width of the real and imaginary parts at half maximum and takes an average, for  $B_0$  from 3T to 9T. The “measurement” is taken between  $r = 0$  and the first zero in the core for  $L_{\text{mode,core}}$ , and between the last and second last zeros at the edge for  $L_{\text{mode,edge}}$ . The corresponding relationship between the orbit width and the mode width is shown in Fig.6.4 (b). The trend line of  $L_{\text{mode}}$  in Fig.6.4 (b) matches Eq. (6.48) and (6.49) respectively in the core and at the edge.

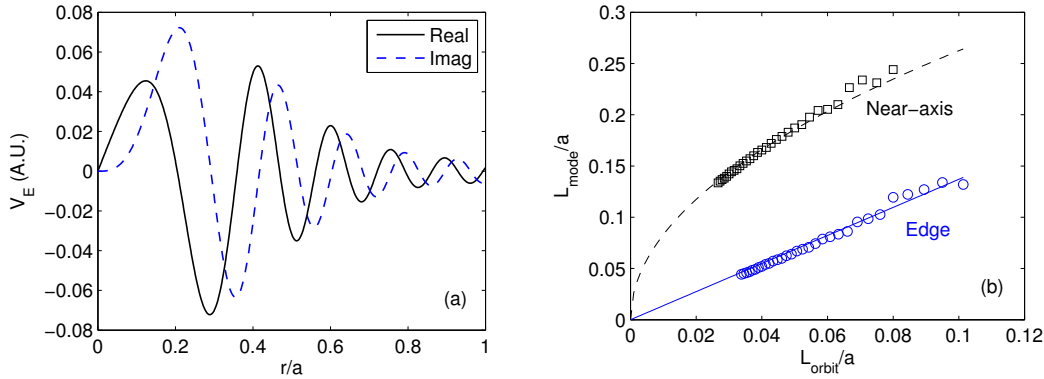


**Figure 6.4:** (a) The radial mode structure of the monotonic shear case with increased field strength  $B_0 = 9T$ . (b) Scanning  $B_0$  from 3T to 9T, the radial mode width as a function of drift orbit width near the axis (black squares) and at the edge (blue circles) for the monotonic shear case, with a square root and a linear trend line, respectively.

### 6.4.2 Reversed shear case

We have repeated our mode structure calculation for the reversed shear case, with  $\tilde{V}_E(r)$  and global/local EGAM frequency given in Fig.6.5. Inspection of Fig.6.5 (b) shows that the thermal GAM continuum is almost identical to the monotonic shear case, since

the same temperature profile is used and the  $O(q^{-2})$  correction to the GAM frequency is eligible for  $q \geq 3$ . However, the local EGAM continuum in the two cases are qualitatively different. In the reversed shear case, an extremum is presented at  $r/a = 0.37$  near the  $q = q_{\min}$  surface. This off-axis extremum is formed due to the extremum of  $\omega_b = v_{\parallel}/qR_0$  the fast ion transit frequency at the same radius, and ultimately due to the shear reversal. The frequency of the most unstable global mode is 1kHz above this maximum at 33.3kHz, with a growth rate of 61.5%. Similar to the monotonic shear case, the mode structure is radially propagating with  $\delta = 0.29$  in core, but the mode amplitude is higher around the core region compared to the edge.

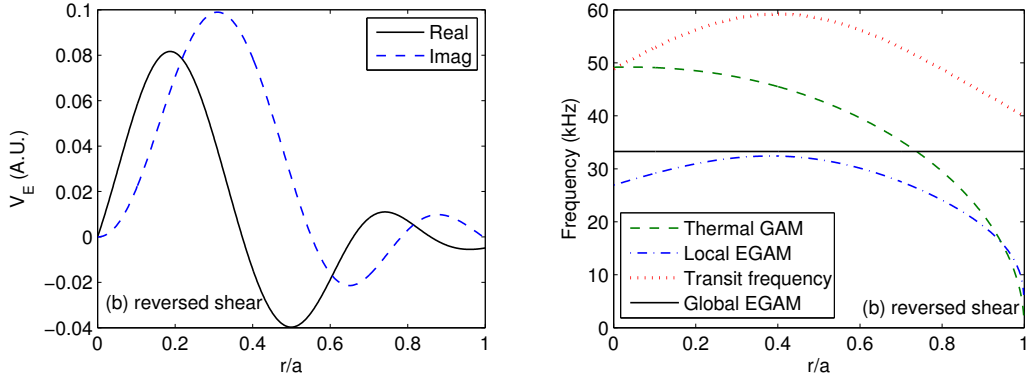


**Figure 6.5:** (a) The radial mode structure of the reversed shear case. (b) The thermal GAM continuum, the transit frequency as a function of radius, the local EGAM frequency and the global EGAM frequency for the reversed shear case.

Again we can simplify Eq. (6.35) around the maximum of the EGAM local continuum, giving that

$$\frac{d^2}{dr^2} \tilde{V}_E(r) + [p(r - r_{\text{ex}})^2 + h\Delta\omega] \tilde{V}_E(r) = 0, \quad (6.50)$$

with the definition of  $p$  and  $h$  the same as Eq. (6.42) and (6.43), but evaluated at  $r = r_{\text{ex}}$  and  $\omega = \omega_{\text{ex}}$ , labeling the radius and the complex frequency at the extremum, respectively. The solution to Eq. (6.50) is given by

$$\tilde{V}_E(r) = \begin{cases} D_\nu[\sqrt{2}(-p)^{1/4}(r - r_{\text{ex}})], & \Re(\sqrt{p}) < 0, \\ D_{-1-\nu}[-\sqrt{2}i(-p)^{1/4}(r - r_{\text{ex}})], & \Re(\sqrt{p}) > 0, \end{cases}, \quad (6.51)$$

in which the parabolic cylinder function  $D_\nu(z)$  is the solution to the Weber's equation

$$y''(z) + \left( \nu + \frac{1}{2} - \frac{1}{4}z^2 \right) y(z) = 0, \quad (6.52)$$

and

$$\nu = -\frac{1}{2} - \frac{ih\Delta\omega}{2\sqrt{p}}. \quad (6.53)$$

Asymptotically, the solution in Eq. (6.51) satisfies

$$\tilde{V}_E(r \rightarrow +\infty) \rightarrow \begin{cases} r^\nu e^{-\frac{1}{2}i\sqrt{p}r^2}, & \Re(\sqrt{p}) < 0, \\ r^{-\nu-1} e^{\frac{1}{2}i\sqrt{p}r^2}, & \Re(\sqrt{p}) > 0, \end{cases}, \quad (6.54)$$

with the outgoing boundary condition satisfied. The parameter  $\nu$ , and thereby the mode frequency, will be determined by the other boundary condition  $\tilde{V}_E(0) = 0$ .

The approximate solution Eq. (6.51) is no longer valid around the magnetic axis, as the  $1/r$  factor in the second order derivative term in Eq. (6.35) becomes important. Near the axis, the solution is given by

$$\tilde{V}_E(r) \approx J_1(\sqrt{\beta}r), \quad \beta = \frac{D(\omega_{\text{ex}}, r=0)}{\alpha \rho_{\parallel}^2 (F_1 B_1 + F_2 B_2)}, \quad (6.55)$$

where  $J_n(z)$  is the Bessel function of the first kind and  $\beta$  is evaluated on axis and at  $\omega = \omega_{\text{ex}}$  so it does not depend on the choice of  $\Delta\omega$ . Theoretically, we can connect the core solution Eq. (6.55) and the outer region solution Eq. (6.51) at  $r = r_c$ . The connection criterion

$$\tilde{V}_E|_{r=r_c^-} = \frac{d\tilde{V}_E}{dr} \Big|_{r=r_c^-}^{r=r_c^+} = 0, \quad (6.56)$$

should define the eigenvalue problem of  $\nu$  and therefore  $\Delta\omega$ . However, in practice, we've found that although the eigenfunction is insensitive to the choice of  $r_c$ ,  $\Delta\omega$  depends quite heavily on  $r_c$ . Therefore, we will not pursue a quantitative match between the full numerical solution and the analytic one in the reversed shear case.

One would expect that the scaling law Eq. (6.48) still holds for the reversed shear case in the core region given the form of the solution in Eq. (6.51). However, as we will show later, this scaling law fails for  $B_0 > 4\text{T}$ . In Fig.6.6 (a), we have plotted the radial mode structure for a increased field strength  $B_0 = 5\text{T}$ . The frequency of the mode is now 32.1kHz, 0.6kHz below the maximum of the continuum. The mode structure becomes quite core-localized, with a low-amplitude propagating tail near the edge. An analogy can be made between Eq. (6.50) and the 1D Schrödinger equation in the quantum mechanics with

$$E - V(r) = \hbar \Delta\omega + p(r - r_{\text{ex}})^2, \quad (6.57)$$

in which  $E$  is the energy and  $V(r)$  is the potential. With  $\Re[h] > 0$  in our case, a global mode frequency lower than the EGAM extremum frequency means  $E < V(r)$  near the extremum, a classically forbidden region. Near the magnetic axis and at the edge, we have  $E > V(r)$  the classically allowed region. A mode excited in the core is allowed to propagate across the forbidden region through quantum tunneling and into the outer region. Therefore, we would expect a significantly reduced mode amplitude at the edge compared to the core since the lower the energy  $E$  is, the less wave will “leak” into the outer region. Due to the observation that as  $B_0$  increases, the global frequency becomes lower than the global continuum, the solution in Eq. (6.51), assuming an extremum mode, is no longer appropriate. As a result, the mode width will not follow Eq. (6.48) for large  $B_0$ , in the region where  $\omega < \omega_{\text{ex}}$ . This is confirmed in Fig.6.6 (b), in which we have plotted a scan of the mode width over the orbit width by increasing the field strength. For orbit width less than  $0.06a$ , the curve is found to follow the trend line  $\propto L_{\text{orbit}}$  instead of a square root, which can be derived from the on axis solution Eq. (6.55). For  $L_{\text{orbit}} > 0.06a$ , the frequency of the global mode is above the EGAM continuum and therefore the scaling law is changed back to the square root dependency predicted by Eq. (6.51). The mode width at the edge, on the other hand, gives a good match to Eq. (6.49), as shown by Fig.6.6 (b).

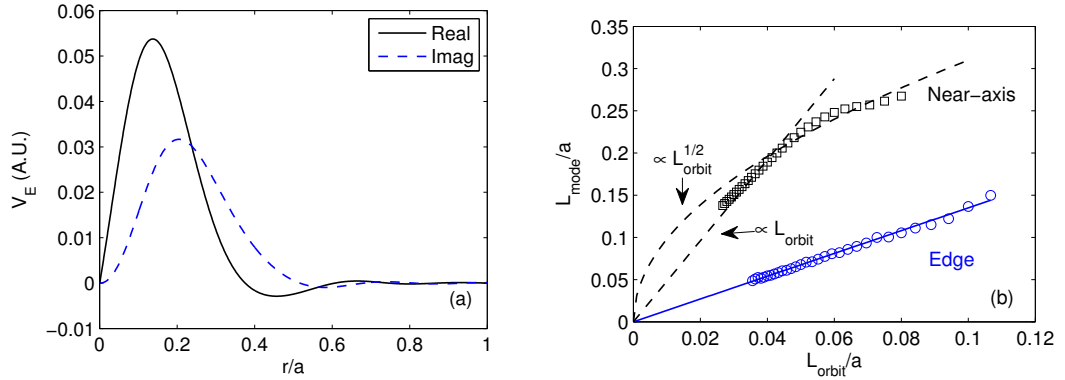


**Figure 6.6:** (a) The radial mode structure of the reversed shear case with increased field strength  $B_0 = 5\text{T}$ . (b) Scanning  $B_0$  from 3T to 9T, the radial mode width as a function of drift orbit width near the axis (black squares) and at the edge (blue circles) for the reversed shear case with trend lines.

### 6.4.3 Dependency on injection direction

In this section, the dependency of the mode frequency and growth rate on the injection direction is studied by changing the sign of  $\omega_b$  (positive for co-passing and negative for counter-passing) and keeping all other parameters unchanged. Figure 6.7 shows a scan of the most unstable global mode frequency and growth rate as a function of the fast ion proportion for the monotonic shear scenario and the reversed shear scenario, but assuming either co-passing or counter-passing fast ions. The frequency of the mode in all the cases decreases as the fast ion density increases, while the mode is becoming more unstable at the same time, similar to the behaviour of the local solutions in Qu *et al* [173]. In fact, the complex frequency of the global mode is mainly determined by the local EGAM continuum as understood from the analysis in Section 6.4.1 and 6.4.2: for an extremum mode,  $\omega = \omega_{\text{ex}} + \Delta\omega$  and  $\Delta\omega$  is small. Looking back into the EGAM local dispersion relationship Eq. (6.33), the only distinction between the co/counter-passing ions comes from the additional term proportional to  $\bar{n}_{f,\delta}$  in Eq. (6.34). As stated in Section 6.2, the sign of  $\bar{n}_{f,\delta}$  will be different for co/counter-passing ions. All other terms come with  $\omega_b^2$  and therefore the effect of direction is canceled, while  $c_f$  is also identical for different injection directions. Therefore, we would expect this additional term, originated from the fact that counter-passing ions have inwardly shifted orbits and co-passing ions outward, to modify the EGAM local continuum, and reflects into the distinction between counter-passing ions and co-passing ions.

Figure 6.7 shows that the real frequency of the counter-passing mode is slightly below the co-passing mode in both the monotonic shear and reversed shear case. But more interestingly, the growth rate of the counter-passing mode is 50% larger than the co-passing one for  $\alpha = 0.05$ . This difference enlarges to 100% when the fast ion density is 15% the total ion density, indicating that the reactive EGAMs in the presence of counter-passing ions is much more unstable than the one with co-passing ions given all other conditions the same. As mentioned in Section 6.2.2 and Fig.6.1, the FOW effects ( $P_\varphi$  being a constant of motion) of counter-passing ions pushes the plasma inward, making  $n_f$  higher at higher  $B$  on a flux surface. This changes the density perturbation induced by

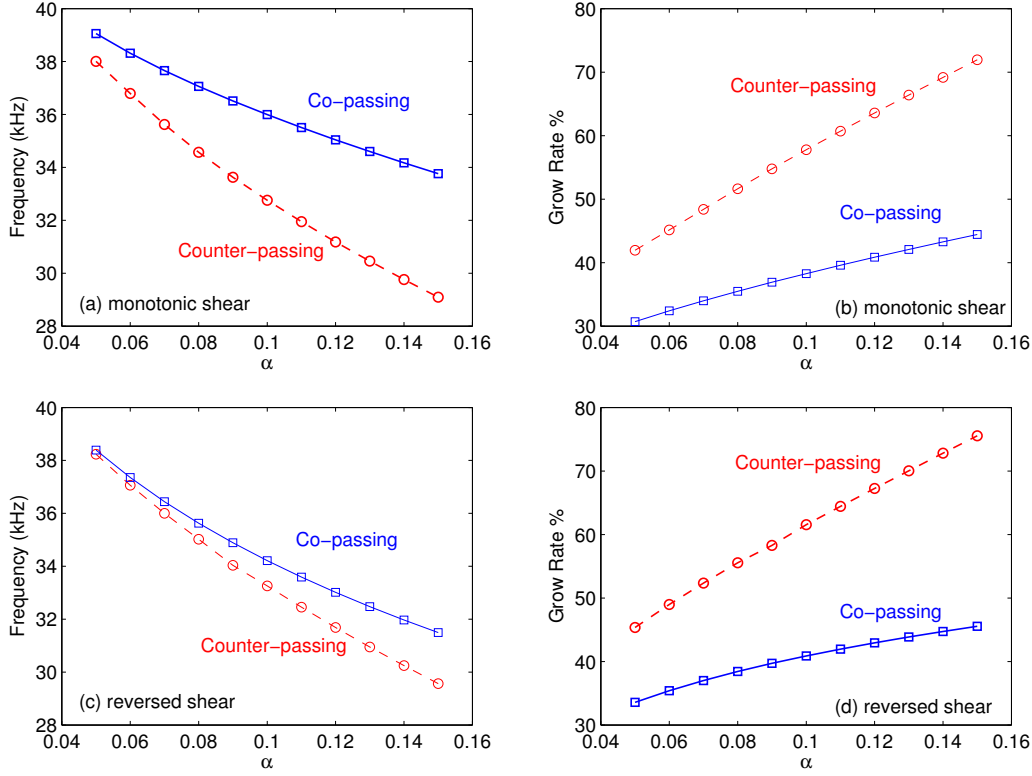


**Figure 6.7:** The frequency (a) and the growth rate (b) for the monotonic case, with counter-passing (red circles) and co-passing (blue squares) fast ions, scanned over fast ion proportion  $\alpha$ . (c)(d) The same scan for the reversed shear case. We have restricted our scan domain to  $\alpha > 0.05$  to satisfy the condition  $L_{\text{mode}} \gg L_{\text{orbit}}$ .

$\tilde{V}_E$  and the geodesic curvature, since on the RHS of Eq. (6.13) we have

$$\nabla \cdot (n_f \tilde{V}_E \frac{B_0}{B} \hat{\pi}) \approx \tilde{V}_E \frac{\partial}{\partial \theta} \left( n_f \frac{B_0^2}{B^2} \right), \quad (6.58)$$

whose absolute value becomes lower when  $n_f$  is higher at higher  $B$  (e.g. if  $n_f \propto B^2$ , the contribution vanishes). Mathematically, for counter-passing particles,  $\bar{n}_{f,\delta}$  is negative in the dispersion relationship Eq. (6.34), lowering the first term in  $G(\omega)$ , even making it zero when the contour shift is strong enough. On the other side, let us suppose that the numerator of the first term in  $G(\omega)$  is increased by  $\Delta C$ , we reach approximately by Taylor expanding Eq. (6.33) that

$$\Delta \omega^2 \approx \frac{(\omega^2 - \omega_b^2)^2}{\alpha \omega_b^4 q^2} \Delta C, \quad (6.59)$$

in which we have assumed  $\Lambda_0 = 0$  and thus  $c_f = 0$  for simplicity. For the profiles we used,  $\Re(\omega^2) < \omega_b^2$ , while for instability we have  $\Im(\omega^2) > 0$ . Therefore,  $\Im[(\omega^2 - \omega_b^2)^2] < 0$ , making  $\Im(\Delta \omega^2) > 0$  if  $\Delta C < 0$ , corresponding to a higher growth rate and a less stable mode. To sum up, the counter-passing ions density contour shifts inward and shrinks the first term in  $G(\omega)$ , leading to a negative  $\Delta C$  and thus  $\Delta \omega^2$ , destabilizing the reactive EGAMs. The story is reversed for the co-passing ions, in which the density contour shifts outward, making  $\Delta C > 0$  and the mode is stabilized. It is possible that in the presence of a strong damping (such as the ion Landau damping), the reactive EGAMs induced by

co-passing ions are suppressed due to their relative lower growth rate, while in the counter-injection scenario, the growth rate is strong enough to overcome the damping. Our result is consistent with experimental observation that EGAMs are more often observed in plasmas with counter-injection [45, 176].

## 6.5 Conclusion

Extending the previous model for local reactive EGAMs, we have added the finite drift orbit width (FOW) effects to our three-fluid model under the assumption that  $L_{\text{orbit}} \ll L_{\text{mode}}$ , leading to a second order ODE as the dispersion relationship. The model is valid when the fast ion distribution function is beam-like: we have therefore used a single-energy single-pitch distribution, consistent with the scenario of early beam heating when the beam is not yet slowed down.

It has been found that with proper boundary conditions, a radially propagating structure can be formed when the  $q$  profile is either monotonic or reversed shear. In the monotonic shear case, the global EGAM frequency is slightly higher than the local frequency at the extremum on axis, while the growth rate is lower than the local growth rate at the extremum. A qualitative analytic solution of the mode structure reveals the relationship  $L_{\text{mode}} \propto L_{\text{orbit}}^{1/2}$  near the axis and  $L_{\text{mode}} \propto L_{\text{orbit}}$  at the edge. This finding is later confirmed by a numerical scan which modifies  $L_{\text{orbit}}$  by increasing the field strength, while keeping the EGAM local continuum unchanged. In the reversed shear case, for  $L_{\text{orbit}} > 0.06a$ , the global EGAM is also an extremum mode residing on the top of the local EGAM extremum at  $r \approx 0.4a$ , the  $q = q_{\text{min}}$  surface. One would expect the relationship between  $L_{\text{mode}}$  and  $L_{\text{orbit}}$  for the monotonic case to be applicable in the reversed shear case. However, when  $L_{\text{orbit}} < 0.06a$ , the global EGAM frequency becomes lower than the value at the extremum. This resembles the case when the energy is lower than the top of the potential barrier in a quantum system, meaning that the mode must be localized at the core where it is excited, although “tunneling” to the other side of the barrier (the edge region) is permitted. In this case,  $L_{\text{mode}}$  is found to scale linearly with  $L_{\text{orbit}}$ .

A different relationship between  $L_{\text{mode}}$  and  $L_{\text{orbit}}$  was found by Fu[46] for the inverse Landau damping driven EGAMs, owing to his assumption that those EGAMs are non-extremum type. Nevertheless, the mode structure in his result and in our Fig.6.5(a) share great similarity: the radial electric field peaks at mid radius and vanishes outward. This is due to the fact that the dispersion relationships (second order ODEs) have almost the same structure (but different coefficients), and we have used the same DIII-D profiles and parameters as Fu. Distinguishing between different types of EGAMs merely by looking at the radial mode structure is therefore difficult at the current stage. In order to enable a detailed comparison between the mode structure of different types of EGAMs, we would propose a thorough scan over the relationship between the EGAM mode structures of both types and the equilibrium profiles.

Based on the two cases with different  $q$  profiles, we have also investigated the dependency of the global mode frequency and growth rate on the injection direction. It is shown that the global EGAM frequency in the presence of a counter-beam is slightly lower than the co-beam, but is significantly more unstable compared to the co-beam case. Given the same amount of damping, it is possible that the counter-beam reactive EGAM can encounter the damping while the co-beam one is suppressed, consistent with the observation that EGAMs are more likely to appear in counter-beam experiments.

In our future work, we plan to release the assumption  $L_{\text{orbit}} \ll L_{\text{mode}}$  and takes into



account the full drift orbit effects of the fast ions. This may involve the use of a non-local fluid closure. The comparison to existing kinetic codes with full drift orbit effects such as LIGKA [178] is also possible. In the perspective of validation, a survey of the mode frequency is needed for different injection directions, while the measurement of the mode structure can be available through spectroscopy with good temporal ( $\sim$  a few ms for beam turn on) and spatial resolution (sufficient for radial structure) such as soft x-ray [179].

## 6.6 Appendix: Higher order $O(\epsilon\delta^l)$ terms in the equilibrium density profile

If we define

$$n_{f,\delta^l} \approx \bar{n}_{f,\delta^l} \left[ 1 - (1 + c_{f,\delta^l}) \frac{r}{R_0} \cos \theta \right] \cos^l \theta, \quad (6.60)$$

after calculating the  $O(\epsilon\delta)$  and  $O(\epsilon\delta^2)$  component of the equilibrium continuity equation, we get that

$$\begin{aligned} c_{f,\delta} &= c_f + \frac{1}{2} \frac{\Lambda_0}{2 - \Lambda_0} c_f, \\ c_{f,\delta^2} &= \frac{2}{2 - \Lambda_0} c_f, \end{aligned} \quad (6.61)$$

which will be used in further calculation in Appendix 6.7.

## 6.7 Appendix: Detail derivation of the higher order fast ion drift current

The parallel direction of Eq. (6.12) gives the equations for the parallel velocity. Retaining only the zeroth order terms in  $\epsilon$ , we have in  $O(\delta)$  that

$$\tilde{V}_{f\parallel,\delta}^{m=\pm 2} = \mp \frac{1}{2} \frac{\bar{V}_{f,\text{mag}}}{\omega \mp 2\omega_b} \left( \frac{d}{dr} - \frac{1}{r} \right) \tilde{V}_{f\parallel,\delta^0}^{m=\pm 1}, \quad (6.62)$$

$$\tilde{V}_{f\parallel,\delta}^{m=0} = \frac{1}{2} \frac{\bar{V}_{f,\text{mag}}}{\omega} \left( \frac{d}{dr} + \frac{1}{r} \right) (\tilde{V}_{f\parallel,\delta^0}^{m=1} - \tilde{V}_{f\parallel,\delta^0}^{m=-1}), \quad (6.63)$$

and in  $O(\delta^2)$  that

$$\tilde{V}_{f\parallel,\delta^2}^{m=\pm 1} = \pm \frac{1}{2} \frac{\bar{V}_{f,\text{mag}}}{\omega \mp \omega_b} \left[ \left( \frac{d}{dr} + \frac{2}{r} \right) \tilde{V}_{f\parallel,\delta}^{m=\pm 2} - \frac{d\tilde{V}_{f\parallel,\delta}^{m=0}}{dr} \right]. \quad (6.64)$$

The perpendicular direction of Eq. (6.12), if the polarization drift and the diamagnetic drift are excluded, gives in  $O(\delta)$  that

$$(\nabla \cdot n \widetilde{\mathbf{V}_{f\perp\text{mag},\delta}})^{m=\pm 2} = \mp \frac{i}{2} \left( \frac{d}{dr} - \frac{1}{r} \right) \bar{V}_{f,\text{mag}} \left( \tilde{n}_{f,\delta^0}^{m=\pm 1} + \bar{n}_{f,\delta^0} \frac{2}{1 + c_f} \frac{\tilde{V}_{f\parallel,\delta^0}^{m=\pm 1}}{\omega_b q R_0} \right), \quad (6.65)$$

$$(\nabla \cdot n \widetilde{\mathbf{V}_{f\perp\text{mag},\delta}})^{m=0} = \frac{i}{2} \left( \frac{d}{dr} + \frac{1}{r} \right) \bar{V}_{f,\text{mag}} \left( \tilde{n}_{f,\delta^0}^{m=1} + \bar{n}_{f,\delta^0} \frac{2}{1+c_f} \frac{\tilde{V}_{f\parallel,\delta^0}^{m=\pm 1}}{\omega_b q R_0} \right. \\ \left. - \tilde{n}_{f,\delta^0}^{m=-1} - \bar{n}_{f,\delta^0} \frac{2}{1+c_f} \frac{\tilde{V}_{f\parallel,\delta^0}^{m=\pm 1}}{\omega_b q R_0} \right), \quad (6.66)$$

in  $O(\delta^2)$  that

$$(\nabla \cdot n \widetilde{\mathbf{V}_{f\perp\text{mag},\delta^2}})^{m=\pm 1} = \pm \frac{i}{2} \left( \frac{d}{dr} + \frac{2}{r} \right) \bar{V}_{f,\text{mag}} \left( \tilde{n}_{f,\delta}^{m=\pm 2} + \bar{n}_{f,\delta} \frac{2}{1+c_f} \frac{\tilde{V}_{f\parallel,\delta}^{m=\pm 2}}{\omega_b q R_0} \right) \\ \mp \frac{i}{2} \frac{d}{dr} \bar{V}_{f,\text{mag}} \left( \tilde{n}_{f,\delta}^{m=0} + \bar{n}_{f,\delta^0} \frac{2}{1+c_f} \frac{\tilde{V}_{f\parallel,\delta}^{m=0}}{\omega_b q R_0} \right) \\ \mp \frac{i}{1+c_f} \bar{V}_{f,\text{mag}} \left( \frac{1}{2} \frac{d}{dr} \bar{n}_{f,\delta} \frac{\tilde{V}_{f\parallel,\delta^0}^{m=\mp 1}}{\omega_b q R_0} - \frac{1}{r} \bar{n}_{f,\delta} \frac{\tilde{V}_{f\parallel,\delta^0}^{m=\pm 1}}{\omega_b q R_0} \right), \quad (6.67)$$

and finally in  $O(\delta^3)$  that

$$(\nabla \cdot n \widetilde{\mathbf{V}_{f\perp\text{mag},\delta^3}})^{m=0} = \frac{i}{2} \left( \frac{d}{dr} + \frac{1}{r} \right) \bar{V}_{f,\text{mag}} \left[ \tilde{n}_{f,\delta^2}^{m=1} - \tilde{n}_{f,\delta^2}^{m=-1} \right. \\ \left. + \frac{2}{1+c_f} \frac{1}{\omega_b q R_0} \left( \bar{n}_{f,\delta^0} \tilde{V}_{f\parallel,\delta^2}^{m=1} - \bar{n}_{f,\delta^0} \tilde{V}_{f\parallel,\delta^2}^{m=-1} \right. \right. \\ \left. \left. + \frac{1}{2} \bar{n}_{f,\delta} \tilde{V}_{f\parallel,\delta}^{m=2} - \frac{1}{2} \bar{n}_{f,\delta} \tilde{V}_{f\parallel,\delta}^{m=-2} - \frac{1}{4} \bar{n}_{f,\delta^2} \tilde{V}_{f\parallel,\delta^0}^{m=1} - \frac{1}{4} \bar{n}_{f,\delta^2} \tilde{V}_{f\parallel,\delta^0}^{m=-1} \right) \right], \quad (6.68)$$

which are used in the calculation of the perturbed density and

$$\langle \nabla \cdot \tilde{\mathbf{J}}_{i\perp,\delta^3} \rangle = e(\nabla \cdot n \widetilde{\mathbf{V}_{f\perp\text{mag},\delta^3}})^{m=0}. \quad (6.69)$$

The perturbed density is calculated through the continuity equation Eq. (6.13), which converts to

$$i(\omega \mp 2\omega_b) \tilde{n}_{f,\delta}^{m=\pm 2} = (\nabla \cdot n \widetilde{\mathbf{V}_{f\perp\text{mag},\delta}})^{m=\pm 2} \pm ik(2\bar{n}_{f,\delta^0} \tilde{V}_{f\parallel,\delta}^{m=\pm 2} + ik\bar{n}_{f,\delta} \tilde{V}_{f\parallel,\delta^0}^{m=\pm 1}) \\ \pm \frac{i}{2R_0} \left( -c_{f,\delta} \bar{n}_{f,\delta} + \frac{R_0}{r} \bar{n}_{f,\delta^2} \right) \tilde{V}_E, \quad (6.70)$$

$$i\omega \tilde{n}_{f,\delta}^{m=0} = (\nabla \cdot n \widetilde{\mathbf{V}_{f\perp\text{mag},\delta}})^{m=0}, \quad (6.71)$$

and

$$i(\omega \mp \omega_b) \tilde{n}_{f,\delta^2}^{m=\pm 1} = (\nabla \cdot n \widetilde{\mathbf{V}_{f\perp\text{mag},\delta^2}})^{m=\pm 1} \pm ik[\bar{n}_{f,\delta^0} \tilde{V}_{f\parallel,\delta^2}^{m=\pm 1} + \frac{1}{2} \bar{n}_{f,\delta} (\tilde{V}_{f\parallel,\delta}^{m=0} + \tilde{V}_{f\parallel,\delta}^{m=\pm 2}) \\ + \frac{1}{2} \bar{n}_{f,\delta^2} (\tilde{V}_{f\parallel,\delta^0}^{m=\pm 1} + \frac{1}{2} \tilde{V}_{f\parallel,\delta^0}^{m=\mp 1})] \pm \frac{i}{8R_0} \left[ -\bar{n}_{f,\delta^2} (1 + 3c_{f,\delta^2}) + 3 \frac{R_0}{r} \bar{n}_{f,\delta^3} \right] \tilde{V}_E \quad (6.72)$$

## 6.8 Appendix: Auxiliary equations

$$F_3 = -\frac{3}{8} \frac{\omega_b^5 q^2}{(\omega^2 - \omega_b^2)(\omega^2 - 4\omega_b^2)}, \quad (6.73)$$

$$F_4 = -\frac{3}{8} \omega_b^5 q^2 \frac{\partial}{\partial \omega_b} \left[ \frac{\omega_b}{(\omega^2 - 4\omega_b^2)(\omega^2 - \omega_b^2)} \right], \quad (6.74)$$

$$B_3 = (1 + c_f)^3 \left( 4 - 2c_{f,\delta} + 2 \frac{\bar{n}_{f,\delta^2} R_0}{\bar{n}_{f,\delta} r} \right), \quad (6.75)$$

$$B_4 = (1 + c_f)^4, \quad (6.76)$$

$$\begin{aligned} F_5 = & -\frac{1}{16} (1 + c_f)^3 \left[ \frac{\omega_b^3 q^2}{\omega^2 - \omega_b^2} \left( 1 - 3c_{f,\delta^2} + 3 \frac{\bar{n}_{\delta^3} R_0}{\bar{n}_{\delta^2} r} \right) + \frac{2\omega_b^5 q^2}{(\omega^2 - \omega_b^2)^2} (1 + c_f) \right] \times r \frac{d}{dr} \frac{1}{r} \frac{\bar{n}'_{\delta^0}}{\omega_b} \\ & + \frac{1}{16} \bar{n}_{\delta^0} B_1 \frac{\omega_b^4 q^2}{\omega} \left( \frac{1}{\omega - \omega_b} \frac{1}{r} \frac{d}{dr} r \frac{1}{\omega - 2\omega_b} r^2 \frac{d}{dr} \frac{1}{r^2} \frac{1}{\omega - \omega_b} \right. \\ & + \frac{1}{\omega + \omega_b} \frac{1}{r} \frac{d}{dr} r \frac{1}{\omega + 2\omega_b} r^2 \frac{d}{dr} \frac{1}{r^2} \frac{1}{\omega + \omega_b} + \frac{4\omega}{\omega^2 - \omega_b^2} r \frac{d}{dr} \frac{1}{r} \frac{d}{dr} \frac{1}{\omega^2 - \omega_b^2} \Big) \\ & + \frac{1}{16} \bar{n}_{\delta^0} B_2 \frac{\omega_b^4 q^2}{\omega} \left[ \frac{1}{\omega - \omega_b} \frac{1}{r} \frac{d}{dr} r \frac{1}{\omega - 2\omega_b} r^2 \frac{d}{dr} \frac{1}{r^2} \frac{\omega_b}{(\omega - \omega_b)^2} \right. \\ & + \frac{\omega_b}{(\omega - \omega_b)^2} \frac{1}{r} \frac{d}{dr} r \frac{1}{\omega - 2\omega_b} r^2 \frac{d}{dr} \frac{1}{r^2} \frac{1}{\omega - \omega_b} \\ & + \frac{1}{\omega - \omega_b} \frac{1}{r} \frac{d}{dr} r \frac{2\omega_b}{(\omega - 2\omega_b)^2} r^2 \frac{d}{dr} \frac{1}{r^2} \frac{1}{\omega - \omega_b} \\ & - \frac{1}{\omega + \omega_b} \frac{1}{r} \frac{d}{dr} r \frac{1}{\omega + 2\omega_b} r^2 \frac{d}{dr} \frac{1}{r^2} \frac{\omega_b}{(\omega + \omega_b)^2} \\ & - \frac{\omega_b}{(\omega + \omega_b)^2} \frac{1}{r} \frac{d}{dr} r \frac{1}{\omega + 2\omega_b} r^2 \frac{d}{dr} \frac{1}{r^2} \frac{1}{\omega + \omega_b} \\ & - \frac{1}{\omega + \omega_b} \frac{1}{r} \frac{d}{dr} r \frac{2\omega_b}{(\omega + 2\omega_b)^2} r^2 \frac{d}{dr} \frac{1}{r^2} \frac{1}{\omega + \omega_b} \\ & + \frac{8\omega\omega_b^2}{(\omega^2 - \omega_b^2)^2} r \frac{d}{dr} \frac{1}{r} \frac{d}{dr} \frac{1}{\omega^2 - \omega_b^2} + \frac{8\omega}{\omega^2 - \omega_b^2} r \frac{d}{dr} \frac{1}{r} \frac{d}{dr} \frac{8\omega_b^2}{(\omega^2 - \omega_b^2)^2} \Big] \\ & - \frac{1}{16} \bar{n}'_{\delta^0} \frac{\omega_b^4 q^2}{\omega} \left( \frac{B_3}{\omega - \omega_b} \frac{d}{dr} \frac{1}{\omega - 2\omega_b} + \frac{B_3}{\omega + \omega_b} \frac{d}{dr} \frac{1}{\omega + 2\omega_b} \right. \\ & + B_4 \frac{\omega_b}{(\omega - \omega_b)^2} \frac{d}{dr} \frac{1}{\omega - 2\omega_b} + B_4 \frac{1}{\omega - \omega_b} \frac{d}{dr} \frac{2\omega_b}{(\omega - 2\omega_b)^2} \\ & \left. - B_4 \frac{\omega_b}{(\omega + \omega_b)^2} \frac{d}{dr} \frac{1}{\omega + 2\omega_b} - B_4 \frac{1}{\omega + \omega_b} \frac{d}{dr} \frac{2\omega_b}{(\omega + 2\omega_b)^2} \right) \quad (6.77) \end{aligned}$$

---

# Conclusion

---

In this thesis, we've focused on the use of fluid theories in studying the equilibrium and stability of tokamak plasmas in the presence of fast ions generated by external heating methods such as NBI and ICRH, as well as the physics implications.

Fast ions induce pressure anisotropy due to their low collision frequency and the strong magnetic field. By considering the whole plasma (the thermal plasma and the fast ions) as a single fluid with bi-Maxwellian distribution, the simplest model that captures pressure anisotropy, we have studied various physics aspects of an anisotropic equilibrium model, as well as its difference from the widely applied isotropic MHD model. In addition, we have implemented pressure anisotropy and flow into the fix-boundary Grad-Shafranov numeric solver HELENA, forming a new branch HELENA+ATF, and computed parameter scans using this code. It is found that the diamagnetic current is mainly determined by the perpendicular pressure, while the Shafranov-shift is determined by  $p^*$ , the average of the perpendicular and parallel pressure. When an isotropic model is used to describe an anisotropic plasma, the accuracy of the former is usually sacrificed for the accuracy of the latter, in which a  $p^*$  approximation is used, i.e.  $p^*$  is taken to be the isotropic pressure. The drawback of the isotropic approximation is divided into different regimes determined by the magnitude of pressure anisotropy and the aspect ratio, with increasing problems for tighter aspect ratio machines and larger anisotropy. For a ST such as MAST, the effect of pressure anisotropy can therefore be significant if an isotropic model is used: the diamagnetic current is different; the constant pressure surfaces are shifted from the flux surfaces contrary to isotropic MHD prediction; and finally for a large anisotropy, the magnetic geometry cannot be reproduced by an isotropic model so the  $q$  profile reported by an isotropic equilibrium reconstruction can be distorted. As a consequence, a fully anisotropic equilibrium model is recommended for STs with strong external heating, such as MAST-U.

Building on the anisotropy equilibrium, we have also added pressure anisotropy into plasma MHD stability code MISHKA, namely MISHKA-A. We have implemented different fluid closures: the incompressible closure, the double-adiabatic closure (CGL), and the recently developed single-adiabatic closure [20]. For the continuum in a large aspect ratio low beta tokamak, different models differ mainly in the prediction of the sound wave frequency and the geodesic acoustic frequency. This is also the case when we scan over the magnitude of pressure anisotropy, while the  $q$  profile and the density profile are kept constant. The impact of anisotropy on  $m = n = 1$  ideal kink mode is also investigated when only the fluid contribution is taken into account. The plasma is stabilized when  $p_{\perp} < p_{\parallel}$ , and destabilized if  $p_{\perp} > p_{\parallel}$ , matching the prediction of Mikhailovskii [120] quantitatively.

The new anisotropic equilibrium and stability tool chain is applied to study two MAST

discharges: #18696@290ms, a discharge with only the inconsistency in the diamagnetic current, and #29221@190ms, a discharge falls into the regime where all three problems reported in Chapter 2 are presented if an isotropic model is used. Not surprisingly, equilibrium reconstructions with/without pressure anisotropy for the latter discharge give distinct  $q$  profiles: reversed shear when the  $p^*$  approximation is used and monotonic shear when anisotropy is resolved properly. The difference in  $q$  profile changes the basic property of stability, leading to a wider TAE gap and TAE radial mode structure in the fully anisotropy case. This difference in the  $q$  profile and therefore particle orbits, along with the difference in mode structure and frequency, result in a higher growth rate and a lower saturation level of the fully anisotropy case.

In summary, the fluid model has been proved useful in resolving the fast ion induced pressure anisotropy and its impact on plasma equilibrium, stability and wave-particle interaction. These fast ions have significantly modified the background plasma supported modes and their nonlinear evolution. In the second half of the thesis, instead of taking the whole plasma as a single fluid, we have considered the fast ions as a separate species. The method has been proved successful in capturing some of the EPs.

We have studied the linear dispersion relationship of the energetic geodesic acoustic modes (EGAMs) in tokamaks, with NBI fast ions taken as a fluid having a collective transit speed along the field lines. The lower frequency mode found by solving the dispersion relationship is unstable. Good qualitative and quantitative agreement with the kinetic theory is found when the beam is cold, even when fluid theory does not capture the physics of wave-particle interaction, contrary to the previous understanding that these EGAMs are driven unstable by energetic particle positive energy gradient. Further inspection on the mode's property reveals its great similarity to the two-stream instability in a beam plasma system, and can transform from a two-stream-like instability (reactive instability) to a bump-on-tail-like instability when the beam profile changes from a mono-energy one to a gentle bump. We named the instability "reactive EGAMs" according to the nature of the instability. We have also shown the consistency of the reactive EGAMs to the EGAMs fast turn-on in DIII-D experiments.

Extending the fluid theory to capture the finite drift orbit width effects of the fast ions, a global theory is developed to solve for the radial mode structure of the reactive EGAMs, under the assumption that the drift orbit width is smaller than the mode width. A robust global mode structure is formed with the mode width depending on the fast ion drift orbit width, a typical characteristic of EPs. We have found that the density change on flux surfaces due to the FOW effect is responsible for the distinction between the co- and counter-passing orbits. The counter-injection scenario has a higher growth rate than the co-injection one, which helps to explain the experimental observation that EGAMs are more commonly observed in counter-injection discharges.

The success of the fluid theory in modeling the reactive EGAMs consolidate the important role it can play in capturing the physics of fast ions in tokamaks, and in complementing the kinetic picture. Without the fluid theory and its simplicity and intuitive nature, the physics of reactive EGAMs would not be revealed and would be confused with that of the wave-particle interaction mechanism.

In conclusion, the fluid theory is proved useful and competent in the physic study of the externally heated tokamak plasmas. Future works in the space of pressure anisotropy involve an inspection on other types of waves and instabilities, such as the peeling-ballooning modes which are responsible for the Edge Localized Modes (ELMs) [180]. A survey on the magnitude of anisotropy and its impact on a variety of machines should be conducted,

---

including MAST-U, NSTX and ITER. On the side of reactive EGAMs, a more realistic description of fast ions in DIII-D plasma requires the relaxation of the small orbit size assumption. A nonlinear study is also possible to fully cover the conversion from the reactive EGAMs to the wave-particle interaction driven ones as the beam slows down. Finally, more general application of the fluid theory on tokamak plasmas with external heating should be further investigated. For instance, the impact of toroidal and poloidal flow on the plasma configuration could be examined across a wider range of parameters. The approach to model EGAMs could be extended to other modes observed immediately after beam turn on.



# Detail derivation of local fluid EGAMs

## A.1 Model

### A.1.1 Equilibrium

Our work extends the fluid model of the conventional GAMs by Sgalla *et al* [75], adding multiple fluid components and the coupling to sound waves. We start with a tokamak plasma with large aspect ratio, circular cross section and low  $\beta$ . We can now use a simplified set of coordinate  $(r, \theta, \varphi)$ , labeling the radial coordinate, the poloidal and toroidal angle, respectively. The outward shift of the flux surfaces, namely the Shafranov shift, is ignored in our treatment. The major radius and the magnetic field strength are approximately given by  $R \approx R_0(1 + r/R_0 \cos \theta)$  and  $B \approx B_0(1 - r/R_0 \cos \theta)$ . The unit vector parallel to the direction of the magnetic field is given by

$$\mathbf{b} \equiv \frac{\mathbf{B}}{B} = \frac{B_\theta}{B} \mathbf{e}_\theta + \frac{B_\varphi}{B} \mathbf{e}_\varphi. \quad (\text{A.1})$$

For convenience, we define the bi-normal unit vector  $\boldsymbol{\pi} \equiv \mathbf{b} \times \mathbf{e}_r$ . So we now have another set of orthogonal unit vector triad  $(\mathbf{e}_r, \boldsymbol{\pi}, \mathbf{b})$ . The geodesic curvature is defined as  $\kappa_g \equiv \boldsymbol{\kappa} \cdot \boldsymbol{\pi}$ , where  $\boldsymbol{\kappa} \equiv \mathbf{b} \cdot \nabla \mathbf{b}$  is the magnetic field curvature. We also have the identity

$$\nabla \cdot \boldsymbol{\pi} \approx -\boldsymbol{\pi} \cdot \nabla \ln B \approx (\mathbf{b} \cdot \nabla \boldsymbol{\pi}) \cdot \mathbf{b} = -\kappa_g \approx -\sin \theta / R_0, \quad (\text{A.2})$$

which are all considered as geodesic curvature.

In the local treatment, we ignore orbit FOW and FLR effects, making  $\delta \equiv q\rho_s \ll L_{\text{mode}} \lesssim a$ , where  $\rho_s$  is the Larmor radius and  $q\rho_s$  gives approximately the drift orbit width.

We assume that the plasma consist of  $s$  ion species (subscript “ $s$ ” for the index of species), each species of ion has a mass  $m_s$  and a charge  $e$  (singly charged). We note that they can either be different types of ions, or the same type of ions but with a different energy as considered in this section, i.e. thermal ions and fast ions. The density  $n_s$ , the flow  $\mathbf{V}_{0s}$ , the parallel pressure  $p_{\parallel s}$  and the perpendicular pressure  $p_{\perp s}$  can be obtained by integrals of the guiding center distribution  $F_s(\mu, E, r)$ , where  $\mu = m_s v_\perp^2 / 2B$  is the magnetic moment,  $E = m_s v^2 / 2$  the energy and  $r$  the flux surface (the  $r$  dependency here is unimportant and removed in later treatments due to our assumption of small orbit width).



For density  $n_s$ , its partial derivatives with respect to  $B$  is given by

$$\left(\frac{\partial n_s}{\partial B}\right)_r = \frac{n_s + C_{Bs}}{B}. \quad (\text{A.3})$$

The equilibrium flow  $\mathbf{V}_{0s}$  is a combination of a pure toroidal flow and a flow along the field line [181]. In this work, we only consider the flow along the field line, which gives the form

$$\mathbf{V}_{0s} = V_{0s} \mathbf{b} = \frac{\psi_s(r)}{n_s} \mathbf{B}. \quad (\text{A.4})$$

This equilibrium parallel velocity will be zero for the thermal ions and electrons in our work, but finite for the hot ion population. Finally, the poloidal dependency of  $p_{\parallel s}$  and  $p_{\perp s}$  are calculated as

$$\left(\frac{\partial p_{\parallel s}}{\partial B}\right)_r = \frac{p_{\parallel s} - p_{\perp s} + m_s C_{Bs} V_{0s}^2}{B}, \quad (\text{A.5})$$

$$\left(\frac{\partial p_{\perp s}}{\partial B}\right)_r = \frac{2p_{\perp s} + \hat{c}_s}{B}, \quad (\text{A.6})$$

where  $C_{Bs}$  and  $\hat{c}_s$  are kinetic integrals.

In this work, we follow the definitions in Antonsen and Lee [106], where

$$\begin{pmatrix} n_s \\ V_{0s} \\ p_{\parallel s} \\ p_{\perp s} \end{pmatrix} = \frac{2\pi B}{m_s^2} \sum_{v_{\parallel} > 0, < 0} \int \begin{pmatrix} 1 \\ v_{\parallel} \\ (v_{\parallel} - V_{0s})^2 \\ \mu B \end{pmatrix} F_s \frac{1}{|v_{\parallel}|} d\mu dE. \quad (\text{A.7})$$

The derivatives of these quantities with respect to  $r, B$  and  $\Phi$  can be obtained from Eq. (A.7), noting that  $v_{\parallel} = \sqrt{2E - 2\mu B}/\sqrt{m_s}$  and has a dependency on  $B$  as well. The results are

$$\begin{aligned} n_{Bs} &= (n_s + C_{Bs})/B, \\ p_{\parallel Bs} &= (p_{\parallel s} - p_{\perp s})/B + m_s V_{0s}^2 C_{Bs}/B, \\ p_{\perp Bs} &= (2p_{\perp s} + \hat{c}_s)/B, \end{aligned} \quad (\text{A.8})$$

where

$$\begin{pmatrix} C_{Bs} \\ \hat{c}_s \end{pmatrix} = \frac{2\pi B}{m_s^2} \sum_{v_{\parallel} > 0, < 0} \int \begin{pmatrix} \mu B \\ (\mu B)^2 \end{pmatrix} \frac{\partial F_s}{\partial E} \frac{1}{|v_{\parallel}|} d\mu dE. \quad (\text{A.9})$$

Due to their fast transit speed, the electrons are assumed to be isothermal on a flux surface with a temperature  $T_e$ . The quasi-neutrality condition provides a relationship between electron density and ion density, which writes

$$n_0 = \sum_s n_s, \quad (\text{A.10})$$

in which  $n_0$  is the electron density and  $e$  is the charge of an electron. Since  $n_s$  has a non-trivial poloidal dependency, we would expect  $n_0$  to depend on poloidal angle as well. This

dependency is sustained by a parallel equilibrium electric field and electrostatic potential  $\Phi$ . This equilibrium parallel electric field is a next order correction in the drift ordering (the zero order being the  $\mathbf{E} \times \mathbf{B}$  drift), and therefore not presented in the ideal MHD theory. We note that the removal of this equilibrium parallel electric field will not change the stability result substantially, therefore we will drop it from now on.

### A.1.2 Ion response

The GAMs are electrostatic modes with  $n = 0$ . We retain only the  $m = 0$  part of the perturbed electrostatic potential and two sidebands with  $m = \pm 1$ , written as

$$\tilde{\Phi} = \tilde{\Phi}_0(r)e^{-i\omega t} + \tilde{\Phi}_{+1}(r)e^{i\theta-i\omega t} + \tilde{\Phi}_{-1}(r)e^{-i\theta-i\omega t}. \quad (\text{A.11})$$

We have assumed all the perturbed quantities are proportional to  $e^{-i\omega t}$ , where  $\omega = \omega_r + i\gamma$  is the complex frequency, with  $\omega_r$  and  $\gamma$  the real frequency and the growth rate, respectively. The response of ion pressures,  $\tilde{p}_{\parallel s}$  and  $\tilde{p}_{\perp s}$ , are described by the double-adiabatic (CGL) fluid closure, given by

$$\frac{d\tilde{p}_{\parallel s}}{dt} = -p_{\parallel s} \nabla \cdot \tilde{\mathbf{V}}_s - 2p_{\parallel s} \mathbf{b} \cdot (\mathbf{b} \cdot \nabla \tilde{\mathbf{V}}_s), \quad (\text{A.12})$$

$$\frac{d\tilde{p}_{\perp s}}{dt} = -2p_{\perp s} \nabla \cdot \tilde{\mathbf{V}}_s + p_{\perp s} \mathbf{b} \cdot (\mathbf{b} \cdot \nabla \tilde{\mathbf{V}}_s). \quad (\text{A.13})$$

The perturbed velocity consists of both the perpendicular and parallel components, written as

$$\tilde{\mathbf{V}}_s = \tilde{V}_{E0}(r)e^{-i\omega t} \frac{B_0}{B} \boldsymbol{\pi} + [\tilde{V}_{s+}(r)e^{i\theta-i\omega t} + \tilde{V}_{s-}(r)e^{-i\theta-i\omega t}] \mathbf{b} + O(\delta), \quad (\text{A.14})$$

where the  $O(\delta)$  terms are higher order corrections such as the magnetic curvature/gradient drift and the diamagnetic drift. Under our assumption of zero orbit width giving local GAM solutions, it is sufficient to keep only  $\tilde{\mathbf{V}}_E$ , the  $\mathbf{E} \times \mathbf{B}$  drift velocity in the perturbed perpendicular velocity in the CGL equations, which is given by

$$\tilde{\mathbf{V}}_E \approx \frac{\tilde{E}_r \mathbf{e}_r \times \mathbf{B}}{B^2} e^{-i\omega t} \approx \frac{\tilde{\Phi}'_0}{B} e^{-i\omega t} \boldsymbol{\pi} = \tilde{V}_{E0}(r) \frac{B_0}{B} e^{-i\omega t} \boldsymbol{\pi}, \quad (\text{A.15})$$

where we have used  $\tilde{\Phi}_0/\tilde{\Phi}_{\pm 1} \gg 1$ , an assumption that we will justify later.

Using Eq. (A.2) and extending  $\tilde{p}_{\parallel s}$  and  $\tilde{p}_{\perp s}$  similarly into poloidal Fourier harmonics, we obtain to the zeroth order of  $r/R$ ,  $\tilde{p}_{\parallel s0} = \tilde{p}_{\perp s0} = 0$  and

$$\tilde{p}_{\parallel s\pm 1} = \pm \left\langle 4p_{\parallel s} - B \left( \frac{\partial p_{\parallel s}}{\partial B} \right)_r \right\rangle \frac{1}{2R_0\omega_{s\pm}} \tilde{V}_{E0} \pm \frac{k}{\omega_{s\pm}} \langle 3p_{\parallel s} \rangle \tilde{V}_{s\pm}, \quad (\text{A.16})$$

$$\tilde{p}_{\perp s\pm 1} = \pm \left\langle 3p_{\perp s} - B \left( \frac{\partial p_{\perp s}}{\partial B} \right)_r \right\rangle \frac{1}{2R_0\omega_{s\pm}} \tilde{V}_{E0} \pm \frac{k}{\omega_{s\pm}} \langle p_{\perp s} \rangle \tilde{V}_{s\pm}, \quad (\text{A.17})$$

in which  $k = 1/qR_0$  and  $\omega_{s\pm} = \omega \mp k \langle V_{0s} \rangle$  is the Doppler shifted frequency, while  $\langle \dots \rangle$  indicates the flux surface average. We can now see clearly that the perturbed pressures only have  $m = 1$  components. Also,  $\tilde{\mathbf{V}}_E$ , therefore  $\tilde{\Phi}_0$ , drives the  $m = 1$  pressure perturbation through the geodesic curvature.

The ion density perturbation is given by the continuity equation:

$$\frac{\partial \tilde{n}_s}{\partial t} = -\nabla \cdot (n_s \tilde{\mathbf{V}}_s) - \nabla \cdot (\tilde{n}_s \mathbf{V}_s). \quad (\text{A.18})$$

Again using Eq. (A.2) and retaining the zeroth order terms in  $r/R$ , the  $m = \pm 1$  harmonics of the ion density perturbation are given by

$$\tilde{n}_{s\pm 1} = \pm \left\langle 2n_s - B \left( \frac{\partial n_s}{\partial B} \right)_r \right\rangle \frac{1}{2R_0 \omega_{s\pm}} \tilde{V}_{E0} \pm \frac{k}{\omega_{s\pm}} \langle n_s \rangle \tilde{V}_{s\pm}, \quad (\text{A.19})$$

and  $\tilde{n}_{s0} = 0$ .

### A.1.3 Electron response

Since the electron transit frequency is much higher than the frequency of the mode, the response of electron is assumed to be isothermal (alias adiabatic in kinetic theory), which means  $\tilde{p}_e = \tilde{n}_e T_e$ , with  $\tilde{p}_e$  and  $\tilde{n}_e$  the perturbed electron pressure and density, respectively. Ignoring electron inertial, the momentum equation of electron gives

$$0 = n_0 e \nabla \tilde{\Phi} - n_0 e \tilde{\mathbf{V}}_e \times \mathbf{B} - T_e \nabla \tilde{n}_e, \quad (\text{A.20})$$

where  $\tilde{\mathbf{V}}_e$  is the perturbed electron velocity. We have used the electrostatic approximation, setting the perturbed magnetic field to be zero. The parallel direction of Eq. (A.20) gives

$$\tilde{n}_e = n_0 e \frac{\tilde{\Phi} - \langle \tilde{\Phi} \rangle}{T_e}, \quad (\text{A.21})$$

in which we have neglected the first term of Eq. (A.20) that is  $O(r/R)$ . Due to particle conservation,  $\langle \tilde{n}_e \rangle = 0$ . The  $m = \pm 1$  harmonics are obtained by expanding Eq. (A.21) poloidally, which are given by

$$\tilde{n}_{e\pm 1} = \langle n_0 \rangle e \frac{\tilde{\Phi}_{\pm 1}}{T_e}. \quad (\text{A.22})$$

Taking in to account Eq. (A.19) and the quasi-neutrality condition Eq. (A.10), we will reach

$$\tilde{n}_{e\pm 1} = \pm \frac{\tilde{V}_{E0}}{2R_0} \sum_s \frac{1}{\omega_{s\pm}} \left\langle 2n_s - B \left( \frac{\partial n_s}{\partial B} \right)_r \right\rangle \pm k \sum_s \frac{\langle n_s \rangle}{\omega_{s\pm}} \tilde{V}_{s\pm}, \quad (\text{A.23})$$

with the perturbed electron pressure obtained by  $\tilde{p}_e = \tilde{n}_e T_e$ .

Equating Eq. (A.19) and (A.21), one can obtain the following relationship:  $\tilde{\Phi}^{m=\pm 1} / \tilde{\Phi}^{m=0} \sim O(\epsilon \delta \sqrt{T_e / m_f V_{f0}^2})$  and thereby  $\tilde{\Phi}^{m=\pm 1}$  is ignored in the  $\mathbf{E} \times \mathbf{B}$  drift.

### A.1.4 The momentum equation

The perturbed momentum equation for each species  $s$  has the form

$$\begin{aligned} m_s n_s \left( \frac{\partial \mathbf{V}_s}{\partial t} + \frac{\tilde{n}_s}{n_s} \mathbf{V}_{0s} \cdot \nabla \mathbf{V}_{0s} + \mathbf{V}_{s0} \cdot \nabla \tilde{\mathbf{V}}_s + \tilde{\mathbf{V}}_s \cdot \nabla \mathbf{V}_{s0} \right) = \\ n_s e (-\nabla \tilde{\Phi} + \tilde{\mathbf{V}}_s \times \mathbf{B}) - \nabla p_{\perp s} - (\tilde{p}_{\parallel s} - \tilde{p}_{\perp s}) \boldsymbol{\kappa} \\ - \mathbf{b} \nabla \cdot [(\tilde{p}_{\parallel s} - \tilde{p}_{\perp s}) \mathbf{b}]. \end{aligned} \quad (\text{A.24})$$

Adding up Eq. (A.24) for all ion species and Eq. (A.20), the potential gradient term cancels out because of charge neutrality. Also using the definition for perturbed current  $\tilde{\mathbf{J}} = \sum_s n_s e \tilde{\mathbf{V}}_s - n_0 e \tilde{\mathbf{V}}_e$ , the sum of  $n_s e \tilde{\mathbf{V}}_s \times \mathbf{B}$  terms becomes  $\tilde{\mathbf{J}} \times \mathbf{B}$ . This perturbed current is then eliminated by the charge neutrality condition  $\nabla \cdot \tilde{\mathbf{J}} = 0$  and the fact that  $\langle \nabla \cdot \tilde{\mathbf{J}}_{\parallel} \mathbf{b} \rangle = 0$ , i.e. by taking the cross product of both sides of the added up equation and  $\mathbf{b}/B$ , followed by a divergence operation, and finally a flux surface average. This treatment also eliminates the parallel components of Eq. (A.25), leaving only the perpendicular components. After integrating both sides over  $r$  the considering  $J_r = 0$  on axis, the result is given by

$$\begin{aligned} \langle \rho \rangle \omega V_{E0} = \frac{1}{2R_0} \sum_s [p_{\perp s+1} - p_{\perp s-1} + p_{\parallel s+1} - p_{\parallel s-1} + m_s(\tilde{n}_{s+1} - \tilde{n}_{s-1}) \langle V_{0s}^2 \rangle \\ + 2m_s \langle n_s V_{0s} \rangle (\tilde{V}_{s+} - \tilde{V}_{s-})] + \frac{1}{R_0} (\tilde{n}_{e+1} - \tilde{n}_{e-1}) T_e, \end{aligned} \quad (\text{A.25})$$

where  $\rho = \sum_s m_s n_s$  is the mass density. Again we have kept the leading order in  $r/R$  and ignored the radial change of equilibrium quantities.

For the parallel component of Eq. (A.24), we use Eq. (A.20) to eliminate the electric field term for individual species  $s$ . The  $m = \pm 1$  harmonics are then given by

$$\begin{aligned} m_s \langle n_s \rangle \omega_{s\pm} \tilde{V}_{s\pm} = \pm \frac{m_s \langle V_{0s} \rangle}{2R_0} \left\langle B \left( \frac{\partial n_s}{\partial B} \right)_r \right\rangle \tilde{V}_E \\ \pm k \left( \tilde{p}_{\parallel s\pm 1} + \left\langle \frac{n_s}{n_0} \right\rangle \tilde{n}_{e\pm 1} T_e \right). \end{aligned} \quad (\text{A.26})$$

Equation (A.25) and (A.26), along with Eq. (A.16), (A.17) and (A.23), close the system and define an eigenvalue problem of  $\omega$ , i.e. the dispersion relationship.

## A.2 Dispersion relationship for thermal plasma with bump-on-tail fast ions

### A.2.1 Bump-on-tail fast ions

We generalize the bump-on-tail fast ion distribution function

$$F_f(v_{\parallel}, v_{\perp}) = A \exp \left[ -\frac{m_f(v_{\parallel} - V_{0f})^2 + m_f v_{\perp}^2}{2T_f} \right], \quad (\text{A.27})$$

to a distribution function  $F(\mu, E)$  that satisfy conservation of energy and magnetic moments on a flux surface. We rewrite A.27 in to a function of  $\mu$ ,  $E$ ,  $r$ ,  $B$  and  $\Phi$ , given by

$$F_f = A \exp \left[ -\frac{E + mV_{0f}^2/2 + \sqrt{2m(E - \mu B_0)} V_{0f}}{T_f} \right]. \quad (\text{A.28})$$

We have replaced  $\sqrt{2m(E - \mu B)}$  by  $\sqrt{2m(E - \mu B_0)}$ , making  $F_f = F_f(\mu, E)$  independent of  $B$ . For this distribution function, we have  $\langle p_{\parallel f} \rangle = \langle p_{\perp f} \rangle = \langle n_f \rangle T_f$ . In the large aspect

ratio scenario, the kinetic integrals are given by

$$\begin{aligned} C_{Bf} &\approx -n_f + n_f \bar{V}_{0f} \text{Re}[Z(-\bar{V}_{0f})], \\ \hat{c}_f &\approx -2p_{\perp f} + 2p_{\perp f} \bar{V}_{0f} \text{Re}[Z(-\bar{V}_{0f})], \end{aligned} \quad (\text{A.29})$$

where  $Z(x)$  is the plasma dispersion function and

$$\bar{V}_{0f} = V_{0f} / \sqrt{\frac{2T_f}{m_f}}. \quad (\text{A.30})$$

The value of  $\bar{V}_{0f} \text{Re}[Z(-\bar{V}_{0f})]$  as a function of  $\bar{V}_{0f}$  is plotted in Fig.A.1. The figure shows

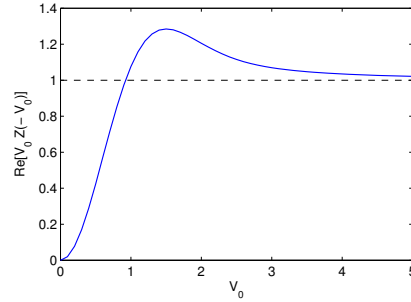


**Figure A.1:** The value of  $\text{Re}[\bar{V}_{0f} Z(-\bar{V}_{0f})]$  as a function of  $\bar{V}_{0f}$ .

that in the limit  $\bar{V}_{0f} \gg 1$ , we have  $\bar{V}_{0f} \text{Re}[Z(-\bar{V}_{0f})] \approx 1$ .

### A.2.2 Dispersion relationship in matrix form

The simplest fluid model of NBI driven EGAMs consists of three species: the thermal electrons, the thermal ions, and the fast ions originated from NBI. The thermal ions and the fast ions share the same mass  $m_i$ . Substituting Eq. (A.16), (A.17) and (A.23) into Eq. (A.25) and (A.26) for each species, we can reach a set of equations in the matrix form given by

$$\mathbf{D}(\Omega) \cdot \mathbf{V} = 0, \quad (\text{A.31})$$

in which  $\mathbf{V}$  is the column vector  $\mathbf{V} = (\tilde{V}_{f-}, \tilde{V}_{i-}, \tilde{V}_E, \tilde{V}_{i+}, \tilde{V}_{f+})^T$  and

$$D_{11} = \alpha \frac{1}{2q^2} \frac{\tau_f + \alpha \tau_e}{\Omega + v/q} - \alpha(\Omega + v/q), \quad (\text{A.32})$$

$$D_{12} = D_{54} = \alpha(1 - \alpha) \frac{1}{2q^2} \frac{\tau_e}{\Omega}, \quad (\text{A.33})$$

$$D_{13} = -\frac{1}{2} \alpha v(1 + c_f) + \frac{\alpha}{q} \left[ \frac{\tau_f}{\Omega + v/q} + \frac{\tau_e}{4} \left( (1 - \alpha) \frac{2}{\Omega} + \alpha \frac{1 - c_f}{\Omega + v/q} \right) \right] \quad (\text{A.34})$$

$$D_{21} = \alpha(1 - \alpha) \frac{1}{2q^2} \frac{\tau_e}{\Omega + v/q}, \quad (\text{A.35})$$

$$D_{22} = D_{44} = (1 - \alpha) \left[ \frac{1}{2q^2} \frac{3 + (1 - \alpha)\tau_e}{\Omega} - \Omega \right], \quad (\text{A.36})$$

$$D_{23} = \frac{1 - \alpha}{q} \left[ \frac{1}{\Omega} + \frac{\tau_e}{4} \left( (1 - \alpha) \frac{2}{\Omega} + \alpha \frac{1 - c_f}{\Omega + v/q} \right) \right], \quad (\text{A.37})$$

$$D_{31} = -\alpha v + \frac{\alpha}{q} \frac{4\tau_f + 2\tau_e + 2v^2}{4(\Omega + v/q)}, \quad (\text{A.38})$$

$$D_{32} = D_{34} = \frac{1 - \alpha}{2q} \frac{2 + \tau_e}{\Omega}, \quad (\text{A.39})$$

$$D_{33} = -\Omega + \frac{1 - \alpha}{\Omega} \left( \frac{7}{4} + \tau_e \right) + \frac{\alpha\Omega}{\Omega^2 - v^2/q^2} \left[ \frac{1}{2}\tau_e(1 - c_f) + \frac{1}{2}v^2(1 - 2c_f) - \frac{1}{2}\tau_f c_f + \frac{5}{4}\tau_f \right], \quad (\text{A.40})$$

$$D_{35} = \alpha v + \frac{\alpha}{q} \frac{4\tau_f + 2\tau_e + 2v^2}{4(\Omega - v/q)} \quad (\text{A.41})$$

$$D_{43} = \frac{1 - \alpha}{q} \left[ \frac{1}{\Omega} + \frac{\tau_e}{4} \left( (1 - \alpha) \frac{2}{\Omega} + \alpha \frac{1 - c_f}{\Omega - v/q} \right) \right], \quad (\text{A.42})$$

$$D_{45} = \alpha(1 - \alpha) \frac{1}{2q^2} \frac{\tau_e}{\Omega - v/q}, \quad (\text{A.43})$$

$$D_{53} = \frac{1}{2}\alpha v(1 + c_f) + \frac{\alpha}{q} \left[ \frac{\tau_f}{\Omega - v/q} + \frac{\tau_e}{4} \left( (1 - \alpha) \frac{2}{\Omega} + \alpha \frac{1 - c_f}{\Omega - v/q} \right) \right], \quad (\text{A.44})$$

$$D_{55} = \alpha \frac{1}{2q^2} \frac{\tau_f + \alpha\tau_e}{\Omega - v/q} - \alpha(\Omega - v/q), \quad (\text{A.45})$$

in which

$$\Omega = \omega / \sqrt{\frac{2T_i}{m_i R_0^2}}, \quad v = \langle V_{0f} \rangle / \sqrt{\frac{2T_i}{m_i}}, \quad \tau_f = \frac{T_f}{T_i}, \quad \tau_e = \frac{T_e}{T_i}, \quad c_f = \frac{\langle C_{Bf} \rangle}{\langle n_f \rangle}, \quad (\text{A.46})$$

and the density fraction

$$\alpha = \frac{\langle n_f \rangle}{\langle n_f \rangle + n_i}. \quad (\text{A.47})$$

Letting  $|D(\Omega)| = 0$  gives the dispersion relationship used in Chapter 5 which is solved numerically using an ordinary root finder.

### A.2.3 Reduction to a single energy beam

We now derive the dispersion relationship for an extreme case, in which a single energy beam is used as the fast ion distribution function, i.e.  $\tau_f \rightarrow 0$ . We also consider the case where the fast ion proportion is small, meaning that  $\alpha \ll 1$ . In such a limit, we can ignore the electron response to the fast ion density, since the perturbed electron pressure due to the perturbed fast ion density through quasi-neutrality is small compared to the perturbed fast ion pressure itself, with  $\tau_e \ll v^2$ . Using these assumptions, we simply get that

$$\tilde{V}_{f+} = \frac{1}{2} \frac{v}{\Omega - v/q} \tilde{V}_E, \quad (\text{A.48})$$

$$\tilde{V}_{f-} = -\frac{1}{2} \frac{v}{\Omega + v/q} \tilde{V}_E. \quad (\text{A.49})$$

Substituting Eq. (A.48) and (A.49) into Eq. (A.31), we reaches a reduced matrix form given by

$$\begin{pmatrix} D_{22} & D_{32} & 0 \\ D_{32} & D'_{33} & D_{32} \\ 0 & D_{32} & D_{44} \end{pmatrix} \begin{pmatrix} \tilde{V}_{i-} \\ \tilde{V}_E \\ \tilde{V}_{i+} \end{pmatrix} = 0, \quad (\text{A.50})$$

in which the new  $D'_{33}$  is given by

$$D'_{33} = -\Omega D_0(\Omega^2), \quad (\text{A.51})$$

and

$$D_0(\Omega^2) = 1 - \frac{1-\alpha}{\Omega^2} \left( \frac{7}{4} + \tau_e \right) - \alpha G(\Omega^2), \quad (\text{A.52})$$

$$G(\Omega^2) = \frac{3}{2} \frac{v^2}{\Omega^2 - v^2/q^2} + \frac{v^4/q^2}{(\Omega^2 - v^2/q^2)^2}. \quad (\text{A.53})$$

We let  $\Omega_0$  be the frequency that makes  $D_0(\Omega_0) = 0$ . Assuming the coupling to continuum is weak, i.e.  $q \gg 1$ , we get from the determinant of Eq. (A.50) being zero that the solution to the dispersion relationship differs from  $\Omega_0^2$  by

$$\Omega^2 - \Omega_0^2 = \frac{1-\alpha}{2q^2} (2 + \tau_e)^2 \Omega_0^{-4} \left( \frac{dD_0}{d\Omega^2} \right)^{-1}, \quad (\text{A.54})$$

describing the coupling to the bulk ion sound waves which  $\sim O(q^{-2})$ . Equivalently the dispersion relationship can be written into the form of Eq. (5.8)

$$D(\Omega^2) = 1 - \frac{1-\alpha}{\Omega^2} \left[ \frac{7}{4} + \tau_e + O(q^{-2}) \right] - \alpha G(\Omega^2), \quad (\text{A.55})$$

where the contribution from the sound wave coupling is added.

# An anisotropic and flowing model for converging magnetic field

## B.1 Introduction

Plasma facing material is a crucial research field in fusion science and technology [182]. Linear plasma devices, although cannot reproduce full tokamak conditions, are capable of generating plasmas with similar property to the edge of tokamaks, namely the scrap-off layer (SOL), for the purpose of material testing. The MaGnetized Plasma Interaction Experiment (MAGPIE) [183] is a linear plasma device at the Australian National University. Figure B.1 gives a schematic plot of MAGPIE. MAGPIE consists of a vacuum tube, a set of source coils and a set of target coil. The plasma in MAGPIE is generated by helicon wave heating, through a set of helicon field coils located at  $z = 0$ m. The plasma travels upstream (to higher  $z$ ) along the field lines into the target region and is pinched by the converging magnetic field. A target plate is located at the end of the target region where the testing material will be placed and interact with the plasma.

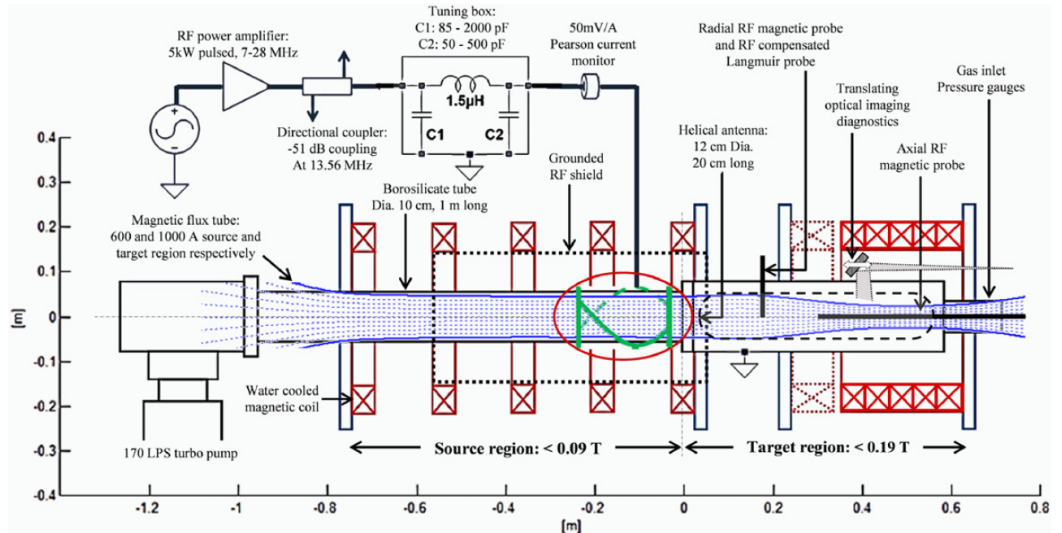


**Figure B.1:** A schematic view of the MAGPIE [183].

Besides its main purpose of material testing, the device is also active in many other research topics of plasma physics, such as helicon waves [184] and negative ion techniques [185]. Various diagnostics are installed currently on MAGPIE, including Langmuir probes [186] and optic diagnostics, making the plasma profiles in MAGPIE well mea-



sured. Recently, optical diagnostics on MAGPIE have identified the possible existence of an anisotropic ion temperature. Also, the azimuthal flow reverses its direction at around  $z = 0.25\text{m}$ , which remains unexplained at the moment. It is possible to extend the current knowledge of pressure anisotropy and flow in tokamaks to capture the physics of flow and anisotropy in a linear pinched devices, enlighten by existing theories of linear devices [187, 188, 189]: this is the purpose of Appendix B.

In this appendix, we will examine **argon** discharges in which pressure anisotropy and flow reversal were observed. We will first introduce a set of magnetic coordinates to describe the pinched magnetic geometry. The basic fluid equations are then written in these magnetic coordinates in MAGPIE conditions. We will first explore the simplest scenario without collisions, plasma source and sink, and pressure anisotropy. These non-ideal effects will be added one by one to study their impact on the plasma equilibrium profiles.

## B.2 Model

### B.2.1 Magnetic Geometry

The plasma induced magnetic field is weak, therefore we take the externally generated field as the MAGPIE magnetic field. Close to the center of the current carrying coils, the field in  $z$  direction  $B_z$  is assumed to be function of  $z$  only, with  $B_r$  obtained from the Maxwell equation  $\nabla \cdot \mathbf{B} = 0$ , giving

$$\mathbf{B} = B_z(z)\mathbf{e}_z - \frac{1}{2}r\frac{dB_z}{dz}\mathbf{e}_r. \quad (\text{B.1})$$

In this work, we will use a set of magnetic coordinates instead of the cylindrical coordinates  $(R, \theta, z)$ , which has the advantage of separating the parallel/perpendicular force balance. We write the magnetic field  $\mathbf{B}$  into a contravariant form, given by

$$\mathbf{B} = -\nabla\psi \times \nabla\theta, \quad (\text{B.2})$$

with

$$\psi = -\frac{1}{2}B_z(z)r^2. \quad (\text{B.3})$$

For an externally generated magnetic field, we have inside the plasma  $\nabla \times \mathbf{B} = 0$ . Therefore, a scalar magnetic potential  $\xi$  exists, having  $\mathbf{B} = -\nabla\xi$ . We note that although Eq. (B.1) does not satisfy  $\nabla \times \mathbf{B} = 0$  exactly, due to the omission of the radial dependency of  $B_z$ , we still have  $\nabla \times \mathbf{B} \approx 0$  as long as the calculation is carried on near  $r = 0$  and  $B_r \ll B_z$ . Integrating along the field line, the magnetic potential  $\xi$  is then approximately given by

$$\xi = -\int_0^z B(z')dz' + \frac{1}{4}r^2\frac{dB_z}{dz}. \quad (\text{B.4})$$

The axial magnetic field as a function of  $z$  is plotted in Fig.B.2 (a) for  $I_{\text{source}} = 50\text{A}$  and  $I_{\text{target}} = 450\text{A}$ , with  $B$  increasing from 0.015T to 0.09T at  $z = 0.45\text{m}$ . We will be using this field setting throughout the appendix. The contour of constant  $\psi$  and  $\xi$  are shown in Fig.B.2 (b) and (c) respectively. The coordinate  $\psi$  labels the flux surfaces, having the property  $\nabla\psi \cdot \mathbf{B} = 0$ . Equation (B.3) and Figure B.2 (b) indicates that the characteristic radius satisfy  $r_c^2 B = \text{constant}$  on a constant  $\psi$  surface due to flux conservation. The magnetic potential  $\xi$  contours mostly coincide with constant  $z$  surfaces, and therefore can

be used as an axial coordinate.

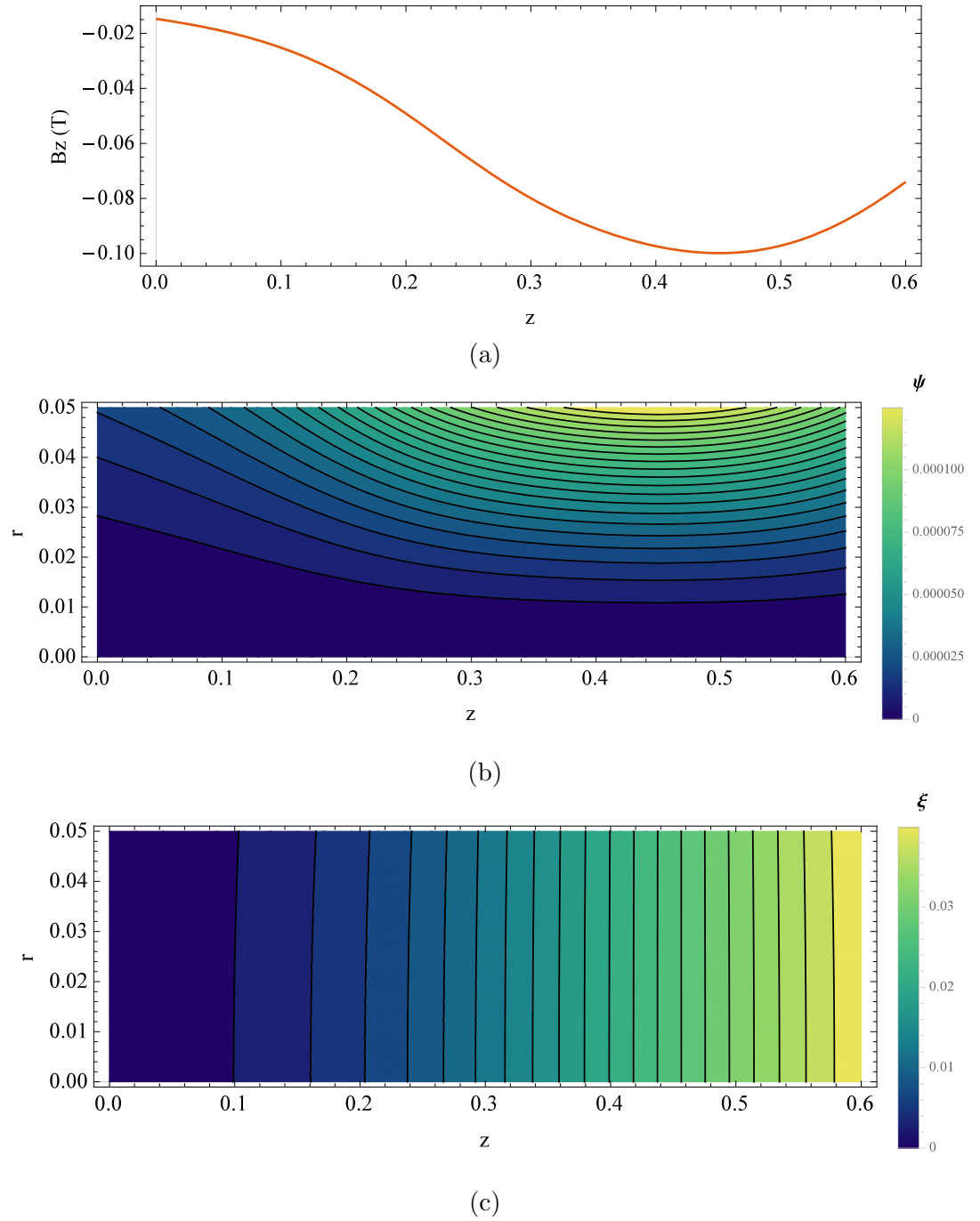


**Figure B.2:** (a) The axial magnetic field  $B_z$  as a function of  $z$ . (b) The radial coordinate  $\psi$  as a function of  $r$  and  $z$ . (c) The axial coordinate  $\xi$  as a function of  $r$  and  $z$ .

Now  $(\psi, \theta, \xi)$  are used as our new coordinate, with the conversion between these magnetic coordinates and the cylindrical coordinate given by Eq. (B.3), (B.4) and  $\theta = \theta$ . The covariant basis vectors  $\nabla\psi$ ,  $\nabla\theta$  and  $\nabla\xi$  are perpendicular to each other, labeling the radial(cross-field), azimuthal and parallel direction, respectively. From Eq. (B.3) and (B.4), the metrics of the magnetic coordinates are given by

$$g^{11} = r^2 B^2, \quad g^{22} = \frac{1}{r^2}, \quad g^{33} = B^2, \quad (\text{B.5})$$

and the Jacobian is given by

$$J = \frac{1}{\sqrt{g^{11}g^{22}g^{33}}} = \frac{1}{B^2}. \quad (\text{B.6})$$

In addition, the covariant and contravariant components of the magnetic field are simply written as

$$B_\xi = -1, \quad B^\xi = -B^2. \quad (\text{B.7})$$

### B.2.2 Continuity equation

The continuity equation for the single fluid is given by

$$\nabla \cdot (m_i n \mathbf{V}) = m_i n (S - L), \quad (\text{B.8})$$

in which  $m_i$  is the ion mass,  $n$  the ion number density,  $\mathbf{V}$  the fluid velocity,  $S$  the source term and  $L$  the loss term. The density of the single fluid is given by  $\rho \approx m_i n$ , since  $m_e/m_i \ll 1$ . Writing Eq. (B.8) into the magnetic coordinates, we get

$$\frac{\partial}{\partial \psi} \frac{n V^\psi}{B^2} + \frac{\partial}{\partial \xi} \frac{n V^\xi}{B^2} = n \frac{S - L}{B^2}, \quad (\text{B.9})$$

in which  $V^\psi$  and  $V^\xi$  are contravariant components of  $\mathbf{V}$ .

A quasi neutrality condition is also needed, given by

$$\nabla \cdot \mathbf{J} = 0. \quad (\text{B.10})$$

Equation (B.10) can be written as

$$\frac{\partial}{\partial \psi} \frac{J^\psi}{B^2} + \frac{\partial}{\partial \xi} \frac{J^\xi}{B^2} = 0, \quad (\text{B.11})$$

in which  $J^\psi$  and  $J^\xi$  are contravariant components of  $\mathbf{J}$ .

### B.2.3 Momentum Equation

The single fluid momentum equation is given by

$$m_i n \mathbf{V} \cdot \nabla \mathbf{V} = \mathbf{J} \times \mathbf{B} - \nabla \cdot \mathbf{P}, \quad (\text{B.12})$$

in which  $\mathbf{P}$  is the pressure tensor. In this work, we ignore the FLR effects and use the CGL diagonal pressure tensor. If we further assume a Maxwellian distribution for the electrons and a bi-Maxwellian distribution for the ions, the pressure tensor will become

$$\mathbf{P} = ZnT_e \mathbf{I} + nT_{\perp i}(\mathbf{I} - \mathbf{b}\mathbf{b}) + nT_{\parallel i} \mathbf{b}\mathbf{b}, \quad (\text{B.13})$$

in which  $Z$  is the ion number charge,  $T_e$  the electron temperature,  $T_{\perp i}$  the ion perpendicular pressure,  $T_{\parallel i}$  the ion parallel pressure,  $\mathbf{I}$  the unit dyad, and  $\mathbf{b} = \mathbf{B}/B$  the unit vector along the field line. All temperatures are in the unit of energy (e.g. electron volt).

We now write Eq. (B.12) into its covariant form, with the components in  $\nabla\psi$ ,  $\nabla\theta$  and

$\nabla\xi$  directions given by

$$\begin{aligned} m_i n \left[ \frac{V^\psi}{rB} \frac{\partial}{\partial\psi} \frac{V^\psi}{rB} - \frac{1}{2} (V^\theta)^2 \frac{\partial r^2}{\partial\psi} + \frac{(V^\xi)^2}{B^3} \frac{\partial B}{\partial\psi} + V^\xi \frac{\partial}{\partial\xi} \frac{V^\psi}{r^2 B^2} \right] \\ = J^\theta - Z \frac{\partial n T_e}{\partial\psi} - \frac{\partial n T_{\perp i}}{\partial\psi} - n(T_{\parallel i} - T_{\perp i}) \frac{\partial \ln B}{\partial\psi}, \end{aligned} \quad (\text{B.14})$$

$$m_i n \left[ V^\psi \frac{\partial}{\partial\psi} V^\theta r^2 + V^\xi \frac{\partial}{\partial\xi} V^\theta r^2 \right] = -J^\psi, \quad (\text{B.15})$$

$$\begin{aligned} m_i n \left[ V^\psi \frac{\partial}{\partial\psi} \frac{V^\xi}{B^2} - \frac{(V^\psi)^2}{2} \frac{\partial}{\partial\xi} \frac{1}{r^2 B^2} - \frac{(V^\theta)^2}{2} \frac{\partial r^2}{\partial\xi} + \frac{V^\xi}{B} \frac{\partial}{\partial\xi} \frac{V^\xi}{B} \right] \\ = -Z \frac{\partial n T_e}{\partial\xi} - \frac{\partial n T_{\parallel i}}{\partial\xi} + n(T_{\parallel i} - T_{\perp i}) \frac{\partial \ln B}{\partial\xi}. \end{aligned} \quad (\text{B.16})$$

#### B.2.4 Generalized Ohm's law

The generalized Ohm's law is derived from the momentum equation for the electrons. Ignoring the electron inertial, we have

$$-\nabla\Phi + \mathbf{V} \times \mathbf{B} = \eta \mathbf{J} + \frac{1}{Zen} [\mathbf{J} \times \mathbf{B} - Z \nabla(n T_e) - 0.71 Z n \mathbf{b} \mathbf{b} \cdot \nabla T_e], \quad (\text{B.17})$$

in which  $\Phi$  is the electrostatic potential,  $\eta$  the resistivity and the last term is due to the thermal force along the field line. The value of  $\eta$  is given by

$$\eta = \frac{\sqrt{m_e} Z e^2}{6\sqrt{2}\pi^{3/2} \epsilon_0^2 T_e^{3/2}} \ln \Lambda, \quad (\text{B.18})$$

in which  $m_e$  is the electron mass,  $\epsilon_0$  is the vacuum permittivity and  $\ln \Lambda \approx 10$  is the Coulomb logarithm constant.

Equation (B.17) is transferred into the covariant form given by

$$-\frac{\partial\Phi}{\partial\psi} + V^\theta = \eta J_\psi + \frac{1}{Zen} \left[ J^\theta - Z \frac{\partial n T_e}{\partial\psi} \right], \quad (\text{B.19})$$

$$-V^\psi = \eta J_\theta - \frac{1}{Zen} J^\psi, \quad (\text{B.20})$$

$$-\frac{\partial\Phi}{\partial\xi} = \eta J_\xi + \frac{1}{Zen} \left[ -Z T_e \frac{\partial n}{\partial\xi} - 1.71 Z n \frac{\partial T_e}{\partial\xi} \right], \quad (\text{B.21})$$

in which we have also used the covariant components of  $\mathbf{J}$ . The set of equations Eq. (B.9), (B.11), (B.14), (B.15), (B.16), (B.19), (B.20) and (B.21) closes the system of equations with eight unknowns ( $n$ ,  $\Phi$ , three components of  $\mathbf{V}$  and  $\mathbf{J}$ ), if the temperature profiles are specified.

### B.3 Collisionless plasma

We first consider the scenario when the resistivity  $\eta = 0$ , i.e. the collision between the electrons and the ions is ignored. An inspection of the set of equations shows that  $J^\xi$  only appears in the quasi-neutrality condition Eq. (B.11) to balance the radial current  $J^\psi$ . Therefore, the variable  $J^\xi$  and Eq. (B.11) are removed from our system of equations and will be evaluated afterwards. We further eliminate the variable  $J^\psi$  by substituting Eq. (B.20) into Eq. (B.15). Equation (B.15) is a statement of the conservation of the angular momentum  $m\omega r^2$  along the motion of the fluid element, since  $V^\theta = \omega$  and  $\omega$  is the azimuthal angular rotation frequency. An ordering analysis on Eq. (B.15) shows that

$$\frac{V^\psi}{V^\xi r} \frac{L}{r} \sim \frac{\omega}{\omega_{ci}} \ll 1, \quad (\text{B.22})$$

in which  $L$  is the typical axial length of the machine and  $\omega_{ci} = ZeB/m_i$  is the ion cyclotron frequency. The contribution from the first term in Eq. (B.9) is therefore less important than the second term.

Based on the experimental observations that the flow speed is less than the ion acoustic speed  $\sqrt{T_e/m_i}$ , an iterative method can be used to solve the system of equations. Ignoring the LHS of Eq. (B.16) and substituting Eq. (B.9) to eliminate  $n$ , we will reach

$$\frac{\partial \ln V^\xi}{\partial \xi} - \frac{S - L}{V^\xi} = 2 \frac{\partial \ln B}{\partial \xi} + \frac{\partial \ln T_e}{\partial \xi} + \frac{1}{ZT_e} \frac{\partial T_{\parallel i}}{\partial \xi} - \frac{T_{\parallel i} - T_{\perp i}}{ZT_e} \frac{\partial B}{\partial \xi}. \quad (\text{B.23})$$

The solution of Eq. (B.23),  $V^\xi$  as a function of  $\psi$  and  $\xi$ , is substituted into Eq. (B.9) to solve for the density profile with the first term ignored. The potential  $\Phi$  is then known by integrating Eq. (B.21) along constant  $\xi$  (magnetic field line). In parallel, with the LHS of Eq. (B.14) ignored in the initial guess,  $J^\theta$  is readily obtained from Eq. (B.14). Substituting the result of  $J^\theta$  into Eq. (B.14), we will finally get  $V^\theta$ . Our initial iteration is completed after  $J^\psi$  is obtained from Eq. (B.15) with the solved profiles. In the next step, the profiles of the first iteration are substituted into the first term of Eq. (B.9) and the LHS of Eq. (B.14) and (B.16). The above procedure is then repeated with the newly added terms calculated from the profiles of the last iteration. The iteration is carried on until the profiles reach a convergence.

We specify the electron temperature profile to be

$$T_e(\psi, \xi) = T_{e0} \exp \left[ -\frac{\psi}{a_{Te}\psi_1} - \frac{z(\psi, \xi)}{b_{Te}L} \right], \quad (\text{B.24})$$

in which  $\psi_1$  is the value of  $\psi$  at  $r = 0.05\text{cm}$  and  $z = 0$ , and  $L = 0.6$  is the length of the target region. The parameter  $a_{Te}$  and  $b_{Te}$  set the radial and axial decay length of the electron temperature profile, while  $T_{e0}$  is the electron temperature at  $\psi = \xi = 0$ . The ion temperature is assumed to be anisotropic  $T_{\parallel i} \neq T_{\perp i}$ , following the same trend as Eq. (B.24), but with different parameters  $T_{\parallel i0}$ ,  $T_{\perp i0}$ ,  $a_{T\parallel i}$ ,  $a_{T\perp i}$ ,  $b_{T\parallel i}$  and  $b_{T\perp i}$ . The density profile at  $\xi = 0$  is given by

$$n(\psi, \xi = 0) = n_0 \exp \left[ -\frac{\psi}{a_n\psi_1} \right], \quad (\text{B.25})$$

where  $n_0 = n(\psi = \xi = 0)$  and  $a_n$  is a parameter defines the radial decay length of  $n$ . The  $n$  and  $T_e$  profile match qualitatively the experimental probe measurement in Samuelli *et*

*al* [186] and Chang *et al* [184]. An inspection of Eq. (B.14) and Eq. (B.19) shows that in the absence of neutral collisions, the radial electric field produces an azimuthal flow and is not coupled to other equations, when the flow speed is much slower than the ion sound speed, i.e. there is no restriction on the radial electric field. Therefore we have a freedom to prescribe  $\Phi$  on  $\xi = 0$  surface, written as

$$\Phi(\psi, \xi = 0) = \Phi_0 \exp \left[ 1 - \frac{\psi}{a_\Phi \psi_1} \right], \quad (\text{B.26})$$

which uses the gauge  $\Phi = 0$  at  $\psi = \xi = 0$ .

### B.3.1 Isotropic, source/sink-free plasma

In the simplest setup of the model, we neglect the contribution from the plasma source and sink. The equilibrium parameters we have used are  $T_{e0} = 4.5\text{eV}$ ,  $T_{\parallel i0} = T_{\perp i0} = 1\text{eV}$ ,  $a_{Te} = a_{T\parallel i} = a_{T\perp i} = 1$ ,  $b_{Te} = 3$ ,  $b_{T\parallel i} = b_{T\perp i} = 0.2$ ,  $n_0 = 5 \times 10^{18}\text{m}^{-3}$ ,  $a_n = 2$ ,  $\Phi_0 = -1\text{V}$  and  $a_\Phi = 1$ . The parallel velocity  $V_{\parallel} = V^\xi/B$  as a function of  $z$  on axis is shown in Fig.B.3, with the boundary condition  $V^\xi/B = 150\text{m/s}$  at  $\xi = 0$ . The solution is converged after the second iteration. The on-axis axial velocity mainly follows the trend of the field strength  $B$ , i.e. increases axially for  $z < 0.4\text{m}$ , peaks at around  $z = 0.4\text{m}$ , and finally decreases. Equation (B.9) states that the mass flow in a magnetic tube,  $nV_{\parallel}S$ , should be constant along the tube if the cross field transport (the first term) is not important, with  $S \sim 1/B$  the area of the tube cross section and  $V^\xi = V_{\parallel}B$ . For  $T_e \gg T_{\parallel i}, T_{\perp i}$ , Eq. (B.23) is simplified to  $V^\xi/(T_e B^2) = \text{constant}$  on a magnetic field line, in the case that the flow speed is much less than the ion sound speed, giving the trend of  $V_{\parallel}$  in Fig.B.3.

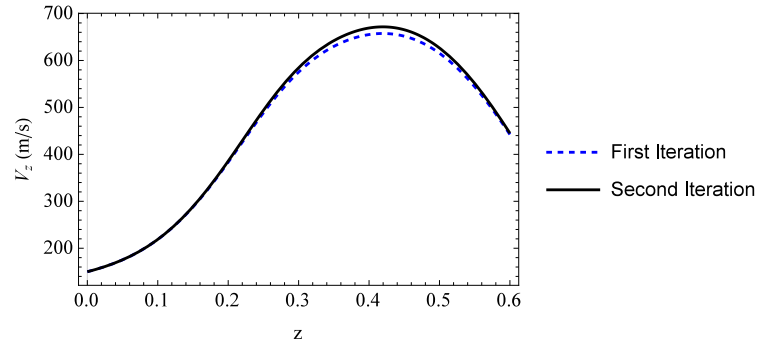


**Figure B.3:** The parallel velocity  $V_{\parallel} = V^\xi/B$  as a function of  $z$  on axis, for the initial iteration (dashed) and the second iteration (solid).

The contour of  $n$ ,  $\Phi$  and  $V_\theta$  are plotted in Fig.B.4, Fig.B.5 and Fig.B.6, respectively. Figure B.4 shows a clear pinch of the plasma when the field increases: the characteristic radius is reduced and reaches its minimum at  $z = 0.4\text{m}$  where the magnetic field strength reaches its maximum. Along one magnetic field line, the density builds up along the axis, as a result of  $nT_e$  being a constant on a magnetic field line by integrating Eq. (B.16) and assuming  $T_e \gg T_{\parallel i}, T_{\perp i}$ . Inspection of Fig.B.5 shows the on-axis potential  $\Phi$  first increases along the axis, reaching its peak around  $z = 0.2\text{m}$  and then decreases. This is the result of a competition between the positive density gradient and the negative temperature gradient. The azimuthal flow velocity  $V_\theta$  is determined by the combination of the radial electric field and ion pressure gradient, which balances the axial electric field. Figure B.6 shows a azimuthal flow reversal point at around  $z = 0.25\text{m}$ , after which the pressure gradient

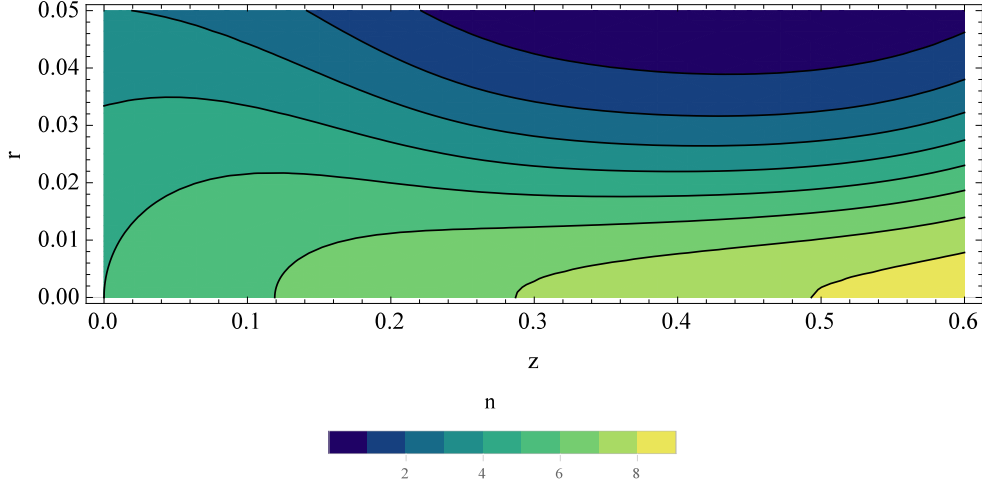


**Figure B.4:** The density contour, in the unit of  $10^{18}\text{m}^{-3}$ .

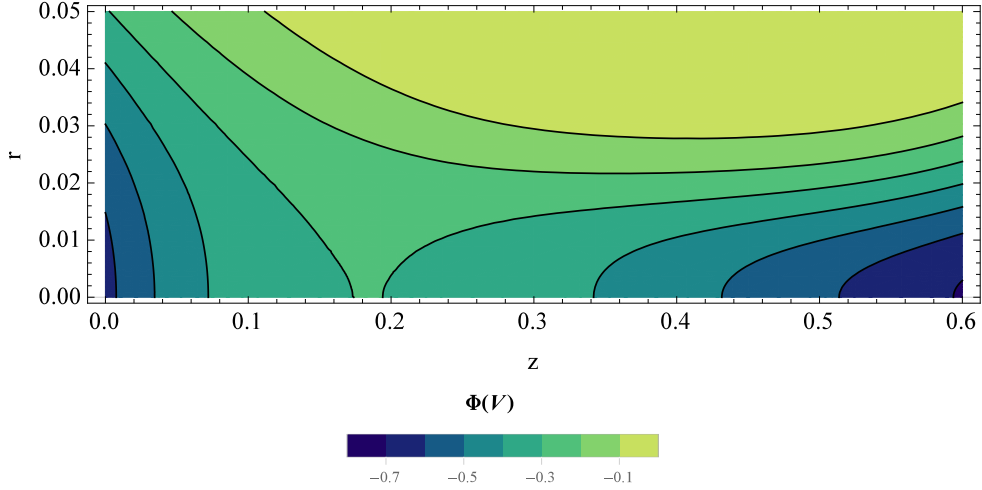


**Figure B.5:** The potential contour, in the unit of V.

vanishes and the radial electric field dominates the force balance. Similar  $V_\theta$  reversal is reported in the experiment using optic diagnostics, but all at the same  $z$  regardless of radius, which requires further investigation.

### B.3.2 Adding anisotropy

In linear devices with large end particle losses, the plasma will be anisotropic if sufficient particles are lost before they are thermalized. In this section, we will investigate the effect of anisotropy to the force balance. Equation (B.14) and (B.16) shows that the perpendicular and parallel pressure have different roles in the force balance:  $T_{\parallel i}$  affects mainly the parallel force balance, while  $T_{\perp i}$  affects main the perpendicular force balance. The impact of pressure anisotropy on the parallel force balance is by changing the ion density, the potential and  $V^\xi$ , while in the perpendicular direction it changes the azimuthal flow profile through its dependency on the radial gradient of the perpendicular ion pressure. Figure B.7 shows the  $V_{\parallel}$  profile for three cases: the isotropic case with  $T_{\perp i0} = T_{\parallel i0} = 1\text{eV}$ , halving  $T_{\parallel i0}$  and halving  $T_{\perp i0}$ . As expected, changing  $T_{\parallel i0}$  to half of the isotropic case

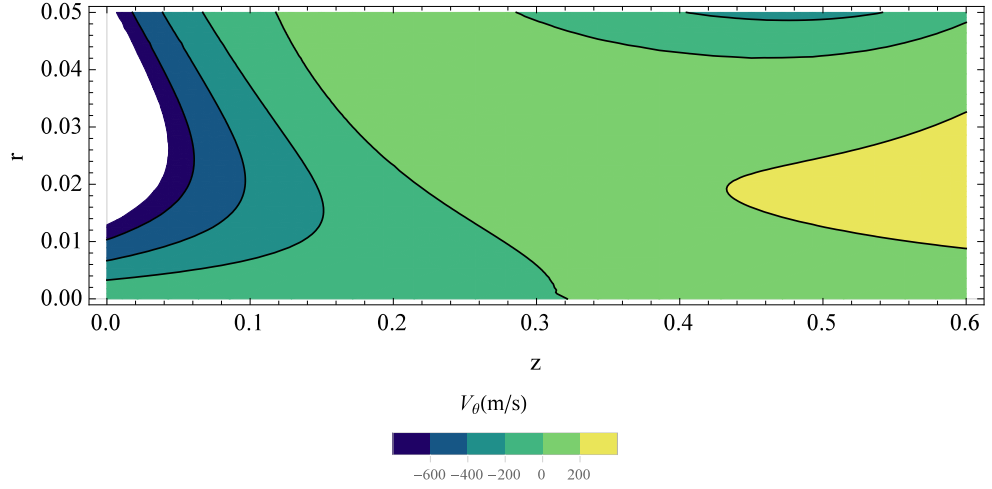


**Figure B.6:** The  $V_\theta$  contour, in the unit of m/s.

induces a more notable change in  $V_\parallel$  compared to the case in which  $T_{\perp i0}$ , increasing its maximum from 650m/s to 760m/s. On the other hand, changing  $T_{\perp i0}$  to half of that in the isotropic case reduces the flow speed slightly.

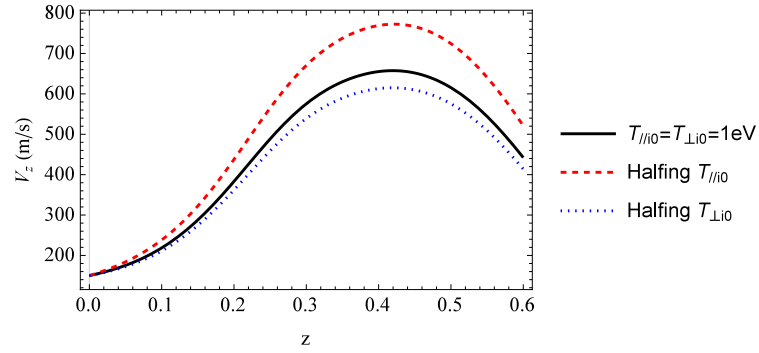


**Figure B.7:** The axial velocity on axis, for the isotropic case and two anisotropic cases with  $T_{\perp i} > T_{\parallel i}$  and  $T_{\perp i} < T_{\parallel i}$ , respectively.

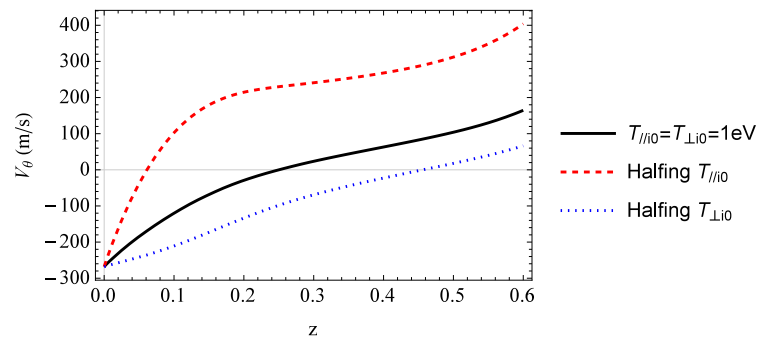


**Figure B.8:** The azimuthal velocity at  $\psi = 0.1\psi_1$ , where  $\psi_1 = \psi(r = 0.06\text{m}, z = 0)$ , for the isotropic case and two anisotropic cases with  $T_{\perp i} > T_{\parallel i}$  and  $T_{\perp i} < T_{\parallel i}$ , respectively.

The modification of anisotropy to the azimuthal velocity is more significant, as shown



in Fig.B.8. There are two mechanisms through which  $V_\theta$  can be modified by pressure anisotropy. First, the direct presence of ion perpendicular gradient in Eq. (B.19) if  $J^\theta$  is eliminated using Eq. (B.14) determines the amount of rotation required to balance it through the Lorenz force. Therefore a change in  $T_{\perp i}$  will reflect directly into a change in  $V_\theta$ . Second, the parallel force balance is modified by pressure anisotropy, resulting in a modified density and thus a modified potential. The difference in potential will also give a change to  $V_\theta$  from Eq. (B.19). In Fig.B.8, if the perpendicular pressure is reduced to half, the flow reversal point moves upstream (higher  $z$ ), while reducing  $T_{\parallel i}$  moves the reversal point downstream (lower  $z$ ). Note that in both cases, the second mechanism is dominant, since when  $T_{\perp i}$  is decreased, we would expected the positive potential gradient to dominate the force balance, and thus reversal point to move to lower  $z$  if the potential is unchanged. However, Fig.B.8 shows the reverse: the reversal point moves upstream if  $T_{\perp i}$  is reduced, indicating a more remarkable change in the potential from the parallel dynamics.

### B.3.3 Adding source term

We have so far ignored the generation of new ions and electrons. In this section, we introduce a plasma source term  $S$  given by

$$S = \frac{P}{E_{iz}n_0} \exp(-z/\Delta z), \quad (\text{B.27})$$

in which  $P$  is the power density of the helicon wave absorption,  $E_{iz} = 15.26$  eV the ionization energy of argon atoms,  $\Delta z$  is the decay length of the heating effect. The parameters we've used are  $P = 50 \text{ kWm}^{-3}$ ,  $\Delta z = 0.1 \text{ m}$ , according to the calculation in Chang *et al* [184]. Again we have used our iterative method to solve for  $V_\xi$ , with the results given in Fig.B.9. When solving for the flow velocity with the source term, we have used the boundary condition to match the solution to the original one at  $z = 0.4$ . It is shown in Fig.B.9 that the plasma source term affects the flow velocity at  $z < 0.15$  where the helicon heating is localized. At  $z = 0.05$  a axial flow reversal is presented: new plasma is generated around this area and “pushes” the existing plasma to the two ends. Besides, no significant difference is found for all the other profiles: when the flow speed is much less than the thermal speed, the effect of  $V^\xi$  on the parallel force balance is small, and the density and potential are thus not affected.

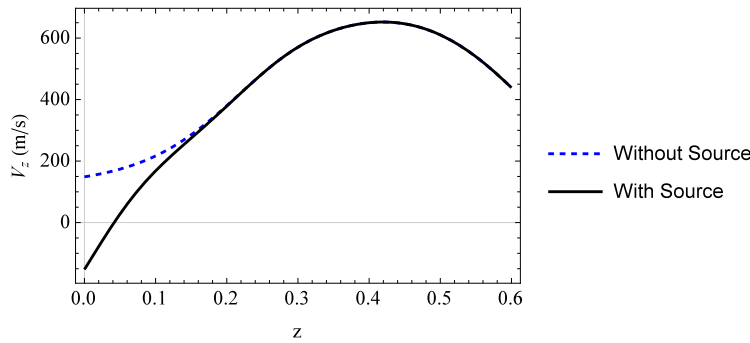


**Figure B.9:** The axial velocity on axis, without/with the source term.

## B.4 Finite resistivity

When the resistivity is taken into account, the solution to Eq. (B.20) is qualitatively different. The  $\eta J_\theta$  term will dominate over the other term on the RHS, which gives an radial cross-field motion of the ions: this is the ambipolar diffusion due to the ion-electron collisions. In ambipolar diffusion, the ions and electrons are diffused at the same outward and down stream velocity, meaning that  $J^\Psi = J^\xi = 0$ . Equation (B.15) thus states the deviation of our system from a purely ambipolar system, which again, is due to the need of a finite  $J^\Psi$  to satisfy the angular momentum conservation as the fluid is compressed. Assuming this deviation is small, we can still solve our system iteratively. In the initial step, we set the LHS of Eq. (B.14) and Eq. (B.16) to zero, along with  $J^\Psi = J^\xi = 0$ . We can also leave Eq. (B.19) and (B.21) out of the system for the moment, since they merely gives the potential and  $V^\theta$  after all the other profiles are solved. Substituting Eq. (B.14) and (B.20) into Eq. (B.9), we will get

$$\frac{\partial}{\partial \xi} \frac{nV^\xi}{B^2} = n \frac{S-L}{B^2} + \frac{\partial}{\partial \psi} \frac{n\eta r^2}{B^2} \left[ Z \frac{\partial nT_e}{\partial \psi} + \frac{\partial nT_{\perp i}}{\partial \psi} + n(T_{\parallel i} - T_{\perp i}) \frac{\partial \ln B}{\partial \psi} \right]. \quad (\text{B.28})$$

Equation (B.28) shows that the resistivity enters the equations by acting as a source/sink term. Therefore, the solution to  $V^\xi$  becomes sensitive to the radial density and temperature gradient.

In Fig.B.10, the on axis axial flow profile as a function of  $z$  is plotted for different initial density profiles at  $\xi = 0$ , by changing the radial density scale length  $a_n$ . We have set the initial condition of the flow profiles to match with the non-resistive solution at  $z = 0.4\text{m}$ . Comparing the solutions with finite resistivity to the one without (the helicon wave source term is retained), it is notable that the peak at  $z = 0.4$  is shifted to  $z = 0.3$ . Moreover, the flow reversal caused by the source term disappears, indicating a strong “sink” effect when the plasma is transported outward radially. Scan over the initial radial density length scale  $a_n$  shows that a smaller density radial gradient (higher  $a_n$ ) reduces the effect of radial transport, making the calculated profile closer to the solution without resistivity. We have also examined the effect of different electron temperature radial gradient as shown in Fig.B.11, giving similar results: the “sink” effect of radial transport due to resistivity is mitigated with a reduced temperature gradient. A consistent check of the density/temperature radial profile is therefore possible through the comparison of  $V_\parallel$  to the experimental data when certain measurement is not available. We note that the inclusion of resistivity does not significantly affect other profiles such as the density or azimuthal rotation profile.

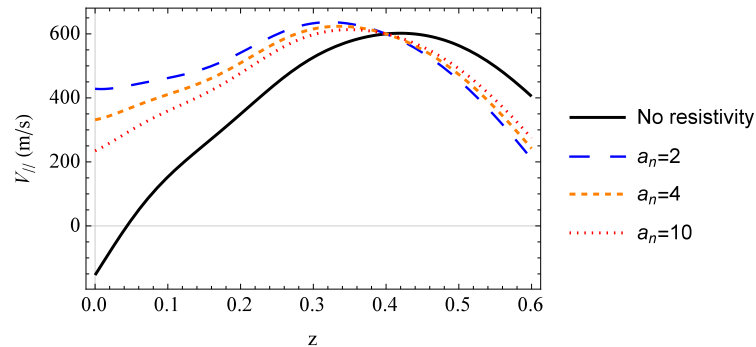


**Figure B.10:** The axial velocity on axis, with different initial density profiles at  $\xi = 0$ .

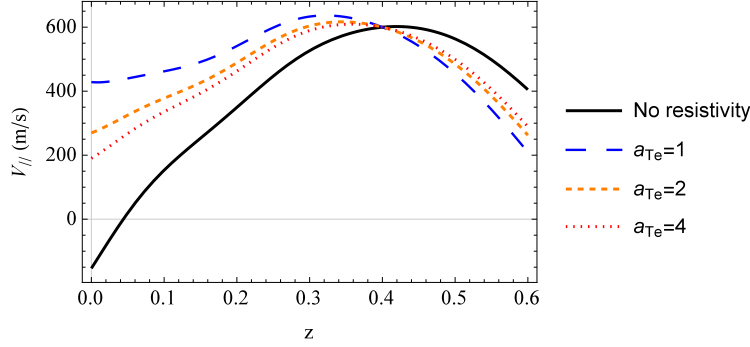


**Figure B.11:** The axial velocity on axis, with different radial temperature gradient.

## B.5 Conclusion

In this appendix, we have briefly investigated the possibility of extending our anisotropic, flowing equilibrium model used in tokamaks to a linear device with a converging magnetic field (MAGPIE). Despite of a few common points, such as the existence of flux surfaces and magnetic coordinates, the properties of equilibria in MAGPIE and tokamaks are significantly different. Most importantly, the magnetic field in a linear device is determined mainly by the external coils and therefore a Grad-Shafranov analysis is not applicable, while in a tokamak, the flux surfaces are a result of the combination of external currents and plasma currents. Also, non-ideal effects, such as source terms and resistivity, are important to the equilibrium in MAGPIE but not in tokamaks. Finally, the flow in MAGPIE argon plasma is mainly subsonic, making the contribution from centrifugal force and other inertial terms to the force balance less important, while in MAST (Chapter 2) the centrifugal force leads to a considerable out-shift of the flux surfaces and constant density contours.

Nevertheless, the extension is proved fruitful. Given the subsonic nature of the plasma flow found by experiments, we are able to solve the set of fluid equations iteratively. A pinch of the plasma is clearly shown as the characteristic radius decreases when the magnetic field strength increases upstream (to higher  $z$ ). The density builds up as the plasma is compressed upstream, meanwhile the axial flow velocity reaches its peak at  $z = 0.4\text{m}$  where the field strength maximized. The azimuthal flow is sheared and found to change its direction at  $z = 0.2$  to  $0.3\text{m}$ , consistent with the observation from the optic diagnostics. The major impact of pressure anisotropy is to change the density profile through the parallel force balance, and thereby the potential and azimuthal flow. In the  $T_{\parallel i} > T_{\perp i}$  and the  $T_{\parallel i} < T_{\perp i}$  cases, the flow reversal point is moved to lower/higher  $z$ , respectively. We have also explored the impact of a finite source term, which modifies the axial flow and creates a region where the plasma flows backward. The solution to the axial flow profile becomes different when resistivity is included, since the radial transport of the plasma due to ion-electron collision serves as a sink in the continuity equation.

Please note that this appendix is an unfinished piece of work. The author does not have the copyright to include the direct comparison with experiment data in this thesis, since most of the data are unpublished and belong to the content of another thesis. We will report the comparison in future publications after the relevant data are publicised.

---

# Bibliography

---

- [1] J. Wesson, *Tokamaks*. Oxford University Press, 4th ed., 2011.
- [2] R. Goldston and P. Rutherford, *Introduction to Plasma Physics*. Taylor & Francis Ltd, 2000.
- [3] J. D. Lawson, “Some Criteria for a Power producing thermonuclear reactor,” *Atomic Energy Research Establishment (Technical Report)*, 1955.
- [4] F. Chen, *Introduction to Plasma Physics and Controlled Fusion*. Springer, 3rd ed., 2015.
- [5] R. Hemsworth, H. Decamps, J. Graceffa, B. Schunke, M. Tanaka, M. Dremel, A. Tanga, H. D. Esch, F. Geli, J. Milnes, T. Inoue, D. Marcuzzi, P. Sonato, and P. Zaccaria, “Status of the ITER heating neutral beam system,” *Nuclear Fusion*, vol. 49, no. 4, p. 045006, 2009.
- [6] J. D. Gaffey, “Energetic ion distribution resulting from neutral beam injection in tokamaks,” *Journal of Plasma Physics*, vol. 16, pp. 149–169, 1976.
- [7] F. Perkins, “Heating tokamaks via the ion-cyclotron and ion-ion hybrid resonances,” *Nuclear Fusion*, vol. 17, no. 6, p. 1197, 1977.
- [8] T. Stix, “Fast-wave heating of a two-component plasma,” *Nuclear Fusion*, vol. 15, no. 5, p. 737, 1975.
- [9] J. P. Goedbloed and S. Poedts, *Principles of Magnetohydrodynamics With Applications to Laboratory and Astrophysical Plasma*. Cambridge University Press, 2004.
- [10] J. Cary and A. Brizard, “Hamiltonian theory of guiding-center motion,” *Reviews of Modern Physics*, vol. 81, pp. 693–738, may 2009.
- [11] G. W. Bowden, a. Könies, M. J. Hole, N. N. Gorelenkov, and G. R. Dennis, “Comparison of methods for numerical calculation of continuum damping,” *Physics of Plasmas*, vol. 21, p. 052508, may 2014.
- [12] H. Grad, “The guiding center plasma,” *Proceedings of Symposia in Applied Mathematics*, vol. 1, p. 162, 1967.
- [13] H. Grad, “Toroidal Containment of a Plasma,” *Phys. Fluids*, vol. 10, p. 137, 1967.
- [14] R. M. Kulsrud, “MHD Description of Plasma,” in *Handb. Plasma Phys. Vol.1: Basic Plasma Phys. 1* (M. N. Rosenbluth and R. Z. Sagdeev, eds.), pp. 115–145, North-Holland Publishing Company, 1983.
- [15] G. F. Chew, M. L. Goldberger, and F. E. Low, “The Boltzmann equation and the one-fluid hydromagnetic equations in the absence of particle collisions,” *Proc. R. Soc. Lond. A. Math. Phys. Sci.*, vol. 236, no. 1204, pp. 112–118, 1956.

- 
- [16] S. Ichimaru and M. N. Rosenbluth, "Relaxation Processes in Plasmas with Magnetic Field Temperature Relaxations," *The Physics of Fluids*, vol. 13, no. 11, p. 2778, 1970.
- [17] S. Braginskii, *Transport Processes in a Plasma*, vol. 1, p. 205. Consultants Bureau, New York NY, 1965.
- [18] Y. Kato, M. Tajiri, and T. Taniuti, "Propagation of hydromagnetic waves in collisionless plasma," *J. Phys. Soc. Japan*, vol. 21, no. 4, p. 765, 1966.
- [19] M. Tajiri, "Propagation of hydromagnetic waves in collisionless plasma, II, Kinetic approach," *J. Phys. Soc. Japan*, vol. 22, no. 6, p. 1842, 1967.
- [20] M. Fitzgerald, M. J. Hole, and Z. S. Qu, "Magnetohydrodynamic normal mode analysis of plasma with equilibrium pressure anisotropy," *Plasma Phys. Control. Fusion*, vol. 57, p. 025018, 2015.
- [21] L. Hau and B. Sonnerup, "On slow mode waves in an anisotropic plasma," *Geophys. Res. Lett.*, vol. 20, no. 17, pp. 1763–1766, 1993.
- [22] Y. C. Whang, "Higher moment equations and the distribution function of the solar-wind plasma," *Journal of Geophysical Research*, vol. 76, no. 31, pp. 7503–7507, 1971.
- [23] J. J. Ramos, "Dynamic evolution of the heat fluxes in a collisionless magnetized plasma," *Phys. Plasmas*, vol. 10, no. 9, p. 3601, 2003.
- [24] J. J. Ramos, "Fluid formalism for collisionless magnetized plasmas," *Phys. Plasmas*, vol. 12, no. 5, p. 052102, 2005.
- [25] M. D. Kruskal and C. R. Oberman, "On the Stability of Plasma in Static Equilibrium," *Phys. Fluids*, vol. 1, no. 4, p. 275, 1958.
- [26] M. N. Rosenbluth and N. Rostoker, "Theoretical Structure of Plasma Equations," *Phys. Fluids*, vol. 2, no. 1, p. 23, 1959.
- [27] V. Shafranov, "Plasma equilibrium in a magnetic field," in *Reviews of Plasma Physics*, vol. 2, p. 103, New York: Consultants Bureau, 1966.
- [28] A. Boozer, "Plasma equilibrium with rational magnetic surfaces," *Physics of Fluids*, vol. 24, no. 11, pp. 1999–2003, 1981.
- [29] S. Hamada, "Hydromagnetic equilibria and their proper coordinates," *Nuclear Fusion*, vol. 2, no. 1-2, p. 23, 1962.
- [30] J. P. Goedbloed, R. Keppens, and S. Poedts, *Advanced Magnetohydrodynamics With Applications to Laboratory and Astrophysical Plasma*. Cambridge University Press, 2010.
- [31] R. White, *The Theory of Toroidally Confined Plasmas*. Imperial College Press, 2006.
- [32] W. W. Heidbrink, "Basic physics of Alfvén instabilities driven by energetic particles in toroidally confined plasmas)," *Physics of Plasmas*, vol. 15, no. 5, 2008.
- [33] W. W. Heidbrink, "Alpha particle physics in a tokamak burning plasma experiment," *Physics of Plasmas*, vol. 9, no. 5, pp. 2113–2119, 2002.

- 
- [34] G. W. Bowden and M. J. Hole, “A singular finite element technique for calculating continuum damping of Alfvén eigenmodes,” *Physics of Plasmas*, vol. 22, no. 2, 2015.
- [35] G. W. Bowden, M. J. Hole, and A. Könies, “Calculation of continuum damping of Alfvén eigenmodes in tokamak and stellarator equilibria,” *Physics of Plasmas*, vol. 22, no. 9, 2015.
- [36] A. Fasoli *et al.*, “Chapter 5: Physics of energetic ions,” *Nuclear Fusion*, vol. 47, no. 6, p. S264, 2007.
- [37] S. Pinches, *Nonlinear Interaction of Fast Particles with Alfvén Waves in Tokamaks*. PhD thesis, 1996.
- [38] H. Berk, D. Borba, B. Breizman, S. Pinches, and S. Sharapov, “Theoretical Interpretation of Alfvén Cascades in Tokamaks with Nonmonotonic  $q$  Profiles,” *Phys. Rev. Lett.*, vol. 87, p. 185002, oct 2001.
- [39] N. Gorelenkov, H. Berk, E. Fredrickson, and S. Sharapov, “Predictions and observations of low-shear beta-induced shear Alfvén–acoustic eigenmodes in toroidal plasmas,” *Phys. Lett. A*, vol. 370, pp. 70–77, oct 2007.
- [40] A. D. Turnbull, E. J. Strait, W. W. Heidbrink, M. S. Chu, H. H. Duong, J. M. Greene, L. L. Lao, T. S. Taylor, and S. J. Thompson, “Global Alfvén modes: Theory and experiment,” *Phys. Fluids B*, vol. 5, no. 7, p. 2546, 1993.
- [41] C. Z. Cheng and M. S. Chance, “Low- $n$  shear Alfvén spectra in axisymmetric toroidal plasmas,” *Phys. Fluids*, vol. 29, no. 1986, pp. 3695–3701, 1986.
- [42] R. Betti and J. P. Freidberg, “Ellipticity induced Alfvén eigenmodes,” *Phys. Fluids B Plasma Phys.*, vol. 3, no. 8, pp. 1865–1870, 1991.
- [43] L. Chen and F. Zonca, “Physics of Alfvén waves and energetic particles in burning plasmas,” *Reviews of Modern Physics*, vol. 88, p. 015008, mar 2016.
- [44] L. Chen, R. White, and M. Rosenbluth, “Excitation of internal kink modes by trapped energetic beam ions,” *Phys. Rev. Lett.*, vol. 52, no. 13, pp. 1122–1125, 1984.
- [45] R. Nazikian, G. Fu, M. Austin, H. Berk, R. Budny, N. Gorelenkov, W. Heidbrink, C. Holcomb, G. Kramer, G. McKee, M. Makowski, W. Solomon, M. Shafer, E. Strait, and M. Zeeland, “Intense Geodesic Acousticlike Modes Driven by Suprathermal Ions in a Tokamak Plasma,” *Physical Review Letters*, vol. 101, p. 185001, Oct. 2008.
- [46] G. Fu, “Energetic-particle-induced geodesic acoustic mode,” *Physical review letters*, vol. 101, p. 185002, Oct. 2008.
- [47] I. B. Bernstein, J. M. Greene, and M. D. Kruskal, “Exact nonlinear plasma oscillations,” *Physical Review*, vol. 108, no. 3, pp. 546–550, 1957.
- [48] H. L. Berk, B. N. Breizman, J. Candy, M. Pekker, and N. V. Petviashvili, “Spontaneous hole–clump pair creation,” *Phys. Plasmas*, vol. 6, no. 8, p. 3102, 1999.
- [49] H. L. Berk, B. N. Breizman, and M. Pekker, “Numerical simulation of bump-on-tail instability with source and sink,” *Phys. Plasmas*, vol. 2, no. 8, p. 3007, 1995.

- 
- [50] H. Berk, B. Breizman, and M. Pekker, “Nonlinear Dynamics of a Driven Mode near Marginal Stability,” *Phys. Rev. Lett.*, vol. 76, pp. 1256–1259, feb 1996.
- [51] H. Berk, B. Breizman, and N. Petviashvili, “Spontaneous hole-clump pair creation in weakly unstable plasmas,” *Phys. Lett. A*, vol. 234, no. 3, pp. 213–218, 1997.
- [52] B. N. Breizman, H. L. Berk, M. S. Pekker, F. Porcelli, G. V. Stupakov, and K. L. Wong, “Critical nonlinear phenomena for kinetic instabilities near threshold,” *Phys. Plasmas*, vol. 4, no. 5, p. 1559, 1997.
- [53] B. N. Breizman, “Nonlinear travelling waves in energetic particle phase space,” *Nucl. Fusion*, vol. 50, no. 8, p. 084014, 2010.
- [54] F. M. Levinton, R. J. Fonck, G. M. Gammel, R. Kaita, H. W. Kugel, E. T. Powell, and D. W. Roberts, “Magnetic field pitch-angle measurements in the PBX-M tokamak using the motional Stark effect,” *Phys. Rev. Lett.*, vol. 63, pp. 2060–2063, Nov 1989.
- [55] L. Lao, H. John, R. Stambaugh, A. Kellman, and W. Pfeiffer, “Reconstruction of current profile parameters and plasma shapes in tokamaks,” *Nuclear fusion*, vol. 25, no. 11, p. 1611, 1985.
- [56] M. J. Walsh, E. R. Arends, P. G. Carolan, M. R. Dunstan, M. J. Forrest, S. K. Nielsen, and R. O’Gorman, “Combined visible and infrared Thomson scattering on the MAST experiment,” *Review of Scientific Instruments*, vol. 74, no. 3, pp. 1663–1666, 2003.
- [57] R. Hawryluk, “An empirical approach to tokamak transport,” 1979.
- [58] G. Huysmans, J. Goedbloed, and W. Kerner, “Isoparametric bicubic Hermite elements for solution of the Grad–Shafranov equation,” p. 371, 1991.
- [59] A. B. Mikhailovskii and G. T. A. Huysmans, “Optimization of computational MHD normal-mode analysis for tokamaks,” *Plasma Physics Reports*, vol. 23, no. 10, p. 844, 1997.
- [60] S. Poedts and E. Schwartz, “Computation of the ideal-MHD continuous spectrum in axisymmetric plasmas,” *Journal of computational physics*, vol. 105, no. 1, pp. 165–168, 1993.
- [61] S. Pinches, L. Appel, J. Candy, S. Sharapov, H. Berk, D. Borba, B. Breizman, T. Hender, K. Hopcraft, G. Huysmans, and W. Kerner, “The HAGIS self-consistent nonlinear wave-particle interaction model,” *Comput. Phys. Commun.*, vol. 111, pp. 133–149, June 1998.
- [62] N. Winsor, J. L. Johnson, and J. M. Dawson, “Geodesic Acoustic Waves in Hydro-magnetic Systems,” *Phys. Fluids*, vol. 11, no. 11, p. 2448, 1968.
- [63] K. Hallatschek and D. Biskamp, “Transport control by coherent zonal flows in the core/edge transitional regime,” *Phys. Rev. Lett.*, vol. 86, no. 1, pp. 1223–1226, 2001.
- [64] G. D. Conway, C. Angioni, F. Ryter, P. Sauter, and J. Vicente, “Mean and oscillating plasma flows and turbulence interactions across the L-H confinement transition,” *Phys. Rev. Lett.*, vol. 106, no. February, pp. 1–4, 2011.

- 
- [65] M. Xu, G. R. Tynan, P. H. Diamond, P. Manz, C. Holland, N. Fedorczak, S. C. Thakur, J. H. Yu, K. J. Zhao, J. Q. Dong, J. Cheng, W. Y. Hong, L. W. Yan, Q. W. Yang, X. M. Song, Y. Huang, L. Z. Cai, W. L. Zhong, Z. B. Shi, X. T. Ding, X. R. Duan, and Y. Liu, “Frequency-resolved nonlinear turbulent energy transfer into zonal flows in strongly heated l-mode plasmas in the HL-2A Tokamak,” *Phys. Rev. Lett.*, vol. 108, no. June, pp. 1–5, 2012.
- [66] D. Zarzoso, Y. Sarazin, X. Garbet, R. Dumont, a. Strugarek, J. Abiteboul, T. Cartier-Michaud, G. Dif-Pradalier, P. Ghendrih, V. Grandgirard, G. Latu, C. Passeron, and O. Thomine, “Impact of energetic-particle-driven geodesic acoustic modes on turbulence,” *Phys. Rev. Lett.*, vol. 110, no. March, pp. 1–5, 2013.
- [67] A. Fujisawa, “A review of zonal flow experiments,” *Nucl. Fusion*, vol. 49, p. 013001, 2008.
- [68] J. C. Hillesheim, W. a. Peebles, T. a. Carter, L. Schmitz, and T. L. Rhodes, “Experimental investigation of geodesic acoustic mode spatial structure, intermittency, and interaction with turbulence in the DIII-D tokamak,” *Phys. Plasmas*, vol. 19, no. 2012, 2012.
- [69] J. R. Robinson, B. Hnat, P. Dura, a. Kirk, and P. Tamain, “Interaction between a low-frequency electrostatic mode and resonant magnetic perturbations in MAST,” *Plasma Physics and Controlled Fusion*, vol. 54, p. 105007, Oct. 2012.
- [70] K. Itoh, K. Hallatschek, and S.-I. Itoh, “Excitation of geodesic acoustic mode in toroidal plasmas,” *Plasma Phys. Control. Fusion*, vol. 47, pp. 451–458, 2005.
- [71] N. Chakrabarti, R. Singh, P. K. Kaw, and P. N. Guzdar, “Nonlinear excitation of geodesic acoustic modes by drift waves,” *Phys. Plasmas*, vol. 14, no. 2007, pp. 0–6, 2007.
- [72] V. B. Lebedev, P. N. Yushmanov, P. H. Diamond, S. V. Novakovskii, and a. I. Smolyakov, “Plateau regime dynamics of the relaxation of poloidal rotation in tokamak plasmas,” *Physics of Plasmas*, vol. 3, no. 8, p. 3023, 1996.
- [73] H. Sugama and T.-H. Watanabe, “Collisionless damping of geodesic acoustic modes,” *Journal of Plasma Physics*, vol. 72, p. 825, Dec. 2006.
- [74] Y. I. Kolesnichenko, B. S. Lepiavko, and Y. V. Yakovenko, “Equations for drift-Alfvén and drift-sound eigenmodes in toroidal plasmas,” *Plasma Physics and Controlled Fusion*, vol. 54, p. 105001, Oct. 2012.
- [75] R. Sgalla, a. Smolyakov, a. Elfimov, and M. Bashir, “Drift effects on geodesic acoustic modes,” *Physics Letters A*, vol. 377, pp. 303–306, Jan. 2013.
- [76] W. Zwingmann, L.-G. Eriksson, and P. Stubberfiel, “Equilibrium analysis of tokamak discharges with anisotropic pressure,” *Plasma Phys. Control. Fusion*, vol. 43, p. 1441, 2001.
- [77] M. J. Hole, G. von Nessi, M. Fitzgerald, K. G. McClements, and J. Svensson, “Identifying the impact of rotation, anisotropy, and energetic particle physics in tokamaks,” *Plasma Phys. Control. Fusion*, vol. 53, p. 074021, July 2011.



- 
- [78] T. Northrop and K. Whiteman, “Minimum-B Plasma Equilibria with Finite Pressure,” *Phys. Rev. Lett.*, vol. 12, no. 2, pp. 639–640, 1964.
- [79] D. Dobrott, “Steady Flow in the Axially Symmetric Torus Using the Guiding-Center Equations,” *Phys. Fluids*, vol. 13, no. 9, p. 2391, 1970.
- [80] G. O. Spies, “Properties of magnetically confined plasma equilibria,” *Phys. Fluids*, vol. 17, no. 10, p. 1879, 1974.
- [81] E. R. Salberta, R. C. Grimm, J. L. Johnson, J. Manickam, and W. M. Tang, “Anisotropic pressure tokamak equilibrium and stability considerations,” *Phys. Fluids*, vol. 30, no. 9, p. 2796, 1987.
- [82] W. Cooper, G. Bateman, D. Nelson, and T. Kammash, “Beam-induced tensor pressure tokamak equilibria,” 1980.
- [83] R. Iacono, A. Bondeson, F. Troyon, and R. Gruber, “Axisymmetric Toroidal Equilibrium with Flow and Anisotropic pressure,” *Phys. Fluids B*, vol. 2, no. 8, pp. 1794–1803, 1990.
- [84] V. D. Pustovitov, “Anisotropic pressure effects on plasma equilibrium in toroidal systems,” *Plasma Phys. Control. Fusion*, vol. 52, p. 065001, jun 2010.
- [85] L. Zakharov and V. Shafranov, *Reviews of plasma physics*, vol. 11, pp. 153–302. 1986.
- [86] N. Madden and R. Hastie, “Tokamak Equilibrium with anisotropic pressure,” *Nuclear Fusion*, vol. 34, no. 4, pp. 519–526, 1994.
- [87] V. D. Pustovitov, “Extension Of Conventional MHD Equilibrium Theory To Model The Fast Particle Effects,” *AIP Conf.Proc.*, no. 1478, pp. 50–64, 2012.
- [88] L. Guazzotto, R. Betti, J. Manickam, and S. Kaye, “Numerical Study of Tokamak Equilibria with Arbitrary Flow,” *Phys. Plasmas*, vol. 11, no. 2, pp. 604–14, 2004.
- [89] M. J. Hole, G. von Nessi, and M. Fitzgerald, “Fast particle modifications to equilibria and resulting changes to Alfvén wave modes in tokamaks,” *Plasma Phys. Control. Fusion*, vol. 55, p. 014007, Jan. 2013.
- [90] E. Belova, N. Gorelenkov, and C. Cheng, “Self-consistent equilibrium model of low aspect-ratio toroidal plasma with energetic beam ions,” *Phys. Plasmas*, vol. 10, no. 8, p. 3240, 2003.
- [91] Y. Todo, K. Shinohara, M. Takechi, and M. Ishikawa, “Nonlocal energetic particle mode in a JT-60U plasma,” *Phys. Plasmas*, vol. 12, no. 1, p. 012503, 2005.
- [92] M. Fitzgerald, L. Appel, and M. Hole, “EFIT tokamak equilibria with toroidal flow and anisotropic pressure using the two-temperature guiding-centre plasma,” *Nuclear Fusion*, vol. 53, p. 113040, nov 2013.
- [93] G. Huysmans, J. Goedbloed, and W. Kerner, “Isoparametric bicubic Hermite elements for solution of the Grad–Shafranov equation,” in *Proc. CP90 Conf. on Computational Physics (Amsterdam)*, p. 371, 1991.

- 
- [94] E. Parker, “Dynamical Instability in an Anisotropic Ionized Gas of Low Density,” *Phys. Rev.*, vol. 109, no. 6, pp. 1874–1876, 1958.
  - [95] R. Akers *et al.*, “Transport and confinement in the Mega Ampere Spherical Tokamak (MAST) plasma,” *Plasma Phys. Control. Fusion*, vol. 45, pp. A175–A124, 2003.
  - [96] W. A. Cooper and A. J. Wootton, “ $\beta_p$  Analysis for Tokamak Plasma With Anisotropic Pressure and Mass Flow,” *Plasma Phys. Control. Fusion*, vol. 24, no. 9, pp. 1183–1185, 1982.
  - [97] L. Lao, H. St.John, and R. Stambaugh, “Separation of  $\bar{\beta}_p$  and  $l_i$  in Tokamaks of Non-circular Cross-section,” *Nuclear Fusion*, vol. 25, no. 10, pp. 1421–1436, 1985.
  - [98] V. Shafranov, “Determination of the parameters  $\beta I$  and  $l_i$  in a Tokamak for arbitrary shape of plasma pinch cross-section,” *Plasma Phys.*, vol. 757, 1971.
  - [99] D. a. Gates, “High  $\beta$ , long pulse, bootstrap sustained scenarios on the National Spherical Torus Experiment (NSTX),” *Phys. Plasmas*, vol. 10, no. 5, p. 1659, 2003.
  - [100] T. R. Barrett, C. Jones, P. Blatchford, B. Smith, R. McAdams, and N. Woods, “Engineering design of the double neutral beam injection system for {MAST} Upgrade,” *Fusion Eng. Des.*, vol. 86, no. 6–8, pp. 789–792, 2011.
  - [101] Z. S. Qu, M. Fitzgerald, and M. J. Hole, “Analysing the impact of anisotropy pressure on tokamak equilibria,” *Plasma Phys. Control. Fusion*, vol. 56, p. 075007, July 2014.
  - [102] I. Bernstein, E. A. Frieman, M. D. Kruskal, and R. M. Kulsrud, “An energy principle for hydromagnetic stability problems,” *Proc. R. Soc. Lond. A. Math. Phys. Sci.*, vol. 244, no. 1236, pp. 17–40, 1958.
  - [103] T. Chust and G. Belmont, “Closure of fluid equations in collisionless magnetoplasmas,” *Phys. Plasmas*, vol. 13, no. 1, p. 012506, 2006.
  - [104] W. Cooper, G. Bateman, D. B. Nelson, and T. Kammash, “Neutral beam effects on Tokamak ballooning mode stability,” *Plasma Phys.*, vol. 23, pp. 105–120, 1981.
  - [105] X.-H. Wang and a. Bhattacharjee, “Ballooning stability of anisotropic, rotating plasmas,” *Phys. Fluids B*, vol. 2, no. 10, p. 2346, 1990.
  - [106] T. M. Antonsen and Y. C. Lee, “Electrostatic modification of variational principles for anisotropic plasmas,” *Physics of Fluids*, vol. 25, no. 1, p. 132, 1982.
  - [107] J. P. Graves, C. Angioni, R. V. Budny, R. J. Buttery, S. Coda, L.-G. Eriksson, C. G. Gimblett, T. P. Goodman, R. J. Hastie, M. a. Henderson, H. R. Koslowski, M. J. Mantsinen, A. Martynov, M.-L. Mayoral, a. Mück, M. F. F. Nave, O. Sauter, E. Westerhof, and J.-E. Contributors, “Sawtooth control in fusion plasmas,” *Plasma Phys. Control. Fusion*, vol. 47, pp. B121–B133, Dec. 2005.
  - [108] I. T. Chapman, “Controlling sawtooth oscillations in tokamak plasmas,” *Plasma Phys. Control. Fusion*, vol. 53, p. 013001, Jan. 2011.
  - [109] J. Connor and R. Hastie, “Effect of anisotropic pressure on the localized magneto-hydrodynamic interchange modes in an axisymmetric torus,” *Phys. Fluids*, vol. 19, no. 11, p. 1727, 1976.

- 
- [110] W. A. Cooper, S. P. Hirshman, P. Merkel, J. P. Graves, J. Kisslinger, H. F. G. Wobig, Y. Narushima, S. Okamura, and K. Y. Watanabe, “Three-dimensional anisotropic pressure free boundary equilibria,” *Comput. Phys. Commun.*, vol. 180, no. 9, pp. 1524–1533, 2009.
- [111] Y. Asahi, Y. Suzuki, K. Y. Watanabe, and W. A. Cooper, “Development of an identification method of pressure anisotropy based on equilibrium analysis and magnetics,” *Phys. Plasmas*, vol. 20, no. 2, p. 022503, 2013.
- [112] J. L. Johnson, R. M. Kulsrud, and K. E. Weimer, “Application of the energy principle to Astron-type and other axisymmetric devices,” *Plasma Phys.*, vol. 11, no. 6, pp. 463–472, 1969.
- [113] D. V. Anderson, W. A. Cooper, R. Gruber, S. Merazzi, and U. Schwenn, “Methods for the Efficient Calculation of the Magnetohydrodynamic (MHD) Stability Properties of Magnetically Confined Fusion Plasmas,” *Int. J. Supercomp. Appl.*, vol. 4, pp. 34–47, Fall 1990.
- [114] W. A. Cooper, Y. Asahi, Y. Narushima, Y. Suzuki, K. Y. Watanabe, J. P. Graves, and M. Y. Isaev, “Equilibrium and stability in a heliotron with anisotropic hot particle slowing-down distribution,” *Phys. Plasmas*, vol. 19, no. 10, p. 102503, 2012.
- [115] S. Sharapov *et al.*, “Energetic particle instabilities in fusion plasmas,” *Nucl. Fusion*, vol. 53, p. 104022, Oct. 2013.
- [116] M. J. Hole and M. Fitzgerald, “Resolving the wave–particle–plasma interaction: advances in the diagnosis, interpretation and self-consistent modelling of waves, particles and the plasma configuration,” *Plasma Phys. Control. Fusion*, vol. 56, p. 053001, May 2014.
- [117] G. T. A. Huysmans, S. E. Sharapov, A. B. Mikhailovskii, and W. Kerner, “Modeling of diamagnetic stabilization of ideal magnetohydrodynamic instabilities associated with the transport barrier,” *Phys. Plasmas*, vol. 8, no. 10, p. 4292, 2001.
- [118] I. T. Chapman, S. E. Sharapov, G. T. A. Huysmans, and A. B. Mikhailovskii, “Modeling the effect of toroidal plasma rotation on drift-magnetohydrodynamic modes in tokamaks,” *Phys. Plasmas*, vol. 13, no. 6, p. 062511, 2006.
- [119] R. K. Chhajlani and S. C. Bhand, “Derivation of CGL theory with finite Larmor radius corrections,” *Journal of Plasma Physics*, vol. 23, no. 02, p. 205, 1980.
- [120] A. B. Mikhailovskii *Sov. J. Plasma Phys*, vol. 9, p. 190, 1983.
- [121] T. Takeda and S. Tokuda, “Computation of MHD equilibrium of tokamak plasma,” *J. Comput. Phys.*, vol. 93, no. 1, pp. 1–107, 1991.
- [122] K. G. McClements, R. O. Dendy, R. J. Hastie, and T. J. Martin, “Modeling of sawtooth destabilization during radio-frequency heating experiments in tokamak plasmas,” *Phys. Plasmas*, vol. 3, no. 8, p. 2994, 1996.
- [123] T. Hellsten and J. Scheffel, “Continuous Double Adiabatic Spectrum in Toroidal Plasmas,” *Physica Scripta*, vol. 30, no. 1, pp. 78–82, 1984.

- 
- [124] M. Bussac, R. Pellat, D. Edery, and J. Soule, “Internal kink modes in toroidal plasmas with circular cross sections,” *Phys. Rev. Lett.*, vol. 35, no. December, 1975.
  - [125] A. B. Mikhailovskii, *Instabilities in a confined plasma*, pp. 257–281. Institute of Physics Publishing, 1998.
  - [126] J. P. Graves, O. Sauter, and N. N. Gorelenkov, “The internal kink mode in an anisotropic flowing plasma with application to modeling neutral beam injected sawtooth discharges,” *Phys. Plasmas*, vol. 10, no. 4, p. 1034, 2003.
  - [127] B. Layden, M. J. Hole, and R. Ridden-Harper, “High-beta equilibria in tokamaks with pressure anisotropy and toroidal flow,” *Phys. Plasmas*, vol. 22, p. 122513, 2015.
  - [128] S. C. Cowley, P. K. Kaw, R. S. Kelly, and R. M. Kulsrud, “An analytic solution of highbeta equilibrium in a large aspect ratio tokamak,” *Phys. Fluids B*, vol. 3, no. 8, p. 2066, 1991.
  - [129] S. C. Hsu, M. Artun, and S. C. Cowley, “Calculation and interpretation of analytic high-beta poloidal equilibria in finite aspect ratio tokamaks,” *Phys. Plasmas*, vol. 3, no. 1, p. 266, 1996.
  - [130] M. Fitzgerald, S. Sharapov, and M. Hole, “High- $\beta$  equilibria in tokamaks with toroidal flow,” *Phys. Plasmas*, vol. 18, no. 9, p. 092508, 2011.
  - [131] Z. S. Qu, M. J. Hole, and M. Fitzgerald, “Modeling the effect of anisotropic pressure on tokamak plasmas normal modes and continuum using fluid approaches,” *Plasma Phys. Control. Fusion*, vol. 57, p. 095005, sep 2015.
  - [132] M. J. Hole, G. von Nessi, J. Svensson, L. C. Appel, and t. M. Team, “An equilibrium validation technique based on Bayesian inference,” *Nucl. Fusion*, vol. 51, p. 103005, 2011.
  - [133] D. L. Keeling, T. R. Barrett, M. Cecconello, C. D. Challis, N. Hawkes, O. M. Jones, I. Klimek, K. G. McClements, A. Meakins, J. Milnes, M. Turnyanskiy, and t. M. Team, “Mitigation of MHD induced fast-ion redistribution in MAST and implications for MAST-Upgrade design,” *Nucl. Fusion*, vol. 55, p. 013021, 2015.
  - [134] B. Coppi and G. Rewoldt, “Collective modes in confined high temperature plasmas,” in *Advances in Plasma Physics* (A. Simon and W. B. Thompson, eds.), vol. 6, p. 421, New York: Interscience, 1976.
  - [135] F. Porcelli, R. Stankiewicz, W. Kerner, and H. L. Berk, “Solution of the driftkinetic equation for global plasma modes and finite particle orbit widths,” *Phys. Plasmas*, vol. 1, no. 3, pp. 470–480, 1994.
  - [136] G. Y. Fu and C. Z. Cheng, “Excitation of high-n toroidicity-induced shear Alfvén eigenmodes by energetic particles and fusion alpha particles in tokamaks,” *Phys. Fluids B*, vol. 4, no. 11, pp. 3722–3734, 1992.
  - [137] B. N. Breizman and S. E. Sharapov, “Energetic particle drive for toroidicity-induced Alfvén eigenmodes and kinetic toroidicity-induced Alfvén eigenmodes in a low-shear tokamak,” *Plasma Phys. Control. Fusion*, vol. 37, no. 10, p. 1057, 1995.

- 
- [138] H. L. Berk, B. N. Breizman, and H. Ye, “Finite orbit energetic particle linear response to toroidal Alfvén eigenmodes,” *Phys. Lett. A*, vol. 162, no. 6, p. 475, 1992.
- [139] T. Fülöp, M. Lisak, Y. I. Kolesnichenko, and D. Anderson, “Finite orbit width stabilizing effect on toroidal Alfvén eigenmodes excited by passing and trapped energetic ions,” *Plasma Phys. Control. Fusion*, vol. 38, no. 6, p. 811, 1996.
- [140] G. A. Cooper, M. Jucker, W. A. Cooper, J. P. Graves, and M. Y. Isaev, “Exact canonical drift Hamiltonian formalism with pressure anisotropy and finite perturbed fields,” *Phys. Plasmas*, vol. 14, no. 10, p. 102506, 2007.
- [141] W. A. Cooper, G. A. Cooper, J. P. Graves, and M. Y. Isaev, “Full-field drift Hamiltonian particle orbits in axisymmetric tokamak geometry,” *Phys. Plasmas*, vol. 18, no. 5, p. 052507, 2011.
- [142] R. B. White, A. H. Boozer, and R. Hay, “Drift Hamiltonian in magnetic coordinates,” *Phys. Fluids*, vol. 25, no. 3, p. 575, 1982.
- [143] B. Hamilton, K. G. McClements, L. Fletcher, and A. Thyagaraja, “Field-guided proton acceleration at reconnecting X-points in flares,” *Sol. Phys.*, vol. 214, no. 2, pp. 339–352, 2003.
- [144] M. Cecconello, O. M. Jones, W. U. Boeglin, R. V. Perez, D. S. Darrow, I. Klimek, S. E. Sharapov, M. Fitzgerald, K. G. McClements, D. L. Keeling, S. Y. Allan, C. A. Michael, R. J. Akers, N. J. Conway, R. Scannell, M. Turnyanskiy, G. Ericsson, and t. M. Team, “Energetic ion behaviour in MAST,” *Plasma Phys. Control. Fusion*, vol. 57, no. 1, p. 014006, 2015.
- [145] I. T. Chapman, M. F. De Bock, S. D. Pinches, M. R. Turnyanskiy, t. M. Team, V. G. Igochine, M. Maraschek, G. Tardini, and t. A. U. Team, “The effect of off-axis neutral beam injection on sawtooth stability in ASDEX Upgrade and Mega-Ampere Spherical Tokamak,” *Phys. Plasmas*, vol. 16, no. 7, p. 072506, 2009.
- [146] I. T. Chapman, M.-D. Hua, S. D. Pinches, R. J. Akers, A. R. Field, J. P. Graves, R. J. Hastie, C. A. Michael, and t. M. Team, “Saturated ideal modes in advanced tokamak regimes in MAST,” *Nucl. Fusion*, vol. 50, no. 4, p. 045007, 2010.
- [147] K. G. McClements, M. P. Gryaznevich, S. E. Sharapov, R. J. Akers, L. C. Appel, G. F. Counsell, C. M. Roach, and R. Majeski, “The effect of off-axis neutral beam injection on sawtooth stability in ASDEX Upgrade and Mega-Ampere Spherical Tokamak,” *Plasma Phys. Control. Fusion*, vol. 41, no. 5, p. 661, 1999.
- [148] T. O’Neil, “Collisionless Damping of Nonlinear Plasma Oscillations,” *Phys. Fluids*, vol. 8, no. 12, p. 2255, 1965.
- [149] Y. Wu, R. B. White, Y. Chen, and M. N. Rosenbluth, “Nonlinear evolution of the alpha-particle-driven toroidicity-induced Alfvén eigenmode,” *Phys. Plasmas*, vol. 2, no. 12, p. 4555, 1995.
- [150] M. K. Lilley, B. N. Breizman, and S. E. Sharapov, “Effect of dynamical friction on nonlinear energetic particle modes,” *Phys. Plasmas*, vol. 17, no. 9, p. 092305, 2010.

- 
- [151] T. Ido, a. Shimizu, M. Nishiura, S. Nakamura, S. Kato, H. Nakano, Y. Yoshimura, K. Toi, K. Ida, M. Yoshinuma, S. Satake, F. Watanabe, S. Morita, M. Goto, K. Itoh, S. Kubo, T. Shimozuma, H. Igami, H. Takahashi, I. Yamada, and K. Narihara, “Potential fluctuation associated with the energetic-particle-induced geodesic acoustic mode in the Large Helical Device,” *Nucl. Fusion*, vol. 51, p. 073046, 2011.
- [152] W. Chen, X. Ding, L. Yu, X. Ji, Z. Shi, Y. Zhang, W. Zhong, G. Yuan, J. Dong, Q. Yang, Y. Liu, L. Yan, Y. Zhou, M. Jiang, W. Li, X. Song, S. Chen, and X. Duan, “Observation of energetic-particle-induced GAM and nonlinear interactions between EGAM, BAEs and tearing modes on the HL-2A tokamak,” *Nucl. Fusion*, vol. 53, p. 113010, 2013.
- [153] R. Fisher, D. Pace, G. Kramer, M. Van Zeeland, R. Nazikian, W. Heidbrink, and M. García-Muñoz, “Beam ion losses due to energetic particle geodesic acoustic modes,” *Nucl. Fusion*, vol. 52, p. 123015, 2012.
- [154] H. Berk and T. Zhou, “Fast excitation of EGAM by NBI,” *Nuclear Fusion*, vol. 50, p. 035007, 2010.
- [155] Z. Qiu, F. Zonca, and L. Chen, “Nonlocal theory of energetic-particle-induced geodesic acoustic mode,” *Plasma Physics and Controlled Fusion*, vol. 52, p. 095003, Sept. 2010.
- [156] Y. I. Kolesnichenko, B. S. Lepiavko, and V. V. Lutsenko, “Geodesic acoustic mode in tokamaks: local consideration and eigenvalue analysis,” *Plasma Phys. Control. Fusion*, vol. 55, p. 125007, 2013.
- [157] L. Wang, J. Q. Dong, Z. He, H. He, and Y. Shen, “Energetic-particle-induced electromagnetic geodesic acoustic mode in tokamak plasmas,” *Physics of Plasmas*, vol. 21, p. 072511, July 2014.
- [158] D. Zarzoso, X. Garbet, Y. Sarazin, R. Dumont, and V. Grandgirard, “Fully kinetic description of the linear excitation and nonlinear saturation of fast-ion-driven geodesic acoustic mode instability,” *Physics of Plasmas*, vol. 19, no. 2, p. 022102, 2012.
- [159] H. Wang and Y. Todo, “Linear properties of energetic particle driven geodesic acoustic mode,” *Phys. Plasmas*, vol. 20, pp. 0–8, 2013.
- [160] H. Wang, Y. Todo, and C. C. Kim, “Hole-clump pair creation in the evolution of energetic-particle-driven geodesic acoustic modes,” *Physical Review Letters*, vol. 110, no. 15, p. 155006, 2013.
- [161] D. Zarzoso, a. Biancalani, a. Bottino, P. Lauber, E. Poli, J.-B. Girardo, X. Garbet, and R. Dumont, “Analytic dispersion relation of energetic particle driven geodesic acoustic modes and simulations with NEMORB,” *Nuclear Fusion*, vol. 54, p. 103006, Oct. 2014.
- [162] J.-B. Girardo, D. Zarzoso, R. Dumont, X. Garbet, Y. Sarazin, and S. Sharapov, “Relation between energetic and standard geodesic acoustic modes,” *Physics of Plasmas*, vol. 21, p. 092507, Sept. 2014.

- 
- [163] A. Hasegawa, “Theory of longitudinal plasma instabilities,” *Phys. Rev. Lett.*, vol. 169, no. 1, pp. 204–214, 1968.
- [164] D. Bohm and E. P. Gross, “Theory of plasma oscillations. B. Excitation and damping of oscillations,” *Phys. Rev.*, vol. 75, no. 12, pp. 1864–1876, 1949.
- [165] A. I. Akhiezer and Y. B. Fainberg *Dokl. Akad. Nauk SSSR.*, vol. 69, p. 555, 1949.
- [166] C. T. Dum, “Transition in the dispersive properties of beam-plasma and two-stream instabilities,” *J. Geophys. Res.*, vol. 94, no. A3, pp. 2429–2442, 1989.
- [167] T. M. O’Neil and J. H. Malmberg, “Transition of the Dispersion Roots from Beam-Type to Landau-Type Solutions,” *Phys. Fluids*, vol. 11, no. 8, pp. 1754–1760, 1968.
- [168] Z. Qiu, F. Zonca, and L. Chen, “Geodesic acoustic mode excitation by a spatially broad energetic particle beam,” *Phys. Plasmas*, vol. 19, no. 8, p. 082507, 2012.
- [169] M. Lesur, K. Itoh, T. Ido, M. Osakabe, K. Ogawa, A. Shimizu, M. Sasaki, K. Ida, S. Inagaki, and S. I. Itoh, “Nonlinear Excitation of Subcritical Instabilities in a Toroidal Plasma,” *Physical Review Letters*, vol. 116, no. 1, pp. 1–5, 2016.
- [170] T. Ido, K. Itoh, M. Osakabe, M. Lesur, A. Shimizu, K. Ogawa, K. Toi, M. Nishiura, S. Kato, M. Sasaki, K. Ida, S. Inagaki, and S. I. Itoh, “Strong Destabilization of Stable Modes with a Half-Frequency Associated with Chirping Geodesic Acoustic Modes in the Large Helical Device,” *Physical Review Letters*, vol. 116, no. 1, pp. 1–5, 2016.
- [171] M. Sasaki, N. Kasuya, K. Itoh, K. Hallatschek, M. Lesur, Y. Kosuga, and S. I. Itoh, “A branch of energetic-particle driven geodesic acoustic modes due to magnetic drift resonance,” *Physics of Plasmas*, vol. 23, no. 10, 2016.
- [172] J. Cao, Z. Qiu, and F. Zonca, “Fast excitation of geodesic acoustic mode by energetic particle beams,” *Physics of Plasmas*, vol. 22, no. 12, 2015.
- [173] Z. S. Qu, M. J. Hole, and M. Fitzgerald, “Energetic Geodesic Acoustic Modes Associated with Two-Stream-like Instabilities in Tokamak Plasmas,” *Phys. Rev. Lett.*, vol. 116, no. 9, p. 095004, 2016.
- [174] T. Zhou, *MHD GAMs and Kinetic GAMs Driven by Energetic Particles*. PhD thesis, University of Texas at Austin, 2009.
- [175] Z. Qiu and L. Chen, “Kinetic Theories of Geodesic Acoustic Modes: Radial Structure, Linear Excitation by Energetic Particles and Nonlinear Saturation,” *Plasma Sci. Technol.*, vol. 13, no. 3, pp. 257–266, 2011.
- [176] R. Nazikian, “Nonlinear Evolution and Radial Propagation of the Energetic Particle Driven GAM,” (<http://w3fusion.ph.utexas.edu/ifs/iaeaep/talks/s1-o2-nazikian-raffi-ep-talk.pdf>), 2011.
- [177] J.-P. Berenger, “A perfectly matched layer for the absorption of electromagnetic waves,” *Journal of Computational Physics*, vol. 114, no. 2, pp. 185–200, 1994.

- 
- [178] P. Lauber, S. Günter, A. Könies, and S. D. Pinches, “LIGKA: A linear gyrokinetic code for the description of background kinetic and fast particle effects on the MHD stability in tokamaks,” *Journal of Computational Physics*, vol. 226, pp. 447–465, sep 2007.
- [179] L. Horváth, G. Papp, P. Lauber, G. Por, A. Gude, V. Igoshine, B. Geiger, M. Maraschek, L. Guimaraes, V. Nikolaeva, G. Pokol, and t. A. U. Team, “Experimental investigation of the radial structure of energetic particle driven modes,” *Nuclear Fusion*, vol. 56, no. 11, p. 112003, 2016.
- [180] P. B. Snyder, H. R. Wilson, J. R. Ferron, L. L. Lao, A. W. Leonard, T. H. Osborne, A. D. Turnbull, D. Mossessian, M. Murakami, and X. Q. Xu, “Edge localized modes and the pedestal: A model based on coupled peeling–ballooning modes,” *Physics of Plasmas*, vol. 9, p. 2037, 2014.
- [181] M. J. Hole and G. Dennis, “Energetically resolved multiple-fluid equilibria of tokamak plasmas,” *Plasma Phys. Control. Fusion*, vol. 51, p. 035014, 2009.
- [182] G. Federici, C. Skinner, J. Brooks, J. Coad, C. Grisolia, A. Haasz, A. Hassanein, V. Philipps, C. Pitcher, J. Roth, W. Wampler, and D. Whyte, “Plasma-material interactions in current tokamaks and their implications for next step fusion reactors,” *Nuclear Fusion*, vol. 41, no. 12, p. 1967, 2001.
- [183] B. D. Blackwell, J. F. Caneses, C. M. Samuell, J. Wach, J. Howard, and C. Corr, “Design and characterization of the Magnetized Plasma Interaction Experiment (MAGPIE): a new source for plasma–material interaction studies,” *Plasma Sources Sci. Technol.*, vol. 21, p. 055033, oct 2012.
- [184] L. Chang, M. J. Hole, J. F. Caneses, G. Chen, B. D. Blackwell, and C. S. Corr, “Wave modeling in a cylindrical non-uniform helicon discharge,” *Phys. Plasmas*, vol. 19, no. 8, p. 083511, 2012.
- [185] J. Santoso, R. Manoharan, S. O’Byrne, and C. S. Corr, “Negative hydrogen ion production in a helicon plasma source,” *Physics of Plasmas*, vol. 22, no. 9, 2015.
- [186] C. M. Samuell, B. D. Blackwell, J. Howard, and C. S. Corr, “Plasma parameters and electron energy distribution functions in a magnetically focused plasma,” *Phys. Plasmas*, vol. 20, no. 3, p. 034502, 2013.
- [187] M. Hole and S. Simpson, “Performance of a vacuum arc centrifuge with a nonuniform magnetic field,” *Phys. Plasmas*, vol. 4, no. April, pp. 3493–3500, 1997.
- [188] M. Hole and S. Simpson, “Separative performance in a vacuum arc centrifuge,” *Plasma Sci. IEEE Trans.*, vol. 27, no. 2, pp. 620–627, 1999.
- [189] M. Hole, R. Dallaqua, S. Simpson, and E. Del Bosco, “Plasma instability of a vacuum arc centrifuge,” *Phys. Rev. E*, vol. 65, p. 046409, mar 2002.